"Cavitation Loading and Erosion Produced by a Cavitating Jet"

by

Takahiro MOMMA, M.Eng.

Thesis submitted to the University of Nottingham
for the degree of Doctor of Philosophy, October, 1991

Abstract

The aim of the project is to investigate the detail of cavitation loading and erosion process using a submerged jet cavitation technique. Large size cavitating jet apparatus in the University of Nottingham was used with an long orifice nozzle and experiments were carried out using tap water as a test liquid with upstream pressure ranging from 80~120bar.

Distribution of the mean pressure, cavity clouds and cavitation damage on a specimen have been obtained and their mutual relation was discussed. Effects of pressures and stand off distances on the characteristics of the erosion produced by the cavitating jet were studied and the results were compared with previous investigations. These include not only the weight loss but also the size of the damage and the jet length both related with the optimum stand off distance.

Indentations on soft aluminium produced by the cavitating jet were investigated. Their size distributions were obtained for various pressures and stand off distances. Variations of the total number and the average size of indentations with stand off distance were also presented.

The cavitation loading pulses were successfully measured by a novel piezoelectric pressure transducer using PVDF polymer and the pulse height measurement system, both of which were developed in the present project. During the process to determine the size of the sensitive area of the transducer, its effect on the pulse height was found. Then, the loading pressure was estimated from the pulse height and the indentation size distribution. The value estimated is around 2GPa and compared with results of the other investigators using similar method with different, vibratory and water tunnel, cavitation facilities. All of them show the similar magnitude. Good correlations of the indentation counting and the pulse height analysis with erosion results were obtained in terms of the intensity of cavitation loading.

Simple calibration apparatus for the pressure transducer which utilises a pencil lead break as a source of high speed loading was also developed.

Acknowledgements

The work described in this thesis was carried out in the Department of Mechanical Engineering of the University of Nottingham. The opportunity and the financial support to undertake the research was granted to the author by Kajima Corporation. This is gratefully acknowledged. The author would like to express his sincere thanks to the following people.

Dr. A. Lichtarowicz who supervised the work and gave much advice and warm encouragement. The large size cavitating jet test rig used in the work was his design. It is uncountable how many times he and the author discussed problems in the L.4 Laboratory until very late at night, or even at weekends.

Mr. T. F. Roylance whose advice in discussion was always helpful.

Dr. N. J. Miles, for the image analyzer provided in the Mining Department.

Mr. M. Allen, a research student in the Mining Department, who helped the author to use the image analyzer and gave useful advice.

Mr. W. F. Ray, for designing a comparator circuit and the facilities provided in the Electrical and Electronic Engineering Department.

Mr. A. Matthews who gave not only assistance to carry out the experimental work but also practical advice to solve the problem in the laboratory.

Mr. V. Hawley and the L.4 Laboratory Staff, for their assistance with always an welcome smile.

Authorities of the University of Nottingham, for providing facilities, and all those not mentioned above who gave advice and assistance on so many occasions.

Last but not least, my wife Naoko, without her forbearance and patience the thesis could not have been completed.

LIST OF CONTENTS

Figures are numbered by a set of three numbers (except the Chapter one and Appendices). The first and the second number mean the number of the chapter and the section, respectively, e.g., Fig.2.4.3 means the third figure in Section 2.4 in Chapter 2. Figures will be found grouped together at the end of each section.

Nomenclature

Symbols are generally defined in the text as they occur, but main symbols are listed below for convenience.

A : nozzle cross sectional area, area of individual cavitation impingement

a : radius of indentation

A_T : area of the sensitive part of the pressure transducer

C : velocity of sound

C_d : discharge coefficient

C_L : velocity of sound for liquid

d : diameter of nozzle, diameter of indentation

d_e : effective diameter of the nozzle

d_s : measurement interval in diameter for size distribution of indentation counting

$\delta_{0.5}$: thickness of an wall jet

E : energy

E_0 : output voltage

F : pulse height, force

F_c : critical pulse height

f_N : natural frequency

h : distance between ring cavity and a surface

h : depth of indentation

h_1 : power index (jet length vs cavitation number)

h_2 : power index (optimum stand off distance vs cavitation number)

I : acoustic intensity of pressure wave

l : length of nozzle

l_j : jet length

m : mass, power index (time to reach the peak erosion rate vs jet velocity)

N : number of indentations

n : power index (erosion rate vs jet velocity)

p : pressure

P_0 : pressure at infinite distance

P_1 : upstream pressure

P_2 : downstream pressure

P_L : cavitation impact loading pressure

P_v : vapour pressure

P_{wh} : water hammer pressure

Q : flow rate

R : radius

r : radial distance on a target specimen from the centre

R_0 : initial radius

R_e : Reynolds number

ρ : density

S_{off} : stand off distance

S_{off1} : the first optimum stand off distance

S_{off2} : the second optimum stand off distance

σ : cavitation number

T_{max} : time to reach the peak erosion rate

ΔT : exposure time

t : thickness of piezofilm

τ : pulse duration

U_j : peak wall jet velocity in velocity profile

U_{j0} : velocity of jet just before impingement

V : flow velocity

ΔW : weight loss

Y : Young's modulus

Abbreviations

CER : Cumulative erosion rate

IER : Instantaneous erosion rate

PER : Peak erosion rate

PER_C : Peak cumulative erosion rate

PER_I : Peak instantaneous erosion rate

PVDF : Polyvinylidene Fluoride

Definitions

Number density of indentations

: number of indentations per unit time and unit area.

Area density of indentations

: sum of each indentation area per unit time and unit area.

CHAPTER ONE - INTRODUCTION

1. INTRODUCTION

If there is a solid boundary very close to a collapsing cavity, it may be eroded. This is cavitation erosion. Figures 1.1 and 1.2 show examples of cavitation erosion produced on a diesel engine cylinder liner and on diaphragms of a rotor of a dynamometer.

Since it significantly affects the life span of hydraulic machinery, the cavitation erosion is a very important problem in designing and manufacture of these machines. Many researchers have been engaged in the study of this problem to clarify the incipient condition, to understand the erosion mechanism or to develop a new material which is more strongly resisting the cavitation erosion.

For these purposes, several types of cavitation erosion testing methods such as an water tunnel and a vibratory cavitation technique have been introduced. Variety of useful experimental data have been obtained using different testing methods. However, because their primary concern was usually to compare one material resistance to cavitation erosion to the others with several types of fluid, most of their works were based only on the measurements of material loss from the erosion target.

One of the major difficulties in cavitation erosion problems is that past experimental results, or some reported damage in practice, have not been easily correlated with each other through some sort of standard measure of the cavitation loading intensity. In many cases, sufficient information about the loading for each particular cavitation condition has not been obtained and so the cavitation loading intensity has not been able to be well quantified.

There are not so many reports available which investigate the cavitation loading in a practical flow situation, although it may be the vital information for conducting the experiments and evaluating their results. Much more accumulation of data about detailed cavitation loading such as its pressure, size and density (or frequency) has been desired so far.

The aim of the project is to investigate the detail of the cavitation loading and erosion process using a submerged jet cavitation technique. Particularly, the magnitude, the size and the density of the cavitation loading and its correlation with the erosion are of main interests. It is also hoped that the detailed and series of data showing the

cavitation loading and erosion with various fluid dynamic conditions may be able to improve the understanding on cavitation erosion phenomena, not only with the submerged jet but also in general.

Fig.1.1 Cavitation erosion produced on a diesel engine cylinder liner.
(The University of Nottingham)

Fig.1.2 Cavitation erosion produced on diaphragms of a rotor of a dynamometer.
(The University of Nottingham)

CHAPTER TWO - LITERATURE SURVEY:
Bubble dynamics and damage mechanism

---

2. LITERATURE SURVEY: Bubble dynamics and damage mechanism

2.1 Introduction

It is perhaps valuable to confirm first here that cavitation damage is basically a mechanical damage. Several sorts of corrosive effects with cavitation damage have been reported and the synergy of both chemical and mechanical effects must not be ignored in some cases. However, at least at the initial stage of damage, the mechanical attack plays a predominant role in most cases.

It is widely accepted that cavitation erosion and cavitating bubble collapse are closely related. This was clearly shown by Knapp [1955]. He observed the behaviour of sheet cavitation bubbles generated on the side of a test body in a water tunnel by using the high speed photographs and counted the number of pits on a soft aluminium section of the body to quantify the intensity of cavitation damage. The pitting rate distribution was well presented with the photographs of the damaged surface as shown in Fig.2.1.1. Knapp concluded that the cavitating bubble generated in a low pressure region collapsed in a stagnation region at the end tail of the sheet cavitation where the pressure was higher and then, its shockwave damaged the specimen surface and produced a pit on the soft aluminium. (This paper will be discussed more in Chapter 3.)

To date, a lot of work on bubble collapse dynamics have been carried out both experimentally and theoretically. It can be said that the final purpose of most of those investigation were to clarify the bubble behaviour in terms of related hydrodynamic parameters from the viewpoint of understanding its damage mechanism as a main cause of cavitation erosion. Therefore, considering the aim of the project, it seems quite reasonable to start the literature review in this chapter with the work on bubble collapse dynamics to understand the basis of cavitation bubble impingement mechanism. Then in following chapters, we are going further into more literature whose subjects are much more directly related to the actual work in the present project, such as cavitation loading or erosion phenomena.

It may be said that the significance of the literature on spherically symmetric bubble collapse is historic interest today, as the existing experimental evidence

obtained by high speed photography shows that it is unlikely for a bubble eroding a solid boundary to collapse spherically. However, a lot of basic and important information required to understand the mechanism of asymmetric bubble collapse can be deduced from it.

Hence, it was decided that some important research on symmetric bubble collapse would be reviewed at first, and then more recent publications on asymmetric condition and multi-bubble effect would be discussed in subsequent sections.

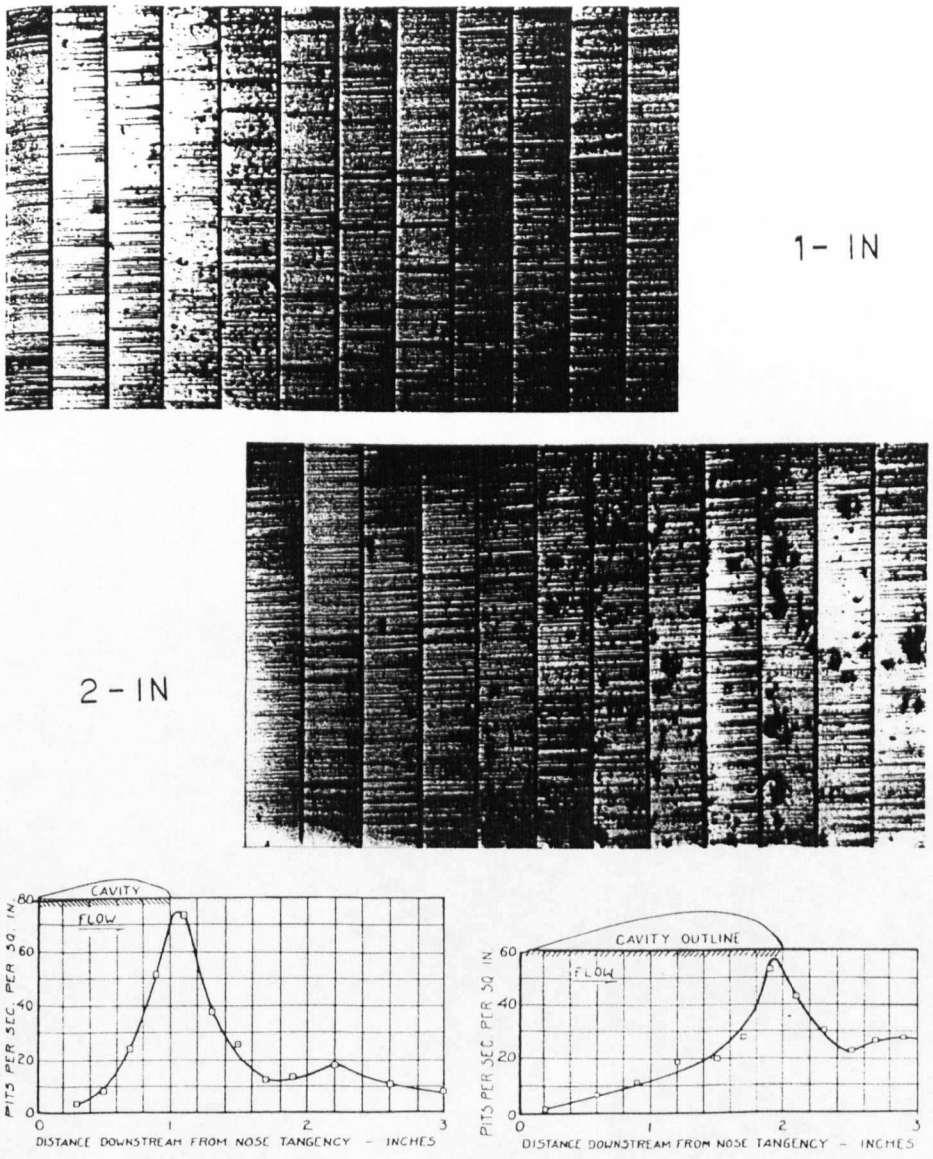

Fig.2.1.1 Distribution and micrographs of pitting for 1- and 2-inches cavity length (from Knapp [1955])

Cavitation phenomena have been recognised for more than a century. However, dynamic bubble collapsing behaviour had not been observed for a long time. One reason is because its collapsing velocity was too high for researchers in those days to visually follow the events.

Historically, Besant [1859] firstly proposed the single spherical bubble collapse problem and solved its mechanics theoretically using the spherically symmetric equations of conservation of mass and momentum. And then Rayleigh [1917] solved the same problem in different way, considering the kinetic energy of the liquid. It is widely accepted that the Rayleigh's analysis has been regarded as pioneering work in the field of investigating cavitation erosion through the bubble collapsing problem. Rayleigh examined the pressure distribution around the bubble during the collapse and stressed an important result that the very high pressure generated within the liquid just outside cavitation bubble is mechanically able to damage the adjacent solid boundary.

There are still many publications referring to this classical paper and as Young [1989] pointed all transient bubbles, whatever additional complications are introduced, start their collapse as he has proposed. Therefore, it seems justifiable that his elegant and very simple analysis is partly repeated here.

It was assumed that a spherically symmetric cavity empty or filled with vapour at constant pressure P_v collapsed in homogeneous incompressible liquid whose pressure also remains constant P_0 at an infinite distance. If $\dot{R}$ is the velocity and R is the radius of the bubble boundary at time t, and $\dot{r}$ is the simultaneous velocity at any distance r (greater than R) from the centre, then

$$\frac{\dot{r}}{\dot{R}} = \frac{R^2}{r^2} \tag{2.2.1}$$

and if ρ is the density of the liquid, the whole kinetic energy of the liquid is

$$\frac{1}{2}\rho \int_R^\infty \dot{r}^2 4\pi r^2 dr = 2\pi\rho\dot{R}^2 R^3 \tag{2.2.2}$$

Again, if R_0 is the initial radius, the work done is

$$\frac{4\pi(P_0-P_v)}{3}(R_0^3-R^3) \tag{2.2.3}$$

Then equating Eq.(2.2.2) and Eq.(2.2.3),

$$\dot{R}^2 = \frac{2(P_0-P_v)}{3\rho}\cdot\left(\frac{R_0^3}{R^3}-1\right) \tag{2.2.4}$$

expressing the velocity of the boundary in terms of the radius. $\dot{R}$ increases without limit as R diminishes.

Also, since $\dot{R}$=dR/dt,

$$\begin{aligned} t &= \sqrt{\left(\frac{3\rho}{2(P_0-P_v)}\right)}\cdot\int_R^{R_0}\frac{R^{3/2}}{(R_0^3-R^3)^{1/2}}dR \\ &= R_0\sqrt{\left(\frac{3\rho}{2(P_0-P_v)}\right)}\cdot\int_\beta^1\frac{\beta^{3/2}}{(1-\beta^3)^{1/2}}d\beta \end{aligned} \tag{2.2.5}$$

if ß=R/R_0. The time of collapse to a given fraction of the original radius is proportional to $R_0\rho^{1/2}(P_0-P_v)^{-1/2}$. The time τ of complete collapse is obtained by putting ß=0 and integrating the above Eq.(2.2.5) numerically. This results in

$$\tau = 0.915R_0\sqrt{\left(\frac{\rho}{P_0-P_v}\right)} \tag{2.2.6}$$

where τ is the time to complete the bubble collapse. For example, in the case of a bubble of radius 0.1mm in water under atmospheric pressure difference P_0-P_v=1.0bar,

$$\tau \approx 10^{-5}\ (s)$$

This is indeed a very fast process to follow without any help of advanced visualizing apparatus.

In order to calculate the pressure at any internal point, the general equation of pressure is used.

$$\frac{1}{\rho}\frac{\partial p}{\partial r} = -\frac{\partial u}{\partial t}-u\frac{\partial u}{\partial r} \tag{2.2.7}$$

u is a function of r and t, reckoned positive in the direction of increasing r.

From Eq.(2.2.1),

$$\frac{\partial u}{\partial t} = \frac{1}{r^2}\frac{d}{dt}(\dot{R}R^2) \tag{2.2.8}$$

substituting Eq.(2.2.4) to Eq.(2.2.8), then

$$\frac{\partial u}{\partial t} = \frac{1}{r^2}\left(2R\dot{R}^2 - \frac{(P_0-P_v)}{\rho}\frac{R_0^3}{R^2}\right)$$

Thus, suitably determining the constant of integration and writing $z=R_0^3/R^3$, we have

$$\frac{p}{(P_0-P_v)} - 1 = \frac{R}{3r}(z-4) - \frac{R^4}{3r^4}(z-1) \tag{2.2.9}$$

At the first moment after release, when z=1, the maximum pressure p is at infinity like,

$$\frac{p}{(P_0-P_v)} = 1 - \frac{R}{r}$$

But as the contraction proceeds, this ceases to be true.

Differentiating Eq.(2.2.9), we get the radius where the maximum value of p occurs,

$$\frac{r^3}{R^3} = \frac{4z-4}{z-4} \tag{2.2.10}$$

and then

$$\frac{p}{(P_0-P_v)} = 1 + \frac{(z-4)^{4/3}}{4^{4/3}(z-1)^{1/3}} \tag{2.2.11}$$

When z exceeds 4, the maximum p is greater than P_0-P_v and as the cavity fills up, z becomes great, and Eq.(2.2.10) and (2.2.11) approximates to

$$r = 4^{1/3}R = 1.587R$$
$$\frac{p}{(P_0-P_v)} = \frac{R_0^3}{4^{4/3}R^3} \tag{2.2.12}$$

It appears from Eq.(2.2.4) and Eq.(2.2.12) that the collapsing velocity of the cavity boundary was rising quickly toward the end of the collapse whilst very high pressure was generated in the liquid near the bubble boundary. For example, if $R=1/20R_0$,

$p=1260(P_0-P_v)$.

Rayleigh also considered that a rigid sphere of small radius R_f is placed inside the cavity and the cavity boundary strikes a surface of the sphere. It was solved with admitting the fluid compressibility at the moment of the strike. Then very high pressure, P=10300atm was obtained for water, taking the final radius $R_f=1/20R_0$. This conclusion might have given subsequent investigators some clues that the impingement of the collapsing cavity wall itself can be also very damaging.

Rayleigh's assumptions are far from the reality, but he has shown basic bubble dynamics and pointed out possible mechanisms of producing high pressure.

It may be said that all of the research work on bubble dynamics which have been achieved until now, have started from this classical paper and it still works in many cases.

One of the earliest experimental support of Rayleigh's analysis and application of it was published after a few decades from his pioneering theoretical work. Two reports from California Institute of Technology are introduced below.

Knapp and Hollander [1948] compared Rayleigh's solutions with their high speed motion picture photographs of the collapse of cavitation bubbles generated on the surface of the body in their water tunnel. They took the constant pressure difference between the pressure at the tunnel wall and the vapour pressure of the water into their calculation of Rayleigh's theoretical curve for bubble growth and collapse. Good agreement between the experimental results and theory was obtained as shown in Fig.2.2.1.

Plesset [1949] tried to simulate the behaviour of cavitation bubble travelling on the surface of the body. Local pressure distribution on the body surface under non-cavitating flow, which had already been measured before, was used as P_a of cavitating flow at corresponding point as shown in Fig.2.2.2 and then a theoretical equation was numerically integrated. Some results of his calculation are presented in Fig.2.2.3, where the maximum bubble radius of his calculation was taken as an integration constant to adjust its peak value to the experimentally observed one. The calculated curves beautifully show the general motion of growth and collapse of bubbles which is quicker in high pressure difference area and vice versa. The agreement is quite good except the both ends of the growth and collapse history where the bubble radius is small and so the effect of neglecting the air content inside the

bubble is large.

Bubble behaviour near the end of the collapse is a very important part of the investigation for the purpose of studying the maximum pressure or damage capacity of a collapsing bubble. It was not main concern of both above papers but soon their importance was realized through more detailed theoretical studies on bubble dynamics with more complicated fluid dynamic conditions, which were carried out by Gilmore [1952], Hickling and Plesset [1964] and others. They will be discussed in the next Section.

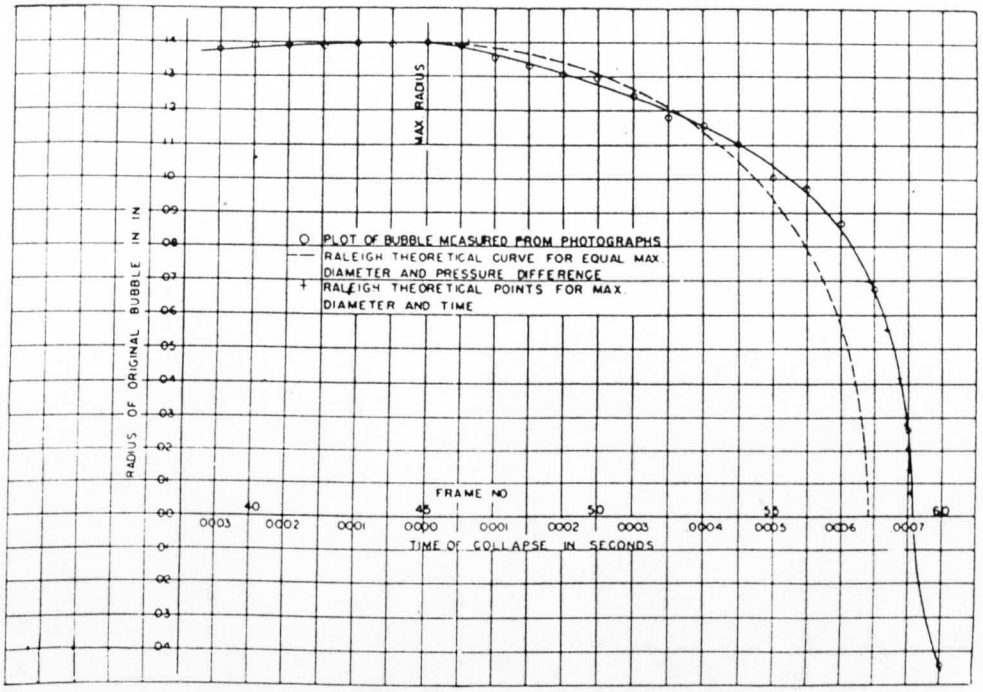

Fig.2.2.1 Comparison of measured bubble size with Rayleigh prediction (from Knapp and Hollander [1948])

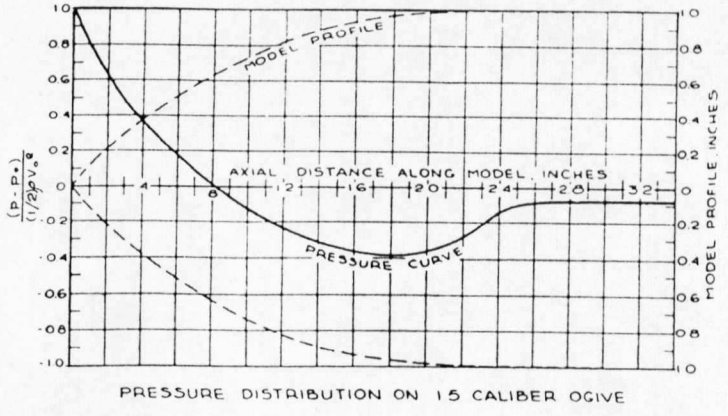

Fig.2.2.2 Experimentally determined pressure coefficient (from Plesset [1949])

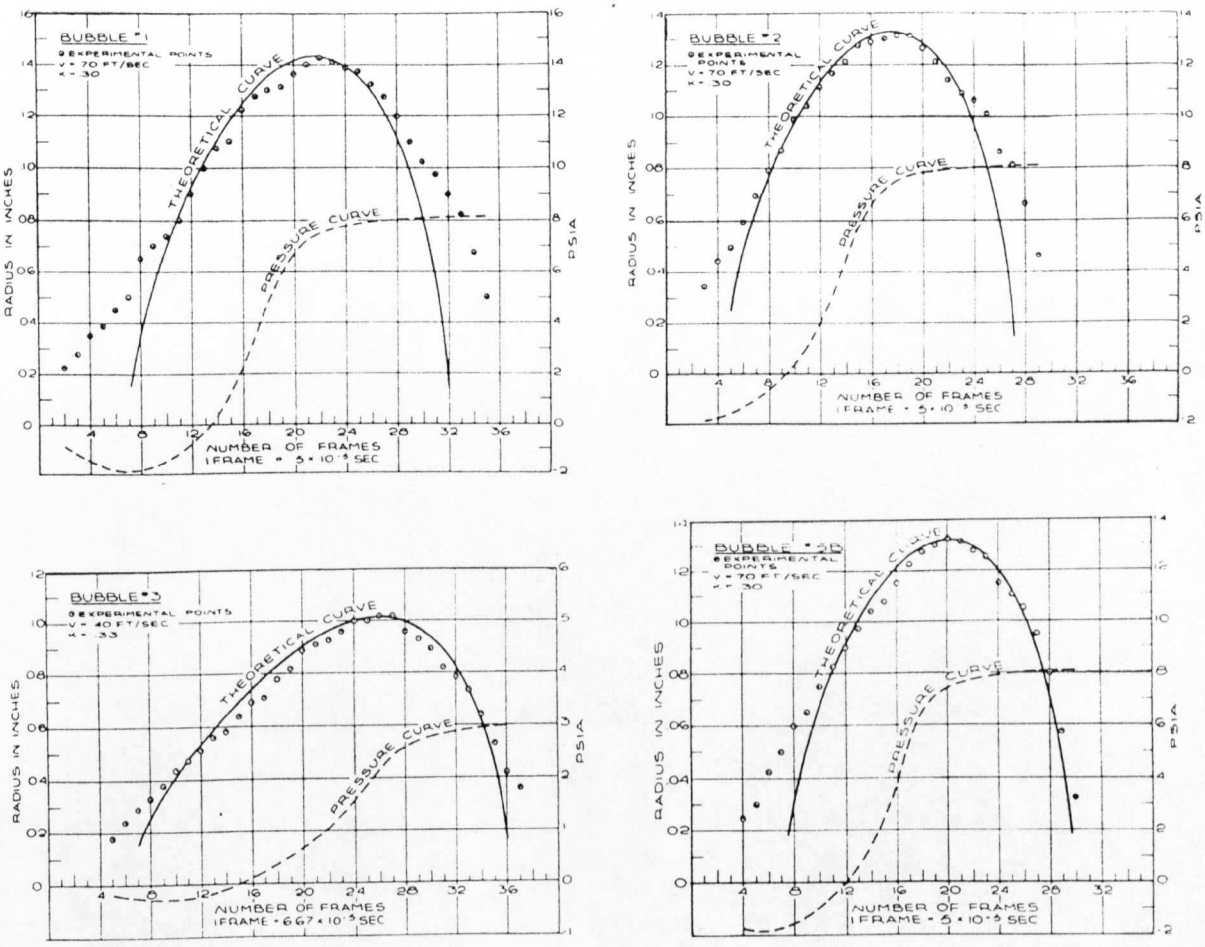

Fig.2.2.3 Comparison of calculated bubble motion to measured one (from Plesset [1949])

Theoretically, the validity of Rayleigh's theoretical analysis on spherically symmetric bubble dynamics is limited only in ideal liquids, and his solution can not provide sufficiently correct information at the final stage of the bubble collapse because mainly the liquid compressibility, gas content and the thermal effect were not taken into account.

In general, the real fluid has following parameters which were not included in Rayleigh's analysis.

(1) Liquid compressibility
(2) Gas content
(3) Thermal effects
(4) Viscosity
(5) Surface tension

In order to take above effects into account and to investigate the bubble motion at the end of the collapse which is of great importance from the viewpoint of cavitation erosion, several theoretical analyses have been carried out and almost "exact" solution of spherically symmetric bubble collapsing behaviour considering all important parameters has been obtained. Some of major work on this matter will be reviewed in this section.

Gilmore [1952] achieved the pioneering theoretical analysis of symmetric bubble collapse in compressible liquid. The Kirkwood-Bethe approximation [1942] was applied in his analysis and then followed by subsequent investigators. This approximation assumes that pressure disturbances are propagated with a velocity equal to the sum of the velocity of sound in the liquid and the liquid velocity, and is more realistic approximation than the acoustic approximation where the velocities in the liquid are always small compered with the velocity of sound in the liquid. The acoustic approximation was used by Herring [1941] and Trilling [1952] to investigate the bubble collapse in compressible liquid but as it was pointed by Gilmore and shown in Fig.2.3.1, the acoustic approximation is insufficient for determining the propagation velocity of disturbances near the cavity at the final part of the collapse where the local liquid velocity is very high.

Gilmore's study was essentially pre-computer analysis and did not present much numerical data for the investigation of cavitation erosion. However, it has been the basis of many studies conducted later.

One of comprehensive solutions to the equations for gas containing bubble collapse and rebound in a compressible liquid was reported by Hickling and Plesset [1964]. They used the high speed (at that time) computer for a direct numerical treatment of the equations of compressible flow. Some of their results were compared with the one obtained from Gilmore's theory and another one from the theory of an empty cavity in an incompressible liquid.

The computations were carried out for a variety of conditions which might occur in cavitation. The value used for the pressure P_0 at infinite distance in the liquid were 1 and 10 atm and the initial pressure p_0 in the gas was varied from 10^{-1} to 10^{-4} atm, which γ was given the values 1 (isothermal compression) and 1.4 (adiabatic compression). The results obtained for the cavity wall velocities are shown in Figs.2.3.2(a)~(c). The gas content limits the minimum size of the bubble and so does the maximum cavity wall velocity. And the thermal effect, changing as γ changes from 1.0 to 1.4, is much stronger than the effect of changing the pressure P_0 from 1 to 10 atm. Since generally very small gas bubbles are regarded as the nuclei of cavities and even the vapour possibly acts like a permanent gas during the final phase of collapse where the collapsing motion is too quick for condensation and for removal of the resultant latent heat which was later confirmed by Fujikawa and Akamatsu [1980], their assumption of the gas existence seems likely. The agreement between the exact solution and Gilmore's theory (Kirkwood-Bethe, in Fig.2.3.2) is remarkable, and so the validity of use of the Kirkwood-Bethe approximation by Gilmore is confirmed.

Figures 2.3.3 and 2.3.4 show the instantaneous velocity and the distribution of pressure in the liquid during the collapse and rebound. Numbers on the curves are dimensionless time measured from the time of minimum bubble size and expressed as

$$\frac{(\tau - t)\cdot 10^4}{\tau}$$

where t is the time elapsed from the start and the collapse time τ was calculated from their numerical solutions. It is clearly shown in Fig.2.3.4(b) that the pressure wave is formed during the rebounding process and it propagates into the liquid and

generates a shook front. This is impossible for the case of incompressible liquid. The pressure peak attenuates as 1/r in moving outwards from the centre of the collapse. The peak pressure of about 1000 atm is obtained at R/R_0=0.3 and about 200 atm at R/R_0~2 with the ambient pressure p_∞=1 atm and the initial gas pressure $p_0=10^{-3}$ atm. This really depends on p_0 and for smaller amount of gas the order of 1000 atm at R/R_0=2 was calculated.

This mechanism of generating high pressure during the rebounding process is obviously different from that of Rayleigh's solution and is more likely because, as mentioned earlier, the presence of slight amount of permanent gas or non-condensable vapour at the final stage of bubble collapse seems inevitable. However, if it is assumed that the location of the centre of the collapsing cavity remains stationarily away from the boundary about R/R_0~2 throughout the event, the peak pressure calculated is not sufficiently high to cause severe damage to tough materials. And if the cavity approaches toward the solid boundary, the assumption of symmetric ambient pressure condition is not valid any more and such a bubble, of cause, can not collapse symmetrically.

Ivavy and Hammitt [1965] carried out calculations similar to those of Hickling and Plesset but including more parameters, such as the effects of surface tension and viscosity. Their results show that the effect of surface tension are not substantially significant in bubble collapse for any engineering liquid, and viscosity can only be substantial for liquid whose viscosity is in the order of heavy oil's.

After the analyses discussed above, a lot of theoretical studies have been made to take account of all sorts of extra factors through a modification of previously existing models. Among them, probably one of the most comprehensive calculation was achieved by Fujikawa and Akamatsu [1980]. They did a large scale numerical analysis taking all of the following effects into account,

(1) Compressibility of the liquid.
(2) Viscosity of the liquid.
(3) Non-equilibrium condensation of the vapour.
(4) Heat conduction inside the bubble and in the surrounding liquid.
(5) Temperature discontinuity at the phase interface.

They consider that the bubble begins to collapse after the instant rise of the ambient

pressure to some value P_0 and this collapsing notion is accompanied by phase change (condensation) and heat conduction through the bubble wall. For writing basic equations the following assumptions are made.

a) The bubble always remains spherical.

b) Liquid compressibility and viscosity do not affect each other.

c) Gravity and diffusion effects are negligible.

d) The pressure is uniform throughout inside of the bubble.

e) The vapour and gas in the bubble are inviscid and obey the perfect gas low.

f) The temperature of this vapour and gas are equal.

g) The thermal boundary layers both inside and outside the bubble are thin compared with the bubble radius.

h) There is a thin but finite non-equilibrium region at the phase interface because of the continued change of phase there.

i) The physical properties of the liquid and gases are constant.

Trevena [1987] comments, "this is a far cry from the relative simplicity of the Rayleigh model!" Based on the above assumptions, three sets of equations were derived for (A) the external region occupied by the liquid, (B) the inside of the bubble occupied by the mixture of vapour and gas and (C) the phase interface.

The results of their calculations generally support the work done by Hickling and Plesset [1964], both regarding the order of magnitude of the peak pressures and the pressure wave attenuation in inverse proportion to distance, 1/r. And it is clearly confirmed that the shockwave is also radiated at the instant of rebound of a bubble that contains vapour only.

The maximum temperatures at the centre and at the interface of the bubble are also obtained and they are 6700K and 3413K, respectively (initial temperature chosen is $T_{l\infty}$=293.15K). This interfacial temperature of the bubble falls to 292.4K at a time 2μs after the first rebound, because the bubble rapidly expands. On the other hand, the maximum interfacial temperature of the liquid is 474K. Although the work of Fujikawa and Akamatsu is significant and provides much detailed information, the pressure of the shockwave calculated attenuates rapidly with distance as reported by Hickling and Plesset and obtained pressure level $p/P_0 \approx 100$ at R/R_0=1.0 which is far below that required to cause damage to an engineering material.

Theoretical work discussed above has been experimentally supported by Ellis [1965], Lauterborn [1974] and others using high speed motion picture technique. However, as described earlier in this section, such photographic works also show that bubbles collapse asymmetrically under various asymmetric collapse conditions, such as the presence of a solid boundary or pressure gradients.

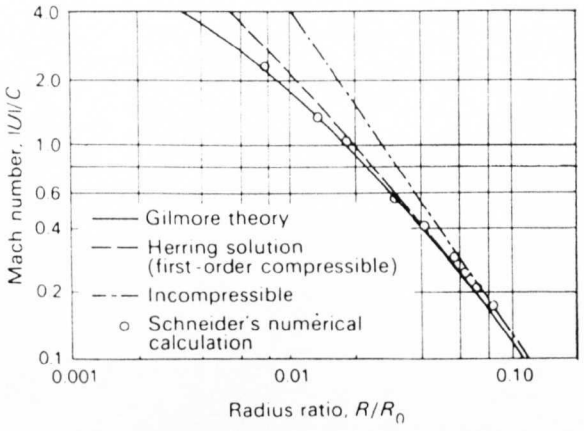

Fig.2.3.1 Comparison of solutions for wall velocity versus radius for collapse of a gas filled bubble. Compressible liquid without viscosity or surface tension. All curves are for p_∞-p_i=0.517atm. (from Gilmore [1952])

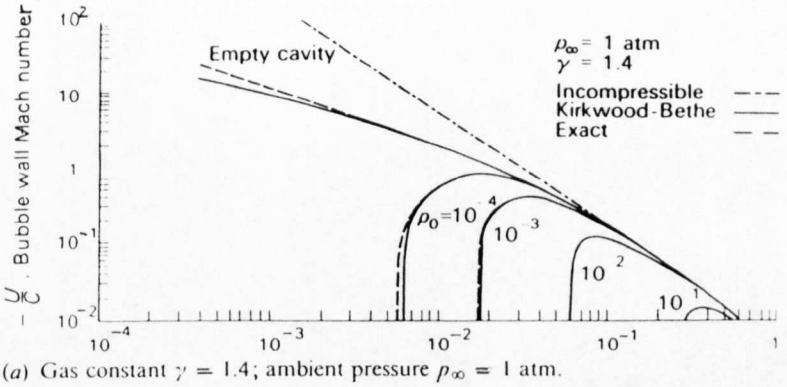

(*a*) Gas constant $\gamma = 1.4$; ambient pressure $p_\infty = 1$ atm.

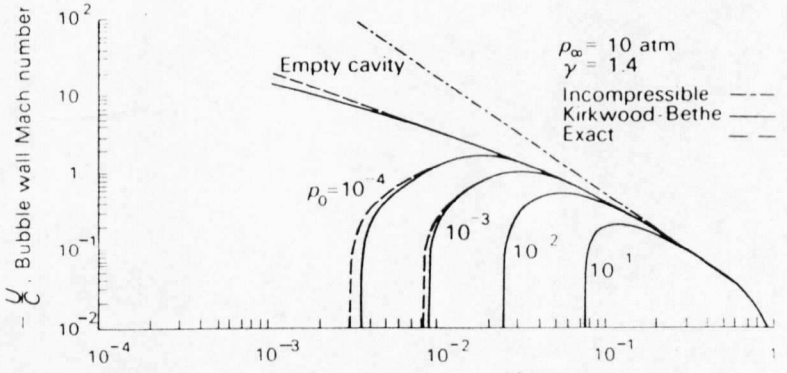

(*b*) Gas constant $\gamma = 1.4$; ambient pressure $p_\infty = 10$ atm.

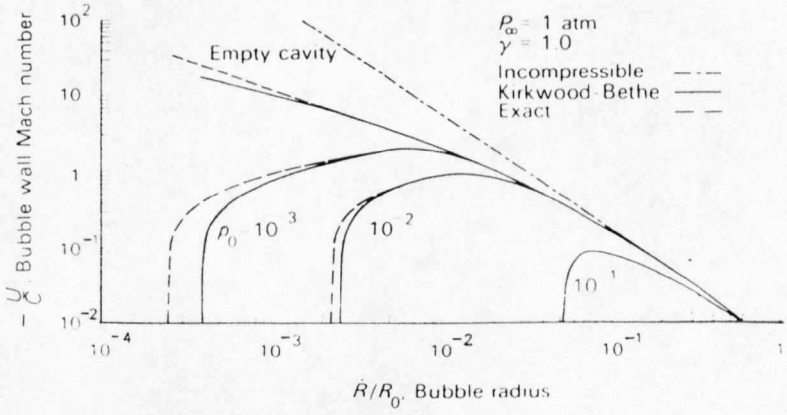

(*c*) Gas constant $\gamma = 1.0$; ambient pressure $p_\infty = 1$ atm.

Fig.2.3.2 Bubble-wall velocity versus bubble radius for decreasing gas content. Compressible liquid without viscosity or surface tension; gas content determined by initial pressure P_0. (from Hickling and Plesset [1964])

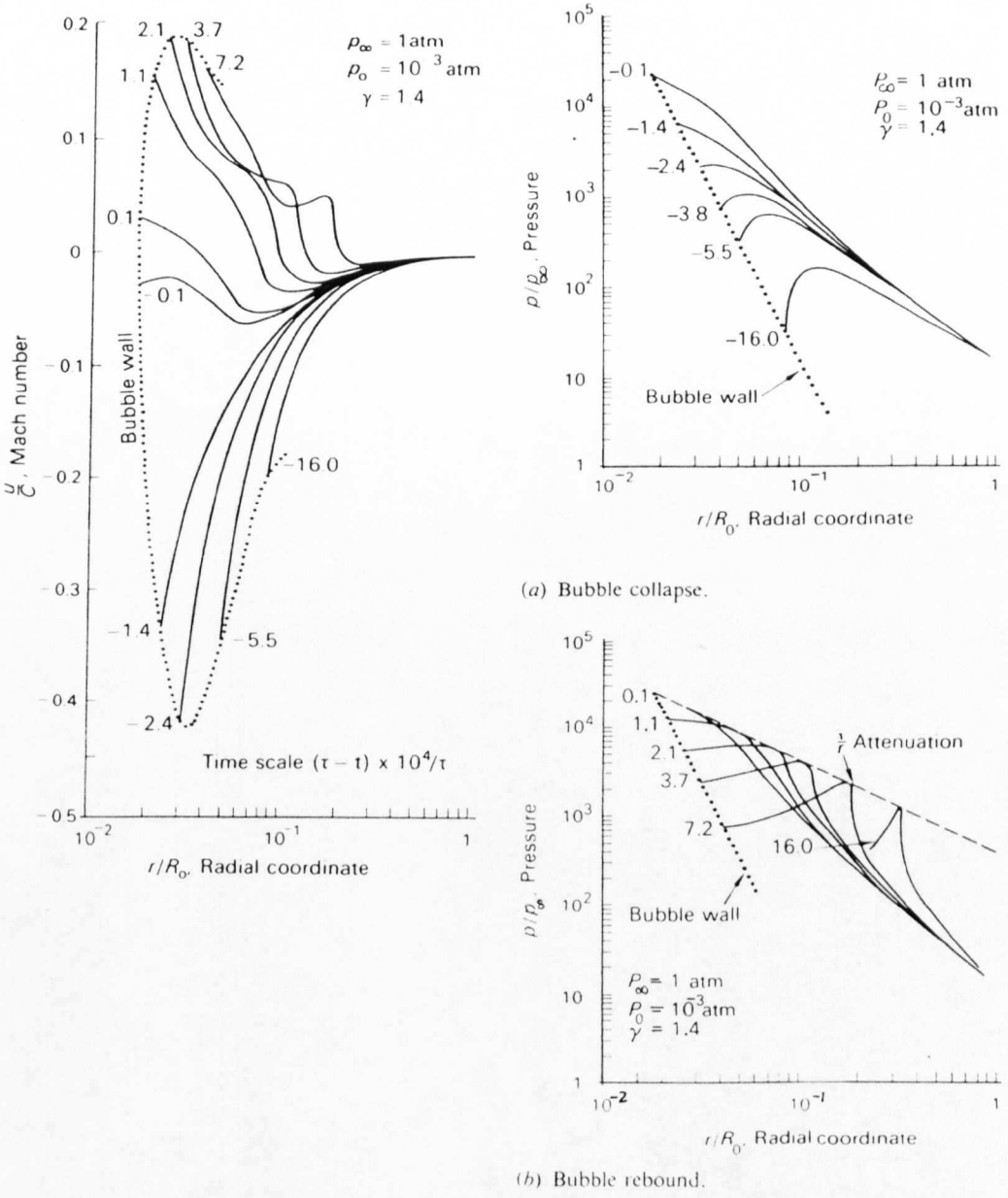

Fig.2.3.3 Curves of instantaneous velocity in the liquid versus distance from the bubble wall during collapse and rebound. Compressible liquid without viscosity or surface tension. Gas constant γ=1.4; ambient pressure p_∞=1atm; initial pressure P_0=10^{-3}atm. (from Hickling and Plesset [1964])

Fig.2.3.4 Curves of instantaneous pressure in the liquid versus distance from the bubble wall. Compressible liquid without viscosity or surface tension. Gas constant γ=1.4; ambient pressure p_∞=1atm; initial pressure P_0=10^{-3}atm.
(from Hickling and Plesset [1964])

2.4 Asymmetric collapse

2.4.1 Proximity of a solid boundary

Since practically in most engineering cases a cavitation bubble exists under asymmetric conditions brought about by a pressure gradient or the presence of a boundary and other bubbles near by, theoretical analyses described in previous section are not directly applicable. Among the various asymmetric conditions, the asymmetry due to the proximity of an object to be damaged is at first apparently of the most importance for the investigation of cavitation erosion.

Naude and Ellis [1961] clearly showed that a hemispherical bubble put on a solid boundary collapsed non-hemispherically. The bubble was induced by a spark method and its collapsing behaviour was recorded using high speed motion pictures. Perhaps the most important result reported in this paper is that they experimentally proved the existence of a minute liquid jet (microjet) impinging the solid boundary during the collapse with very high velocity. A pit generated on a soft pure aluminium specimen was used to show how the microjet impingement was actually damaging. Although the possibility of this mechanism of cavitation damage had been already suggested by Kornfeld and Suvorov [1944], there had not been any evidence showing the damage capability of a microjet to support the idea until Naude and Ellis.

In actual flow cavitation, however, it seems very unlikely that there are many such hemispherical bubbles initially attached to the solid boundary and they continue to damage it. One of the first experimental evidence of the possibility of this microjet impingement mechanism for a spherical cavity detached from the solid boundary was provided by Benjamin and Ellis [1966]. They created a large vapour cavity from a tiny hydrogen bubble nuclei by means of shock pressure technique in water which was depressurized until P_0=0.04 atm to reduce the collapse velocity for photography, and presented exceptionally beautiful photographs as shown in Figs.2.4.1(a)~(b). The bubble motion was recorded by high speed motion pictures. Figure 2.4.1(a) shows a cavity during collapse (A,B) and rebound (C,D) at far from solid boundary. The microjet is formed in the third frame because of the presence of gravity, i.e., hydrostatic pressure gradient, and it is still seen as a minute line inside the cavity in

the fourth frame as well.

Bubble collapse in proximity to a solid boundary is shown in Fig.2.4.1(b) (a solid boundary is located vertically at the right edge of the frame). The initially almost spherical shape in the first frame can not be kept until the final stage of collapse. A microjet is passing through the cavity from slightly down left to upper right, since the joint effect of boundary proximity and the gravity is being applied. The velocity of this microjet was estimated about v=10m/s at p_0=0.04 atm, but reevaluated later to v=100m/s at atmospheric pressure p_0=1.0atm by taking the vapour pressure P_v=0.03 atm at 76°F into account (Plesset and Chapman [1971]).

If we assume that the impact pressure of the microjet can be given by the water hammer equation,

$$P_{wh} = \rho_L C_L v \left(\frac{\rho_S C_S}{\rho_L C_L + \rho_S C_S} \right)$$

where ρ and C are the density and the sound velocity, and the L and S subscripts refer to the liquid and the solid, respectively. Usually $\rho_s C_s$ is much larger than $\rho_L C_L$, thus

$$P_{wh} \approx \rho_L C_L v$$

For water with v=100m/s and C_L ~ 1500m/s, the water hammer pressure P_{wh}≈1500bar is obtained. This is a possible value for damaging some soft materials particularly through fatigue process, though still it is not so high to seriously damage tough materials.

Moreover, at the impact a radial wall jet of high velocity is formed and it may locally produce a significant shear stress, especially if there is small roughness on the surface such as the one after several impingements as shown in Fig.2.4.2. The significance of this radial jet flow was experimentally pointed out by Thomas and Brunton [1970].

The duration time of the water hammer pressure may be estimated no longer than the time for the impact signal to traverse the radius of the jet. Assuming that the microjet radius is one tenth of the initial radius of the bubble R_0 and the velocity of the traverse is about the same order of magnitude of the microjet velocity v, we have τ_{wh}≈0.5μs for a bubble of R_0=1.0mm with a microjet velocity v=100m/s.

Theoretical analysis of the collapse of a spherical cavity adjacent to a solid

boundary was achieved by Plesset and Chapman [1971]. They supposed all assumptions of Rayleigh's ideal bubble in ideal incompressible liquid, except the assumption of spherically symmetric collapse. Collapsing behaviour of a bubble initially tangent to a solid wall (case 1) and another case of a bubble detached from the boundary at a distance of half an initial cavity radius (case 2) were numerically simulated. The results are given in Fig.2.4.3 and Table 2.4.1. In both cases, firstly the spherical bubble is slightly distorted toward the solid surface like an ellipse. Then, the bubble wall at the opposite side of the solid boundary becomes dented and is approaching to the other side wall of the cavity (solid boundary side) with very high velocity accelerated until it actually reaches there. This clearly reproduces and theoretically supports the experimental results reported by Benjamin and Ellis.

The microjet velocities and the collapse time in Table 2.4.1 were calculated for the pressure difference $\Delta P=P_0-P_v=10^5$Pa with liquid density $\rho=10^3$kg/m^3. However, the results can be applied generally for the velocities scaled like $(\Delta P/\rho)^{1/2}$. The collapse times listed in Table 2.4.1 are given in units of $R_0(\rho/\Delta P)^{1/2}$. The microjet velocity obtained at the final stage are 128m/s (case 1) and 170m/s (case 2), and these are about the same orders as obtained by Benjamin and Ellis [1966]. Since the microjet impingement takes place in a relatively early stage of collapse, it may reach the solid wall before the impingement of shockwave due to the rebound of the bubble and the calculated microjet velocity is not greatly affected by the assumption of liquid's incompressibility.

Table 2.4.1 Time interval from initiation of collapse and the velocity of the bubble boundary at the axial point most distant from the wall, for the cases illustrated in Fig.2.4.3. (from Plesset and Chapman [1971])

	Case 1		Case 2	
Shape	Time	Velocity (m/s)	Time	Velocity (m/s)
A	0.63	7.7	0.725	10
B	0.885	19	0.875	17
C	0.986	42	0.961	35
D	1.013	65	0.991	53
E	1.033	100	1.016	94
F	1.048	125	1.028	142
G	1.066	129	1.036	160
H	1.082	129	1.044	165
I	1.098	128	1.050	170
J	1.119	128	-	-

The simulation results of Plesset and Chapman were experimentally verified later by Lauterborn and Bolle [1975]. They used a laser induced cavity near a solid boundary. Series of nice photographs are shown in Fig.2.4.4. They clearly show the asymmetric collapse of an initially spherical bubble and the formation of a microjet. Although the distance between the initial bubble centre and the solid wall b/R_{max}=2.45 is relatively large, the microjet produced was clearly capable to reach the wall. It is also observed that a cavity is approaching to the solid boundary during the collapse, and then the microjet is produced to the solid wall during the rebounding process. The bubble rebounds and collapses several times. Moreover, photographs of a bubble collapsing at distance of b/R_{max}=1.5 were taken and they were compared with the calculations by Plesset and Chapman (case 2) as shown in Fig.2.4.5. The agreement is quite remarkable and both fits each other almost quantitatively.

The maximum microjet velocity (at a protrusion tip) of 120 m/s at a distance of b/R_{max}=3.08 was measured. However, they pointed out that the dark funnel like protrusion observed in high speed photographs were not the real jet. Therefore, the real jet should be much thinner as seen inside the rebounding cavity in Fig.2.4.4 and its velocity is much faster than that of protrusion tip, though how faster is not known yet. This indication seems important for estimating the velocity of a microjet from photographic experiments.

Kling and Hammitt [1972] carried out a photographic study of spark induced cavitation bubble collapse in actual flow system; i.e., two dimensional venturi. Figure 2.4.6 shows one of their results that the cavity in a flow collapses asymmetrically near the solid boundary and produces a microjet just like Benjamin and Ellis's experiment in still water. The detailed sketch of the collapse behaviour of the same bubble is presented in Figs.2.4.7(a)~(b). The damage due to the bubble collapse impingement was actually produced on a thin soft aluminium sheet (thickness = 50μm). The comparison of the diameter of damaged area with the size of the microjet at the final stage in Fig.2.4.7(b), suggests that the more likely damage mechanism, at least for this case, is microjet impingement rather than the shockwave propagated from the centre of the rebounding cavity. The velocity of this microjet was estimated 120m/s at the static pressure of 1.0atm. The bubble centre migration toward the solid boundary during the collapse was also observed.

Significance of this work is that it undoubtedly shows the process of cavitation impingement; i.e., the series of incidents from producing a vapour bubble which is

travelling near a solid boundary to the asymmetric bubble collapse resulting a microjet toward the boundary which makes a pit like damage on it.

The investigation of asymmetric bubble collapse has required much more sophisticated testing methods and complicated numerical analyses than before, and the conditions with which the bubble dynamics is being treated have been becoming more realistic. However, cavitation bubbles seldom exist single in an actual flow.

The works on multi-bubble effect will be reviewed later in this chapter.

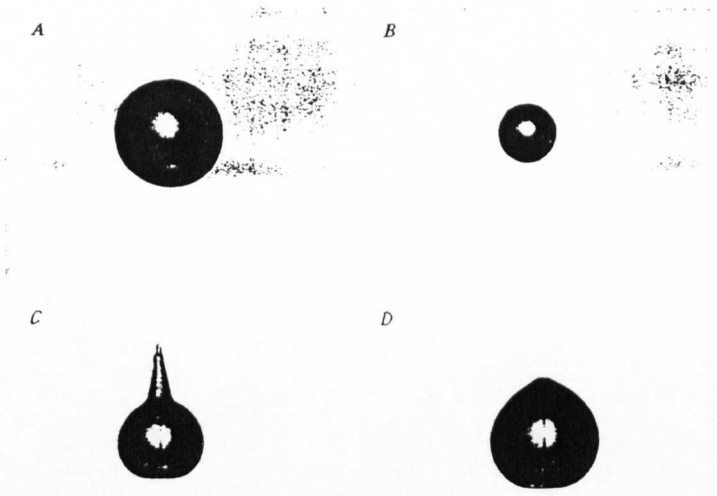

Fig.2.4.1(a) Photographs taken during collapse (A, B) and rebound (C, D) of cavity far from boundaries of liquid

Fig.2.4.1(b) Collapse of cavity near a solid wall
(Both (a) and (b) from Benjamin and Ellis [1966])

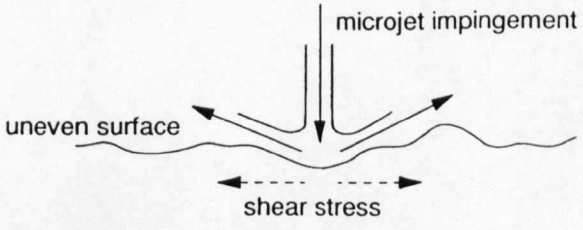

Fig.2.4.2 Shear stress produced by liquid jet impingement, schematic diagram

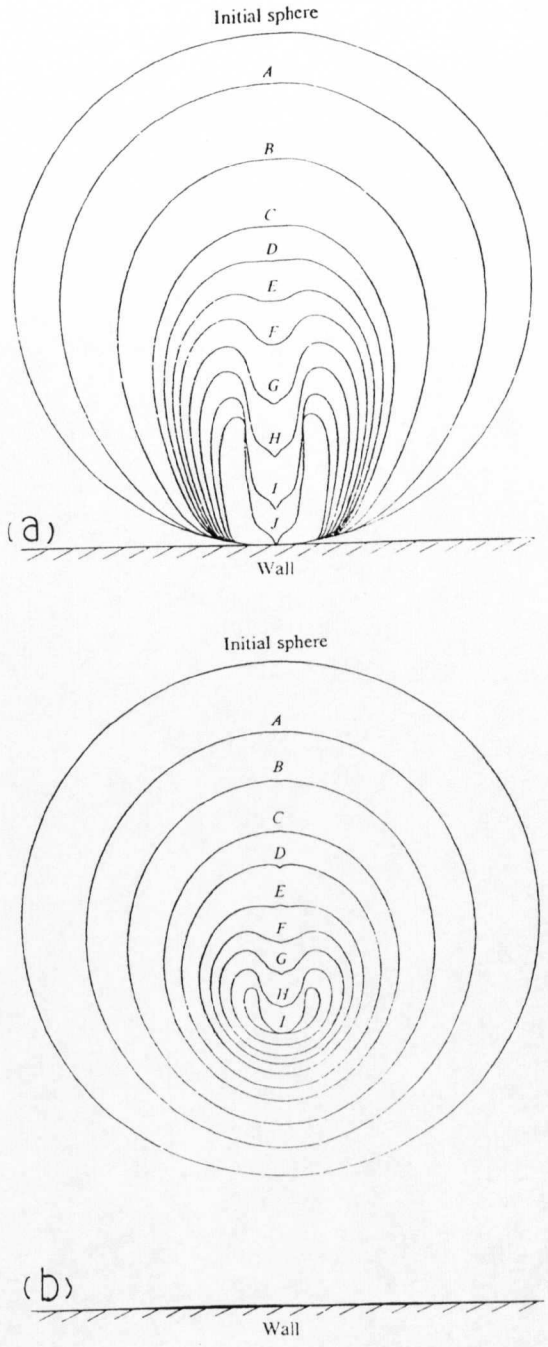

Fig.2.4.3 Bubble surfaces from case 1 (above) and case 2 (below) (from Plesset and Chapman 1971])

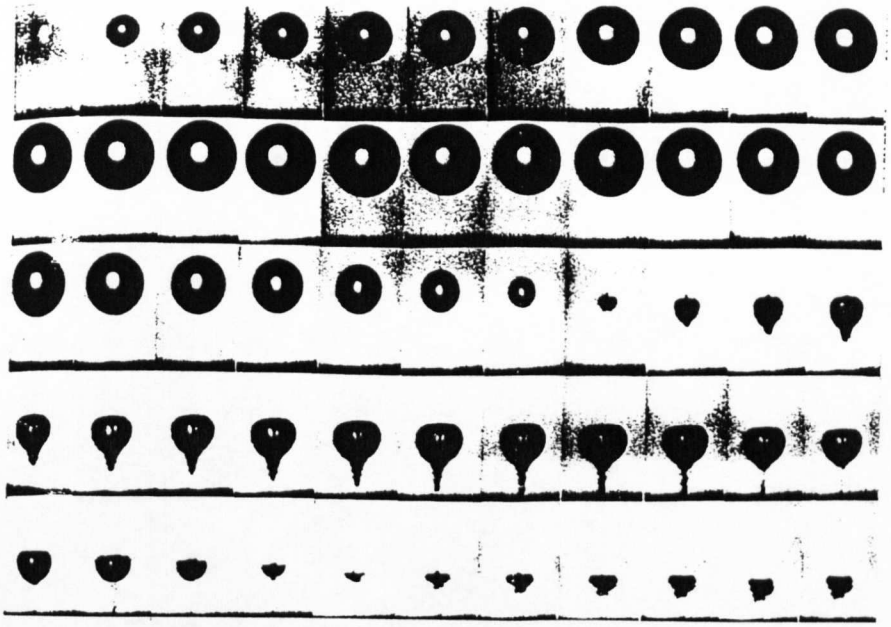

Fig.2.4.4 Dynamics of a laser-produced spherical bubble near a solid boundary. The framing rate is 75000 frames/s, the maximum bubble radius R_{max}=2.0mm, the distance of the bubble centre from the boundary b=4.9mm and the size of the individual frames is 7.2x4.6mm. (from Lauterborn and Bolle [1975])

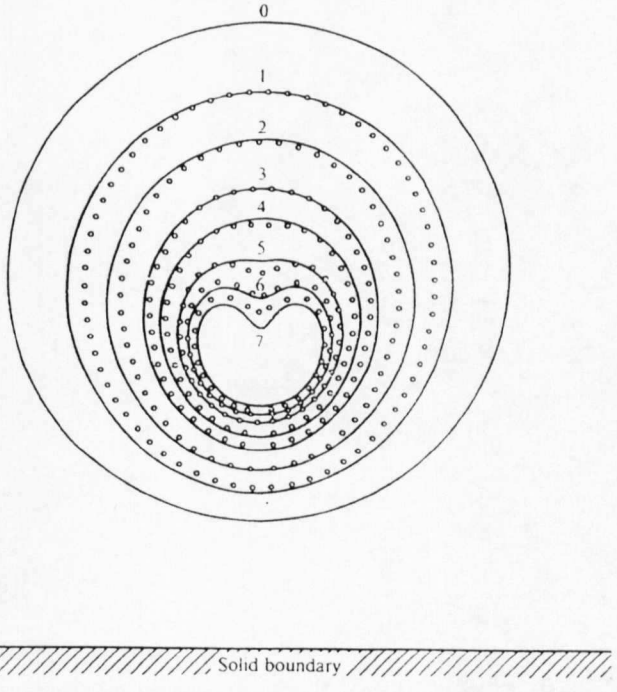

Fig.2.4.5 Comparison of experimentally determined bubble shapes (open circle) on collapse of a spherical bubble near a plane solid wall with theoretical curves taken from Plesset and Chapman [1971] (solid curves). The framing rate is 300000 frames/s, the maximum bubble radius R_{max}=2.6mm, the distance of the bubble centre from the boundary b=3.9mm and b/R_{max}=1.5. (from Lauterborn and Bolle [1975])

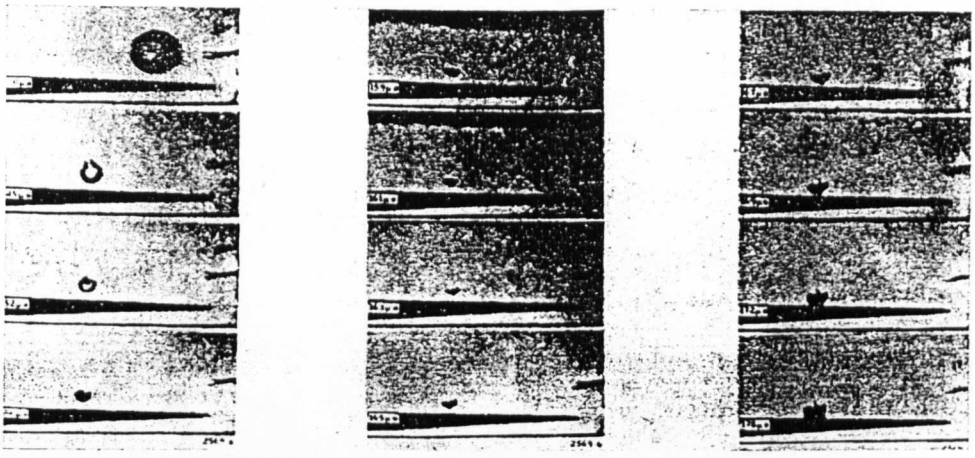

Fig.2.4.6 High speed photographs of a spark induced cavitation bubble collapsing in the modified aluminium two-dimensional venturi, diffuse back lighting, time measured from the first frame, 1.8μs exposure /frame, fluid velocity 26.7m/s, right to left, initial wall distance, h=1.14, magnification 6.0 (for the original). Air content 0.6 percent. (from Kling and Hammitt [1972])

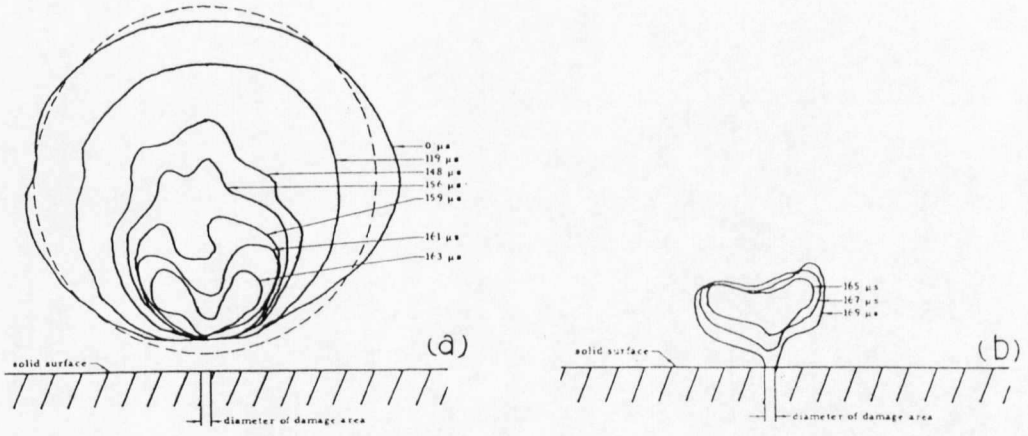

Fig.2.4.7 Outlines of the spark induced cavitation bubble at various stages of collapse showing the mode of deformation. (from Kling and Hammitt [1972])

2.4.2 Compliant boundary

In the previous section the asymmetric collapse due to the proximity of a solid boundary and subsequent formation of a liquid microjet were introduced, the solid boundary was always assumed to be rigid. Although that is likely in most engineering cases, it is possible to investigate the growth and collapse of a cavity near soft and compliant boundary condition. And in general, recent experimental and theoretical studies have shown that the cavity behaviour is influenced by the mechanical properties of the adjacent boundary.

The growth and collapse of a spark induced bubble near a compliant boundary was first observed by Gibson [1968]. He found that the bubble collapses near the flexible boundary migrating away from the boundary and forming a liquid microjet in the same direction of the bubble migration. Figure 2.4.8 shows that the flexible boundary actually repels the pulsating cavity and its microjet. The significance of this work is that these results lead the possibility of preventing the cavitation damage by coating a rigid structure with a deformable material.

This idea was followed by Gibson and Blake [1982]. They used a one-dimensional oscillating system of a compliant surface to estimate the range of possible surface properties which would repel the cavities, and they also experimentally presented the motion of a pulsating bubble in the vicinity of various compliant boundaries. Spark induced bubbles were used and high speed photographs of their motion were taken. They found that there are some appropriate parameters of boundary properties, such as dimensionless surface inertia and stiffness, under that the microjet is directed away from the boundary. Examples of pulsating bubbles with various deformable surfaces are shown in Fig.2.4.9 and the corresponding surface properties are in Table 2.4.2. The maximum bubble size in Fig.2.4.9 is 37~41mm. In the case of a soft and light surface, (a) natural rubber whose thickness is 1.3mm and (d) composite coating of 8mm thick foam rubber covered with 0.8mm thick natural rubber sheet on a Perspex board in Fig.2.4.9, the microjet formed is in fact directed away from the boundary.

Similar experiments of a pulsating spark induced cavity near a compliant surface with more detailed sets of parameters were carried out by Shima, Tomita, Gibson and Blake [1989]. It was shown in their results that the surface stiffness and

inertia are both considered to be effective parameters but the stiffness seems more important factor. They also found that the bubble migration depends not only on the surface properties but also on bubble size and distance from the surface.

Duncan and Zhang [1991] performed numerical study and showed the behaviour of a collapsing cavity near a compliant boundary. They treated only the collapsing motion of the cavity (not pulsating) and the calculation is in qualitative agreement with the experimental results achieved by Gibson and Blake [1982] and Shima et al. [1989].

As described above, there is a possibility that a suitable soft and light surface coating material will be formed which will resist the cavitation erosion by repelling the cavitation bubbles and their microjets. Particularly, the possibility would be higher for not so severe hydrodynamic condition with relatively low flow velocity where the high level of mechanical strength is not required for the surface. More detailed study and accumulation of experience through various cavitation erosion testing would be needed to actually develop the proper material.

Table 2.4.2 Dimensionless surface stiffness and inertia properties and bubble/surface interaction records presented in Fig.2.4.9. (from Gibson and Blake [1982])

Deformable surface type	Boundary distance (h/R_m)	Boundary inertia (m^*)	Boundary stiffness (k^*)	Record of bubble/boundary interaction
4mm thick vulcanised rubber	0.64	1.20	158	Fig.2.4.9(b)
7mm thick vulcanised rubber	0.64	2.18	125	Fig.2.4.9(c)
1.3mm thick natural rubber	0.58	0.31	6.62	Fig.2.4.9(a)
8mm thick composite (natural/foam) rubber coating	0.56	~0.19	8.0	Fig.2.4.9(d)

h: distance from the centre of the bubble to the boundary.
$m^* = m/(\rho R_m 3)$, $k^* = k/((p_\infty - p_c)R_m)$, where m and k are the mass and the stiffness of the circle boundary with radius R_m (maximum horizontal radius of the bubble), respectively, and p_∞ and p_c are the pressure in the liquid before the bubble growth and the saturation vapour pressure, respectively.

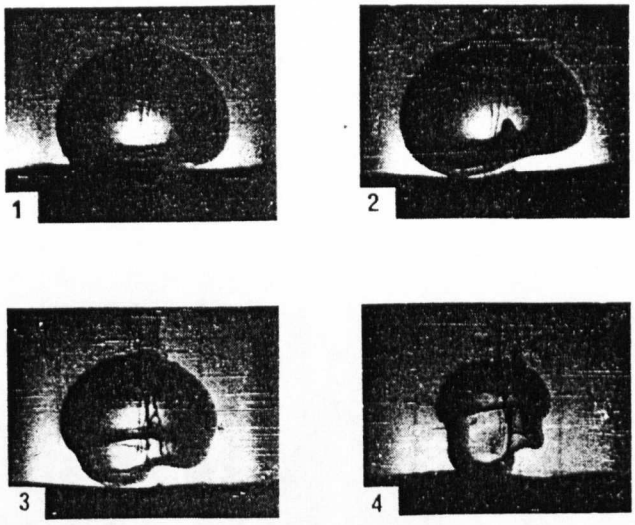

Fig.2.4.8 Jet reversal for collapse adjacent to a flexible boundary (from Gibson [1968])

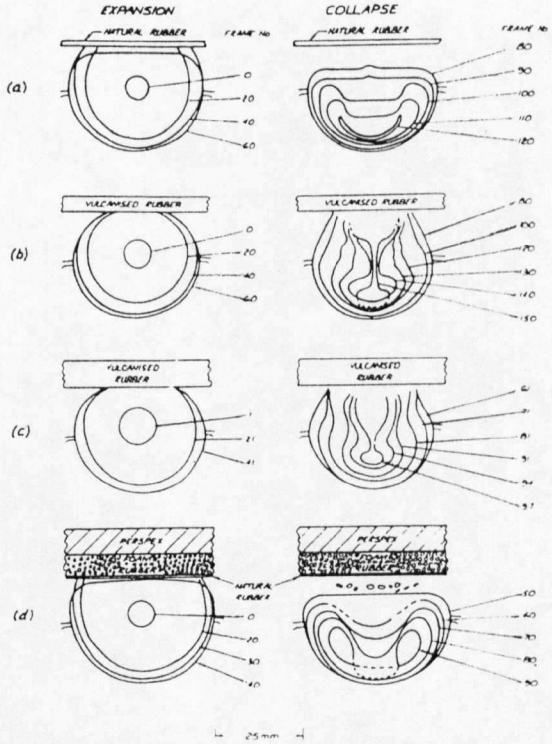

Fig.2.4.9 Examples of the interaction of pulsating bubbles with various deformable surfaces described in Table 2.4.2. All bubbles generated at frame zero. Camera speeds (frame/ms) were: (a) 11.7, (b) 13.5, (c) 12.9, (d) 12.3.
(from Gibson and Blake [1982])

2.4.3 Bubble-shockwave interaction

After Kornfeld and Suvorov [1944] pointed out the possibility of a liquid microjet impingement as a cavitation loading mechanism and Naude and Ellis [1961] beautifully presented the process of forming the liquid jet on a solid boundary, there has been a number of studies carried out on behaviour of collapsing bubbles near a solid boundary and on the damage capability of a liquid microjet by investigators mentioned in Section 2.4.1. Their results from experiments or theoretical calculations have consistently shown the liquid microjet velocity in the range 100~170m/s in a static liquid under atmospheric pressure (Benjamin and Ellis [1966], Plesset and Chapman [1971], Kling and Hammitt [1972], Lauterborn and Bolle [1975], Tomita and Shima [1986] and Vogel et al. [1989]). The water hammer pressure for such velocities can be calculated as P_{wh}=150~260MPa. In particular case of a liquid jet with a conical or round tip, it can be increased up to about three times the water hammer calculation (Lush [1983]), so the pressure would be P_{wh}=450~780MPa. These values are actually the same magnitude or higher than the yield strength of common materials (the tensile yield stress of mild steel is about 250MPa).

However, since the duration time of such an water hammer impingement is as short as 10^{-6}~10^{-8} second as mentioned in Section 2.4.1, the yield strength can become much higher than that statically obtained. Lush [1983] reported that the dynamic hardness of 99% pure aluminium measured by a falling ball test was 1300MPa while the static hardness of the same material was 400MPa; i.e. the dynamic value can be more than three times larger than the static one, and the water hammer loading due to the minute liquid jet is a much quicker process than the impact due to a falling ball. Then it has become realized that much faster microjet velocity may be required to produce an appreciable damage on relatively hard materials. In fact, Tomita and Shima [1986] reported that the microjet whose impact velocity was under 200m/s did not cause an appreciable damage pit on an indium specimen. A static yield point of the indium used was smaller than 30MPa but the water hammer pressure for this critical velocity 200m/s is P_{wh}=300MPa, or up to 900MPa for the one with a conical jet tip. However, such speeds of liquid jet have been seldom obtained from the experiment of a single bubble collapsing near a solid boundary in a static liquid achieved by many investigators.

Tulin [1969] pointed out the possible mechanism of producing such a high speed jet; i.e. when a pressure wave passes over a bubble, a very high speed liquid jet whose velocity is greater than half the velocity of sound in the liquid can be formed. Actually in most practical cases, the bubble which is responsible for cavitation damage must exist near a solid boundary and may be surrounded by the cloud of cavitation consisting of numerous cavities collapsing and rebounding. Therefore it is very likely that such a bubble-shockwave interaction usually takes place in reality. Then accordingly, it has been recognized that the effect of the presence of the other bubbles near by is an important field to investigate.

The problem of a shock interaction with a spherical void in inhomogeneous explosives was numerically solved by Mader [1965]. He showed that when an 8.5GPa shockwave with a shock velocity of 4500m/s and a particle velocity of 1710m/s arrives at the spherical void with a diameter of 0.4mm, the free surface velocity of the cavity boundary becomes 3420m/s (twice the original particle velocity) at first. Then the free surface velocity is increased to 5200m/s by a convergence effect, which is approximately one and half times greater than the initial free surface velocity at the moment of the first shockwave striking. Although the shockwave pressure 8.5GPa is too high to directly apply the results to the normal condition of cavitation, the formation of a liquid jet during the collapse and the convergence effect to accelerate the liquid jet velocity were shown.

Brunton [1970] used a disc shaped two dimensional air bubble and a detonator as a source of shockwave. The bubble whose size was about 3mm in diameter was held in a liquid layer between parallel transparent plates so that the collapsing process could be observed. He experimentally visualised the formation of the liquid microjet during the collapse and obtained a very high jet velocity 500m/s, though unfortunately the magnitude of the applied shock pressure was not mentioned in the paper. The bubble collapsing process is shown in Fig.2.4.10. The shape of the microjet viewed is slightly different from and is much wider than the microjet produced in a bubble collapsing close to a solid boundary. The diameter of the liquid jet in Fig.2.4.10 is about one third of the original bubble diameter while the diameter of the microjet during the collapse of a spark induced bubble near a solid boundary is likely to be one tenth of the original bubble size. He also measured the ratio of the size of the pit like damage on an annealed aluminium specimen, d, to its original bubble size, D. The results showed that d/D was approximately 0.5 and roughly agreed to the liquid jet

size.

This testing method was further improved by Dear and Field [1988]. They used arrays of two dimensional air bubbles instead of a single disc shaped air bubble to enable them to reproduce a more realistic situation of the bubble-shockwave interaction with multi-bubble effects. Bubbles were well positioned between the narrow gap of two transparent plates in water containing 12% by weight of gelatine, which was used to "fix" bubbles in between the plates. A plane ended striker was used as a source of initial shockwave. Figure 2.4.11 shows one of their results, rectangular array of nine cavities. Process of layer by layer collapse is clearly shown. At first, the initial shockwave by the striker passes over all of these cavities but only the first layer of three cavities are collapsed and at this time the second and the third row of cavities are almost shielded from the initial shock. Then, the first three cavities completely collapse in frame 4 and rebound in frame 5 with radiating shockwave which collapses the next row of three cavities. They reported that a high fraction of the collapse energy (80~90% estimated from the ratio of the jet velocities squared) of one collapsing row is transmitted to the next. As Hansson and Mørch [1980] pointed out in their discussion (see next section) for hemispherical layers of bubble cluster arrangement, the high fraction of energy transmission indicates that a focusing effect of the collapse energy toward the centre of the hemispherical arrangement would be possible. The formation of a rather wide microjet with a sharp cornered tip (conical tip, if it is in three dimension) is seen in frame 2 and 3. The jet velocity of 400m/s was obtained in a cavity with 3mm in diameter for the initial shock pressure of 0.26GPa which was produced by the striker at a velocity of 150m/s. The jet velocity of 400m/s is greater than the free surface velocity of 300m/s (twice larger than the particle velocity of 150m/s) because of the convergence effect as pointed out by Mader [1965]. This value can be even increased if the experiments were achieved with three dimensional spherical bubbles with which the convergence effect would be greater.

Tomita and Shima [1986] carried out a very comprehensive work on single bubble collapse near a solid boundary, including an air bubble struck by a shockwave. Firstly impact velocities of a liquid microjet were measured for a spark induced bubble collapsing near a solid boundary. They are ranging from 80m/s to 150m/s for bubbles whose maximum sizes are R_{max}=3.5mm and 5.1mm at a distance about L/R_{max}=0.8~1.1, where L is the distance from a spark gap to the surface. Then their

study was extended with the air bubble struck by a shockwave with amplitude of about 5MPa. They obtained clearly much higher jet velocities up to 370m/s for air bubbles with an equivalent radius of R_e=0.40~0.79mm. And as mentioned earlier in this section, only the microjet whose impact velocity was over 200m/s did produce an appreciable damage pit on a soft indium specimen.

From the results of these experimental investigations above, it may be accepted that the very high speed liquid microjet by the bubble-shockwave interaction is more likely as the most probable mechanism of cavitation damage than the relatively low speed microjet produced in the bubble which asymmetrically collapses only due to the proximity of a solid boundary. If this is the case, formation of a reverse microjet which is repelled by a compliant boundary as mentioned in the previous Section would be of less significance.

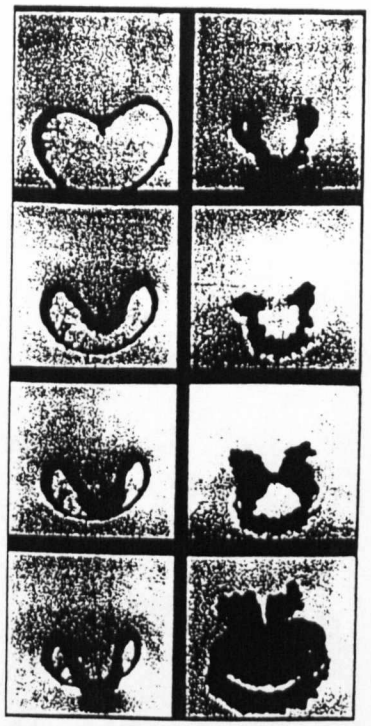

Fig.2.4.10 The collapse and expansion of a disc-shaped air bubble in water. The initial bubble diameter was 3mm and the relative timing of the frames reading down was 0, 4, 5, 6 and 7, 8, 9, 15 sec. (from Brunton [1970])

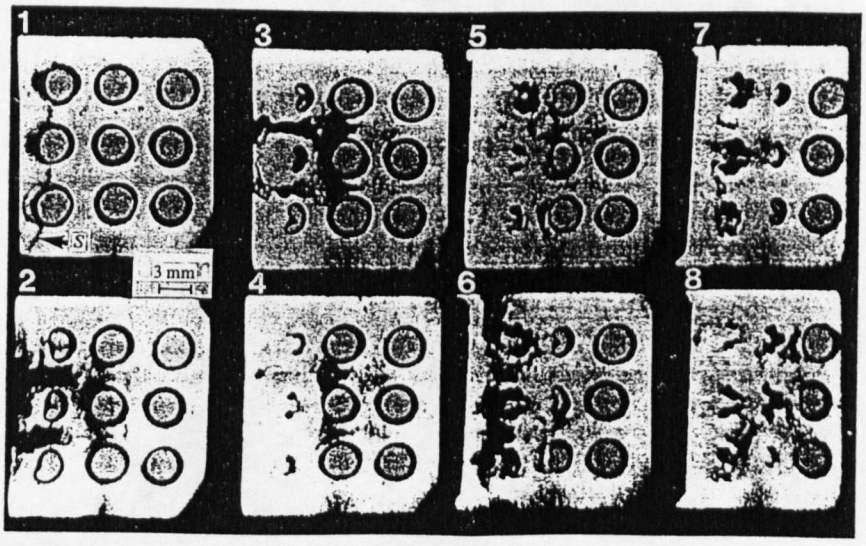

Fig.2.4.11 Rectangular array of nine cavities, diameter 3mm, collapsed by shockwave S. Inter frame time, 4.25μs. (from Dear and Field [1988])

Cavitation bubble dynamics has been increasingly sophisticated, but most of its objectives have been confined more or less to the behaviour, particularly erosion capability, of a single cavity as introduced in previous sections in this chapter. A considerable amount of study with experimental information has been accumulated with regard to the single bubble dynamics. In real engineering situation, however, cavities normally exist with numbers of the other bubbles and form a "bubble cluster". Figure 2.5.1 shows an example of the bubble cluster of an ultrasonic vibratory cavitation. Under such a condition where bubbles are densely populated, those bubbles must affect each other and the fluid must be treated as a two phase medium. One notable example of the former effects is a bubble-shockwave interaction which was described at the end of the previous section. For the latter problem, there are only a few publications reported, which dealt with the cavitating bubble cluster dynamics.

In order to investigate the reason of ship propeller blades bent at the trailing edge, van Wijngaarden [1964] theoretically treated the dynamic behaviour of a water-bubble mixture uniformly distributed on a flat plate. He considered that an extended uniform layer of bubbles containing gas and vapour would collectively collapse when the ambient pressure outside the mixture was suddenly increased from a small value to atmospheric at t=0. The pressure was firstly applied at the boundary between the mixture and the surrounding water and then was assumed to initiate the collapse throughout the mixture layer. The continuity and momentum equations were derived for the layer and were solved to obtain the maximum pressure on the plate. For the case of the initial ambient pressures ranging from $2x10^3$Pa to $3.3x10^2$Pa, which were then increased to 10^5Pa, it was found that the maximum pressure on the plate would become 10^6~10^7Pa. He concluded that the pressures in this range were sufficiently high to explain the observed phenomenon of bent trailing edges of ship propellers. Any possible effect of these high ambient pressures on cavitation erosion was not stated in this paper. However, as Mørch [1979] mentioned, it can be easily inferred that the damage capability of cavitating bubbles would be very much strengthened by these high pressures. For example, if the ambient pressure is increased during the

collapse by a factor of 10~100, the microjet velocity of a bubble collapsing near a solid boundary and so its water hammer impact pressure may be augmented by a factor of up to 3~10.

Ellis [1956] and Mørch and co-workers (Mørch [1980, 1982], Hansson and Mørch [1980] and Hansson, Kedrinskii and Mørch [1982]) visualized the growth and collapse of the cavitating bubble clusters in an acoustic field, in a flow system and in an one-dimensional shock tube. Figure 2.5.2 shows a series of high speed photographs of collapse of the almost hemispherical bubble cluster on the surface of a photoelastic material bar immersed in a 10,000 cycle acoustic field in water (from Ellis [1956]). The picture repetition rate was set at 150,000 pictures per second and so the series of fifteen pictures show the growth and collapse of the bubble cluster in one cycle of acoustic excitation. In each cycle, the cluster is developed and collapses completely. It is clearly seen that the bubbles are simultaneously formed at first and then grow within the hemispherical region. But the collapse of the bubble cluster is initiated from the outer boundary of the cluster, not from inside, by the ambient pressure of the surrounding liquid and then it is gradually forwarded toward the centre of the hemispherical cluster.

Mørch [1978] considered the collapse of the hemispherical bubble cluster at the end of the ultrasonic horn (, and soon the theory was extended to a spherical bubble cluster by Mørch [1980]). It was assumed that the collapse of the cluster is initiated at the outer boundary of the cluster by a pressure increase in the ambient liquid as experimentally observed, and a hemispherical shape shock front is formed at the boundary. The shock leads the collapse of the first hemispherical shell of cavities and is propagated into the cluster shell by shell at the velocity of the sound of the two phase medium, the water-bubble mixture. He treated this problem theoretically based on the momentum in radial direction relative to the centre of the cluster and derived the cavity cluster collapse equation which is similar, in shape, to the Rayleigh's equation for spherical collapse of a single bubble. Then it was concluded that the concerted collapse of the hemispherical and spherical bubble cluster would significantly increase the pressure at the final stage, though appropriate quantitative calculation of the pressure is difficult. The same model was extended to a cylindrical cluster and a layer of bubbles on a solid plate by Hansson and Mørch [1980] and Mørch [1982].

Although the approach above by van Wijngaarden and Mørch and co-workers

clearly shows the possibility of the high pressure generation at the end of the collapse of the bubble cluster due to the rapid change of the momentum in the liquid, the effects of a shockwave from the individual bubble collapse is not included in the theory. Each cavity collapse emits a shockwave and a part of the energy from the shockwave is more or less transmitted to the next inner layer of cavities. If the geometry of the bubble cluster is appropriate so that a convergence effect on the transmitted energy is expected, such energy can be accumulated through the successive collapse of following layers and is able to contribute to intensify the damage capability of the cavitating bubbles near a solid boundary at the last stage of the collapse of the bubble cluster. The possibility of this individual shockwave energy transmission and its accumulation were experimentally shown through the bubble-shockwave interaction process by Dear and Field [1988].

On the other hand, the bubble cluster dynamics have effects not only on the collapse but also on the growth of individual bubbles. Arakeri and Shanmuganathan [1985] carried out cavitation noise measurement with various artificially "controlled" number density of cavitation nuclei on a test body in an water tunnel. The number of nuclei, so bubbles, was controlled by electrolysis using a stainless steel ring embedded on the head of the test body. Figure 2.5.3 shows high speed photographs of the cavitation on the test body with different electrolysis voltage. The photographs and the acoustic noise measurements clearly showed that under same flow parameters increasing the number density of cavitating bubbles decreases the growth, or the size, of each bubble and the level of the cavitation noise which can be regarded as a measure of the cavitation loading intensity. This means that if the bubble volume fraction is high as shown in Fig.2.5.3, the behaviour of individual bubbles is affected by the pressure field in the cavitating flow which is partly generated by bubbles themselves. Therefore, it is obvious that there is a bubble-pressure field interaction and the theory for single bubble dynamics cannot be directly applied in such a cavitating field with the high bubble volume fraction.

The above phenomenon observed by Arakeri and Shanmuganathan was theoretically confirmed by d'Agostino and Brennen [1989]. They considered the dynamics of the one dimensional, unsteady flow of a spherical bubble cluster subject to harmonic far field pressure excitation, and then the results can be generalized by Fourier synthesis to the arbitrary far field pressure excitation. A set of equations was

derived satisfying the continuity and momentum equations with the Rayleigh-Plesset equation for determining the bubble motion (firstly in d'Agostino and Brennen [1983]). Though their approach provided no quantitative information, it was qualitatively shown that the increase of a bubble void fraction decreases the maximum amplitude of the each bubble growth at the surface and at the centre of the spherical bubble cluster. Their results revealed that the dynamics of each bubble is strongly coupled through the pressure and velocity field with the global dynamics of the flow in the bubble cluster.

Further study will be required in this highly complex field. Particularly it is important to accumulate much more experimental information on the bubble cluster dynamics problems for more refined theoretical treatment which will allow us to predict the bubble cluster effects quantitatively.

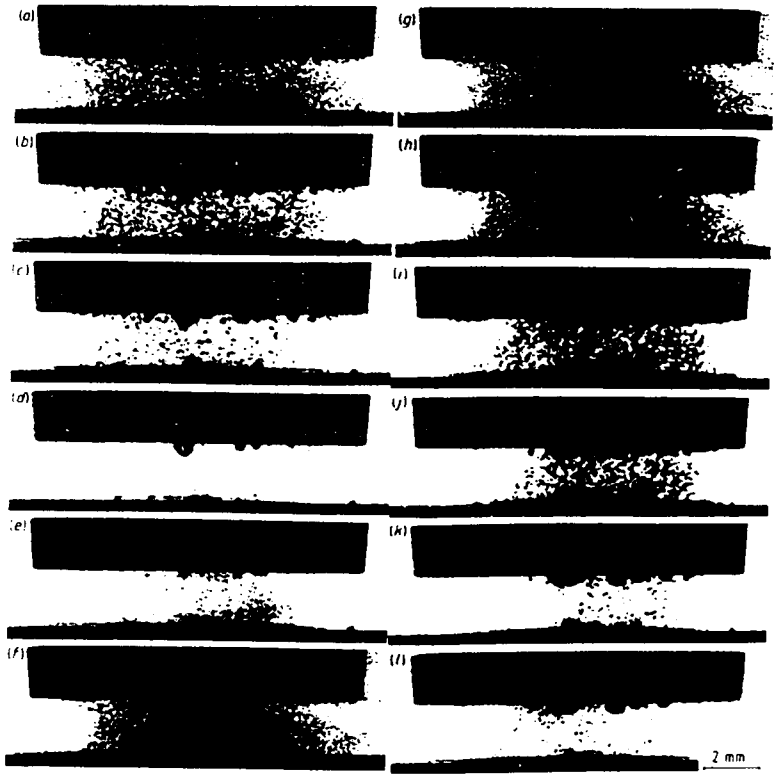

Fig.2.5.1 High speed sequence showing the cavity cluster life cycle in the space between the vibrating horn (above) and stationary specimen (below) during two cycles of the horn oscillation. Time interval between the picture 8μs. Frequency of the horn 20kHz. (from Hansson, Kedrinskii and Mørch [1982])

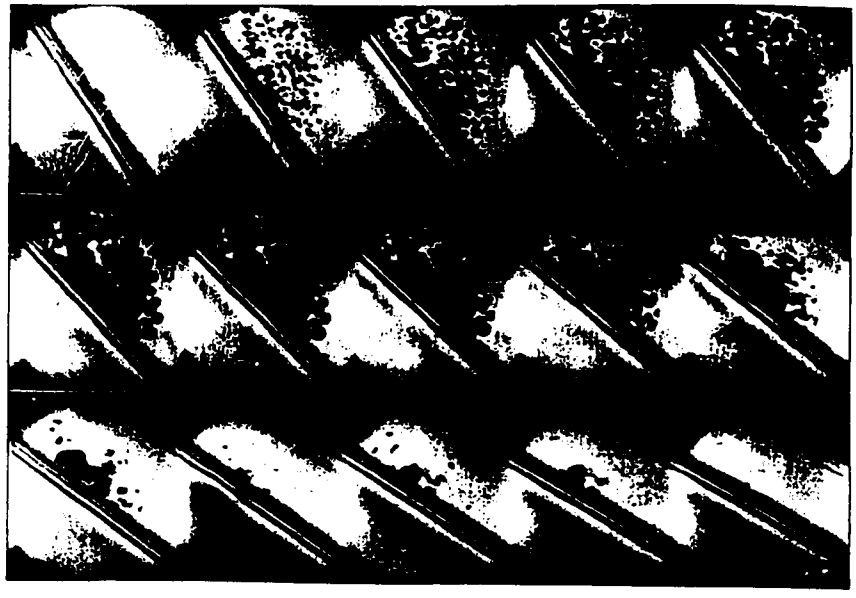

Fig.2.5.2 10000 cycle acoustic cavitation bubbles in water collapsing on CR-39 photoelastic plastic. Picture rate 150000 per second. Magnification 10x. (from Ellis [1956])

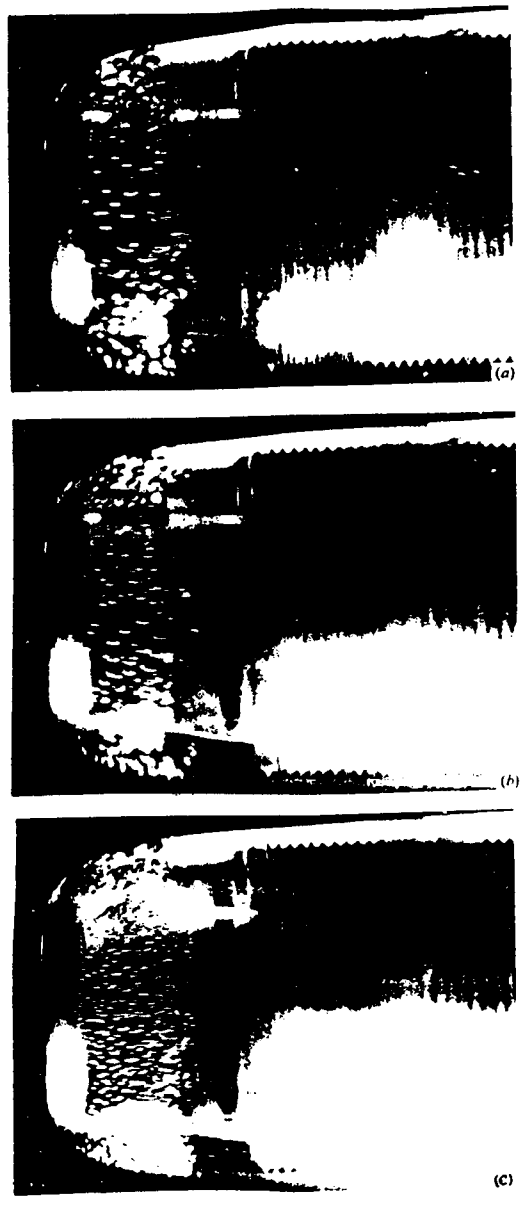

Fig.2.5.3 Photographs of cavitation with different electrolysis voltages for U_∞=10.8m/s, σ=0.52: (a) E=20V: (b) 40V: (c)60V.
(from Arakeri and Shanmuganathan [1985])

CHAPTER THREE - LITERATURE SURVEY: Experimental work on cavitation loading

---

3. LITERATURE SURVEY: Experimental work on cavitation loading

3.1 Introduction

For many years, investigators have been working on cavitation erosion. Vast numbers of theoretical and experimental publications have been reported and each one of them has contributed to the progress of understanding this subject. Especially, it may be true that our knowledge and understanding of these phenomena have been significantly improved with the advancement of various sophisticated testing techniques. For example high speed photography shows us the "fixed sheet" cavitation as a pack of numerous individual cavities, and if it is high speed "motion" picture, we can see even the detailed process of bubble collapse on a solid boundary. Some techniques are already well established and a lot of data have been accumulated for various cavitation conditions by using them, while some others are still under the developing stage and more refinement have been being hoped. A pit counting technique may be somewhere between two and direct measurements of cavitation loading pressure is one of the latter.

The pit counting technique does not require a long testing duration and is able to show much more variety of information about cavitation damage, such as a size of loading, the intensity of each damage, loading frequency and so on. Another advantage is that such pit counting data are not affected by the surface condition. The weight loss type erosion data depend on the progress of erosion on the material surface and accordingly depend also on the test duration so that particular care must be paid in order to evaluate the results. However, there have not been so many publications employing this technique. One major reason would be that it is not a easy and quick work to quantify the cavitation intensity from pits distributed and for many cases weight loss measurements are a much easier option. In the present project, the difficulty in quantifying the data has been overcome by a sophisticated method of analysis, a computer image analyzer.

On the other hand, there are several difficulties in the direct measurements of cavitation loading pressure as follows.

(1) Cavitation loading is applied to a boundary only on very small area. Indentation counting test using a very soft material shows that the size of each cavitation damage ranges from about a few microns to a few hundred microns and most of pressure transducers commercially available are not designed for such a small area loading. In fact, Tomita et al. [1984] reported that the spacial sensitivity of a commercial pressure transducer (Kistler 603B) is not uniform.

(2) Duration time or rise time of the loading pressure is very short, as short as 1~5μs. Therefore, the pressure sensor must respond very quickly and the sampling frequency for a digital data treatment, if necessary, must be extremely high. For example, the resonance frequency of above Kistler 603B is 400kHz with a rise time of about 1μs so that it may not be suitable for such an application, and digital sampling frequency of 5~10MHz requires high performance data processing devices and vast memory which, at this moment of technology, practically limits the measuring time up to a few second.

(3) Pressure magnitude of the loading itself is very high and so very damaging. Not only mechanically fragile pressure sensors cannot be used for a relatively long term measurement but also the surface condition of the boundary of the sensor which directly faces the cavitation loading can be quickly changed. The pressure measurements of such a damaging impact may be much more difficult for a cavity cluster in a practical situation than the ones for a single cavity in an ideal situation.

In this chapter, only several publications which treat the pit counting and the loading pressure measurements will be reviewed in mainly chronological order. Simple application of cavitation noise measurements in which the microphone is not placed directly against the cavitation loading will not be included. But the work by Fry [1989] will be discussed. It was hoped that the nature of cavitation loading and important technical points in measurements would be more clarified.

A testing technique of counting pits on a soft and ductile material was firstly introduced by Knapp [1955] for the purpose of investigating the development of cavitation damage in a flow system. (Knapp termed the single circular damage on the pure aluminium surface "pit" in the paper and this term has been accepted by many investigators. However, if there is no material loss from the surface as it will be described for Knapp's case below, the term "dent" or "indentation" would be more correct expression. On the other hand, some studies including Robinson and Hammitt [1967] discussed in this section may have treated both "pits" and "indentations" for various types of material with different hardness. Therefore, it was decided that "pit" would be used only in this section to avoid unnecessary confusion and "indentation" is used in the other part of the present thesis unless there is any material loss.) A two inches diameter cylindrical body with a hemispherical nose was used for the testing in a water tunnel. At first Knapp studied the mechanics of fixed type cavitation by using high speed motion pictures and observed the now well known (1) the formation and growth, (2) filling with re-entrant flow and (3) break off process. The cavitation damage along the length of the test section in relation to the position of the fixed cavity were also investigated. For this purpose, cavity lengths were set 1 in. and 2 in. from the head of the body in the testing with a constant tunnel velocity of 90ft/s. The intensity of the cavitation damage was quantified by counting the number of pits; i.e., plastic deformations produced on a soft material by mechanical blows by collapse of cavitating bubbles. Pure annealed aluminium was chosen as the soft material to register such deformations on its surface at a centre section of the test body. Figure 3.2.1 is the damage development with testing time. Pits in white circles show that they were formed by a single blow and no metal was removed from the surface, since the tool marks can be seen. Knapp also confirmed that the number of pits appearing per unit time per unit area was approximately constant for at least first 20min. until duplicate hits were obvious.

Distributions of number of pits were beautifully presented with the idea of the size of the fixed cavity, 1 in. and 2 in., as shown with photographs in Fig.2.1.1. The number of the pits at the maximum damage distance is more for 1 in. cavity, but the surface is actually much more severely damaged by relatively larger size pits for 2 in.

cavity. Since the flow velocity, 90ft/s, was kept constant for both 1 in. and 2 in. cavities, in order to obtain twice the longer fixed cavity length the ambient pressure in the tunnel must be smaller in the case of 2 in. cavity. The cavitation number σ can be defined as

$$\sigma = \frac{P_0 - P_v}{\frac{1}{2}\rho V_0^2}$$

where P_0 and P_v are the constant pressure in the tunnel and the vapour pressure of the liquid, respectively and V_0 is the constant tunnel velocity. Therefore cavitation number would be also smaller and so the each bubble size and pit size could be greater for 2 in. cavity case.

The distributions of pits were further investigated later by Knapp et al. [1970]. Figure 3.2.2 shows the distribution of the same pits as in Fig.2.1.1, but this time they are plotted with several set of data for various size categories. It will be noted that, while most size of pits are similarly distributed as the entire pits, the largest size category group where pits range 0.005~0.01 in. in diameter are found more in a downstream region from the maximum damage zone. This observation seems to indicate that the travelling cavities continue to grow for the entire length of the fixed cavity so that there are more large ones available to produce large pits in downstream region. Moreover it was calculated, from the high speed photographs of cavities, that only one in 30,000 travelling cavities produced a damage on this very soft material. Although Knapp [1955] commented "surprising fact" about this relatively low damaging rate, same order of the pitting rates have been reported later by many investigators.

One of the important results Knapp obtained is the sixth power variation of pitting rate with velocity. The pitting rates which is the number of pits per unit time per unit area are plotted with flow velocities from 60ft/s to 100ft/s in Fig.3.2.3. In this set of measurements, it is thought that the cavitation number was kept constant for various flow velocities, since the cavity lengths were constant (Knapp et al. [1970]). Similar effects of a flow velocity on an erosion rate, such as mass loss rate or volume loss rate which is used as a measure of the cavitation erosion intensity, has been measured by numerous investigators. Some of their velocity exponent are listed in Table 3.2.1 (from Ramamurthy and Bhaskaran [1979]) with their testing method and conditions.

Table 3.2.1(a) Summary of experimental studies - Velocity exponent for cavitation erosion (from Ramamurthy and Bhaskaran [1979])

TYPE OF TEST EQUIPMENT	MATERIAL (TEST SPECIMEN)	CAVITATION NUMBER OR CAVITY LENGTH	TEST DURATION	VELOCITY mps	EROSION CRITERION D	VEL. EXPONENT $D = Ku^{n_1}$ $D = K(u - u_0)^{n_2}$
Axi-symmetric water tunnel, hemispherical nose ogival after body (1)	Aluminium 2S-F	ℓ = 25 mm ℓ = 51 mm	10 min. to 30 min.	18 to 30	Number of pits per second per sq. in.	n_1 = 6
Field test on 30,000 KW Francis turbine (2)	Aluminium 2S-O test piece on runner	ℓ = 152 to 203 mm	5 min. to 20 min.	18 to 30	Number of pits per second per sq. in.	n_1 = 6 (5.6 - 6.3)
2-Dimensional water tunnel, cylindrical source.(8)	Lead	λ = 3 Near peak erosion	--------	14 to 23	Rate of volume erosion	n_1 = 4 to 5, Near peak erosion
Field hydraulic turbine (3)	Steel runner	----------	Up to 100 min.	5 to 9	Radio isotope technique	n_1 = 5 to 8
Venturi test rig, cylindrical source (13)	Steel, Aluminium and Plexiglass	Near peak erosion	Varied	15 to 30	Volume loss	n_1 = 1.7 to 5, n_1 increases with test time
2-Dimensional water tunnel, cylindrical source (12)	Lead	λ = 3	Varied	9 to 14	Weight loss	n_1 = 2 to 5, n_1 increases with test time
Venturi test rig, tapered piece projecting into the venturi, mercury (14)	Stainless steel 302	Varied	30 to 100 hrs	6 to 20	Volume loss	n_1 = 1 to 2
Venturi test rig, same as above (15)	Stainless steel 302	Varied	--------	6 to 20	Volume loss	n_1 = 0 to 5 depends on σ
Venturi test rig (6)	Brass	Constant	--------	37 to 49	Weight loss	n_1 = 7
2-Dimensional water, tunnel, cylindrical source (40)	Lead	λ = 2.5 to 3	Incubation period	12 to 20	Volume loss	$D \propto L^3 u^{n_1}$ n_1 = 5
Rotating disk in water, holes on the disk to induce cavitation (10)	8 different alloys	σ = .084 σ = .125 and σ = .217	Up to 40 hrs	39 to 63	Volume loss	$1 < n_1 < 12$ $1 < n_2 < 7$ High exponent at low volume loss
Rotating disk, cylindrical source (20)	Lead-Antimony alloy.	σ = 0.25 σ = 0.5 and σ = 0.75	90 min.	23 to 50	Weight loss	$7 < n_2 < 10$ $.25 < \sigma < .75$ u_0 depends on static pressure
Rotating disk, holes on the disk to induce cavitation (41)	Aluminium	σ = 0.23	30 min.	26 to 34	Weight loss	n_1 = 9.55
Venturi test rig, cylindrical source (7)	Lead	λ = 1 to 10	---------	15 to 25	Volume loss	$5 < n_1 < 8$ For noise and erosion
Venturi test rig, cylindrical source, mercury (5)	Stainless steel 304	At peak erosion	For constant rate erosion	7 and 9	Weight loss rate	n_1 = 3.7
2-Dimensional water tunnel, cylindrical source (16)	Lead	Near peak erosion	Varied 0-14 hrs	7 to 25	Weight loss	n_1 = 2 to 5 n_1 increases with test time
2-Dimensional water tunnel, cylindrical and 30° wedge sources (25)	Lead	Near peak erosion	--------	9 to 14	Volume loss rate	n_1 = 5 for erosion and noise, depends on σ

Table 3.2.1(b) Summary of experimental studies - Velocity exponent for cavitation erosion (from Ramamurthy and Bhaskaran [1979])

Water tunnel (11)	-------	------	Varied up to 5 hrs	-------	Weight loss	n_1 = 10 to 2.5, decreases with test time
2-Dimensional water tunnel, cylindrical source (18)	Aluminium	Varied	Varied up to 100 minutes	20 to 30	Volume loss	n_1 = 6, initial cavitation n_1 = 17, for peak erosion
Venturi test rig, circular pin (22)	Aluminium & copper	---------	1 hour	18 to 27	Weight loss	n_1 = 7
Rotating foil facility, hydrofoil (NACA-16-021) source (9)	Aluminium 1100-F	At peak erosion	10 to 70 hrs	49 to 59	Erosion intensity	n_1 = 6, Erosion depends on source size & σ
2-Dimensional water tunnel, Cavitation behind a step (4)	Aluminium 1100-F	σ = 0.33	10 min. to 190 min.	17 to 21	Number of pits per second per sq. in.	n_1 = 6
Rotating disk, equi-lateral prism - Apex facing downstream (19)	Aluminium 1100-0	σ = 0.196	30 min.	39 to 46	Weight loss	n_1 = 5.5 for peak erosion and optimum source size

Although velocity exponents in Table 3.2.1 are ranging from -1 to 12, many of them are around six. One of the major reasons for this large variation in the velocity exponent is that the erosion rate must be dependent on the state of the material surface damage. Hutton and Lobo Guerrero [1975] pointed out that material properties of the surface are varied with time during the test by progressing plastic flow, work hardening and brittle fracture, and also by hydrodynamic variations due to surface roughness and, later, even shape changing as the surface becomes badly damaged. Therefore, the erosion rate in early stage of damage is different from that in matured erosion stage and hence it becomes extremely difficult to compare such erosion rates from various levels of surface damage condition with each other. In Knapp's experiments, this is not a problem since he only counted number of pits on a surface which still kept more or less the original surface condition. Furthermore in testing listed in Table 3.2.1, there is a difference in way of setting test pressures; i.e., some kept cavitation number constant while others kept a constant ambient pressure in a tunnel.

An effect of velocity on the size of pits was also discussed in the Knapp's paper. Table 3.2.2 shows the percentages of large pits above 0.0025 in. diameter with flow velocities. It appears that the percentage of large pits increases with the velocity, and then the damage rate, cavitation erosion intensity, can become even greater than

the sixth power of the velocity. Anyway it was firstly made clear in this paper that the flow velocity is very important parameter in cavitation damage and that relatively small variations in the velocity can be sufficient to produce significant changes in erosion intensity.

Variety of facts were found and lots of direction of future study were suggested in this classical paper, and actually most suggestions have been followed by numerous investigators. As one of those examples, it was realized that the pit counting is a simple but useful and reliable method to investigate the cavitation damage. Several experiments using this method have been done and the method itself has also been refined in many respects, though the basic purpose has still been the same.

Table 3.2.2 Effect of velocity on pit size

Flow velocity (ft/sec)	Percentage of large pits*
100	5.1
90	4.1
77.5	2.6
71	2.65
63	0
59	0

* Above 0.0025 in. diameter. (from Knapp [1955])

Robinson and Hammitt [1967] carried out more detailed pit counting on a surface of a damage specimen in cavitating venturi with water and mercury. Flow velocity at the throat was up to 200ft/s for water and 20ft/s for mercury. A profilometer was used to measure the vertical profiles of cavitation pits and they were compared with profiles due to water droplet impacts on a similar material. Figure 3.2.4 shows both examples. All of them are very similar each other and show almost conical shapes rather than a segment of sphere-type round shape. They concluded that this would indicate the microjet impingement as a more probable damage mechanism.

The size of pits was also measured and, for both water and mercury, the

maximum pits diameter up to several mils (1mil=0.001in.=25.4μm) were found. Figure 3.2.5 shows the detailed pit size distributions for 304 stainless steel, carbon steel and Cb-1Zr in mercury and for 304 stainless steel in water. It appears that there is a peak value in size for mercury at around 0.05mils (=1.27μm), whereas it is not clear for water. Figure 3.2.6 is made from the data directly read from "Fig.14 and Fig.15" in their paper and shows the distribution of number of pits along the specimen for various size of pit diameter. The static pressure above the vapour pressure, $(P-P_v)$, on the specimen surface is also shown. The number of larger pits increases with distance from a leading edge of the specimen, while the number of smaller pits and also the total number seem rather constant or slightly decrease except the points at the distance 0.15 in. from the edge. This is because only relatively large cavities are able to penetrate into high pressure region at the downstream end of the specimen. Similar tendency had been observed in the results obtained by Knapp et al. [1970], which was already discussed and is shown in Fig.3.2.2. They also reported that the ratio between number of bubbles and number of pits for Cb-1Zr and 304 stainless steel in mercury was about the order of 10^4 for the maximum damage region.

Hutton and Lobo Guerrero [1975] developed soft aluminium "foil" technique in water tunnel instead of the solid pure aluminium plate and investigated the scale effects in cavitation erosion. The aluminium foil was stuck to a test surface by a soft double sided adhesive tape so that it was mechanically weaker and more sensitive against the cavitation damage than the solid aluminium plate and accordingly produced more pits for same duration. Testing time was usually from 2~5 minutes to produce sufficient isolated pits for throat velocity 5~45m/s. The damaged surface was photographed on 35mm film and printed with magnification of 4x and then only the number of pits were counted with an eye-piece having a 6x magnification. (A microscope 50x was used only for a solid aluminium specimen in a comparison test, since then the minimum pit size was smaller.)

They at first carried out tests with both aluminium foil and solid aluminium for similar flow condition and compared the results. It was found that the minimum pit sizes were much smaller in solid aluminium (8μm) than the foil (50μm), because of the difference in magnification (50x microscope for the solid and 6x eye-piece for the foil) and different mechanical properties, although the maximum sizes did not differ so widely (300μm for the solid and 400μm for the foil). Figure 3.2.7 shows the number of pits per second per mm^2 with distance from a throat distributed at the

centre line of specimens. Convergent divergent wedges were used as the throat in test section of 40mm(H)x10mm(W). The flow velocity and the cavity length are 36.0m/s and 45mm for the aluminium foil and 37.7m/s and 50mm for the solid aluminium and so the damaging capacity of cavitation should be slightly greater in the case for the solid aluminium. Regardless of the difference between two method in such damaging capacity and the minimum size of the pit counted, the aluminium foil technique (a broken line in Fig.3.2.7) recorded much more pits than that on the solid aluminium with only the exception at the most severely damaged distance for the solid aluminium at about 50mm to 60mm. These results indicate not only the advantage of the foil technique but also the dependency of the pit counting results on the mechanical property of the specimen material used. The general distribution patterns were similar.

They have obtained velocity exponent e_1=2~10 and scale exponent e_2=2.2~3.5 in a following equation.

$$\textit{Cavitation intensity} \propto V^{e_1} \cdot D^{e_2}$$

where V and D are velocity and typical dimension of model, respectively, and "cavitation intensity" is defined as the number density of pitting; the number of pit per second per mm^2.

Okada et al. [1989] carried out the pit counting for 2024-aluminium alloy, 99.9% pure copper and mild steel with a magnetostrictive vibratory cavitation test apparatus. An image analyzer was used for their counting pits to obtain the precisely quantified information about the pit size. The very detailed pit size distributions were obtained and compared with cavitation impact loading distributions which were directly measured by a small piezoelectric pressure transducer. Since their objectives are rather to estimate the critical impact loading pressure to produce a pit on materials and not to study the pit distribution itself, the results will be discussed in the next section.

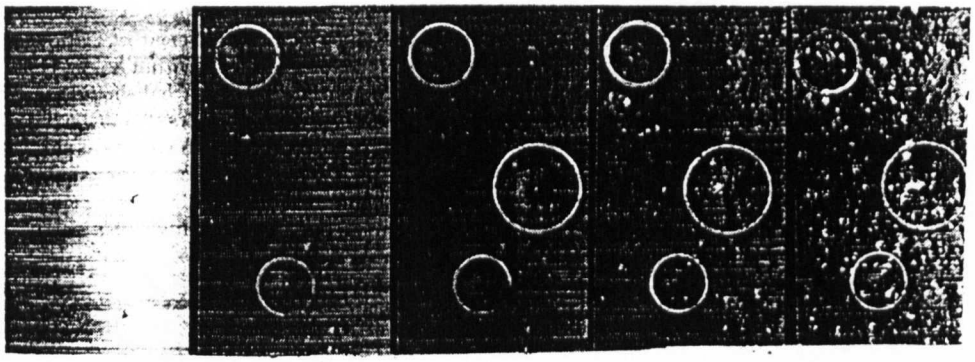

Fig.3.2.1 Damage development (from Knapp [1955])

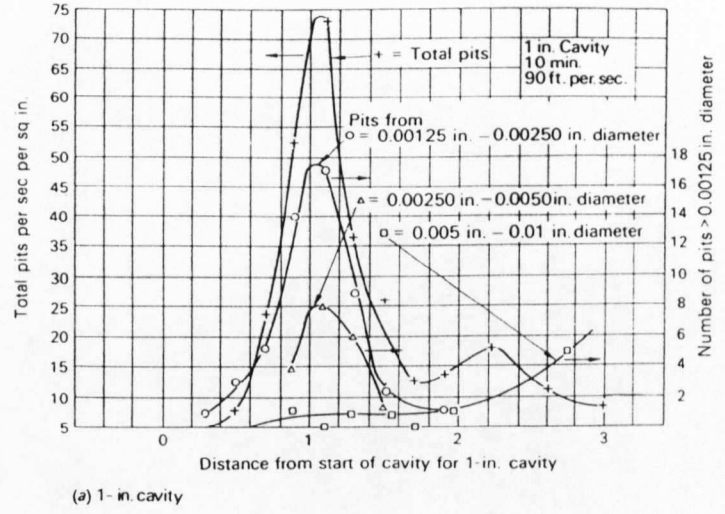

(*a*) 1-in. cavity

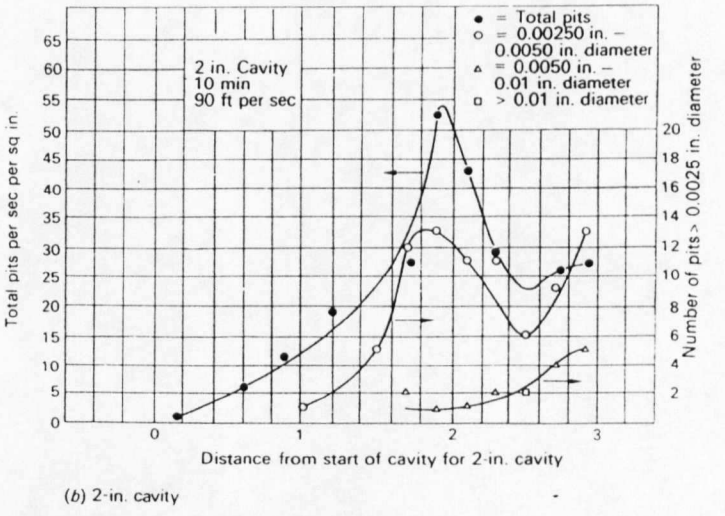

(*b*) 2-in. cavity

Fig.3.2.2 Distributions of pitting frequency by pit size on soft aluminium in the CIT tunnel. (from Knapp et al. [1970])

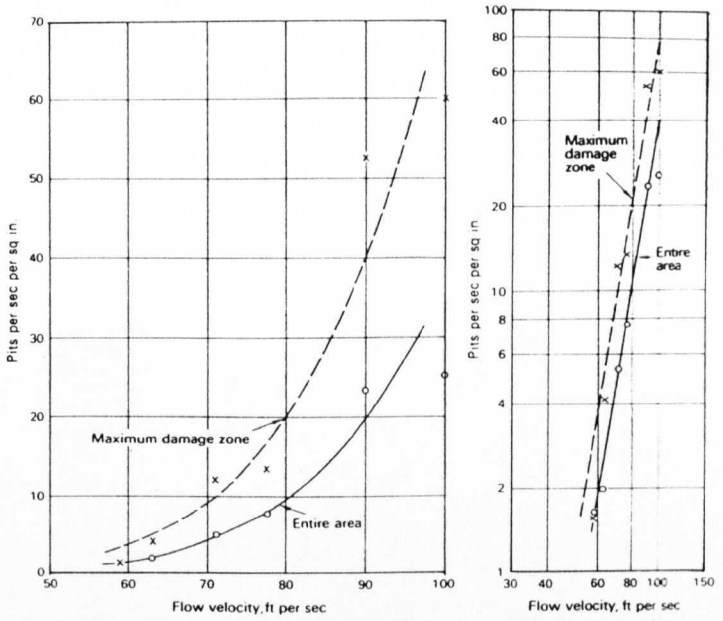

(*a*) Linear plot (*b*) Logarithmic plot

Fig.3.2.3 Variation of pitting rate with flow velocity for soft aluminium in the CIT water tunnel. (from Knapp [1955])

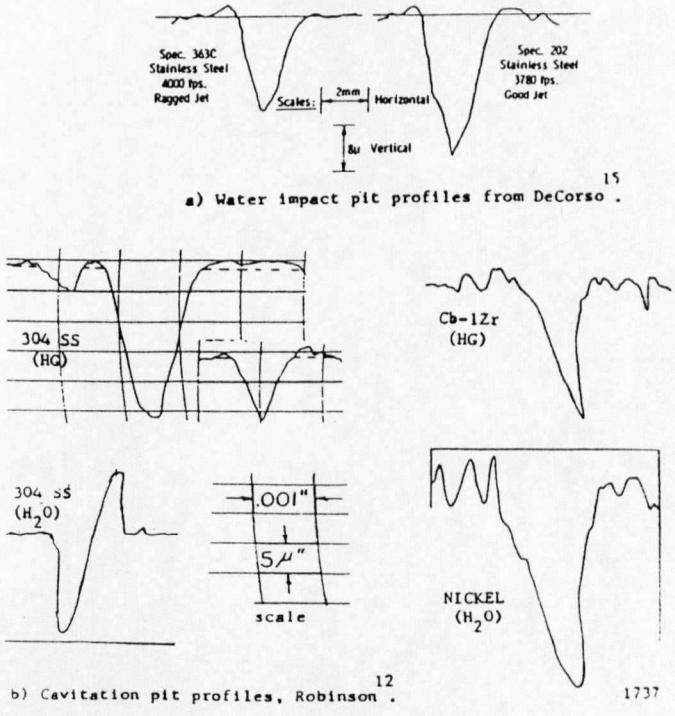

Fig.3.2.4 Comparison of jet impact craters to cavitation craters (from Robinson and Hammitt [1967])

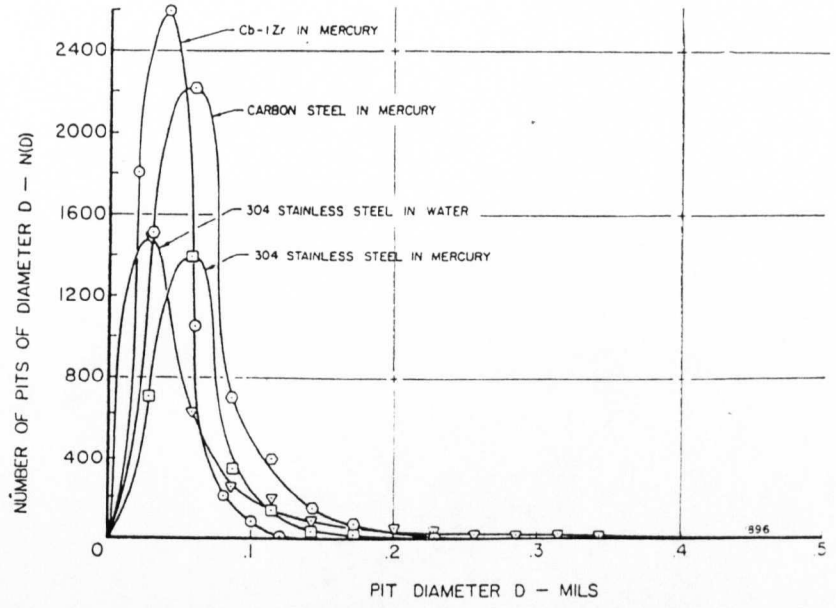

Fig.3.2.5 Pit-size spectrum for downstream position on specimen surface for SS in H_2O and SS, CS, Cb-1Zr in mercury (from Robinson and Hammitt [1967])

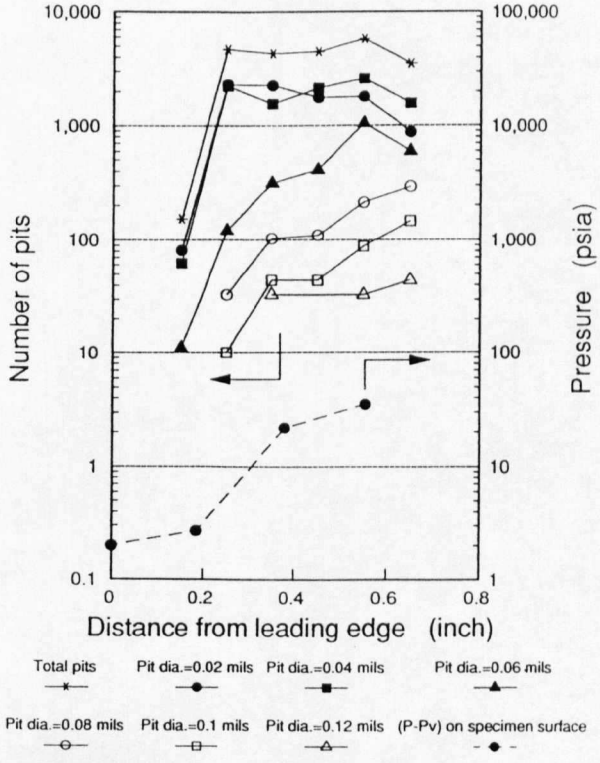

Fig.3.2.6 Distributions of pits by size along test specimen, Cb-1Zr in mercury (from Figs.14 and 15 in Robinson and Hammitt [1967])

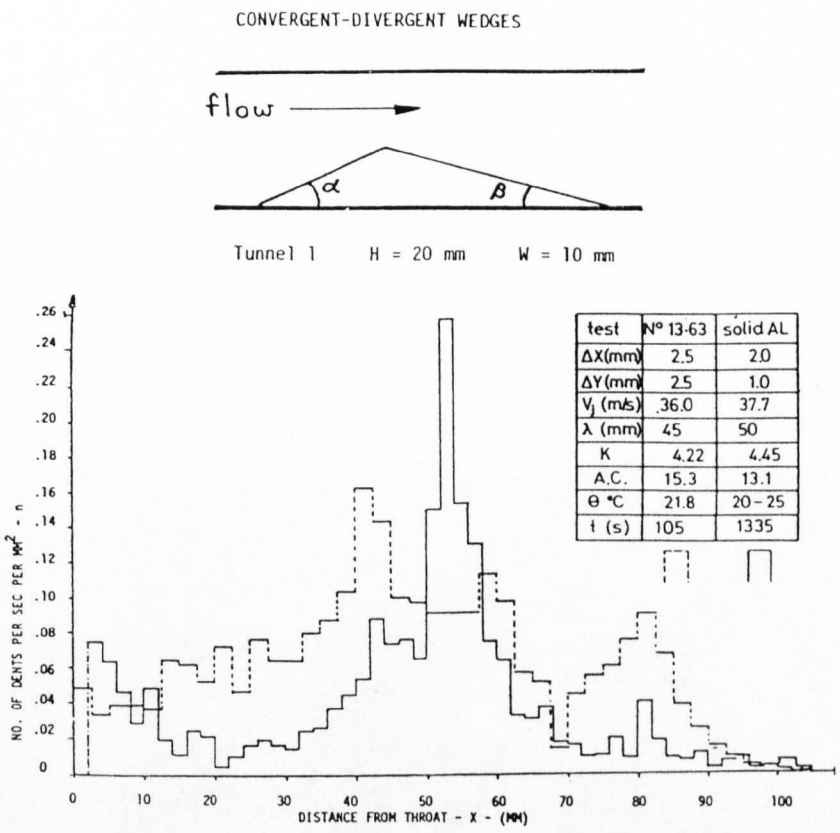

Fig.3.2.7 Comparison of the central distribution of dents over aluminium foil and solid aluminium for slightly different cavitation extent.
(from Hutton and Lobo Guerrero [1975])

Jones and Edwards [1960] investigated the peak pressure during the collapse of a single spark induced bubble at the end of their "pressure bar" submerged in tap water. Figure 3.3.1 shows their apparatus. They made their own pressure transducer bars with a piezoelectric quartz disc as a pressure sensor. A hemispherical cavity was created on a top end surface of the bar by a spark at a gap between a tungsten needle and the pressure end of the bar. Pressure bars of two diameters, 1/2 and 1/4 in., were used and calibrated by the short duration stress waves produced by the impact of steel balls on the pressure end. Those duration time for a 1/2 and 1/4 in. diameter bar was about 12 and 6μs, respectively. Figure 3.3.2 shows series of high speed photographs of the growth and collapse of the cavity. The cavity keeps its hemispherical shape during the growth and collapse and the peak force was obtained at its minimum size. The peak pressure was calculated from the obtained peak force and the minimum size of the cavity estimated from streak schlieren photographs. The minimum size of the cavity observed and the calculated peak pressure were about 0.8mm in diameter and 10^3MPa, respectively. However, considering that the minimum cavity size, 0.8mm, was the diameter of the tungsten electrode and so the cavity could be even smaller, they concluded that the peak value would be more likely to be ~10^4MPa. The width of the measured pressure pulse at the half peak height was about 3μs by 1/4 in. bar (quicker one in response). They also found that the peak pressure generated on collapse of the rebounding cavity becomes the same magnitude as that obtained at the collapse of the initial cavity. High speed dynamic pressure transducers were successfully designed and manufactured with piezoelectric materials as a sensor, and this work is regarded as one of the first reasonably accurate pressure measurements of this kind.

Surface loading produced by ultrasonic vibratory cavitation apparatus was investigated by Vyas and Preece [1976]. In order to measure the loading pressure, a piezoelectric quartz pressure transducer, 2mmx2mmx6.368mm (thick), was put just below the vibratory horn in distilled water. Therefore, a bubble cluster was created and collapsed right on the quartz transducer. The transducer was dynamically calibrated by dropping 12mm-diameter glass balls on its surface from various heights and measuring the amplitude of the first peak recorded on a storage oscilloscope. The

maximum pressure during the impact was calculated by Hertz law of contact and then the ratio of the output voltage to the maximum pressure calculated was used throughout the paper. This indicates that the cavitation loading size was assumed to be about same area as the contact area between the 12mm-diameter glass ball and the surface of the quartz pressure transducer at the moment of the maximum pressure. Unfortunately, since the material property of the transducer surface and ball dropping heights are not clear in this paper, it is impossible to estimate the actual contact size at the calibration. If, however, it is supposed that the surface of the transducer is hard material like stainless steel and the dropping height is about the order of a few centimetre, the contact radius would be well below one millimetre and so the assumption seems not very unlikely. But still the cavitation loading size in this particular condition is not known and hence it should be noted that the measured pressure value can be easily varied by the area ratio of the assumed contact size to the actual loading size. As results, the maximum pressure of about 900MPa and the half peak width of about 5μs were measured. They concluded that the measured stress pulses are attributed to the concerted collapse of a whole bubble cluster rather than to the independent collapse of individual bubbles.

Fujikawa and Akamatsu [1978] carried out pressure measurements of bubble collapse in an water filled shock tube. The water shock tube apparatus and experimental arrangement are shown in Fig.3.3.3. Hydrogen bubbles are generated as cavitation nuclei by electrolysis of water and then an expansion wave (the cavity grows.) and a subsequent compression wave (the cavity collapses.) are applied on them. The impulsive pressure was measured by a dynamic pressure transducer using a piezoelectric ceramic disc put between two zinc bars. Figure 3.3.4 shows the pressure transducer. The size of its circular detective face is 4mm in diameter. The pressure transducer was calibrated by means of a shock tube and its output was 10.30kgf/V with a rise time less than 0.3μs. It was confirmed from their high speed photographs that, even under such expansion and compression pressure gradients, bubbles grow and collapse in spherically symmetric form when they are at far from a vertical boundary wall and they collapse asymmetrically and produce a microjet toward the wall when they are close to the boundary.

They closely investigated both the output from the pressure transducer and the high speed photographs and concluded that no experimental evidence supported the idea of a microjet impingement mechanism as a source of the impulsive pressure and

the pressure measured was brought about by the shockwave generated at the instant of the rebound of a collapsing bubble.

Detected impulsive forces in their test were up to about 180N for a large bubble with the original radius of R_0=3.57mm collapsing at about L/R_0=0.3~0.6 (L is the distance from a boundary shown in Fig.3.3.4.), which is about only 14MPa if it is averaged over the entire surface of the pressure transducer. Then, the pressure inside the bubble at its minimum radius was estimated as the maximum impulsive pressure and the estimated values are of the order of 10^3~10^4MPa which agrees very well with Jones and Edwards [1960]. However, the maximum impulsive pressure based on the minimum size of the bubble can be only applied to the case of bubbles directly attached to the wall throughout the collapsing process. This seems not likely in flow cavitation and so the loading pressure would become much smaller than the estimated values if it is in flow condition. Observed impulsive pressure duration was 2~3μs.

One interesting study on this shockwave-or-microjet problem has been recently reported by Kimoto [1987] and Kimoto et al. [1987]. Kimoto made a very unique design of local pressure sensor which consists of four thin plates (thickness; 0.45mm each) of piezoelectric material with resonance frequency of 500kHz set in parallel as shown in Fig.3.3.5. The local pressure sensor was calibrated with another pre-calibrated standard pressure transducer (PCB 111A24, resonance frequency of 400kHz) using a shockwave from spark induced bubble collapse as a source for calibration.

A single bubble was generated by an electric discharge system and collapsed on the set of the local pressure sensor. Then, each one of four plates acts as a small independent pressure transducer. The bubble position was adjusted so that the microjet impinged on to one of the plates and its impulsive pressure was distinguished. High speed photographs of the bubble collapse and its microjet formation are shown in Fig.3.3.6 and Fig.3.3.7, respectively. Figure 3.3.8 is the output of the four channel local pressure sensor corresponding the bubble collapse in Fig.3.3.6 and Fig.3.3.7. The microjet impact is clearly distinguished from the one from shockwave. From the high speed photographs, it was observed that the diameter of the microjet is about 0.5mm and its tip velocity ranges 100~110m/s. Figure 3.3.9 shows the impulsive pressure distribution of the shockwave (P_{sm}) and the microjet (P_{jm}) for bubbles at various vertical distances from a boundary at a horizontal distance,

L. The maximum values of P_{sm} and P_{jm} are both found at around L=0 and are about P_{sm}=3~6MPa and P_{jm}=1~3MPa, respectively. Shockwave pressures are distributed more widely. It should be noted that (a) the detecting area of each local pressure sensor, 1.8mm^2 (0.45mmx4mm), is about ten times larger than the sectional area of the microjet impact, 0.2mm^2 (from its diameter, 0.5mm), and moreover (b) there was a possibility that the microjet might have not impinge the exact centre of the sensor. Accordingly, the microjet pressure can be reevaluated as about P_{jm}=10~30MPa or even higher. It is likely that the first one, (a) area effect, might have happened in the measurement by Fujikawa and Akamatsu [1978] and the microjet pressure was covered behind the noise. Therefore, the pressure transducer with sufficiently small detective area would be needed to correctly measure the microjet pressure, though it is very difficult for actual flow cavitation where the bubble size is smaller than the single bubble tests and the exact location of the microjet impingement is not known beforehand.

On the other hand, the water hammer pressure calculated from the observed jet velocity, 100~110m/s, is about 150MPa and is much larger than the measured value of P_{jm}. Then, Kimoto concluded that the detected impulsive pressure of the microjet is likely to be the stagnation pressure rather than the water hammer pressure. If it is assumed that the duration of the water hammer pressure is the jet radius divided by the jet velocity, it would be about τ_{wh}=2.5μs in this case. This is just the same level as the resonance frequency of the pressure sensor 500kHz. Therefore, one may think the possibility that the water hammer pressure may not have been detectable, even if there was any.

In all above investigations with single bubble collapse or cyclic collapse of vibratory cavitation, pressure transducers were especially developed for their particular purpose and the measurements were achieved by manually tracing the electric output on the storage oscilloscope screen. These were able to be relatively easily carried out in tests above, because the variation of the type and the magnitude of data obtained from those single bubble collapse tests were not so large; i.e., the testing time was short so that the large amount of data treatment was not necessary and the damage to the pressure transducer was not so severe. In actual flow cavitation, however, there are certain distribution for the physical size and impulsive force amplitude in cavitation loading and so the data must be treated as a sort of statistic distribution. This requires

much longer testing time with somewhat sophisticated data treatment and much more durable pressure detecting device.

Kirejczyk [1979] measured cavitation loading pulse height distributions and size distributions of pits produced on aluminium in both vibratory and water tunnel cavitation facilities. The pressure transducer PCB Piezotronics type M113A22 (detective area size; 5.5mm in diameter) was used. Although its natural frequency has not been given in his paper, it is reported in the paper that the pulses shorter than 2μs were not recorded. The transducer was mounted 7mm apart from the horn in vibratory cavitation or 33mm downstream from a cylinder as shown in Fig.3.3.10 in flow cavitation. In both cases, the transducer position was the same as the specimen for pit counting so that it was possible to directly compare the pulse height data with the pit size distribution. This enabled him to estimate the pressure of cavitation loading later. Figures 3.3.11 and 3.3.12 show the distribution of loading pulse heights measured in both vibratory and flow cavitation. They were drawn for the counting period equal to 10s. It is clear that the share of high amplitude pulses increases with the increase of cavitation intensity. The pit counting was then carried out for vibratory cavitation with the double amplitude of 50μm and for flow cavitation with flow velocity 30.5m/s. Soft aluminium was used as the specimen material, though neither the chemical composition nor mechanical property like hardness are described in the paper. The pits were measured by using a microscope (125x) and the measurements covered about 1/4 of the transducer sensitive part area. Size distributions of pits are shown in Figs.3.3.13 and 3.3.14. Kirejczyk commented that the pits smaller than 4μm were not observed, in general. The maximum number in the size distribution is found at 10~20μm for vibratory cavitation and at 0~10μm for flow cavitation. The maximum pit size counted for vibratory cavitation (160μm) is larger than the one for flow cavitation (130μm), while the maximum pulse height for vibratory cavitation (80N) is half the maximum value for flow cavitation (160N). From these pulse height distributions and pit size distributions, the pressure values of cavitation loading were estimated. The results were similar for both vibratory and flow cavitation and ranging from $4.8 \times 10^3 \sim 8.1 \times 10^3$MPa.

Although unfortunately Kirejczyk did not explain any of the detailed process how he used both distribution data and calculated the pressure in the paper, his method to estimate the cavitation loading pressure seems logical and actually has the possibility to overcome one experimental difficulty which has been experienced by

many investigators; i.e., how to get the area of cavitation loading. The positioning of the pressure transducer, set directly at the damaging area, is important because it enables one to directly correlate the loading data to the size data. This technique is particularly advantageous for cavitation in actual flow condition where the cavitation does not exist as a single cavity but forms clusters and each pressure pulse and loading size are not the same as the others. It should be also noted that the pulse height distribution and the pit size distribution clearly show the difference in cavitation loading and damage between vibratory and flow cavitation. This indicates the possibility that this sort of detailed information on cavitation intensity may shed the light on the complicated cavitation erosion phenomena which has not been fully understood from the simple erosion tests or the simple r.m.s. noise measurements; e.g., the difference in relative resistance of materials to cavitation erosion due to variation of cavitation testing facilities.

De and Hammitt [1982] investigated cavitation noise in a venturi. A commercial pressure transducer (Kistler 601A; natural frequency is ~130kHz.) was used to acquire the bubble pulse height spectra. They also designed their own "pressure-bar", but failed to use it in the venturi because of its relative fragility. Since the duration of cavitation loading, 1~5μs, has been reported by several other investigators, it is obvious that the natural frequency of the pressure transducer were not sufficiently high. A microprocessor based data acquisition system was designed, constructed and used, but the sampling rate to convert the analog peak data to the digital ones was rather poorly limited to 70kHz. Then, as Fry [1989] pointed out, there must be a "dead time"; i.e., peaks that occur within 14μs from the previously recorded one are missed. Therefore, the results they obtained are not to be so much reliable.

Fry [1989] employed the analog data treatment and achieved the pulse height analysis of a cavitating flow in an water tunnel. With his analog pulse height analyzer (PHA), the peak pulse amplitude can be accurately measured down to the minimum pulse width 0.5μs, though a commercial pressure transducer (Kistler 603B) whose resonance frequency (400kHz) is much slower than the PHA limit was used in the noise measurement. The transducer was flush-mounted in the Perspex window, which is different from the sidewall location used by Selim [1981] and Selim and Hutton [1983] for the erosion test described below and is even remote from the collapse zone. Experiments were conducted using a same test sections and flow passage geometry

as that used by Selim [1981], with which Selim had carried out cavitation erosion tests on 99.0% pure aluminium sidewall specimens for two cavitation sources; a 60 deg. symmetric wedge and a circular cylinder. Figure 3.3.15 shows the test section. Selim found that, despite generating similar r.m.s. noise level, the wedge is 21 times as damaging as the circular cylinder at peak noise flow conditions at flow velocity of 16m/s.

To find the reason of such a large difference in erosion capacity between two cavitation source geometries, Fry at first measured r.m.s. pressure of cavitation noise for both cavitation sources as shown in Fig.3.3.16. Then pulse height spectra were obtained at their peak r.m.s. condition as shown in Fig.3.3.17. There is a difference in r.m.s. noise level in Fig.3.3.16, but it is much smaller than Selim's erosion ratio, 21 times. On the other hand, in the pulse height spectra (Fig.3.3.17) it is clear that there are much more high energy pulses in the case of the wedge. Therefore, it may be natural to have an idea of distinguishing the higher energy part (damaging for pure aluminium) from the lower part (not damaging) by imposing a suitable threshold on the pulse height spectra to obtain relatively large erosion ratio. Then, he finally found the threshold value which provides Selim's 21 times erosion ratio. Three levels of noise spectra parameters were investigated, such as (1) number of pulses, (2) number of pulses times their amplitudes and (3) number of pulses times the squares of their amplitudes. It was concluded that even simply measuring the number of pulses above a suitable threshold might show a good correlation between cavitation noise and erosion.

As Fry commented, this results are significant because it is the first time to show the possibility of a linear calibration between the cavitation noise and its erosion capability, and it also indicates the way how the bulk data of cavitation loading from the practical condition, like flow cavitation, can be treated.

It may be valuable, however, to make clear a few points which can be improved in his measurements.

(1) Since the resonance wave length of the commercial pressure transducer Kistler 603B is 2.5μs and the duration of the cavitation impulsive pressure reported is the same length or even shorter, one may have a doubt that the transducer might have been vibrating with its natural frequency during the measurement as clearly shown in Fig.1(a) in his paper (Fry [1989]).

Considering the nature of the measurement, counting the number of pulses, it is obvious that this sort of vibration should be strictly avoided. Moreover, some very fast pressure pulses might not be correctly counted.

(2) The pressure pulses were obtained at the different location from the corresponding erosion testing point. It is well known that this sort of pulse amplitude measurements are very much affected by the position of the transducer. Therefore, ideally, both measurement must be carried out at the same place, though the problem must be the durability of the pressure transducer.

(3) It was difficult to estimate the loading pressure level by his measurement, because of the remote position of the transducer. Even if this can be solved, a considerable compensation from the area ratio between the size of Kistler 603B and the cavitation impingement must be necessary. Therefore, some sort of the measure to estimate the cavitation loading size is desired.

The method of Kirejczyk [1979] and some of the points above described have been improved in the work by Okada et al. [1989]. They carried out the cavitation loading pressure pulse height measurements and pit counting with various materials in ultrasonic vibratory cavitation. The pulse height measurements were done at the same configuration against the vibratory horn as the pit counting was conducted and the results were compared each other in order to estimate the magnitude of the loading pressure as introduced by Kirejczyk [1979]. A pressure detector found in Fig.3.3.18 was developed by them and was mounted in close proximity under the ultrasonic vibratory horn (18mm in diameter) submerged in water as shown in Fig.3.3.19. Therefore, the pressure pulse was able to be measured at the same location as the cavitation damage would take place. The pressure transducer was calibrated by dropping a steel ball, though the estimated duration of the calibration load, steel ball dropping, was rather long, 20μs. However, since a very thin (0.5mm) piezoelectric ceramic disk is used for the pressure detector, it can be expected that the detector has much higher resonance frequency than that of commercial transducer often used by many investigators; e.g., Kistler 603B (400KHz). Unfortunately, the specification of the material frequency was not given in the paper.

They used a little different data acquisition system with a "peak holder" as shown in Fig.3.3.20. First it was decided that all the pressure pulses smaller than the largest one in each ultrasonic vibration cycle (14.5kHz) would not be counted. Then the maximum peak pressure value was held "by peak holder" and sampled with interval time of 110μs. Since the one cycle of the ultrasonic horn was 69μs (14.5kHz), a pulse measured was only the maximum impact load produced in one or two cycles. Therefore, in addition to neglecting the second largest pulses in each vibration cycle, even the largest ones in each cycle can be missed once in every three cycles. The effect of this sampling method may not be so small. Pit counting was conducted with an optical microscope and an image analyzer for the cavitation damage on 2024-aluminium alloy, 99.9% pure copper and mild steel. Since they employed the sophisticated device, pits were measured with individual size in terms of the diameter of a circle of equivalent area. The minimum size detected was set at 4μm.

Figure 3.3.21 shows distribution curves of accumulated counts of pulse heights and pit sizes they obtained. If it is assumed that each individual pit was produced by a single impact pulse and the larger size pit was the contribution of the larger pulse height, the cumulative count of pits should be the same as that of pulses. Then, again assuming that the area of the cavitation loading is the same as the size of the damage, the loading pressure can be estimated by the pulse height divided by the corresponding pit area.

They used the smallest observable pit size of 4μm in diameter and corresponding "critical" pulse height at the same accumulated counts for calculating the pressure magnitude. The critical pulse height can be understood as the smallest pulse height which is required to produce an observable pit on the used material surface. The "critical" loading pressure was then calculated for the cavitation generated by the vibratory horn with a double amplitude of 40μm, which was set at 3mm above the centre of the specimen (or the pressure detector) in tap water at a temperature of 25°C. The calculated values are 7.2×10^5, 7.7×10^5 and 1.1×10^6MPa for the aluminium alloy, pure copper and mild steel, respectively. These values are roughly 1000 times larger than the yield strengths of each material. They explain that this is because the materials are deformed at very high speed and the elastic deformation at the outer circumference of each pit is not taken into account. The present author thinks that, if the latter is the reason, the effect can be much reduced by taking the greater pit size for the pressure calculation, since the ratio of the elastic

deformation at the outer circumference to the total elastic-plastic deformation may be smaller in the greater pit size. It seems that there is no reason not to apply the same assumption to the greater pit size and not to try to calculate and to compare the results with each other. In fact, if the maximum pit size of aluminium alloy (about 70 μm) and the pulse height at the same accumulated counts are read from Fig.3.3.21 and are taken for the pressure calculation, the pressure value becomes about 4.3×10^3MPa. This is more than 100 times smaller than the pressure calculated from the smallest observable pit size (4μm) and the critical pulse height and agrees very well with the one obtained by Kirejczyk [1979]. This will be discussed more in Chapter 9.

Pulse height measurements were further conducted under various test conditions, such as the vibratory horn double amplitude 20~40μm and the radial distance from the centre of the horn 0~8mm, and very constant critical pulse heights were obtained for each material; 8.9N±0.8N, 9.9N±0.8N and 13.4N±0.7N for the aluminium alloy, pure copper and mild steel, respectively. The very constant threshold values, i.e., critical pulse heights, for each material encouragingly support the idea of correlating the pulse data to cavitation erosion, which leads the possibility of developing the cavitation damage meter as Fry [1989] pointed. For this purpose, positioning the pressure detector directly at the damaging area would be vital and hence the development of the durable but the sensitive pressure transducer which can resist against cavitation damage is very important. On the other hand, in order to estimate the loading pressure the precise pit counting and the selection of the sufficiently soft material for specimens will be the another crucial factor in the measurements. Details of these for the present work will be discussed in Chapter 5 and Appendix A2 and A3.

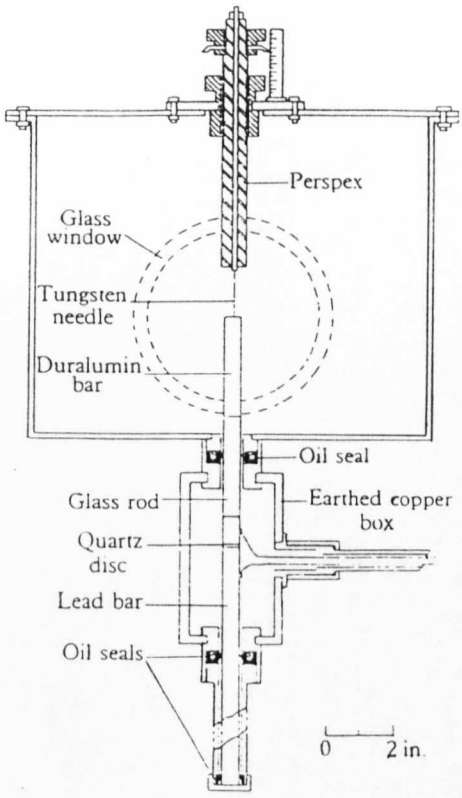

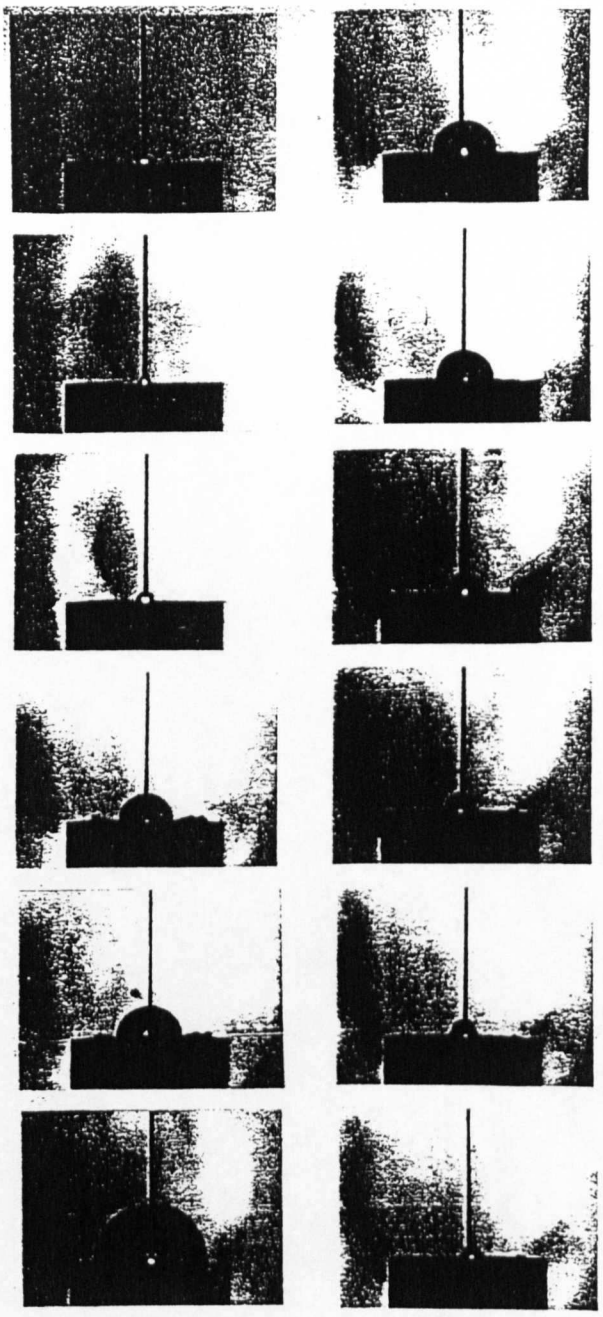

Fig.3.3.1 Diagram of the experimental tank, the spark-gap adjustment and the pressure bar and its housing. (from Jones and Edwards [1960])

Fig.3.3.2 Series of spark photographs of the growth and collapse of a cavity generated by a spark discharge in water. Total cavity lifetime is roughly 800μs and the pressure bar diameter is 1/2in. (from Jones and Edwards [1960])

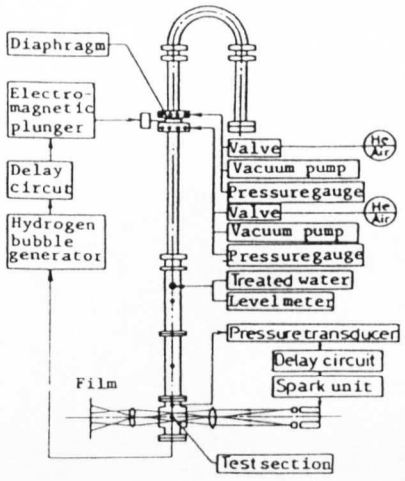

Fig.3.3.3 Water shock tube apparatus.
(from Fujikawa and Akamatsu [1978])

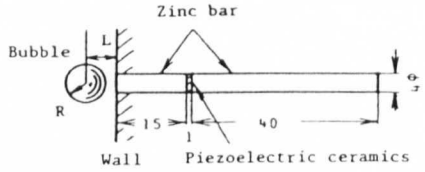

Fig.3.3.4 Pressure gauge.
(from Fujikawa and Akamatsu [1978])

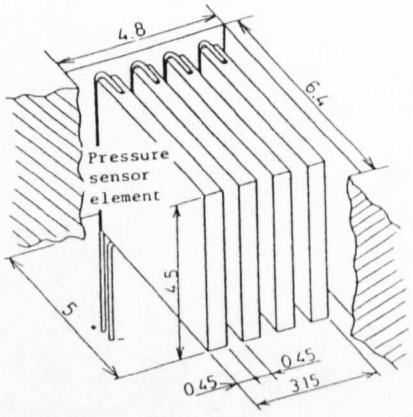

Fig.3.3.5 Detail of the local pressure sensor.
(from Kimoto [1987])

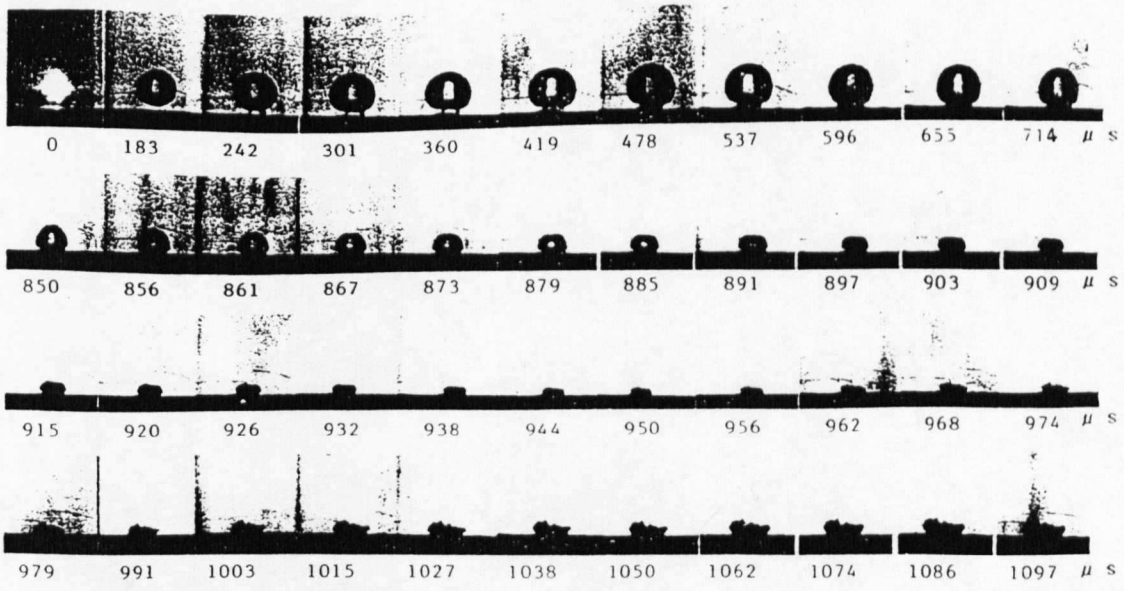

Fig.3.3.6 High speed photographs of a cavitation bubble for L_n=1.03.
(from Kimoto [1987])

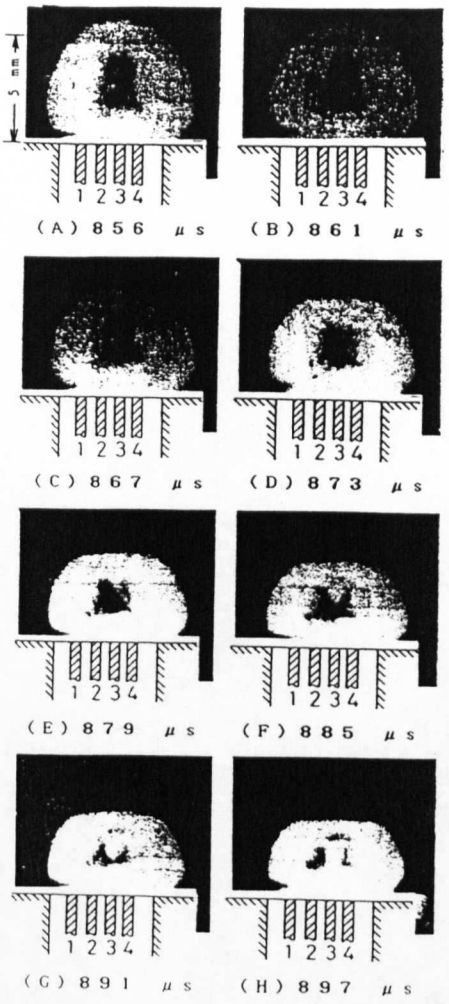

Fig.3.3.7 Microjet formation in a collapsing bubble (L_n=1.03). (from Kimoto [1987])

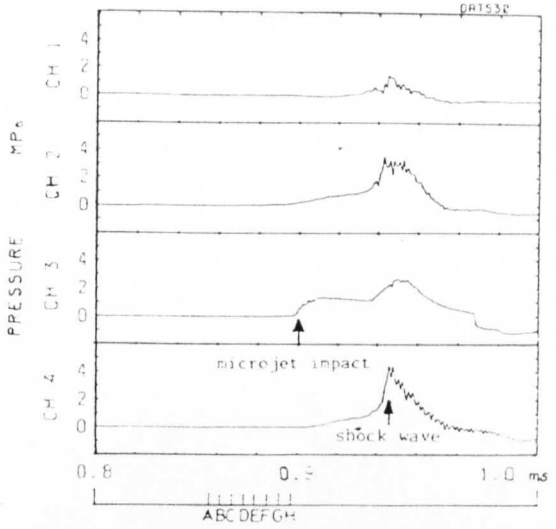

Fig.3.3.8 Output wave forms of the local pressure sensor elements corresponding to Fig.3.3.6. (from Kimoto [1987])

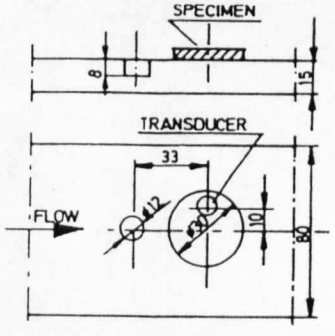

Fig.3.3.10 Cavitation chamber. (from Kirejczyk [1979])

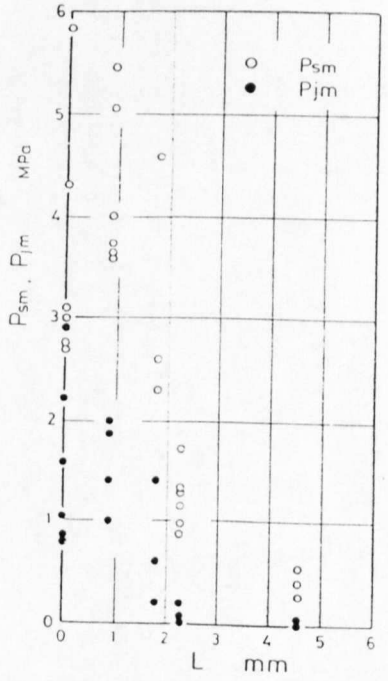

Fig.3.3.9 Impulsive pressure distributions of the microjet and the shockwave measured by the local pressure sensor elements. (from Kimoto [1987])

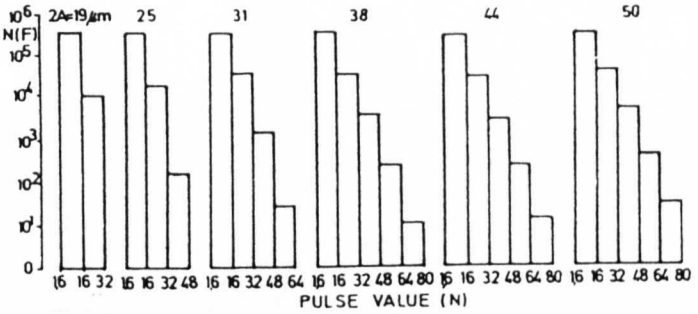

Fig.3.3.11 Histograms of the pulse distribution - vibratory facility (from Kirejczyk [1979])

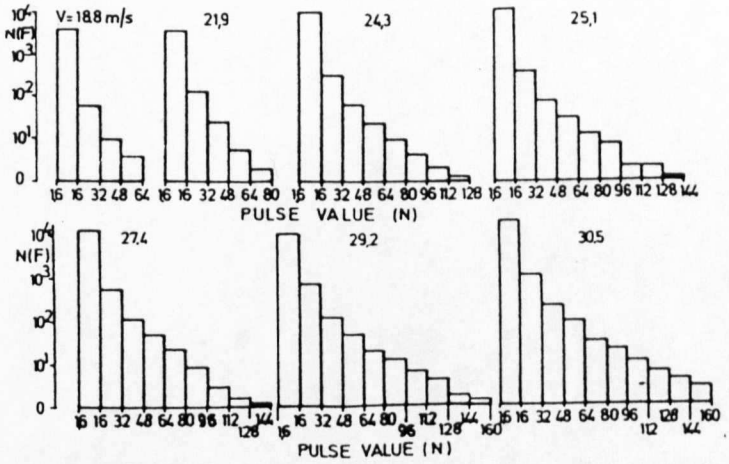

Fig.3.3.12 Histograms of the pulse distribution - flow cavitation (from Kirejczyk [1979])

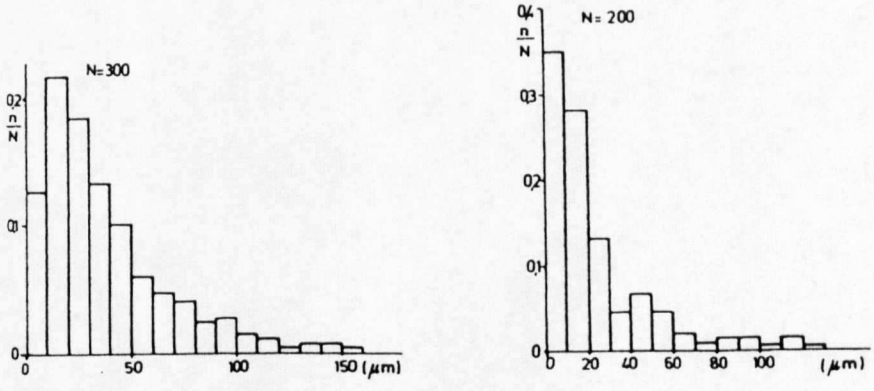

Fig.3.3.13 Crater diameter distribution - vibratory facility (from Kirejczyk [1979])

Fig.3.3.14 Crater diameter distribution - flow cavitation (from Kirejczyk [1979])

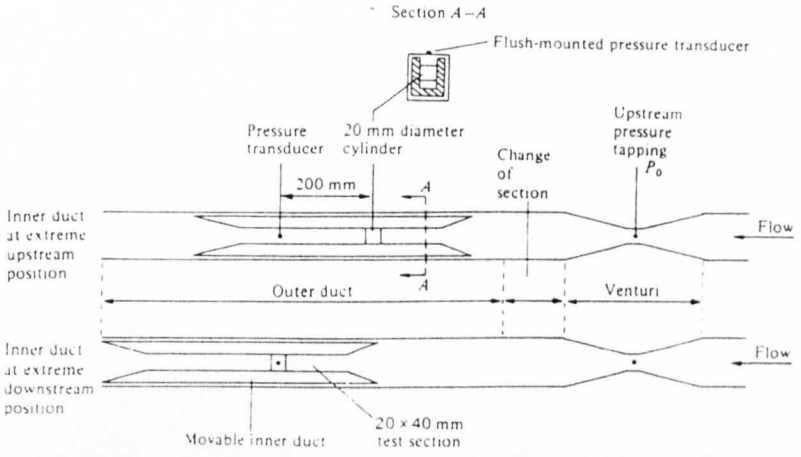

Fig.3.3.15 Schematic diagram of test section, plan view (from Fry [1989])

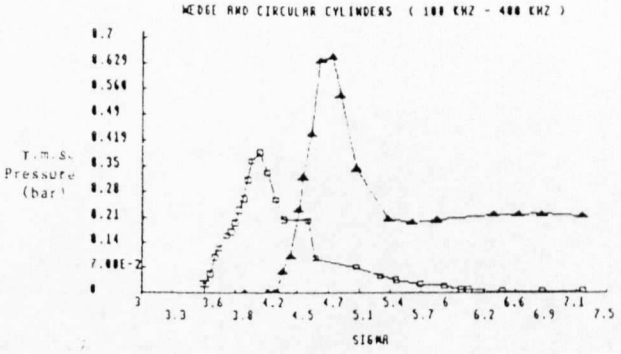

Fig.3.3.16 Comparison of noise cavitation number characteristics for wedge and circular cylinders in high frequency range (100~400kHz) (from Fry [1989])

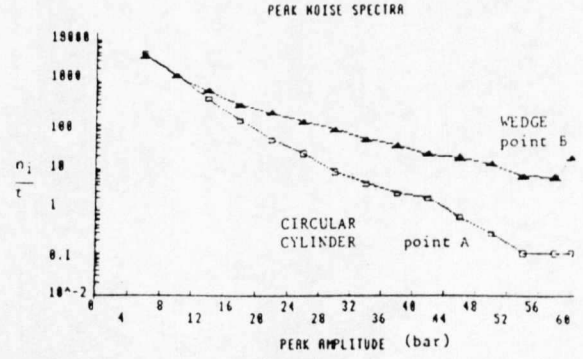

Fig.3.3.17 Pulse height spectra for 60deg wedge and circular cylinder at peak noise flow conditions (from Fry [1989])

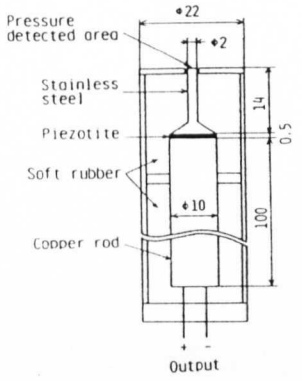

Fig.3.3.18 Structure of a pressure detector. (from Okada et al. [1989])

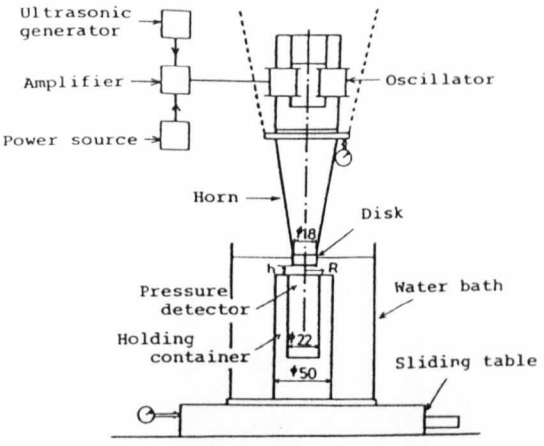

Fig.3.3.19 Schematic view of the test apparatus. (from Okada et al. [1989])

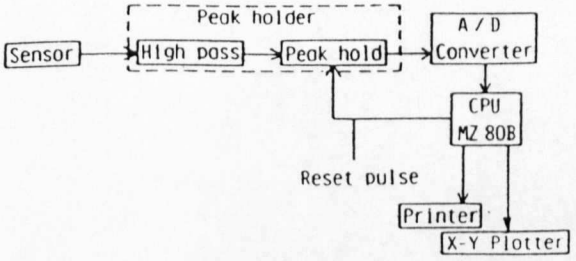

Fig.3.3.20 Data acquisition system (from Okada et al. [1989])

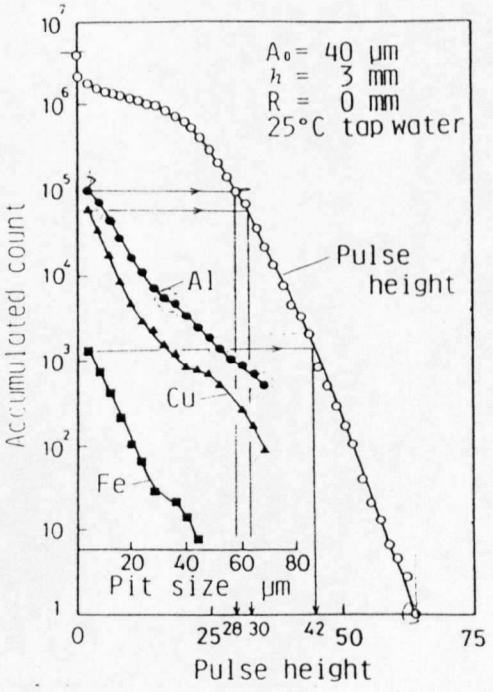

Fig.3.3.21 Distribution curves showing accumulated counts of pulse height and pit size (from Okada et al. [1989])

CHAPTER FOUR - LITERATURE SURVEY:
Cavitation erosion produced by a submerged jet

4.1 Introduction

It has been well known that when a submerged jet emerges into the stationary liquid, numerous eddies are formed in a shear layer in the mixing zone. The mixing zone spreads inwards as well as outwards and consequently, the potential core disappears as shown in Fig.4.1.1 (Rouse [1953]). The formation of the mixing zone of a submerged jet is seen as the spreading phenomena of the mean longitudinal component of velocity and the root mean square of longitudinal velocity fluctuation as shown in Fig.4.1.2 and 4.1.3 (Rouse [1953]). When the rate of the shear is sufficiently high, local pressures in the eddies fall to the point of vaporisation and cavitation starts. Photographs of cavitation around the submerged jet were presented by Rouse [1953] as shown in Fig.4.1.4 and by Yamaguchi and Shimizu [1987] in Fig.4.1.5. Photographs in Fig.4.1.5(b) were taken through a transparent Perspex target. Some cavity clouds show a tip at the centre of the cloud and so it can be confirmed that cavities already spread inwards and exist even at the centre of the jet.

When such cavitating jet is caused to strike a surface of a solid object, the cavitation bubbles collapse and erode the object. The idea to apply the cavitating jet to the cavitation erosion testing was firstly proposed by Lichtarowicz [1972] and then followed by several investigators. A schematic diagram of apparatus used by Lichtarowicz is shown in Fig.4.1.6. The cavitating jet is obtained by maintaining a sufficiently high pressure difference across a suitable nozzle and a specimen placed in a path of the cavitating jet will be eroded. The erosion can be quantified by measuring the mass lost in a given time. Interestingly, Lichtarowicz [1974] showed that a cavitating submerged jet was much more erosive than the jet in air with same flow condition. This result indicates that the most part of the erosion was produced not by the jet power but by the cavitation loading. The detail of the cavitating jet method of testing has been described by Lichtarowicz [1979]. Further description can be found in Chapter 5. As Trevena [1987] described, the jet method has many advantages over some of the other cavitation erosion testing methods. The apparatus is small and uses flow effects to produce cavitation; it thus offers all the advantages

of venturi-type and tunnel methods without their drawbacks of relatively large size and long testing times. For example, Brunton [1970] pointed out that in vibratory type cavitation testing there is a possibility that the first damage, or crevices, produced on a specimen can become the surface nuclei for the formation of the next generation of cavities and will carry on damaging by successive cavitation collapses at the same point. In the jet method, the formation of cavitation and the erosion process is as natural as that in practical flow situation. Another great advantage is the fact that the flow parameters can be easily controlled independently.

A useful parameter when dealing with cavitation is cavitation number σ which is a form of pressure coefficient

$$\sigma = \frac{P - P_v}{\frac{1}{2}\rho V^2}$$

where P is the ambient pressure, P_v and ρ are the vapour pressure and the liquid density respectively and V is velocity. Physically cavitation number can be regarded as the ratio of forces tending to suppress cavitation to the forces tending to produce it.

In the cavitating jet method, the velocity is generated by a pressure reduction across a nozzle. Then the cavitation number is rewritten as

$$\sigma \quad \frac{P_2 - P_v}{P_1 - P_2}$$

where P_1 and P_2 are upstream and downstream pressures, respectively.

A long orifice type nozzle is often used for the jet method with sufficiently large pressure difference across the nozzle. In that case the jet flow is already cavitating from the inlet edge of the nozzle and is said to be "choked" because it depends only on the upstream pressure P_1 and the vapour pressure P_v and it is independent of the downstream pressure P_2. Now P_v, not P_2, is a virtual downstream pressure to control the jet flow. When P_v is much less than both P_1 and P_2, the cavitation number finally becomes

$$\sigma = \frac{P_2 - P_v}{P_1 - P_v} \approx \frac{P_2}{P_1}$$

where absolute pressure must be used for P_1 and P_2.

When the cavitation number is kept constant, the cavitating jet length can be

almost same and it is possible to establish the same optimum stand off distance where the maximum erosion occurs for various upstream and downstream pressure combinations. This means that the geometric configuration can be kept same throughout the testing with various levels of cavitation intensity. Then the erosion results from various pressure levels can be correlated each other. Therefore, Lichtarowicz [1981] has suggested that the tests should be carried out at constant cavitation number with the specimen set at the optimum stand off distance.

As the final part of literature survey, basic features of the erosion testing with submerged jet cavitation will be discussed in this chapter. The effects of flow parameters and other test conditions on the erosion results will be described.

Pressures used in this chapter are in absolute units as in the other part of the present thesis, unless it is stated. Since each investigator referred in this chapter has used slightly different configuration in the cavitating jet test rig, some of the major types, such as used in Nottingham by Lichtarowicz et al., in Aachen by Kleinbreuer et al. and in Yokohama by Yamaguchi and Shimizu, are shown together in Fig.4.1.7. However, the working mechanics are all same and it is not the primary purpose of this chapter to discuss the detailed effect of shapes and sizes of the apparatus apart from the basic phenomena.

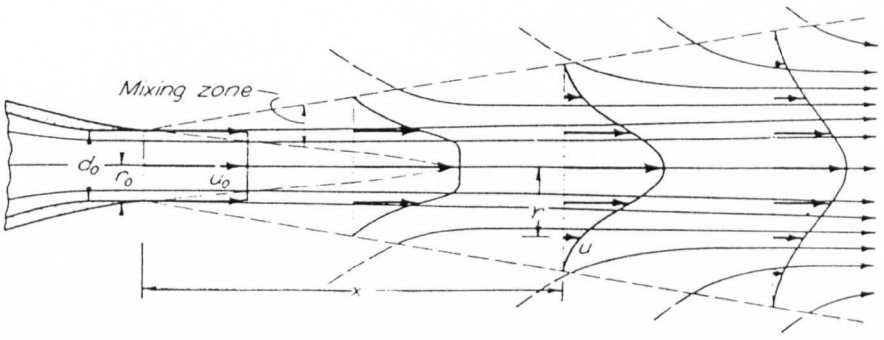

Fig.4.1.1 Sketch for characteristics of mean flow in a submerged jet (from Rouse [1953])

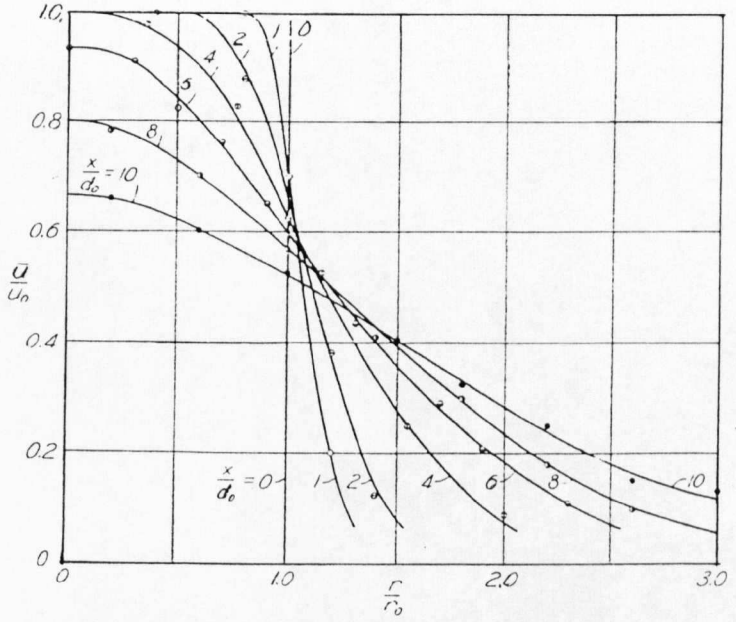

Fig.4.1.2 Stagnation tube measurements of mean longitudinal component of velocity (from Rouse [1953])

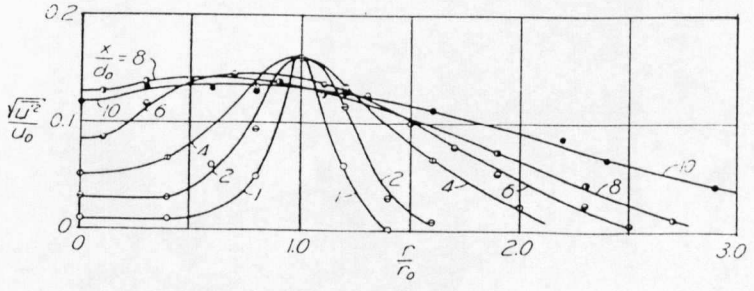

Fig.4.1.3 Hot wire measurements of root-mean-square longitudinal velocity fluctuation (from Rouse [1953])

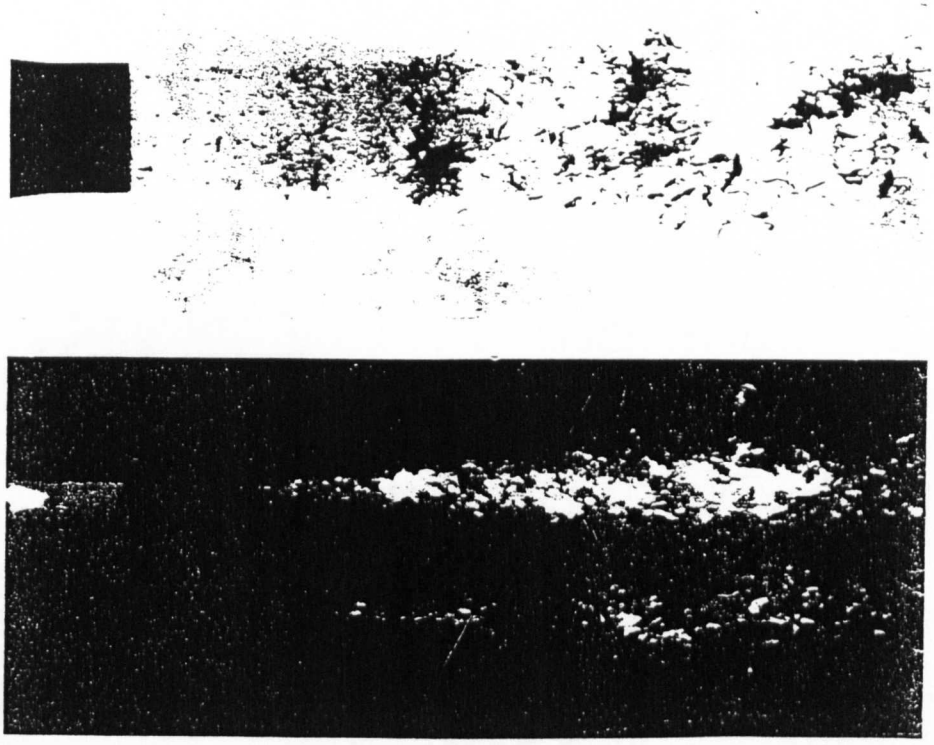

Fig.4.1.4 Photographs of jet cavitation at σ=0.2. Above, single exposure with rear illumination. Below, 25 exposures with only central plane illuminated.
(from Rouse [1953])

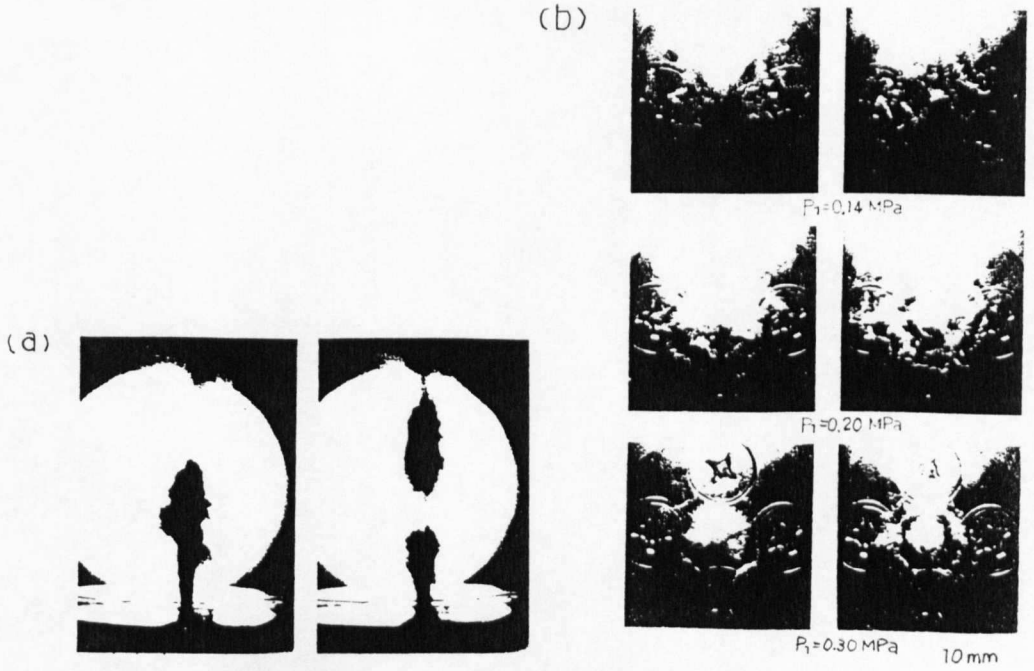

Fig.4.1.5 Photographs of (a) cavitating jet and (b) cavity clouds
(from Yamaguchi and Shimizu [1987])

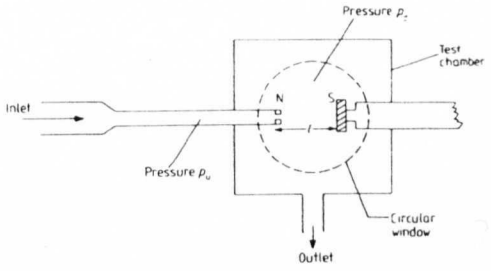

Fig.4.1.6 Schematic diagram of apparatus used by Lichtarowicz (from Trevena [1987])

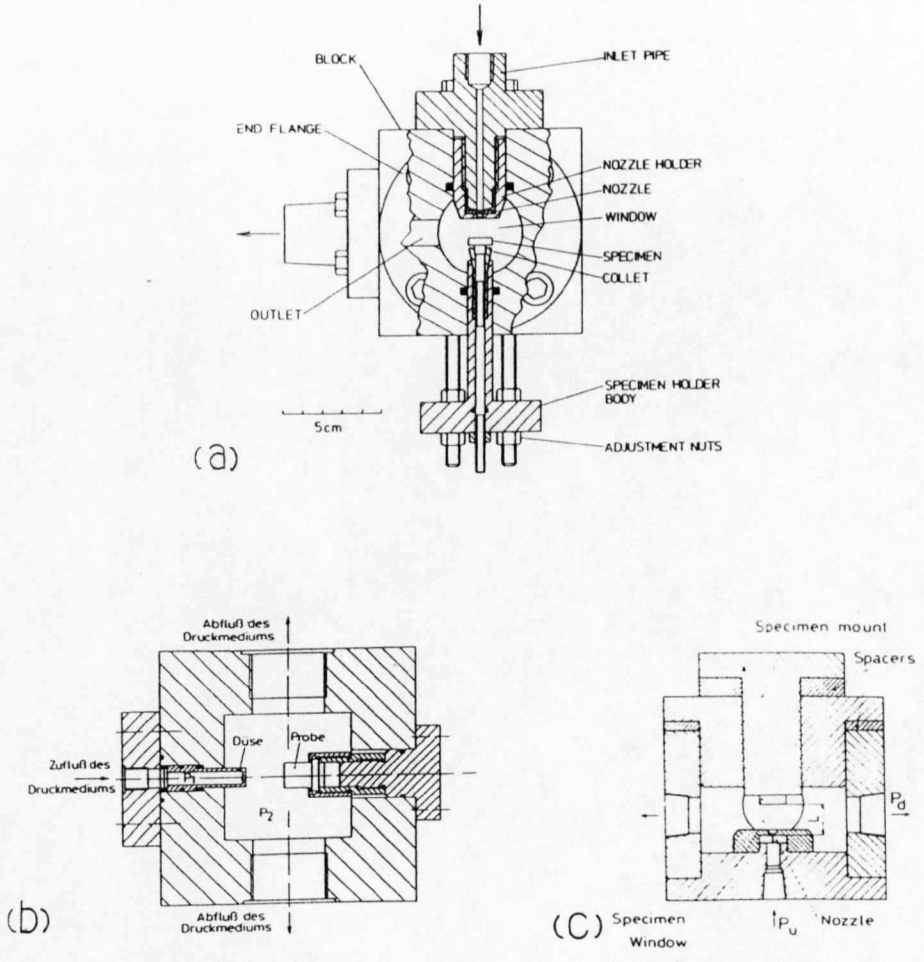

Fig.4.1.7 Jet cavitation erosion test rig, (a) Nottingham (from Lichtarowicz [1979]), (b) Aachen (from Kleinbreuer [1976]) and (c) Yokohama (from Yamaguchi and Shimizu [1987])

When the cavitating jet strikes the target specimen, the flow is directed radially outwards and a stagnation region is formed at the centre of the specimen. Then ring shape erosion is produced with uneroded area at the centre. Lichtarowicz [1979] shows the erosion pattern on an aluminium specimen at various stages of erosion as Fig.4.2.1. The mass loss and the cumulative erosion rate (CER) which is defined as a following equation for the specimen No.7 in Fig.4.2.1 are shown in Fig.4.2.2.

$$CER = \frac{\Delta m_c}{\Delta T_c}$$

where Δm_C and ΔT_C are the total (cumulative) mass loss and the total cavitation exposure time, respectively. The mass loss starts after a short period of incubation time whose length basically depends on the material resistance against the given cavitation intensity and shows a peak value in CER. Figure 4.2.3 shows a set of CER curves for various pressures at constant σ=0.025. As the upstream pressure is increased, the CER increases and the peak point becomes more obvious and occurs at a shorter time. More CER curves obtained for various pressure conditions ranging P_1=8~12MPa, P_2=0.17~0.3MPa and σ=0.014~0.025 were presented in normalised form in Fig.4.2.4. All the values show very similar tendency and are found within a narrow band.

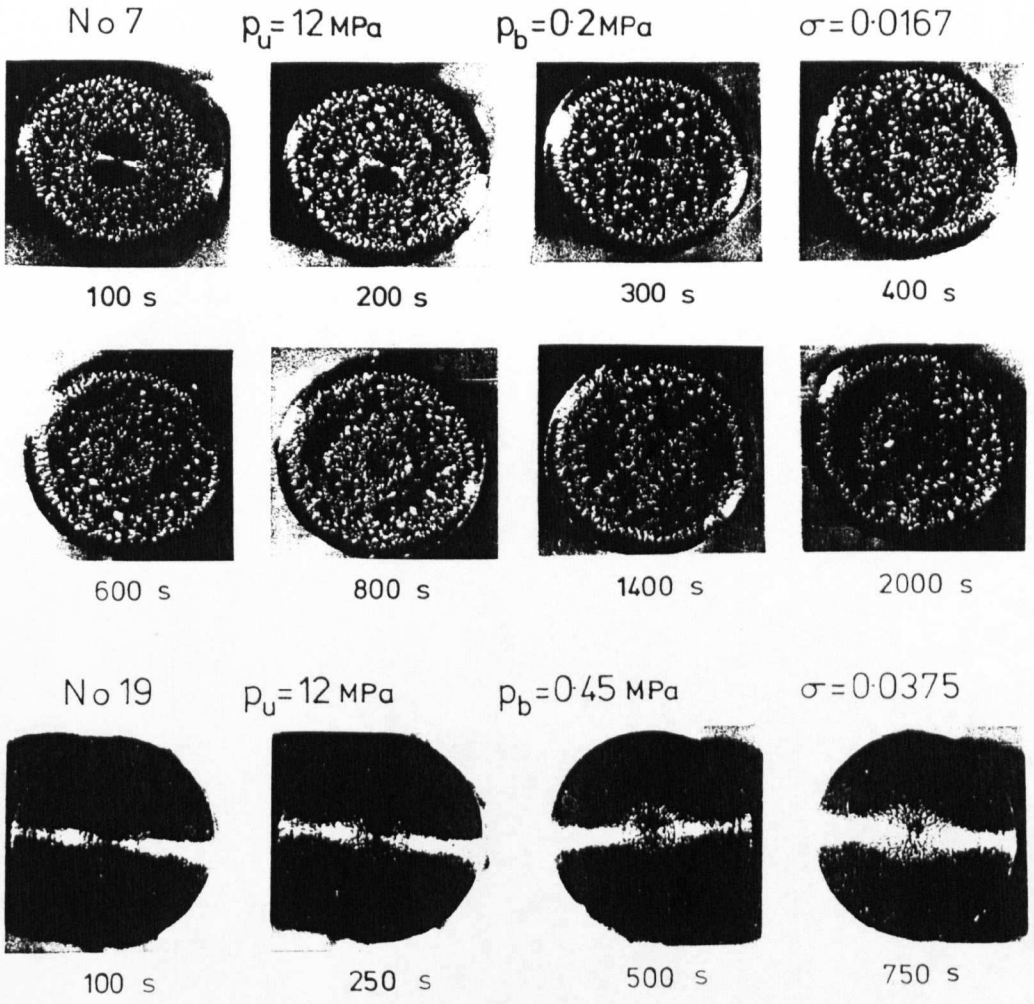

Fig.4.2.1 Erosion patterns on an aluminium specimen (from Lichtarowicz [1979])

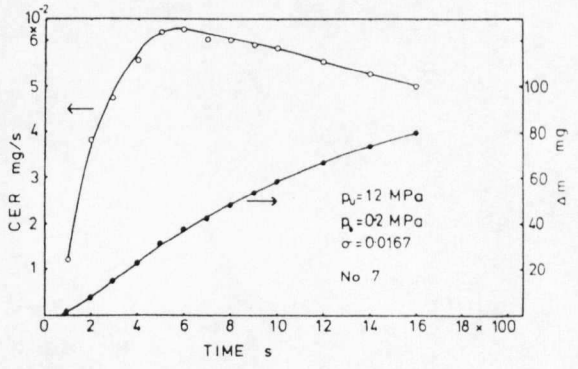

Fig.4.2.2 Typical mass loss and cumulative erosion rate time graphs (from Lichtarowicz [1979])

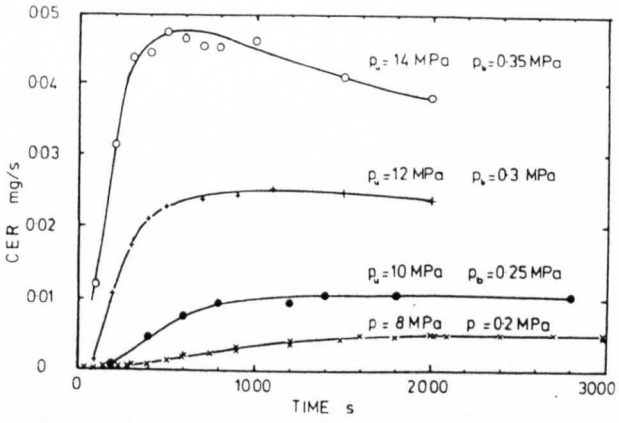

Fig.4.2.3 Cumulative erosion rate for various pressures at constant σ=0.025 (from Lichtarowicz [1979])

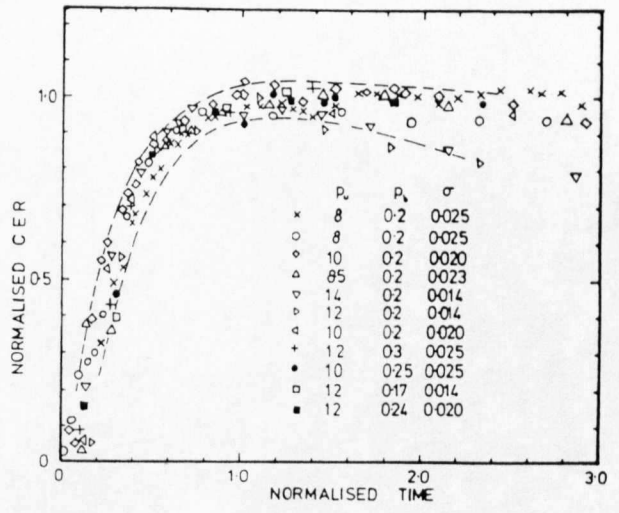

Fig.4.2.4 Normalised cumulative erosion rate-time graph (from Lichtarowicz [1979])

A stand off distance is usually defined from the inlet edge of the nozzle to the surface of the specimen. If it is too long, obviously there will be no erosion. Lichtarowicz [1974] reported that there was one optimum stand off distance where the maximum erosion occurs, and Kleinbreuer [1976] carried out more sets of tests using aluminium alloy specimen with hydraulic oil as shown in Fig.4.3.1 and 4.3.2. An upstream pressure P_1 and exposure time were kept constant throughout the tests. At first it should be stressed that gauge pressures, not absolute, have been used in the figures of Kleinbreuer and his co-workers' at Aachen. Kleinbreuer measured mass loss against various stand off distances for each different downstream pressure; i.e., the cavitation number was different for each downstream pressure. There is at least one optimum stand off distance for each down stream pressure. One of the reasons for this may be considered as follows. When the stand off distance is very small, cavities have not sufficiently grown to their maximum size yet and may not be able to collapse fully on the surface because the flow velocity is still high. On the other hand, cavities must collapse completely before they reach the specimen when the specimen is set too far. Therefore, there must be an optimum distance between these two extreme conditions. Another very tiny peak can be found at relatively smaller stand off distance for P_2=0.6 and 0.8bar in Fig.4.3.2. However, the reason why there is another peak stand off distance near the nozzle for some cases has not been understood yet. The existence of the optimum stand off distance has been reported by all the investigators who have tried (Lichtarowicz [1979], Kleinbreuer [1977], Yamaguchi and Shimizu [1987] and so on).

Yamaguchi and Shimizu [1987] reported another effect of stand off distance which is on the size of erosion ring. Figure 4.3.3 shows the erosion ring diameter on an aluminium alloy specimen with variation of stand off distance under the constant upstream and downstream pressure condition. High water base fluid of chemical solution type (HWBF) was used as a test liquid. In this case, the optimum stand off distance, about 27.5mm, had already been obtained. The diameter gradually increases with stand off distance until the region of the optimum stand off distance and then decreases. Considering the erosion area is proportional to the square of the diameter,

the effects of this phenomenon on mass loss rate may not be negligible.

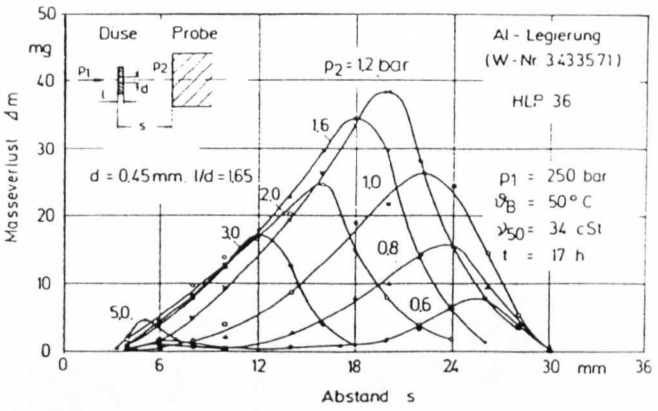

Fig.4.3.1 Variation of mass loss at stand off distance s with downstream pressure p_2 as a parameter (from Kleinbreuer [1976])

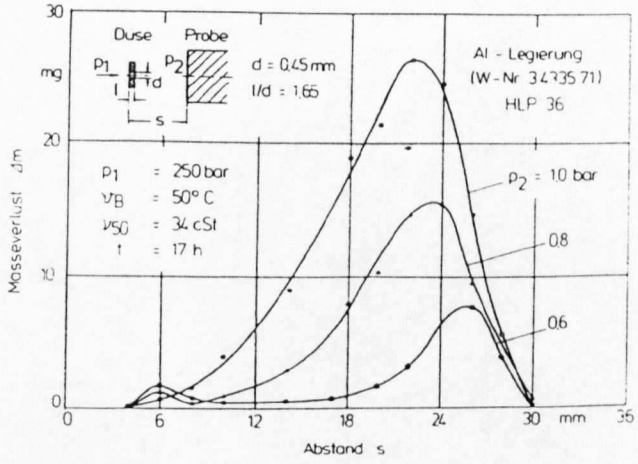

Fig.4.3.2 Variation of mass loss at stand off distance s with downstream pressure p_2 as a parameter (from Kleinbreuer [1976])

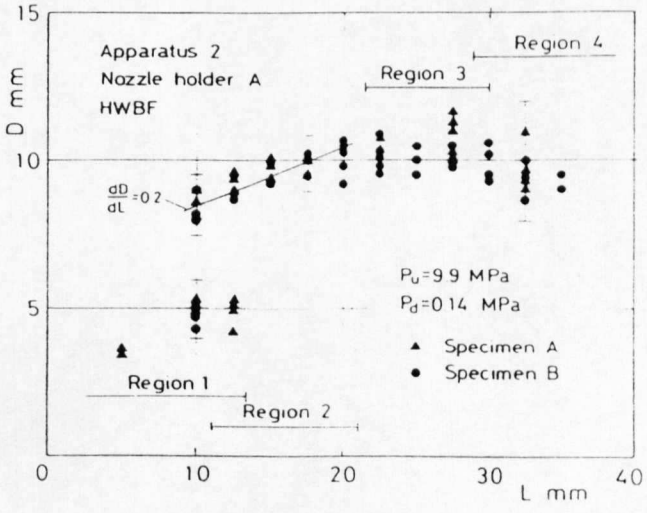

Fig.4.3.3 Effect of specimen diameter on erosion ring diameter (from Yamaguchi and Shimizu [1987])

Since basically the flow velocity and the power of the jet flow is determined by the upstream pressure, effects of cavitation number can be virtually same as the effects of the downstream pressure. As described before, cavitation number can be regarded as the ratio of forces tending to suppress cavitation to the forces tending to produce it. Therefore, smaller the cavitation number, more the cavitation would be likely to be formed.

Shimizu and Yamaguchi [1988] took seventy high speed photographs of cavitating jet in tap water for two different cavitation numbers, σ=0.02 and 0.03, with a constant upstream pressure, P_1=9.9MPa, and measured the probability distribution of cavity clouds existence as shown in Fig.4.4.1. A cavitating jet for smaller cavitation number is clearly much larger in length and width, since cavities can survive until farther distance with lower suppression pressure. Then, naturally it is inferred that there would be an effect of cavitation number on the optimum stand off distance, and it is obvious in Fig.4.3.1 in the previous section. Kleinbreuer changed only the downstream pressure P_2, while keeping the upstream pressure P_1 constant and so cavitation number is proportionally changed with P_2. The optimum stand off distance increases with decrease of cavitation number (or a downstream pressure P_2). In Fig.4.3.1, the mass loss at the optimum stand off also seems to show the peak value with P_2=1.2bar at the stand off distance 20mm. When the downstream pressure is about 2bar (abs.) or lower, a lot of gas (air) bubbles were observed in downstream chamber in Nottingham. Not all of them collapse on the specimen and probably play a role as a cushion for the collapse of the other vapour cavities. This may be one of the reason for the peak of the mass loss at the optimum stand off distance to occur at a certain downstream pressure (or cavitation number).

Lichtarowicz and Scott [1979] plotted the recalculated Kleinbreuer's optimum stand off distance and their own results in a dimensionless form with cavitation number. As shown in Fig.4.4.2 (from Lichtarowicz and Kay [1983] with slightly more data), all points for each test apparatus are found on the same straight line in a log-log graph.

Backè and Berger [1984] carried out erosion test with water-oil emulsion (3%) for various pressures with constant cavitation number σ=0.0091~0.0093, and obtained

slightly different results as shown in Fig.4.4.3. Again the pressures are gauge pressures. Optimum stand off distances are increased from 19mm to 23mm with the increase of the pressure level from P_1=150bar to 350bar, but all these data are obtained from testing for some individually fixed exposure time, 2.5~10hr.

Lichtarowicz [1981] and Lichtarowicz and Kay [1983] presented the pressure exponent against the cumulative erosion rate at the optimum stand off distance with constant cavitation number which is similar to the velocity exponent to the pitting rate of Knapp [1955]. Then they showed that the index n may be dependent of cavitation number as shown in Fig.4.4.4, though the number of data is limited. This will be fully explained in the next section.

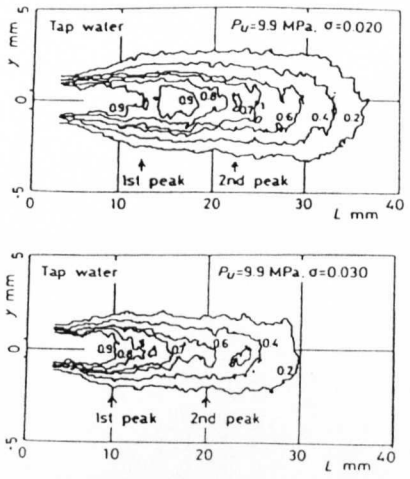

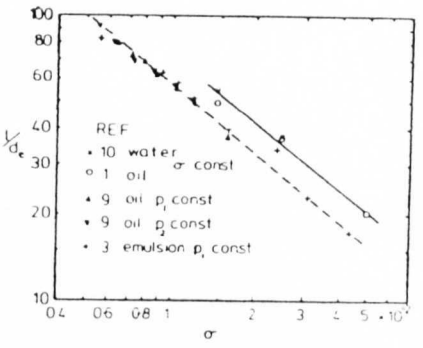

10, 1 - Nottingham; 9, 3 - Aachen;
(see Lichtarowicz and Kay [1983] for detail)

Fig.4.4.1 Probability distributions of cavity clouds existence
(from Shimizu and Yamaguchi [1988])

Fig.4.4.2 Variation of stand off distance with cavitation number σ
(from Lichtarowicz and Kay [1983])

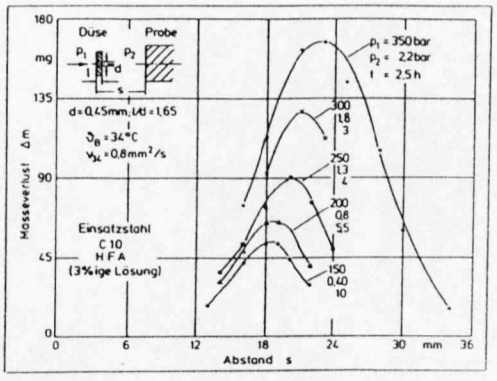

Fig.4.4.3 Variation of mass loss with constant cavitation number
(from Backè and Berger [1984])

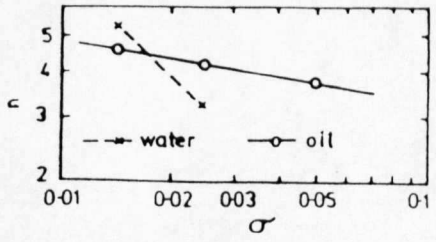

Fig.4.4.4 Variation of index n with cavitation number σ
(from Lichtarowicz and Kay [1983])

As Knapp [1955] found, the effects of flow velocity (or upstream pressure P_1) on erosion rate can be expressed as

$$Erosion\ rate \propto P_1^{\,n}$$

where n is the pressure exponent.

Kleinbreuer [1977] examined the pressure exponent for the mass loss of aluminium alloy in hydraulic oil at the optimum stand off distance, and obtained the index n=4.5. The downstream pressure and test time were kept constant.

Lichtarowicz and Scott [1979] obtained similar values n=4~4.6 for various materials including a Perspex specimen with hydraulic oil as a working liquid, but keeping the cavitation number constant. Figure 4.5.1 shows their results. They used the peak cumulative erosion rate at the optimum stand off distance. The index n taken for data with constant cavitation number may be smaller than that with a constant downstream pressure, because the downstream pressure is going to be higher for the higher upstream pressure in the former way of choosing the index n so that the erosion rate should become lower in most cases. A similar result of n=4.0 was reported by Yamaguchi and Shimizu [1987] using aluminium alloy in high water base fluid of chemical solution type.

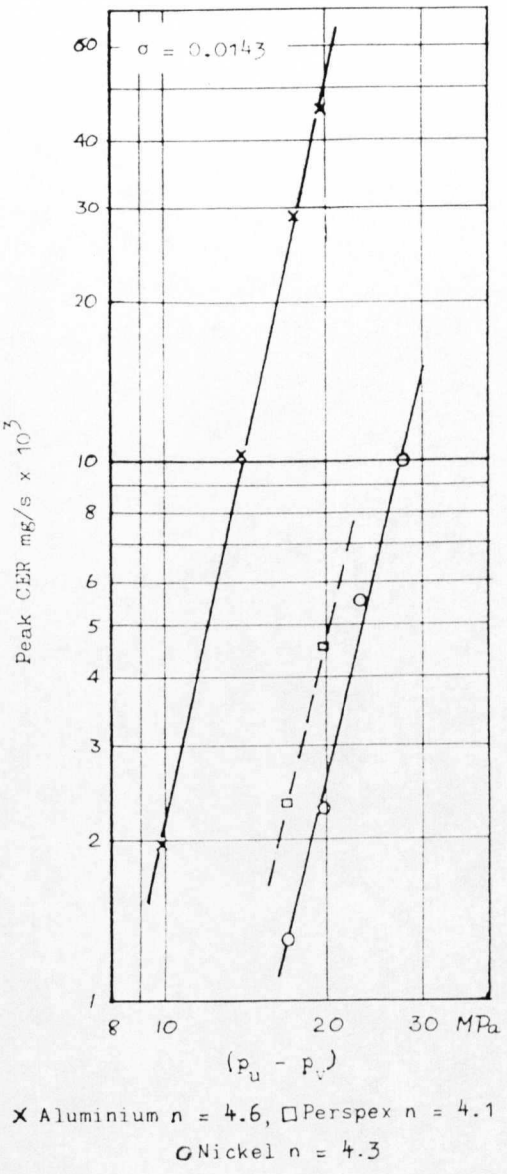

Fig.4.5.1 Variation of peak cumulative erosion rate with pressure for various materials (from Lichtarowicz and Scott [1979])

Kleinbreuer [1980] examined the erosion performance of long orifice type nozzles using hydraulic oil with three different inlet edges; namely, with a sharp corner finish, with a plain chamfered finish and with a round chamfered finish. The diameter and thickness of all long orifice nozzles were maintained identical. Figure 4.6.1 shows the flow rate and the section of each nozzle. Discharge coefficients are C_d=0.65, 0.78 and 0.84 for a sharp corner, a plain chamfered and a round chamfered nozzle, respectively at P_1=250bar and P_2=0bar. Mass loss obtained with those three nozzles for P_1=250bar and P_2=0.8~5.0bar is shown in Fig.4.6.2. The effects of the corner treatment at the inlet edge of the nozzle is obvious; sharp corner nozzle shows the greatest erosion capacity, while the round chamfered nozzle produces no measurable result. The longest optimum stand off distance with the sharp corner nozzle is also observed. Kleinbreuer compared the cavity clouds of cavitating jets from the sharp corner nozzle to that from the round chamfered nozzle as shown in Fig.4.6.3. It is clearly seen that a much larger and longer cavitating jet is created by the sharp corner nozzle, and so it is obviously understood as the reason for much greater erosion produced at a longer stand off distance for the sharp corner nozzle. Therefore, if it is desired to obtain reliable results constantly throughout a period of testing, it is extremely important to maintain the constant geometric condition of the inlet edge.

A nozzle is positioned at the end of the high pressure region and in many cases, the nozzle plate is tightly held by a so-called nozzle holder. In this case, the flow around the jet from the nozzle may be affected by the lip of the nozzle holder and so the cavitation erosion capability of the jet. Actually, although most investigators appear to be using long orifice type nozzles these days for its various merits, they have been still using their own designed nozzle settings including several types of nozzle holders.

Shimizu and Yamaguchi [1989] studied four different types of nozzle holders with a long orifice nozzle as shown in Fig.4.6.4 and found type B enhances the erosive power of the jet very much. The effects of the configuration around a nozzle exit on the flow of cavitating jet were then numerically simulated by a two dimensional discrete vortex method by Shimizu et al. [1990] and it was confirmed that a more violent cavitating jet would be produced with a lip of a nozzle holder. Figure

4.6.5, 4.6.6 and 4.6.7 show the distribution of vortex elements, the trajectories of the vortex elements and instantaneous pressure distributions at the same moment for the nozzle with and without two side walls which are simulating a lip of a nozzle holder. The flow inside the walls is very complicated. Firstly the flow separates at the exit edge of the lip and the shear layers are directed into the lip by the reverse flows along the lip wall. Then, the flow around the jet is more restricted by the lip so that the jet is likely to be much more cavitating. It is seen in Fig.4.6.5, 4.6.6 and 4.6.7 that the two side walls apparently enhance the flow turbulence more violently and generate more low pressure region along the jet.

Bin-Ujang [1990] in Nottingham carried out erosion tests with water using various shape and size of nozzle holders, and obtained similar results. Figure 4.6.8 shows the optimum stand off distances with variation of cavitation numbers for three different lip diameters of a nozzle holder; namely, 2.4mm, 3.7mm and 4.5mm with constant lip thickness of 3.0mm. The long orifice nozzle with diameter of 0.410mm and thickness of 0.689mm was used. The smallest lip diameter, 2.4mm, shows the longest optimum stand off distances. The peak cumulative erosion rate with variation of upstream pressure P_1=120bar~180bar and constant cavitation number σ=0.0143 using same nozzle and nozzle holder settings are plotted in Fig.4.6.9. The smallest lip diameter (2.4mm) and the others (3.7mm and 4.5mm) show different tendency. In relatively low pressure conditions P_1=120bar and 140bar, the smallest lip diameter shows greatest erosion rate of all, but for high pressure P_1=180bar, the smallest lip diameter is the weakest one.

Although more accumulation of experiments with more detailed geometric parameters is needed before to fully understand these effects, it is at least clear that the cavitation and its erosion capacity are significantly affected by the shape of a nozzle and the configuration around outside edge of the nozzle.

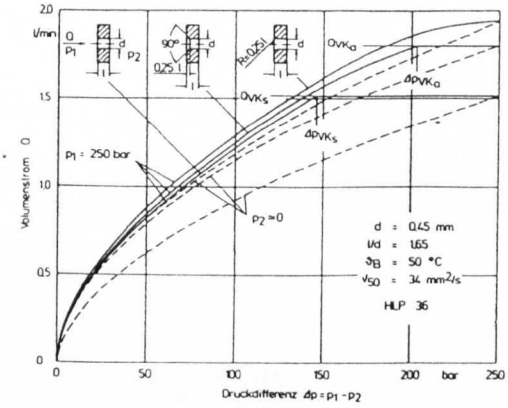

Fig.4.6.1 Effect of inlet edge finish on flow rate. (from Kleinbreuer [1980])

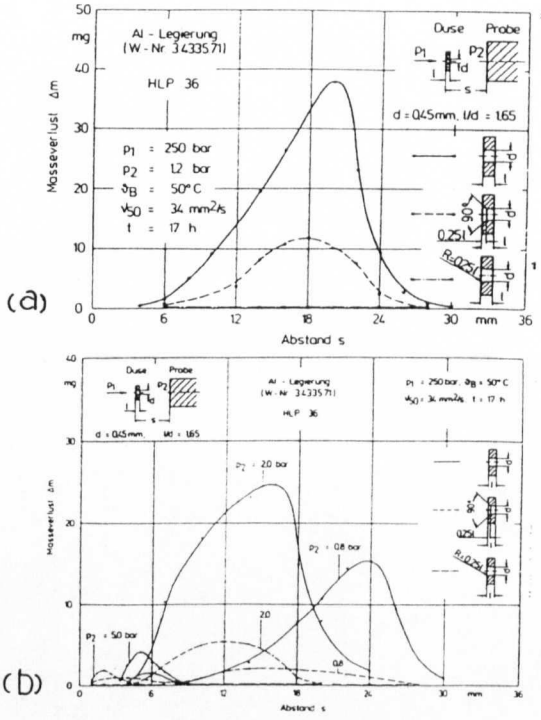

Fig.4.6.2 Effect of inlet edge finish on mass loss. (from Kleinbreuer [1980])

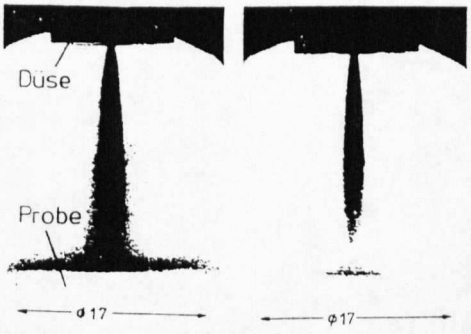

Fig.4.6.3 Photographs of cavitating jet through the nozzle with a sharp corner inlet edge (left) and with a rounded inlet edge (right). (from Kleinbreuer [1980])

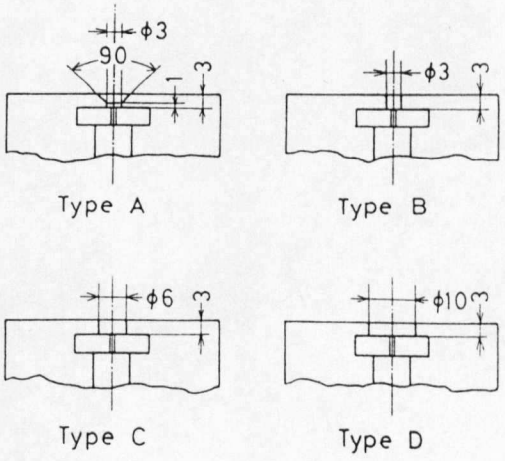

Fig.4.6.4 Nozzle holders (from Shimizu and Yamaguchi [1989])

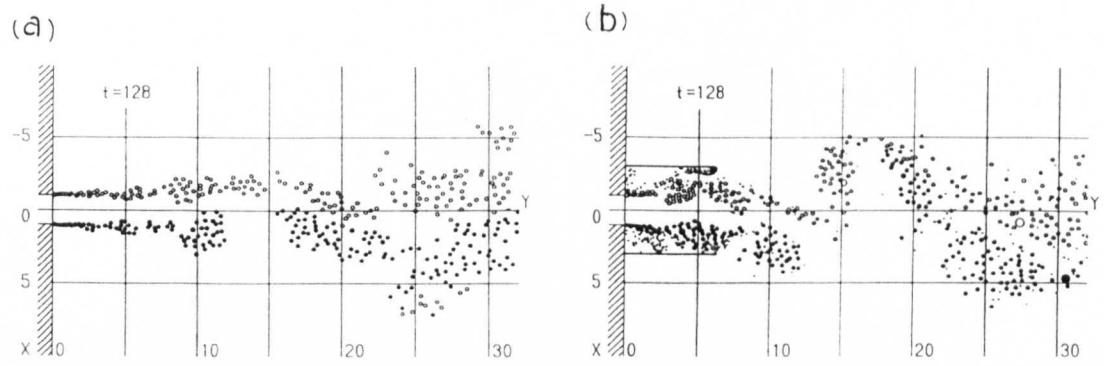

Fig.4.6.5 Distribution of vortex elements of (a) a free jet and (b) a restricted jet (from Shimizu et al. [1990])

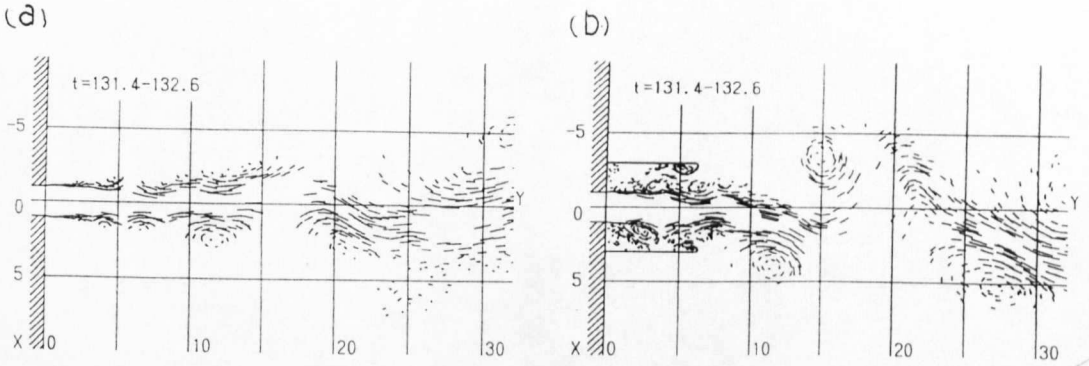

Fig.4.6.6 Trajectories of vortex elements of (a) a free jet and (b) a restricted jet (from Shimizu et al. [1990])

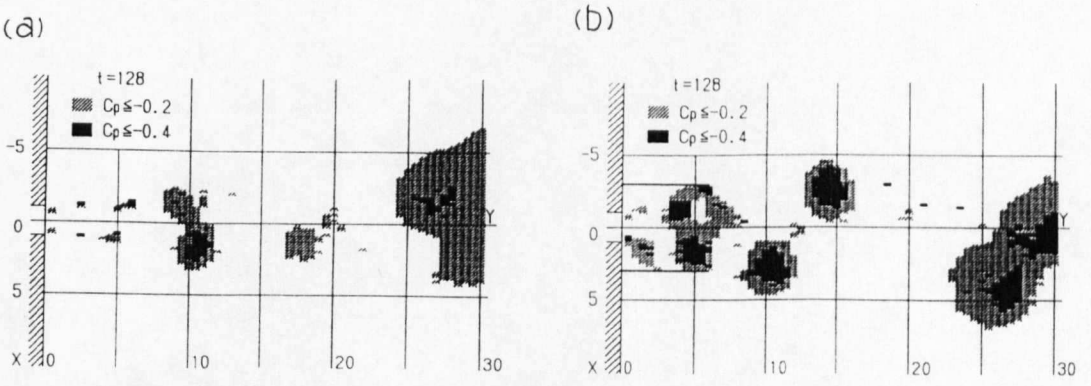

Fig.4.6.7 Instantaneous pressure distribution of (a) a free jet and (b) a restricted jet (from Shimizu et al. [1990])

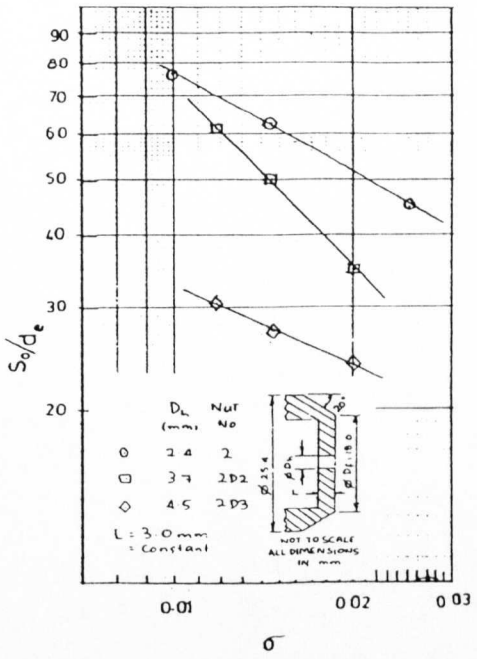

Fig.4.6.8 Effect of variation in a nozzle holder diameter with constant lip thickness on optimum stand off distance at various cavitation numbers (from Bin-Ujang [1990])

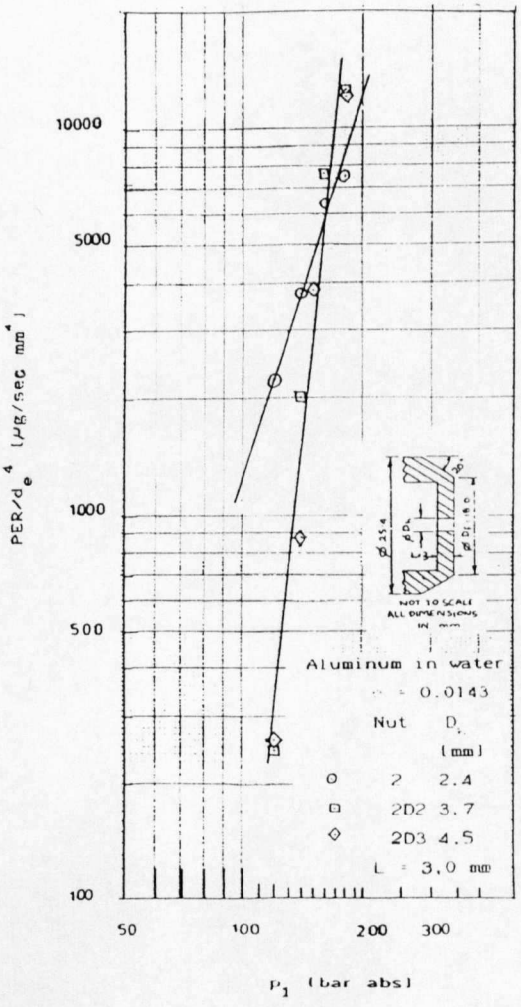

Fig.4.6.9 Effect of variation in a nozzle holder diameter with constant lip thickness on the peak erosion rate (from Bin-Ujang [1990])

It is well accepted that the surface finish condition is practically important parameter and it may influence the erosion rate. However, no comprehensive investigation has been achieved in this field for jet cavitation.

Kleinbreuer and Pohl [1981] carried out a few testing with brass specimens whose surface were treated in different manner. Figure 4.7.1 shows the mass loss-time curve of cavitation erosion for the specimens with coarse-ground, fine-ground, lapped and polished surfaces. The peak to valley height R_t and the arithmetic mean height R_a of the each surface treatment are listed in Table 4.7.1. Mineral oil was used as a working liquid. Although the number of samples is limited, the coarse-ground shows the weakest resistance to cavitation erosion and then is followed by fine-ground and lapped surface in the order of surface roughness in Table 4.7.1, except the polished surface. The reason why the polished surface was weaker than the fine-ground and the lapped one is not fully understood. Unfortunately they have not reported necessary information to judge their results, for example, the change in surface hardness due to each material treatment and/or any particular heat treatment in order to release such difference in hardness by soften the material to the extreme condition. Therefore there is a possibility that the work hardening of the polished surface was much less than the one to the others by some reasons so that the polished one was weaker than some of the others regardless of its smallest surface roughness.

It can be concluded that there is a marked effect of the surface treatment on erosion rate and so the golden rule is to keep the surface roughness constant during the tests for the other parameters.

Table 4.7.1 Surface roughness for the specimens in Fig.4.7.1

	Surface treatment			
	coarse-ground (grobgefräst)	fine-ground (feingefräst)	lapped (geläppt)	polished (poliert)
R_t (μm)	31.5	2.52	1.24	0.65
R_a (μm)	5.54	0.28	0.11	0.07

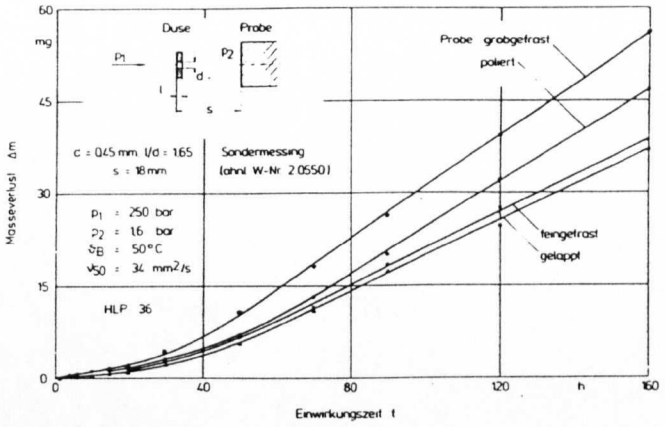

Fig.4.7.1 Effect of the specimen surface roughness on mass loss (from Kleinbreuer and Pohl [1981])

Effects of temperature on cavitation erosion obtained by several investigators with vibratory cavitation testing apparatus were plotted by Thiruvengadam [1974] and are shown in Fig.4.8.1. These results indicate that the rate of mass loss generally tends to peak at temperatures from 20°C to 60°C. If the liquid temperature is sufficiently high, the vapour pressure can be comparable to the ambient pressure and the vapour inside cavities acts more like a permanent gas. In this case, the cavities are probably rebounding in much earlier stage than the ordinary collapsing mode at room temperature. Consequently such an individual cavity may have much weaker damaging capability and, moreover, such a liquid with a gaseous cavity cluster may show a sort of cushioning effect which also reduces the cavitation erosion. However, the mechanics of the temperature effects have not been fully understood yet.

The effects of temperature on cavitation erosion with a cavitating jet method have not been examined at Nottingham or Aachen so far and as far as the present author's knowledge, there is only one experiment reported by Yamaguchi et al. [1986] from Yokohama National University. Figure 4.8.2 shows the mass loss results with tap water at the liquid temperature from 17°C~50°C. The magnitude of upstream pressure, cavitation number and cavitation exposure time were fixed, P_1=9.9MPa, σ=0.03 and T=3hrs, respectively. There is large difference in the rate of mass loss at the peak stand off distance, 10mm, among the temperature range 17°C~40°C, but is only a small difference between 40°C and 50°C. This agrees very well with the graph summarized by Thiruvengadam [1974] (Fig.4.8.1). Then, Yamaguchi et al. decided that the all the following tests would be carried out at the constant temperature 40°C. In Fig.4.8.2, cavitation number σ is defined with only an upstream pressure P_1 and a downstream pressure P_2 as

$$\sigma = \frac{P_2}{P_1}$$

which excludes the effects of the vapour pressure of the liquid used, P_v. However, the peak stand off distance 10mm was not affected by the temperature difference from 17°C to 50°C, since the vapour pressure of water at the corresponding temperature range P_v=0.002MPa~0.012MPa is negligibly smaller than the downstream pressure they used P_2=0.3MPa and so the real cavitation number was not changed.

It is obvious that there are large effects of temperature on cavitation erosion, but it seems difficult to know how it affects for each particular cavitation condition. Therefore it is important to keep the temperature of the liquid as constant as possible, unless it is the parameter of the tests.

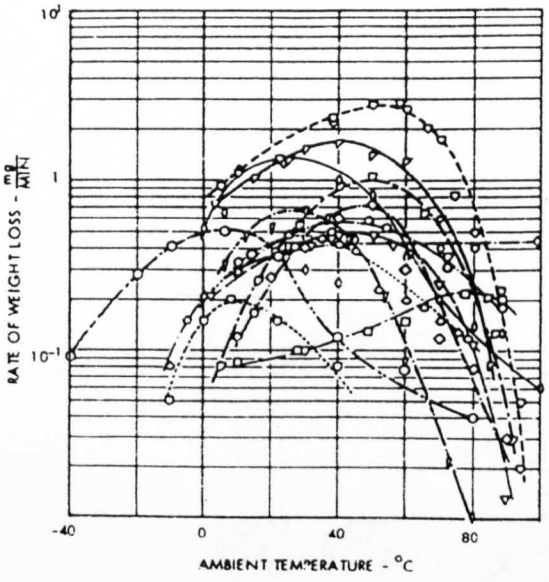

INVESTIGATOR	TEST MATERIAL	TEST LIQUID	FREQUENCY (kc/s)	AMPLITUDE (mils)	PRESSURE ATMOSPHERES	DATA SYMBOL
KNAPP, ALLEN AND MILLIGAN	ALUMINUM 51 - ST	WATER	8.7	1.0	1.0	▽
NOWOTNY	MAGNESIUM	WATER	9.0	1.8	1.0	◇
KERR AND LEITH	CAST IRON	WATER	6.5	1.71	1.0	○
	CAST IRON	WATER	6.5	1.71	2.4	□
BESCHUCK	ALUMINUM	WATER	8.0	—	1.0	▽
	ALUMINUM	BENZENE	8.0	—	1.0	□
	ALUMINUM	KEROSENE	8.0	—	1.0	◇
WILSON AND GRAHAM	WROUGHT ALUMINUM	ANILINE	12.0	—	1.0	◊
DEVINE AND PLESSET	ALUMINUM 2 / H 129	WATER	15.0	1.00	1.0	▽
WHITE	ALUMINUM	WATER	14.0	0.69	1.0	○
	ALUMINUM	BENZENE	14.0	0.69	1.0	▽
	ALUMINUM	TOLUENE	14.0	0.69	1.0	○
	ALUMINUM	ANILINE	14.0	0.69	1.0	◊

* DATA OBTAINED BY MRS. S. W. WHITE WITH THE HYDRONAUTICS MAGNETOSTRICTION APPARATUS.

LIQUID PROPERTY RANGE COVERED BY CAVITATION DAMAGE

LIQUID	VAPOR PRESSURE dynes/cm²	VISCOSITY Centipoises	SURFACE TENSION dynes/cm	DENSITY g/cm³	VELOCITY OF SOUND m/sec
WATER	8.13×10^{3} - 8.14×10^{4}	1.79 - 0.284	75.6 - 59.8	0.9998 - 0.9584	1431 - 1552
ANILINE	1.46×10^{3} - 6.09×10^{3}	10.2 - 1.27	44.1 - 39.4	1.03893 - 0.97787	1643
BENZENE	9.06×10^{3} - 7.27×10^{4}	0.758 - 0.329	30.2 - 25.0	0.88936 - 0.82446	1317
TOLUENE	1.37×10^{3} - 3.86×10^{3}	0.772 - 0.354	27.7 - 25.0	0.92393 - 0.86913	1318

Fig.4.8.1 Effect of temperature on cavitation erosion (from Thiruvengadam [1974])

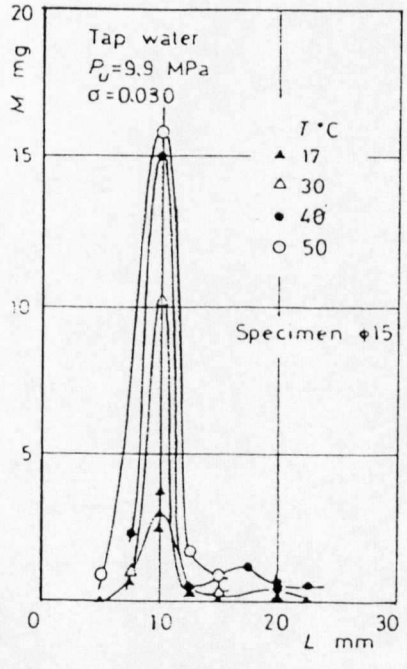

Fig.4.8.2 Effect of temperature of the test fluid on cavitation erosion (from Yamaguchi et al. [1986])

CHAPTER FIVE - TESTING METHOD

5.1 Programme

5.2 Test rig requirements

5.3 Main circuit

5.4 Test chamber

5.5 Nozzle assembly

5.6 General Testing procedure - Use of the test rig

5.7 List of parameters and dimensions

5.8 Testing preparation and procedure - Erosion test

- 5.8.1 Mean pressure distribution due to a cavitation impinging jet
- 5.8.2 Erosion test

5.9 Testing preparation and procedure - Indentation counting

5.10 Testing preparation and procedure - Loading pulse height analysis

- 5.10.1 Pressure transducer preparation
- 5.10.2 Calibration
- 5.10.3 Testing procedure

5.11 List of tests

5.12 Chronological summary of experimental work

5. TESTING METHOD

5.1 Programme

In order to investigate the cavitation loading and erosion, it was decided to use the submerged jet as a source of cavitation. Four kinds of main experimental studies were proposed.

(1) Cavitation erosion tests

Erosion tests provide basic information about the characteristics of the new test rig on the cavitation erosion using the conventional weight loss technique.

For example, optimum stand off distance is important when one evaluates the various test results with different pressure conditions. Erosion rate, erosion area and shape are also shown so that erosion intensity and erosion area can be correlated to the cavitation loading measurement test results below.

Additionally, it was also decided that mean pressure distributions produced by a cavitation impinging jet on a flat target would be measured to obtain the pressure condition at around the damaged area on the specimen.

(2) Cavitation indentation counting

When a ductile material is used for a target specimen, impingements from cavitating flow produce numbers of plastic deformations, i.e., indentations, on the target surface at the beginning of erosion. It is generally accepted that each indentation is produced by a single incident of impingement. Therefore the measured number of indentations, their size and distribution show the similar information about cavitation loading. It was also hoped that the shape of indentation on very soft material would tell many things about which is the main source of cavitation damage, microjet or shockwave.

(3) Cavitation loading pulse height analysis

As mentioned in Chapter 3, several experimental investigations into

measurements of loading pressures produced by cavitation have been published. Some of them were carried out in a water tunnel or in vibratory apparatus, but none with the cavitating jet.

This test provides information not only on the magnitude of the cavitation loading pressure, but also its duration time, frequency and correlation with the erosion results.

(4) High speed photographs of cavitation bubbles

Visual information always enhances the understanding of events. In the history of cavitation research, a number of superb high speed photographs enabled us to observe the mechanism of bubble collapse. There are quite a few publications showing high speed photographs of cavitation clouds produced by a submerged jet. However, as the existing jet cavitation rigs were primarily designed for erosion testing of small specimens, the size of nozzle diameter and the chamber was too small and the location of the window through which the photographs were taken restricted the view, so details were missing. Then, it was thought that the new large cavitating jet test rig in Nottingham would be able to provide better conditions for high speed photography with much larger nozzle and chamber. Such photographs will add some information to the results obtained from the tests described above.

In this chapter, detailed information about the apparatus, preparation and procedure of tests is described in each section. Most of test parameters and dimensions will be listed in Section 5.7 for convenience. The list of tests and chronological summary of experimental work are also in separate sections at the end of this chapter.

Since primarily a larger scale chamber has been needed for installation of a pressure transducer in the present investigation, it was decided that a large size cavitating jet rig in Nottingham would be used. The rig had recently been designed by Dr.Lichtarowicz and had not been used before the present project.

It satisfies the following requirements to carry out the envisaged experimental programme.

(1) To supply a steady flow of liquid at sufficiently high pressure and flow rate to produce a cavitating jet with a wide range of pressure levels.
(2) To control and measure both the upstream and the downstream pressures.
(3) To control and measure the temperature.
(4) To vary and measure the nozzle size.
(5) To maintain the nozzle quality by polishing and checking the inlet edge of the nozzle so that the performance of the cavitating jet and the discharge coefficient can be also maintained unchanged.
(6) To use the replaceable target specimen which is large enough to carry out detailed investigation of loading pressure measurements, indentation counting and photography.
(7) To vary and measure the stand off distance from the nozzle to the target.
(8) To control exposure time of a cavitating jet even for a few seconds.
(9) To take the photographs of cavitating jet from a wide range of angles.

The test rig is shown in Fig.5.2.1. Its main hydraulic circuit, test chamber, nozzle assembly and targets used will be described in following sections.

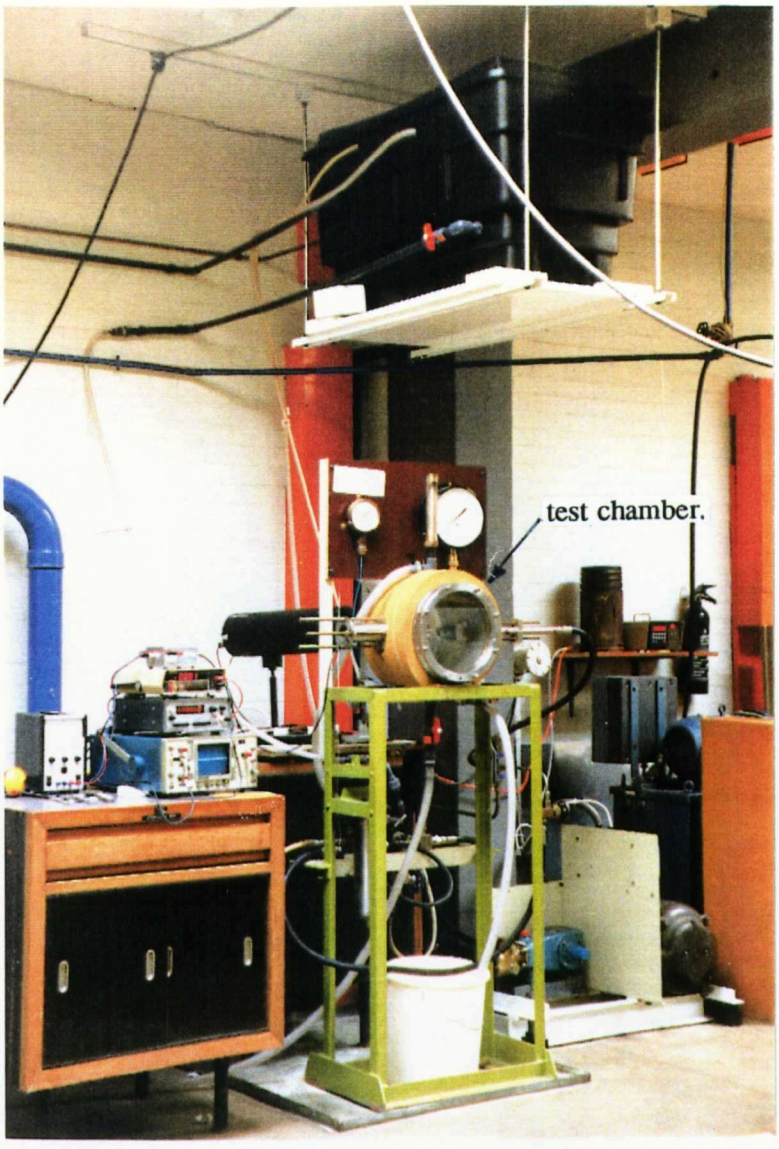

Fig.5.2.1 Photograph of a cavitating jet test rig.

The main hydraulic circuit consists basically of a high pressure pumping unit, a test chamber, an water reservoir, main loop and two by-pass lines used to control the pressure. The circuit diagram is shown in Fig.5.3.1.

To deliver liquid from the large reservoir to the test chamber, a triple piston pump (Cat Pumps Model 650) is used with an A.C.Motor (15H.P.; Brook Motors Ltd.). Pump output capacity is slightly limited by the rotation speed of the A.C. motor but reaches 25.6 l/min with the maximum pressure of 210bar. The high pressure pulsating flow from the pump passes through a hydraulic accumulator pressurized with nitrogen to damp its pulsation. Then, upstream pressure, P_1, is controlled by regulating the flow through a by-pass line back to the reservoir and downstream pressure, P_2, is separately controlled by a needle valve in the downstream line of the main loop. The downstream flow is returned through the filter to the reservoir or just drained so that the circuit can be used as a closed one as well as an open one.

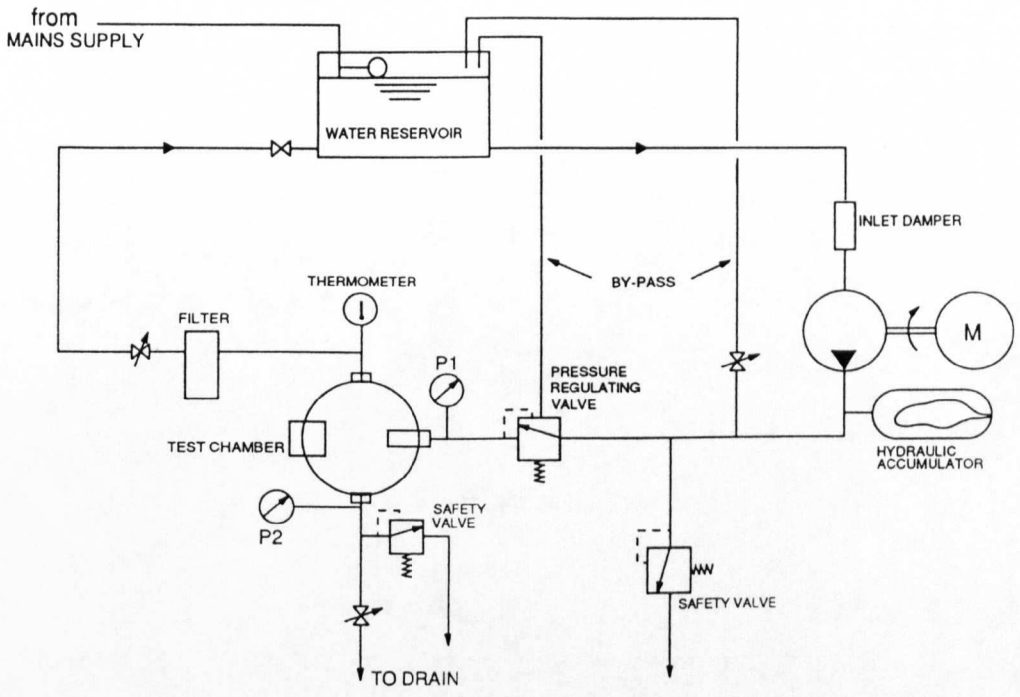

Fig.5.3.1 Main hydraulic circuit diagram.

The test chamber (inside diameter: 246mm) is shown in Fig.5.4.1. The position of the high pressure inlet pipe with a nozzle at its end and the target holder tube are both adjustable along their common axis. This enables to change their locations inside the chamber as well as to change the stand off distance between the nozzle and a specimen surface. Various kinds of target specimen were prepared to meet the requirement of each test and they were mounted at the end of the target holding tube facing the jet emerging from the nozzle.

Erosion time is controlled by a shutter mechanism which during cavitation testing is normally pulled out to the side of the nozzle as shown in Fig.5.4.2. It is important to minimize the interference with the circulating flows inside the chamber. Replacing the target specimen or the nozzle is easily carried out after removing the front window.

An advantage of this chamber is its large size. This is the largest jet cavitation erosion cell of this kind ever reported. Obviously, the large space in the chamber allows to use a large target with a large diameter of nozzle. It was expected that the advantage of large size would provide better specimen for detailed indentation counting and much better photographs.

All parts are made from stainless steel.

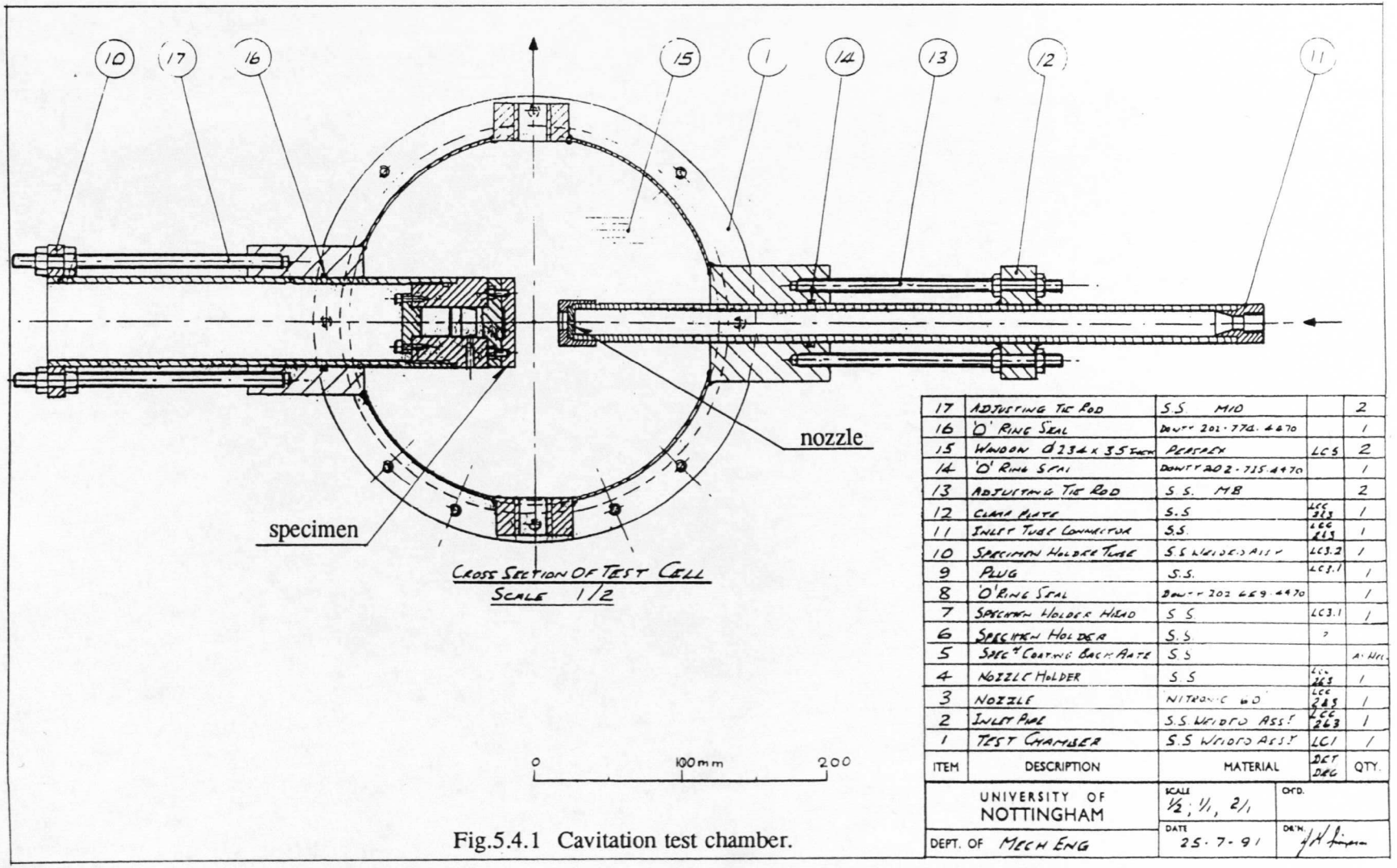

ITEM	DESCRIPTION	MATERIAL	DET DRG	QTY.
17	ADJUSTING TIE ROD	S.S M10		2
16	'O' RING SEAL	DUNT 202-770-4470		1
15	WINDOW Ø234 x 35 THICK	PERSPEX	LC5	2
14	'O' RING SEAL	DUNT 202-715-4470		1
13	ADJUSTING TIE ROD	S.S. M8		2
12	CLAMP PLATE	S.S	LCC 263	1
11	INLET TUBE CONNECTOR	S.S.	LCC 263	1
10	SPECIMEN HOLDER TUBE	S.S WELDED ASSY	LC3.2	1
9	PLUG	S.S.	LC3.1	1
8	'O' RING SEAL	DUNT 202 469 4470		1
7	SPECIMEN HOLDER HEAD	S.S	LC3.1	1
6	SPECIMEN HOLDER	S.S	?	
5	SPEC^{N} COATING BACK PLATE	S.S		AS REQ.
4	NOZZLE HOLDER	S.S	LCC 263	1
3	NOZZLE	NITRONIC 60	LCC 263	1
2	INLET PIPE	S.S WELDED ASS^{Y}	LCC 263	1
1	TEST CHAMBER	S.S WELDED ASS^{Y}	LC1	1

UNIVERSITY OF NOTTINGHAM	SCALE 1/2; 1/1, 2/1	CHD.
DEPT. OF MECH ENG	DATE 25-7-91	DR'N.

Fig.5.4.1 Cavitation test chamber.

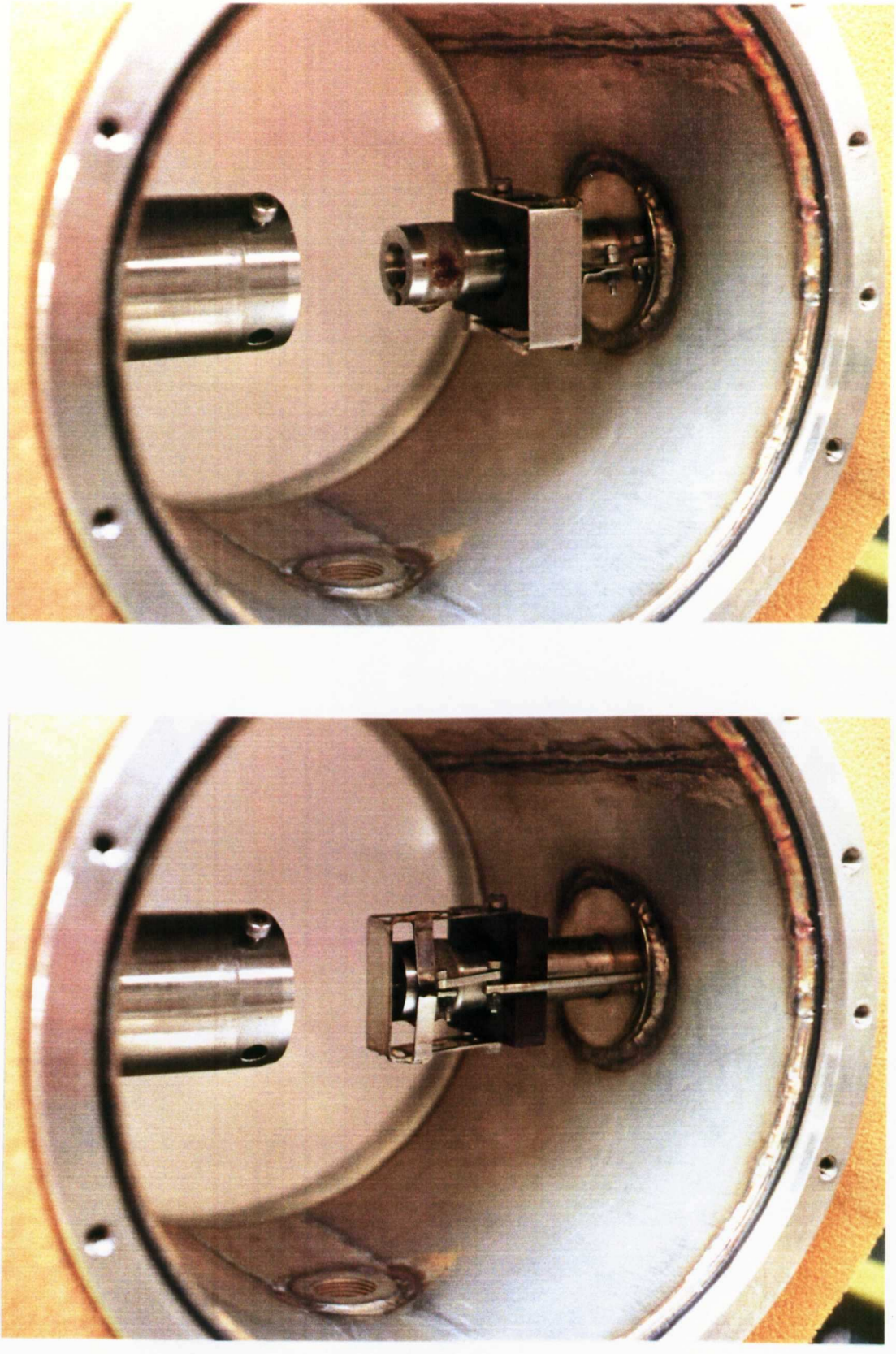

Fig.5.4.2 Shutter mechanism (Photograph).
Top: open, Bottom: closed.

A long orifice type nozzle was used for the test, since its geometry is simple, the cavitation produced is very intensive and a lot of experience on its characteristics of cavitation erosion had been already obtained in Nottingham.

The nozzle plate was made from stainless steel as shown in Fig.5.5.1. Both inlet and outlet sides of the nozzle surface were polished with wet emery paper 1200 grade until the sharp corner at especially the inlet edge was assured. This polishing process was repeated several times during the test to maintain the nozzle characteristics consistent.

Initially, two sizes of nozzles with nominal diameter 1.4mm and 2.0mm were examined to find out which size would be better to have appropriate length of cavitating jet and right size of erosion on the target specimen under the available pressure conditions. Then, the nominal size of 2.0mm was chosen because of its larger size which was expected to provide more benefit from the large scale of chamber. The precise nozzle diameter was measured by a microscope fitted with a scale. Its value was 2.08mm. This nozzle was being used throughout the all test cases including indentation counting, loading pulse height measurements and high speed photography.

The nozzle plate is fitted into the end of a high pressure tube and is held and partially covered by a nozzle holder as shown in Fig.5.5.1. Since it was pointed by Bin-Ujang [1990] and Shimizu et al. [1990] that the geometry around the nozzle outlet directly affects the circulating flow pattern around the jet and hence its influence on cavitation erosion is significant, the same nozzle holder was used throughout the test without any modifications to keep all the flow parameters constant, except the stand off distance.

The nozzle was calibrated to determine its submerged flow characteristics by measuring the flow rate at various upstream pressures. A typical set of results is presented in Fig.5.5.2.

Flow rate Q is calculated as

$$Q = C_d \cdot A \cdot V$$

where C_d is discharge coefficient, and A and V are the area of the nozzle and jet

velocity at the nozzle exit, respectively.

The velocity V can be derived from the Bernoulli equation as

$$V = \sqrt{\frac{2\Delta P}{\rho}}$$

where ρ is the density of fluid used and ΔP is the pressure difference across the nozzle.

When the jet is cavitating, pressure difference ΔP is not P_1-P_2 but P_1-P_v where P_1, P_2 and P_v are upstream pressure, downstream pressure and vapour pressure, respectively.

Then, the discharge coefficient C_d is given as

$$C_d = \frac{Q}{A} \cdot \sqrt{\frac{\rho}{2(P_1 - P_v)}}$$

Since the vapour pressure of water at 20°C is P_v=0.0234bar and is negligibly small compared with the upstream pressure P_1=23~123bar, the flow rate plotted in Fig.5.5.2 shows almost constant proportional relations with square root of upstream pressure P_1. The discharge coefficient calculated was C_d=0.614.

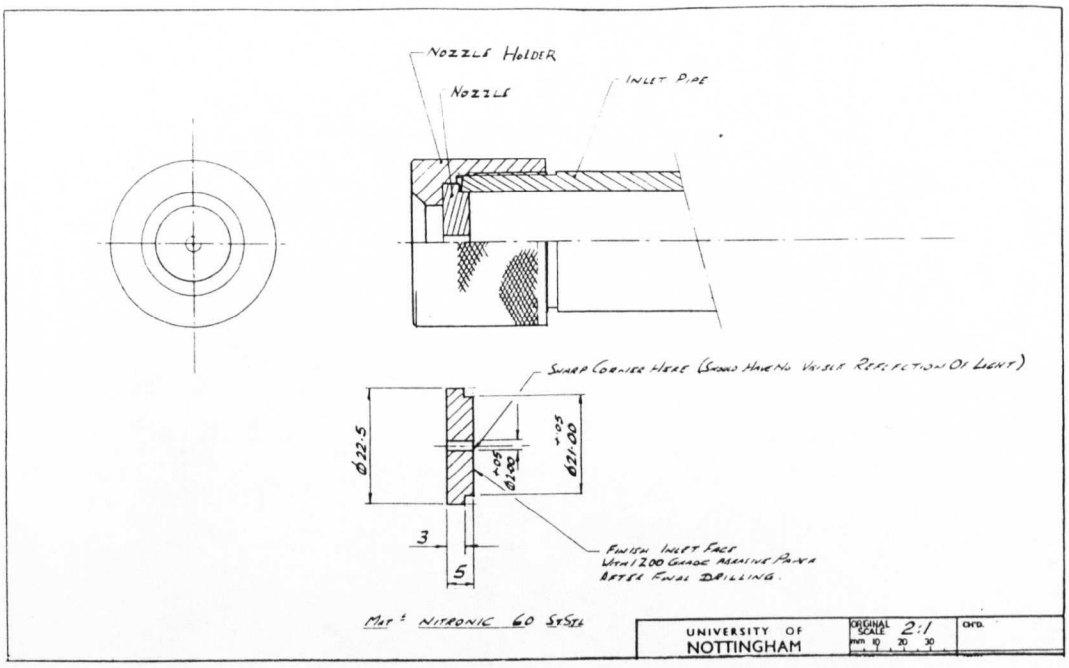

Fig.5.5.1 Nozzle assembly.

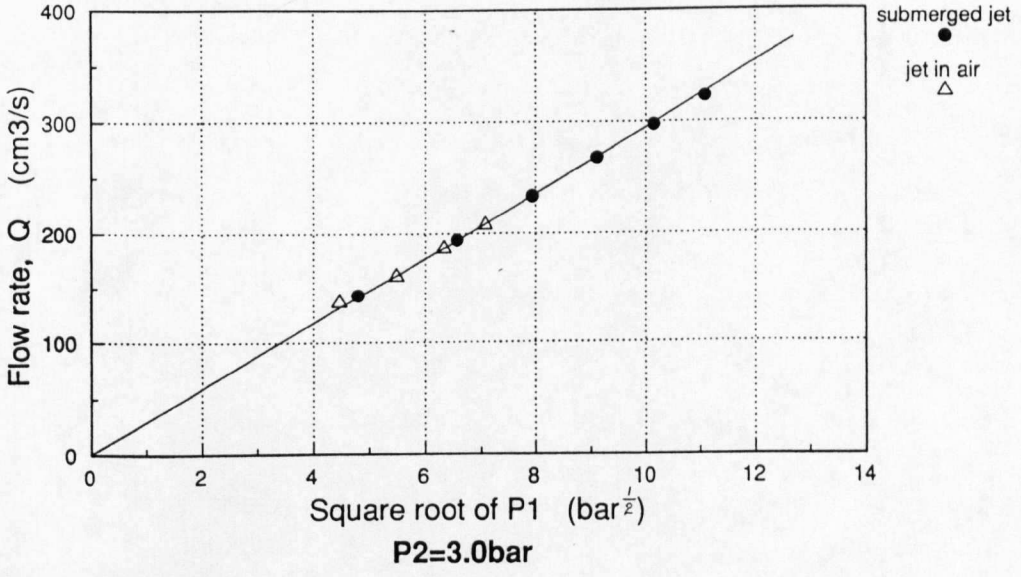

Fig.5.5.2 Variation of flow rate with upstream pressure. Long orifice nozzle (diameter: 2.08mm), liquid water, temperature 23°C.

The common experimental procedure is briefly described in this section and detailed steps particularly taken for each test will be explained in following sections with preparation of specimens and particular testing devices.

First of all, a Plexi-glass window was detached and a target specimen was carefully mounted at the target holder. In order to avoid the error from the change of geometric relation between the nozzle and the target, all the targets and the nozzle plate were marked at some edge and those marks were always kept at the top at their installation. Then, after reattaching the window, the chamber was filled with the liquid used - this time it was tap water.

To measure and adjust the stand off distance - defined as the distance from the inlet edge of the nozzle to the target surface, the total thickness of the nozzle plate and the nozzle holders lip (S_{lip}) was measured as shown in Fig.5.6.1. The target surface was attached to the nozzle holder at first and gradually pulled until desired stand off distance was obtained. The stand off distance was measured from outside the chamber by the change in distance between the end flange of the target holder tube and the surface of the chamber tube which are facing each other.

As described in the previous section, testing time was precisely controlled using the shutter mechanism. The upstream pressure P_1 and the downstream pressure P_2 can be measured and varied separately by adjusting a valve at each side. In addition to the two pressure parameters, an well known useful parameter, cavitation number σ, was also used. For cavitating jet, it was introduced by Lichtarowicz [1979] as follows.

If the ratio between the static pressure suppressing the vaporization, cavitation, and the stagnation pressure of submerged jet generating a vortex as a core of cavitation is defined as cavitation number σ, it can be expressed as

$$\sigma = \frac{P_2 - P_v}{\frac{1}{2}\rho V^2}$$

$$= \frac{P_2 - P_v}{P_1 - P_2}$$

Since the long orifice nozzle is used here, the jet is already cavitating from the inlet edge inside the nozzle and the flow velocity is controlled by vapour pressure P_v, not by the downstream pressure P_2.

Then, the cavitation number σ is

$$\sigma = \frac{P_2 - P_v}{P_1 - P_v}$$

The vapour pressure P_v of water is negligibly small compared to P_1 and P_2 in most cases and so the cavitation number σ becomes a form of simple pressure ratio,

$$\sigma = \frac{P_2}{P_1}$$

Slight problem of this rig is controlling the temperature of testing fluid, because there was no heating nor cooling system initially prepared. The temperature of tap water from a large underground reservoir of the University of Nottingham is reasonably constant throughout the year from 16°C in winter to 20°C in summer. But when the rig is being run as a closed circuit, the liquid temperature is gradually increasing up to as high as 40°C with operating time by the heat from the pump. After considering several possible options including the installation of fully equipped temperature controlling systems, the simplest, the cheapest and the quickest method was chosen- running the rig as a semi-open circuit; i.e., part of circulating water was being drained constantly by adjusting the valve in the main drain line in Fig.5.3.1 and simultaneously new cold water was supplied from tap to cool down the circuit and to keep the temperature within the desired level. The temperature was checked several times during operation even for the test shorter than half an hour. Although the amount of drain and supply water was different in each case, its effect on the air content or numbers of cavitation nuclei is negligible since basically all water used can be regarded as very fresh tap water with similar history of treatment in the large underground reservoir of the University throughout the year.

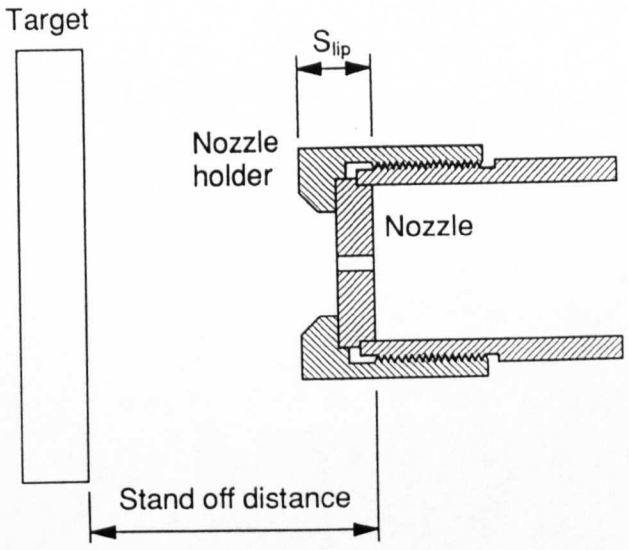

Fig.5.6.1 Stand off distance.

5.7 List of parameters and dimensions

Since the primary concern in this project is to investigate the fundamental characteristics of cavitation loading, most of parameters were treated as unchanged except the pressure, cavitation number and stand off distance. Parameters and dimensions used commonly in all tests are listed as follows.

(1) Nozzle shape and size - unchanged

· Long orifice nozzle.

· The length and the diameter is l=5.0mm and d=2.08mm, respectively. (see Fig.5.5.1.)

· The effective nozzle diameter is $d_e=d\cdot C_d^{1/2}$=1.63mm. (see Section 6.2)

(2) Nozzle holder shape and size - unchanged

(see Fig.5.5.1.)

(3) Test chamber shape, and size - unchanged

· Inside diameter of the chamber is 246mm. (see Fig.5.4.1.)

(4) Target and specimen configuration - unchanged

· All target and specimens used in all tests were flat disc shape mounted perpendicular to the jet axis. (see Section 5.8~5.10 for detail.)

a) Mean pressure distribution

· A flat disc target (diameter: 57mm) made from brass with small taps (diameter: 0.4mm) on the surface.

b) Erosion tests

· A flat disc specimen (diameter: 59mm and thickness: 9mm) made from 6063-aluminium alloy. The surface was polished by an wet and dry 1200 grade abrasive paper and then the specimen was annealed in 400°C for 2hr. and cooled in air at room temperature. Vickers hardness is 29.7±1.9.

c) Indentation counting

· A flat disc specimen (diameter: 57mm and thickness: 2mm) made from 1200-aluminium alloy. The surface is polished with 1 micron diamond paste and then the specimen is annealed 400°C for 2hr. and cooled in air at room temperature. Vickers hardness is 19.6±0.3.

d) Pulse height measurement

· A sheet of PVDF piezofilm is mounted in a shallow grove on a flat disc target (diameter: 57mm) made from stainless steel. (see Section 5.10.1 and Appendix A3)

e) High speed photography

· A flat and well polished disc target (diameter: 57mm) made from stainless steel.

(5) Liquid used - unchanged

Tap water.

(6) Temperature - unchanged

22.5 ± 1.5°C.

(7) Upstream pressure

P_1=80, 100 and 120bar.

(8) Downstream pressure

P_2=2.4, 3.0 and 3.6bar.

(9) Cavitation number

σ=0.02, 0.025, 0.03 and 0.0375.

(10) Reynolds number

Reynolds number, R_e=2.1~2.5x10^5, is obtained from an effective nozzle diameter, d_e=1.63mm, and jet velocity calculated from the upstream pressure.

(11) Stand off distance

S_{off}=13~65mm (S_{off}/d_e=8.0~39.9).

(12) Cavitating jet exposure time

From a few seconds for indentation counting tests to as long as 50 hours for erosion tests.

Details of each testing condition will be explained in following Section 5.8~5.11. Pressure conditions and stand off distances for erosion test, indentation counting and pulse height analysis will be listed in Section 5.11.

5.8.1 Mean pressure distribution due to a cavitation impinging jet

In order to make sure that the downstream pressure P_2 in the chamber can be regarded as the ambient pressure at the damaged area on the specimen, mean pressure distributions on a flat target were measured. The results also show the effect of the cavitation on the decay of the submerged jet velocity.

The flat target with several fine taps (0.4mm in diameter) on the surface was prepared as shown in Fig.5.8.1 and 5.8.2. Stainless steel tubes were soldered to the back side of the taps for some at the centre high pressure area to conduct the obtained pressure to the pressure gages while fittings and plastic tubes were used for the others in lower pressure area.

The target was exposed to various cavitating jets and mean pressures from those taps were simply recorded. Since the hole location was designed asymmetrically, the target can be rotated through 180 degrees so as to double the number of measuring points. The pressures on the target were fluctuating especially at the centre of the high pressure zone, so an average values had to be taken.

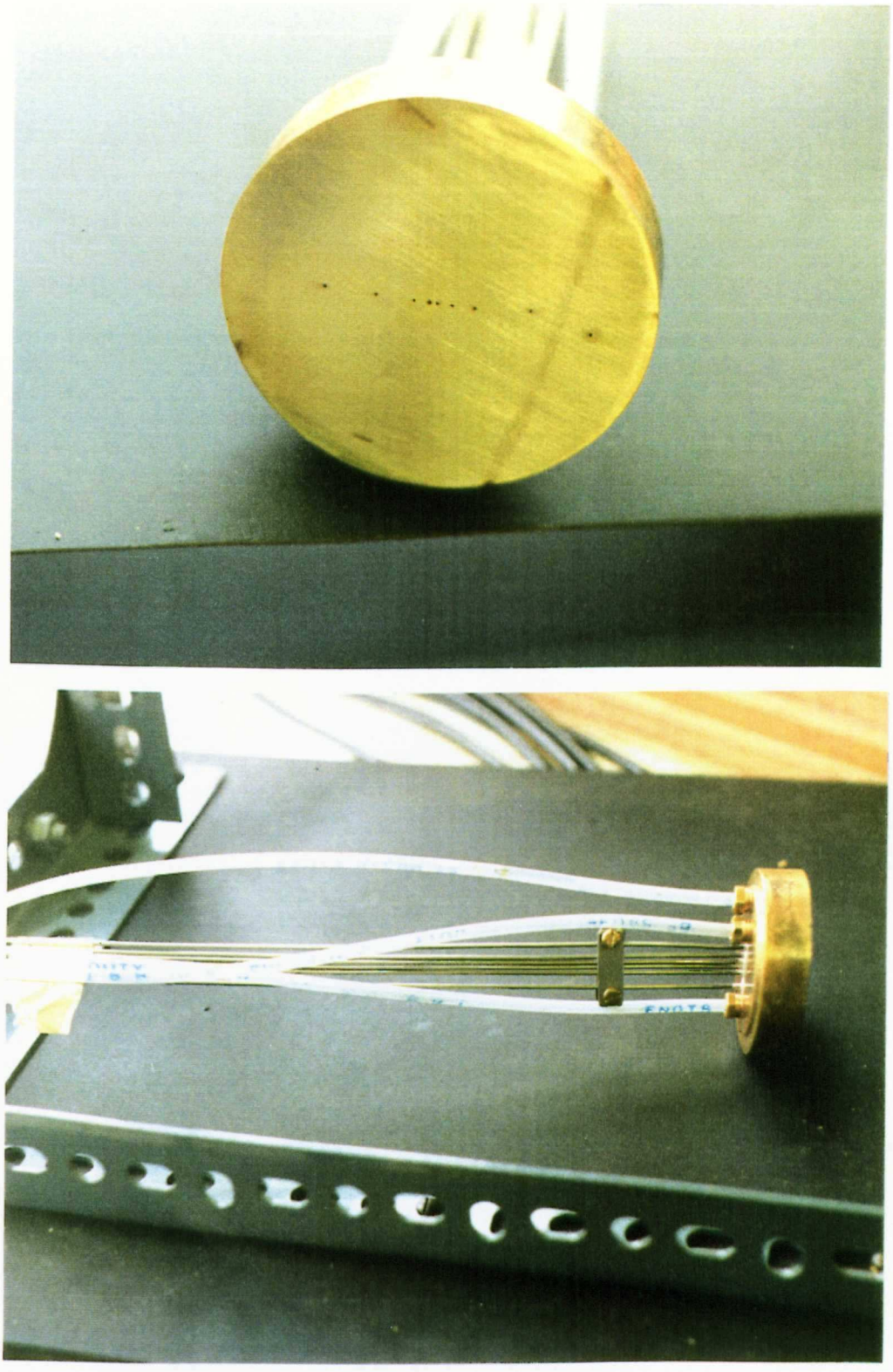

Fig.5.8.1 Flat plate target with taps for measurements of mean pressure distribution. (Photographs)

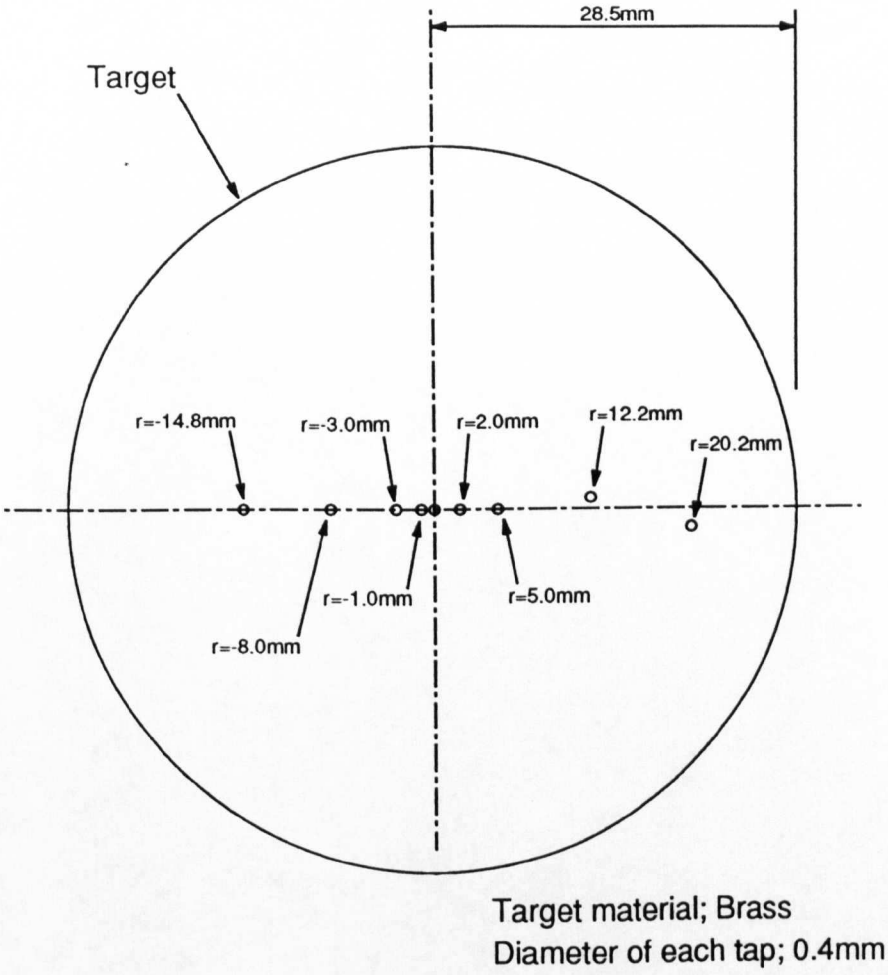

Fig.5.8.2 Arrangement of taps on flat target for mean pressure measurements.

5.8.2 Erosion test

In order to clarify the erosion capacity of the cavitating jet at various stand off distances and to provide some other basic information to later tests, erosion tests were conducted with several pressure conditions.

A 6063-aluminium alloy was chosen as the target material of the erosion test because the 6063-aluminium alloy is not chemically active in water and relatively very weak against cavitation erosion, which means only the mechanical effect of the cavitation erosion can be obtained within relatively a short testing time. Chemical composition of the 6063-aluminium alloy as specified is listed in Table 5.8.1.

Table 5.8.1 Chemical composition of the 6063-aluminium alloy

Material Designation	Si	Fe	Cu	Mn	Mg	Cr	Zn	Ti	Others		Al
									Each	Total	
6063	0.20 -0.6	0.35	0.10	0.10	0.45 -0.9	0.10	0.10	0.10	0.05	0.15	Rem

The target specimen and its holder were prepared as shown in Fig.5.8.3. The holder was made from stainless steel and easily fitted at the end of the target holder tube in the test chamber. The surface of the target specimen was finished by polishing with wet abrasive paper 1200 grade. Then the specimen was annealed in furnace at 400°C for 2 hours and cooled in air at room temperature. Vickers hardness of all specimens was measured and was reasonably consistent at 29.7±1.9.

For setting the pressure condition, it was decided at first that,

(1) Upstream pressure would be around 100bar bearing the maximum working pressure of the pump, 200bar, and for leaving the possibility of replacing the nozzle to the one with larger diameter.

(2) Downstream pressure would be larger than about 2.5bar abs. below which the air bubble was not sufficiently suppressed in the chamber so that erosion

capacity became very small due to the existence of air cushion effect.

(3) Cavitation number should be taken as small as possible to obtain sufficient erosion efficiency and to minimize testing time.

Then, to meet above requirements, pressure condition listed in Table 5.8.2 was proposed. It was thought that three different pressure combination, P_1 and P_2, would be taken keeping one of three parameters, P_1, P_2 and σ, constant, as shown by arrow 1, 2 and 3 in Table 5.8.2.

Table 5.8.2 Pressure conditions for experiments

Upstream pressure, P_1 (bar)	Downstream pressure, P_2 (bar)		
	2.4	3.0	3.6
80	O (σ=0.03)	O (σ=0.0375)	-
100	-	1 O 3 (σ=0.03)	-
120	O (σ=0.02)	2 O (σ=0.025)	O (σ=0.03)

Arrow 1, --- constant σ=0.03 with various P_1 and P_2

Arrow 2, --- constant P_1=120bar with various P_2 and σ

Arrow 3, --- constant P_2=3.0bar with various P_1 and σ

In order to correlate the erosion data to the indentation data with the same pressure conditions in the future, it was confirmed, before finally starting erosion tests, that clearly detectable indentations were able to be produced on a soft aluminium specimen (annealed 1200-aluminium alloy) by even the weakest pressure combinations, P_1=80bar and P_2=3.0bar.

Various stand off distances S_{off} were taken until they clearly showed the

optimum stand off distance where the peak erosion intensity for the given pressure condition was obtained.

Actual erosion testing was carried out as follows.

(1) A pre-weighed specimen is mounted in the test chamber and the stand off distance is adjusted.

(2) The chamber is filled with water.

(3) Jetting is started and the pressure conditions, P_1 and P_2, are set with a shutter closed.

(4) The erosion test is started. Starting time can be precisely controlled by using the shutter.

(5) After the cavitating jet exposure for pre-set time interval was completed, the water in the chamber is drained and the specimen is taken out.

(6) The specimen is gently soaked into a beaker of methanol to remove residual water and some unknown chemical materials in it. (This treatment also minimizes drying up time in the next step.)

(7) After drying up the specimen with slight heating, it is weighed and weight loss from its original weight is calculated and recorded. Then, in order to quantify the erosion intensity and its area, cumulative erosion rate explained below is calculated and the erosion diameter is measured.

(8) If the cumulative erosion rate calculated is larger than that of previous testing time interval (namely, the peak value is not obtained in the cumulative erosion rate), this testing process must back to (1) and the specimen is tested again for the next time interval. If the peak cumulative erosion rate is confirmed, the erosion test can be finished.

As above, erosion test was continued at least until it showed the peak value in the cumulative erosion rate CER which is expressed as

$$CER = \frac{weight\ loss}{exposure\ time}$$

Similarly the instantaneous erosion rate IER can be defined as,

$$IER = \frac{\textit{weight loss during the interval}}{\textit{the interval time of measurements}}$$

Since the instantaneous erosion rate IER depends more on the length of time interval between two measuring points as shown in Fig.5.8.4, the cumulative erosion rate CER can be regarded as more stable and reliable value to compare the erosion intensity among several different cases each other. In other words, it can be said that the instantaneous erosion rate IER is more sensitive than the cumulative erosion rate, although appropriate time interval must be maintained.

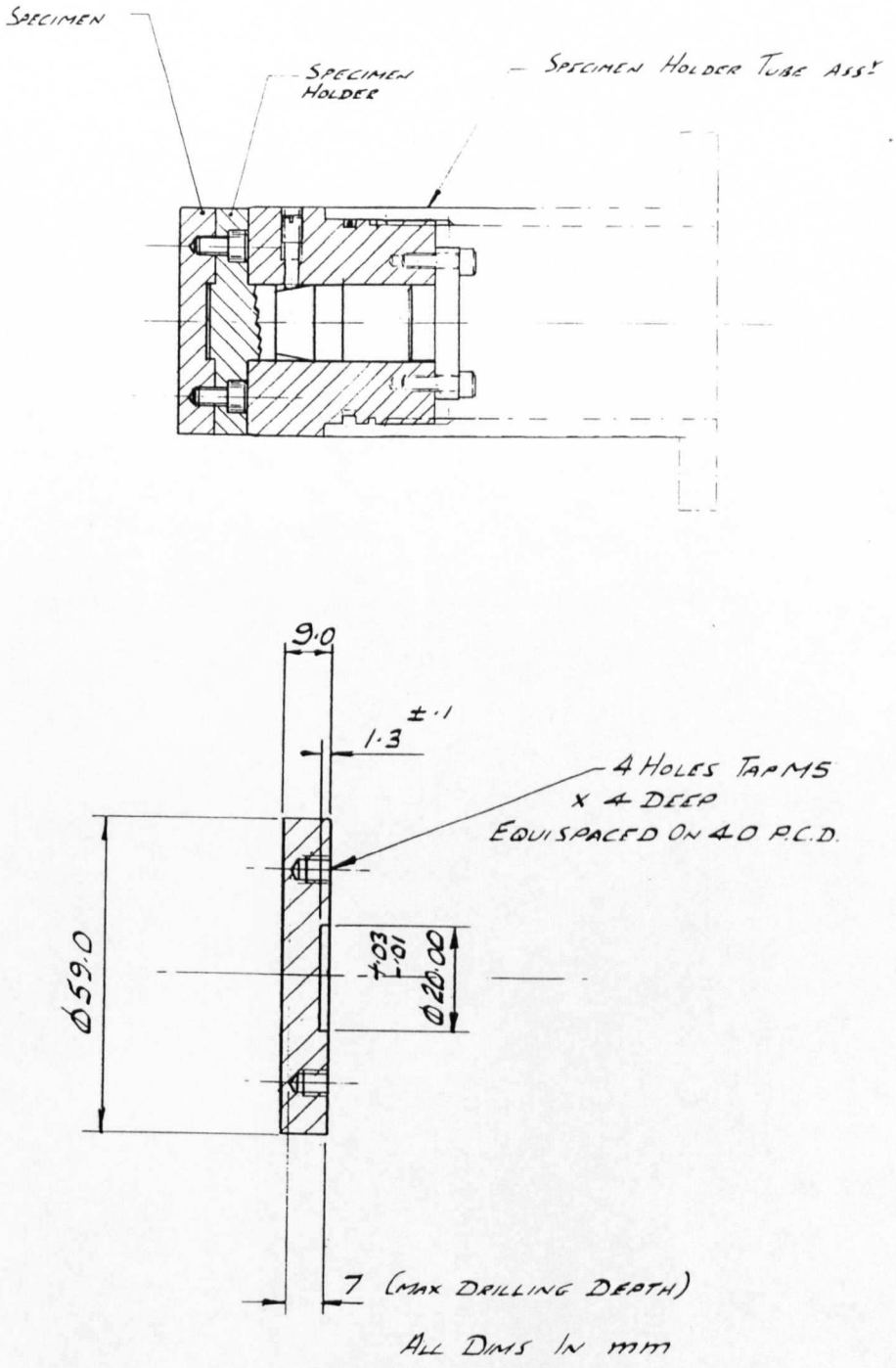

Fig.5.8.3 Specimen and specimen holder assembly of erosion tests.
Material is annealed 6063-aluminium alloy (specimen), and stainless steel (holder).

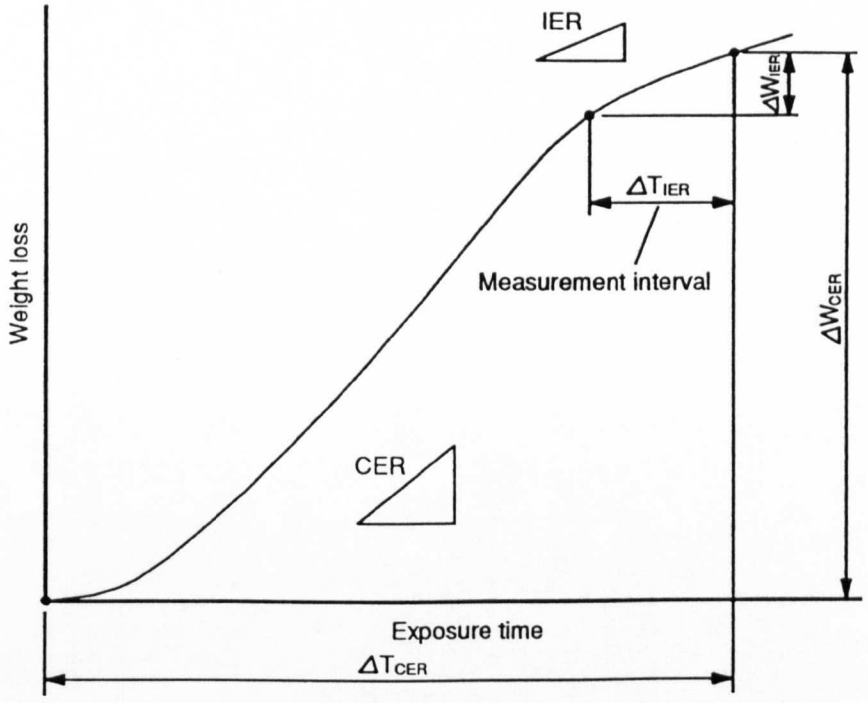

Fig.5.8.4 Definition of CER (cumulative erosion rate) and IER (instantaneous erosion rate).

Experimental procedure and testing condition of indentation measurement were basically same as those of erosion tests except the testing time, the material of specimens and their preparation.

In order to record even the very weak cavitation impingement on the surface, an annealed 1200-aluminium alloy sheet (99.00% purity, thickness: 2mm) was selected as the material of the target. Chemical composition of the 1200-aluminium alloy as specified is tabulated in Table 5.9.1. The 1200-aluminium alloy has very consistent softness and ductility. It was expected that it would show similar characteristics on the process of damage to the 6063-aluminium alloy used for erosion tests, because of the material similarity. The 1200-aluminium alloy was used as a disc which was attached on the erosion target with double sided adhesive tapes as shown in Fig.5.9.1.

Table 5.9.1 Chemical composition of the 1200-aluminium alloy

Material Designation	Si	Fe	Cu	Mn	Zn	Ti	Others		Al
							Each	Total	
1200	1.0 Si + Fe		0.05	0.05	0.10	0.05	0.05	0.15	99.00

Quantifying the information from the image, such as counting the number of indentations with each size and location, is not always an easy task. Especially in this case, the size of indentations ranges from a few hundred down to a few micron or even smaller and the area where the counting must be carried out is very large. Scanning length from the erosion centre to the outside edge of the erosion in four directions on one specimen may add up to almost 10cm. Naturally, this is not a job for human beings!

Image Analyzer with a top range of optic microscope was used to perform this work. Schematics for setting up the machine and the machine scanning direction on a specimen with image capturing frames are presented in Fig.5.9.2 and Fig.5.9.3, respectively. The size of each frame is 0.84mmx0.84mm. The "image" captured in the square shaped frame through the microscope consisted of a lot of indentations

produced by the cavitation loading with some polishing scratches and original surface flaws. They were taken by a video camera, and then digitized and analyzed by a computer system. The specimen was scanned from the centre to the outside edge of distributed indentations in four directions. The scanning motion of the specimen was also automatically and remotely controlled by the computer. The detailed image analyzing process is explained in Appendix A2.

The images were enhanced by special object lens with optical liquid between the lens and the specimen, and so they were clearer and better than the ones obtained with the ordinary microscope without such enhancement. Photographs of indentations were taken directly from the computer display and observed.

The size of indentations was as small as few microns and for such automatic measurement, the ability of judging indentations from surface scratches is still relatively poor. Therefore, the surface condition of the specimen disc was very important to have reliable data about the size and numbers of indentations. At first the disc surface was polished by wet abrasive paper 1200 grade and then, it was further polished by diamond paste 9 micron and 1 micron until the surface became like a mirror. The surface condition was being monitored several times during the process of 1 micron diamond paste polishing by an optic microscope with magnification of x100~200. After confirming satisfying conditions by the microscope, the specimen discs were heat-treated at 400°C for 2hours and then air-cooled at room temperature as described for erosion specimens. The hardness of all disk specimens was measured and was impressively consistent value of 19.6±0.3 in Vickers hardness.

As the final checking to judge whether the surface finished of the disc was sufficiently good or not, all the polished blank discs were pre-analyzed by the image analyzer as exactly the same process and conditions as the actual analysis after cavitation damage. If more than one indentation, or small scratch, per an analyzing frame (see Appendix A2) was found on an average or more than three were found in the worst frame, the disc was not used for the test and was returned to the polishing and annealing process again. The minimum size limit above which indentations could be detected by the image analyzer had to be set before starting the measurements. Ten micron in equivalent circle diameter was chosen here for the minimum size limit. One micron seemed to be too small for the limit, since the same size of diamond paste was being used in polishing. Because of some slight difference between the image of the microscope used during polishing and of the microscope used in the image

analyzing, several discs were actually rejected more than twice. Since the material was very soft and delicate and the area of the specimen to be polished was large, the polishing was not an easy process. Usually more than 3 hours excluding heat treatment were spent for each specimen disc surface preparation.

In contrast to the polishing time, actual jet exposure time for indentation counting was very short, just a few to ten seconds. The jet exposure was controlled by operating the shutter and the duration was measured by a stop watch. After adequate amount of cavitating jet exposure, indentations produced were analyzed by the image analyzer.

Distributions of indentations were ring shape which was similar to erosion shape. They were measured radially from the centre of the distribution to the outside edge of the specimen disc. Four direction of radial scanning paths were taken for each disc and the data from eight frames (adjacent two frames from four scanning directions) at the same radial distance were averaged. Each indentation larger than 10 micron in diameter was recorded in computer memory with its size and the radial distance of the frame to which it belonged.

In addition to those quantitative measurement described above, indentations on the well polished surface were observed and their photographs were taken directly from the computer display of the image analyzer. A scanning election microscope was also used to take three dimensional photographs. They will be shown and discussed in Chapter 8.

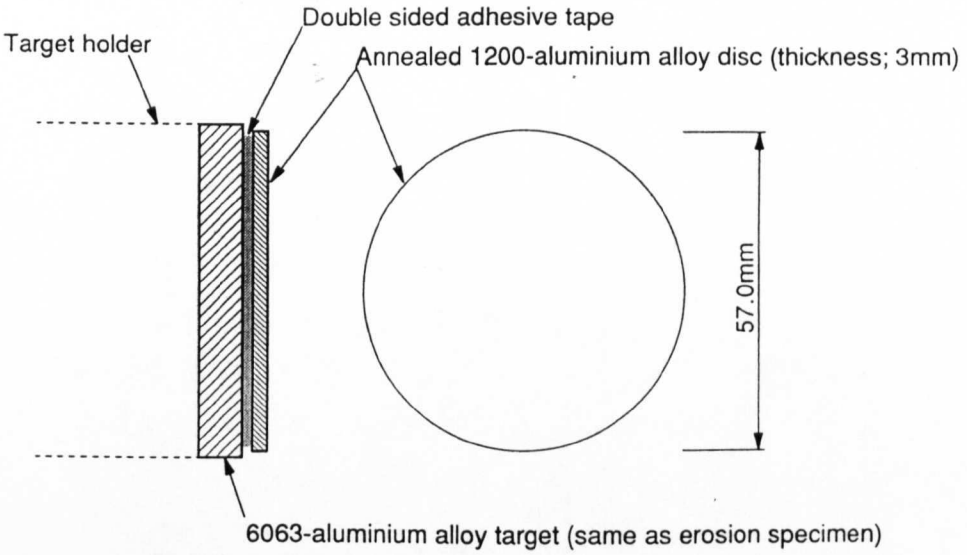

Fig.5.9.1 Specimen assembly of indentation counting tests.
Material is annealed 1200-aluminium alloy (specimen disc).

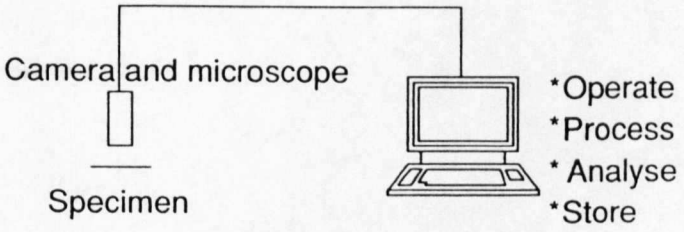

Fig.5.9.2 Image analyzer.

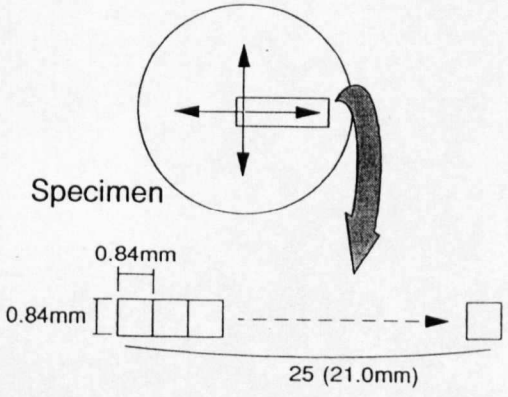

Fig.5.9.3 Scanning path for image analysis.

5.10 Testing preparation and procedure - Loading pulse height analysis

In order to investigate the cavitation loading, the loading pulse was directly measured and its pulse height distribution was analyzed.

As a sensor for this particular measurement where the impingement area is very small, each impact duration time is extremely short and impact itself is very damaging, a piezoelectric pressure transducer using piezoelectric polymer, PVDF (Polyvinylidene Fluoride) piezofilm, was developed. The largest merit of using this relatively new material, piezofilm, is its ease of manufacture. It can be cut simply by a knife or scissors into any size and any shape. At the same time, analog pulse height measurement system consisting of the pressure transducer, a input pulse height gate circuit and an event counter was also designed.

A calibration device using high speed "breaking load" was also developed for the PVDF piezofilm pressure transducer.

In this section, the pressure transducer preparation and the calibration device will be presented at first in subsections 5.10.1 and 5.10.2, respectively, whilst the testing procedure of the cavitation loading pulse measurements will be described later in subsection 5.10.3.

5.10.1 Pressure transducer preparation

Piezoelectric pressure transducer was especially designed and manufactured to meet the particular requirements of this measurement. Polyvinylidene fluoride (PVDF) piezofilm was chosen as a pressure sensing material because it can be much more easily cut into different sizes and shapes than any other piezoelectric materials such as ceramics or natural crystals. Another noteworthy features of PVDF is its high frequency response. The catalog value of the sound velocity is $C=2.2\times10^3$m/s. Its natural frequency, f_N, is calculated as

$$f_N = \frac{C}{2t}$$

where t is the thickness of the film. In the present measurements, the thickness of PVDF used is $t=110\mu$m. Then, the natural frequency is $f_N=10$MHz which is much higher than the most commercial pressure transducers and is expected to be sufficiently high for the cavitation loading measurements. The details of working principles, other material specifications, designing principles and manufacturing procedures are described in Appendix A3.

Figures 5.10.1 and 5.10.2 show photographs and a drawing of the transducer mounted on a stainless steel target. The transducer consists of a PVDF piezofilm, two electric leads, two layers of polyimide adhesive tapes for outer protection and a sheet of Kapton (also polyimide) thin film for insulation at the bottom. They are mounted into the shallow groove (150μm in depth) on the target and are bonded with cyanoacrylate type adhesives. A cross painted part by silver conductive paint is the sensitive area and is located at the distance of r=7.0mm from the centre which corresponds to the most severely damaged region for the cases at the second optimum stand off distance $S_{off2}=40$mm with cavitation number of $\sigma=0.03$. A lead connection to the piezofilm is mechanically the most fragile part in this transducer and so it is safely placed outside the maximum damage area around r=7.0mm. The shape of the cross painted part is always designed square shape because of ease of manufacture.

Various kinds and thickness of tapes, such as polyester, nylon and polyimide with thickness from a few micron up to 70μm, were tested for the protection material under various cavitation loading condition. Then, it was found that the polyimide tape (thickness, 70μm) was the strongest tape available. But even for them, it was

extremely difficult to protect the transducer at the first optimum stand off distance where the flow velocity is much higher than that at the second optimum stand off distance. Therefore, it was decided that the measurements were carried out only at the second optimum stand off distance with cavitation number of σ=0.03.

Unfortunately neither the acoustic impedance nor the natural frequency of the polyimide are available. The velocity of sound, C, is calculated from Young's modulus, Y, and the density, ρ, by the known formula,

$$C = \sqrt{\frac{Y}{\rho}}$$

where $Y=2.5\times10^9 N/m^2$ and $\rho=1.42\times10^3 kg/m^3$ are given for the polyimide used, though the former is a static value, and so the velocity of sound can be calculated as $C=1.3\times10^3 m/s$. However, it is generally accepted that such a static value of Young's modulus of polymer is much smaller than the one in high frequency. In fact, the velocity of sound of PVDF piezofilm, $C=2.2\times10^3 m/s$, is twice as high as the value calculated from its static Young's modulus by the above formula, which is $C=1.1\times10^3 m/s$. Therefore, it may not be too far from the reality to assume that the velocity of sound of the polyimide is also twice as high as the value calculated above ($C=1.3\times10^3 m/s$), and so it becomes $C=2.6\times10^3 m/s$. The natural frequency and the acoustic impedance of the polyimide tapes are also estimated f_N=9.3MHz and $\rho C=3.7\times10^6 kg/(m^2 \cdot s)$, respectively. Then, though the detailed cavitation loading mechanism has not yet been clear, if we assume the direct impingement of the water microjet to the polyimide surface, the water hammer pressure can be calculated as $P_{wh} \approx 0.7\rho_L C_L V$. This is lower than the water hammer pressure $P_{wh} \approx \rho_L C_L V$ expected from the hard surface of metals.

Duncan and Zhang [1991] achieved calculation on the cavity collapse near a compliant boundary and show the possibility of the microjet formation away from the boundary. Therefore, one may think that the polyimide surface may be able to affect the bubble motion and to repel the microjet. The boundary they studied, however, is very soft. In terms of a dimensionless form, its spring constant ranges $K^*=K \cdot R_0/\Delta P=1.0\sim3.5$ where K is a spring constant, R_0 is the initial bubble radius and ΔP is the ambient pressure. From the Young's modulus $Y=2.5\times10^9 N/m^2$ of the polyimide, R_0=1.0mm and ΔP=3.0bar, the spring constant becomes $K^*=33000$ in the present tests. Then, it appears that the polyimide boundary used in the present

transducer should be sufficiently stiff to neglect the effect of the compliant boundary. The compliant boundary which Gibson and Blake [1982] and Shima et al. [1989] experimentally investigated seems also to be much softer than the present polyimide boundary.

Since there are two layers of polyimide protection tapes, the top layer is replaceable without removing any silver painting on the piezofilm to renew the material surface condition and to extend the life of the transducer under such a damaging measurement condition. On the other hand, however, the existence of the medium with such thickness between the actual loading surface (on top of the protection tapes) and the sensitive material (PVDF piezofilm) may harm the reliability of the data obtained; i.e., the impact loading can be attenuated through those tapes or the part of the loading pressure may dissipate through the medium to outside the sensitive zone of the transducer as a form of propagating shockwave and vice versa. To make sure whether these effects are likely or not, the transducer with various number of layers of protection tapes from two layers (thickness, 140μm) to six layers (420μm) were tested.

Another parameter whose effects are unknown is the size of the transducer. Although several investigators have tried to use the smallest possible transducer, if its size is not sufficiently large compared with the size of cavitation loading, the smallest possible one may not be the best choice; i.e. in such a case, the cavitation loading over the edge of the sensitive part of the transducer may often occur and the magnitude of the pulse height can be decreased. This effect due to the relative size of the sensitive area of the transducer to the cavitation loading size can be particularly obvious at around the edge of the sensitive part, but how effective or negligible has not been investigated so far. Therefore, six transducers were made with each different sensitive area, such as 0.140mm^2, 0.301mm^2, 0.777mm^2, 1.35mm^2, 4.43mm^2 and 8.88mm^2, and it was decided that the pulse height distributions under the same pressure condition would be measured by them and would be compared with each other.

In order to carry out the pulse height analysis, analog pulse counting system with an input pulse height gate circuit[1] (comparator) was constructed as shown in Fig.5.10.3.

[1] The circuit was designed by Mr.W.F.Ray in Electrical and Electronic Engineering Department of the University of Nottingham.

Firstly, every input signal detected by the transducer is transmitted to the gate circuit. Then, only the pulse whose peak height is higher than the preset threshold level generates a trigger signal to activate the counter. After all, by changing the preset level from small to large, an accumulated pulse count distribution in pulse height can easily be obtained. The merit of the analog signal treatment is its quickness and accuracy on catching peak pulse height value. For example, to expect a reasonably accurate peak value from a pulse as wide as one micro second, the frequency of ten million counts per second or faster is needed for digital sampling and ten million data points per second must be stored in a computer memory. The minimum duration time of a detectable pulse for the gate circuit with various pulse input voltage is plotted in Fig.5.10.4. The system can count the pulses whose duration time at the half peak is as short as 0.8μs within the input voltage range up to 10V which was the highest input voltage obtained in the present measurements.

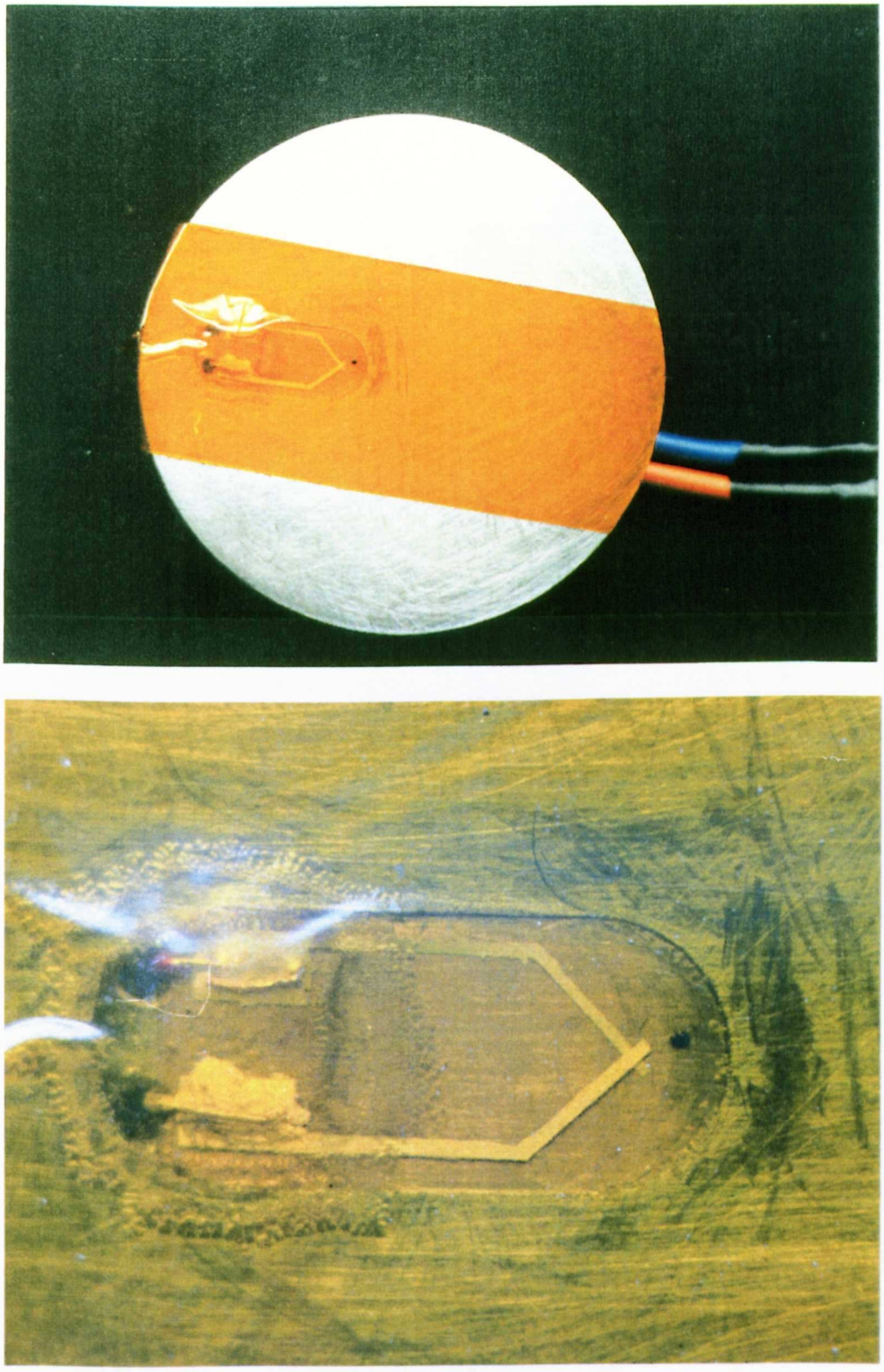

Fig.5.10.1 PVDF piezoelectric pressure transducer (Photograph).

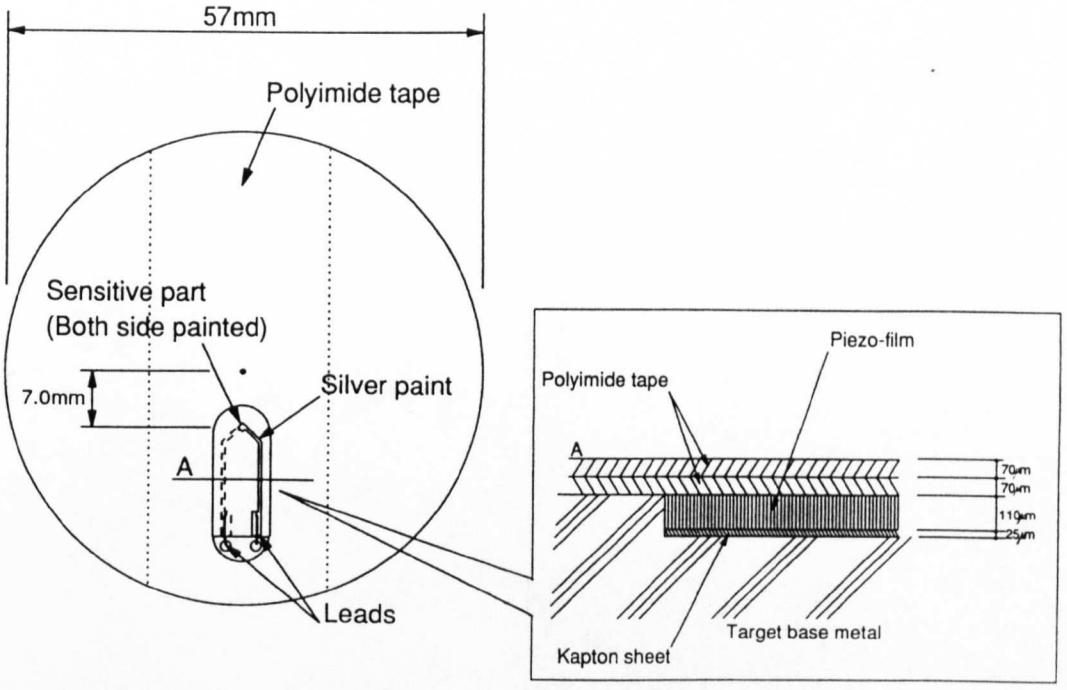

Fig.5.10.2 PVDF piezofilm assembly for a pressure transducer.

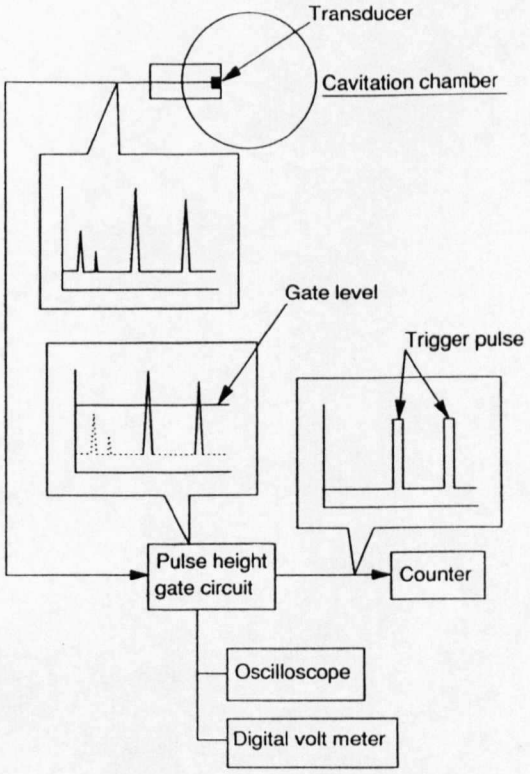

Fig.5.10.3 Diagram of pulse height counting system.

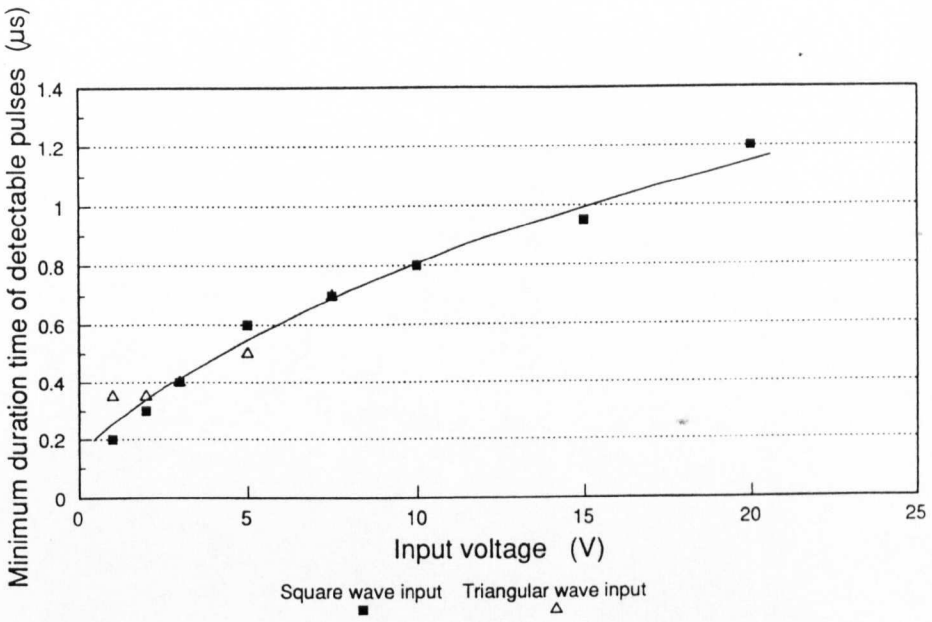

Fig.5.10.4 Variation of minimum countable pulse width for comparator circuit with input voltage.

5.10.2 Calibration

Since it was already known from literature that the duration time of the cavitation loading would be as short as around 1~5μs, dynamic loading with extremely fast rise time has to be used for calibration.

As the first trial in this project, a steel ball dropping method which has been most widely used for calibrating the dynamic pressure transducer so far was tested. Small steel balls of 3.96~7.00mm in diameter were dropped from several different potential heights, 10~50mm, and the maximum force F_{max} was calculated from the equation below.

$$F_{max} = \frac{F_{ave}}{0.64}$$

$$F_{ave} = \frac{m(V_1+V_2)}{\tau}$$

$$V_n = \sqrt{2g \cdot h_n} \qquad (n = 1,2)$$

where m is the mass of the steel ball, g is the acceleration due to gravity and h_1 and h_2 are the potential and the rebound height, respectively. The impact duration time τ is an experimentally obtained value recorded by a digital oscilloscope. This calibration results showed fairly constant values but the rise time to reach the maximum loading was rather slow, around 40~80μs.

In order to get more accurate calibration value from much faster loading, a calibration device using breaking load was developed. Figure 5.10.5 and 5.10.6 show its general view and a drawing of main parts. It consists of a steel horizontal beam with a pencil lead at one end and supported at another end and a bottle hanging at the middle of the horizontal beam. Details are shown in Appendix A4. The transducer is placed right under the tip of the pencil lead and then the centre bottle is gradually filled up with water to provide a load. When water amount reaches the breaking point of the pencil lead, it breaks and slowly accumulated loading on the piezofilm is suddenly released. Such releasing motion is much quicker than the motion of the ball in the dropping test, because this time, virtually there is no inertial mass on it. The rise time of this calibration was 7~8μs which is up to ten times faster than that of the ball dropping method. Moreover, there is no need to keep trying to drop the ball right at the centre of the transducer nor to accurately measure its rebounding height so that

the test procedure can be simpler and easier.

Calibration results obtained by both calibration method, ball dropping and pencil lead breaking, are compared in Fig.5.10.7. Regardless of the rise time difference, they show good agreement. This may suggest that the response of the PVDF piezofilm is constant and reliable at least within this loading magnitude and frequency range. Results of the ball dropping method in Fig.5.10.7 were averaged from three drops. However, scatters of the results of both the ball dropping method and the pencil lead breaking method are within almost same range. This means that the pencil lead breaking calibration can yield more constant results. From these various merits, it was decided to use the breaking method calibration in this measurement.

Since the piezofilm of the transducer is not very tough, it is necessary to use the transducer "protection cover" under the tip of the pencil lead of the calibration device when the calibration load is applied on the transducer. Such a "cover" must be much smaller than the transducer sensitive area to ensure that the loading of the calibration force is within the inside boundary of the sensitive area, and at the same time it must be sufficiently large otherwise it may damage the piezofilm by the large load concentration on the small area. Therefore, in the case when the sensitive area of the transducer is very small, the calibration becomes extremely difficult.

In this project, unfortunately the calibration of very small size transducers, such as 0.140mm^2, 0.301mm^2, 0.777mm^2 and 1.35mm^2, was not able to be achieved, and so the calibration result measured for 8.88mm^2 were directly applied to them together with the exactly same arrangement, cables, adhesives, total capacitance and so on. Since all of the piezofilm were cut from an identical sheet, it can be expected that all the transducers show almost the same calibration values, and hence this treatment may be justified as one of a few practical solutions.

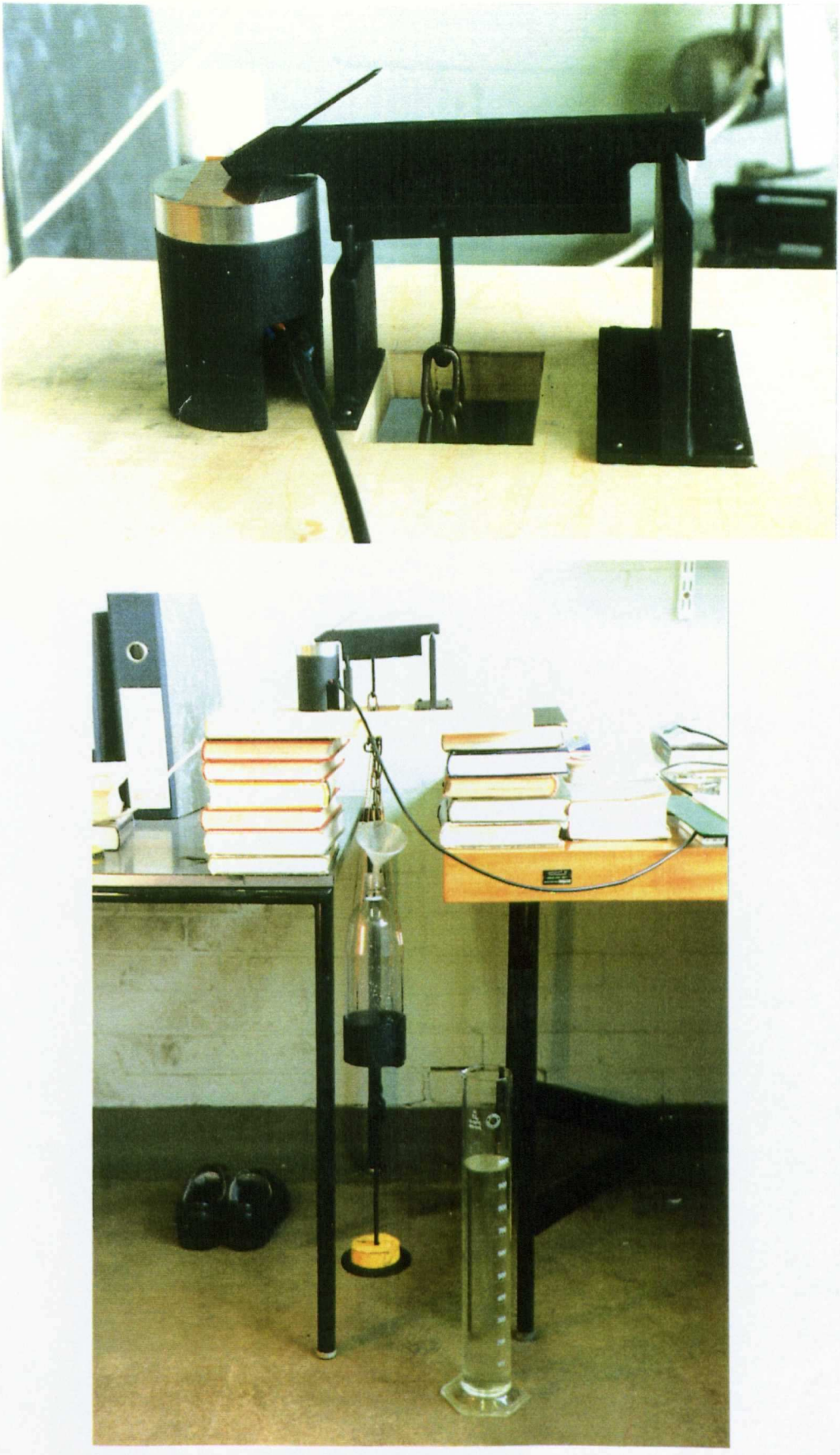

Fig.5.10.5 Calibration apparatus using pencil lead breaking load (Photograph).

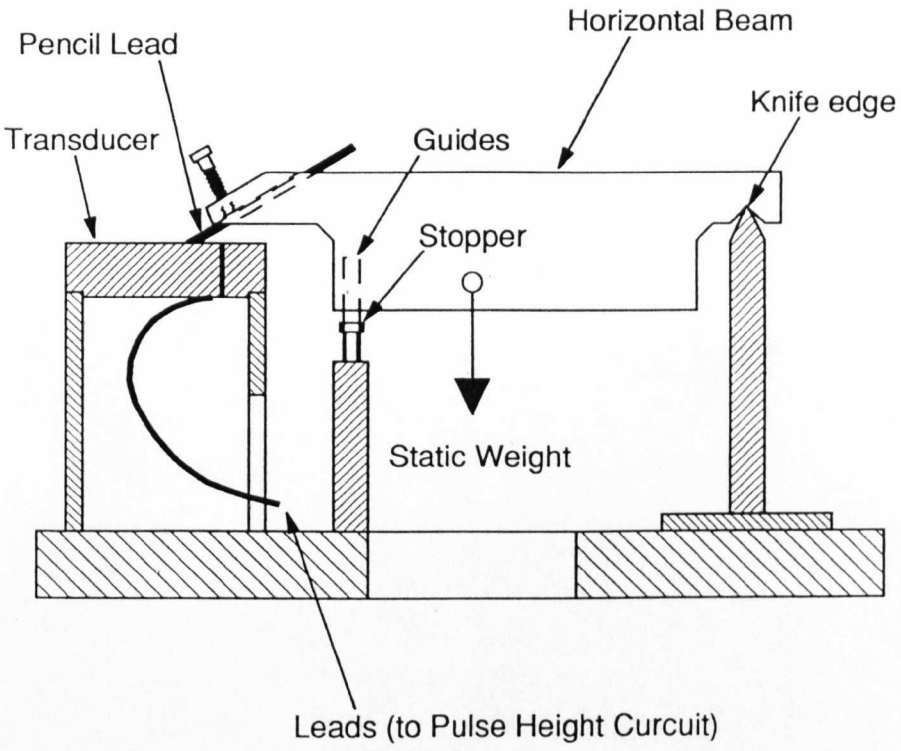

Fig.5.10.6 Calibration apparatus using pencil lead breaking load.

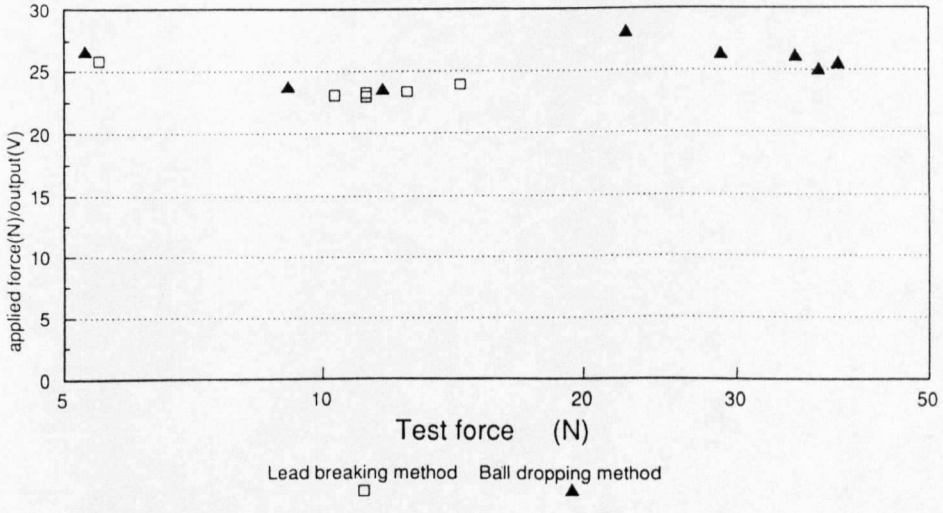

Fig.5.10.7 Comparison of calibration values for PVDF pressure transducer between pencil lead breaking method and ball dropping method.

5.10.3 Testing procedure

Procedures of the pressure pulse height measurements are neither difficult nor time consuming. Before the measurement, the pulse height measurement system consisting of a gate circuit, a counter, a digital oscilloscope and a voltmeter was set up and placed by the test chamber. Then, the pressure transducer was calibrated by the calibration device with all the system and cables connected exactly same as the actual testing condition.

First, the pressure transducer and its holder were mounted in the test chamber and then it was exposed to the cavitating jet with desired pressure condition. The number of loading pulses above the threshold value was counted by the counter. The exposure time was controlled manually and was measured with a timer. This simple routine was repeated several times with a slightly higher pulse height threshold value each time until the pulse counting frequency was decreased to the desired frequency level.

The pulse height measurements were achieved with six different sizes of transducer sensitive area from 0.140mm^2 to 8.88mm^2 for each test condition.

In addition to the pulse height measurement described above, many photographs of each loading pressure pulse on the digital storage oscilloscope were taken, and the shape and the duration time were observed.

Results and discussion of tests listed in Table 5.11.1(a)~(e) will be discussed in Chapter 6~9. Photographs are not included in Table 5.11.1(a)~(e) but will be presented and discussed in an appropriate part in later chapters.

Table 5.11.1(a) List of tests

Upstream pressure (bar)	Downstream pressure (bar)	Cavitation number	Stand off (mm)	Erosion test	Indentation counting	Pulse analysis
80	2.4	0.03	15	▬		
			18	▬	▬	
			20	▬		
			25	▬		
			30	▬		
			35	▬		
			40	▬	▬	▬
			45	▬		
80	3.0	0.0375	13	▬		
			15	▬	▬	
			17	▬		
			20	▬		
			25	▬		
			30	▬		
			35	▬	▬	
			40	▬		

Table 5.11.1(b) List of tests

Upstream pressure (bar)	Downstream pressure (bar)	Cavitation number	Stand off (mm)	Erosion test	Indentation counting	Pulse analysis
100	3.0	0.03	15	▬	▬	
			18	▬	▬	
			20	▬	▬	
			25	▬	▬	
			30	▬	▬	
			35	▬	▬	
			38	▬		
			40	▬	▬	▬
			42	▬		
			45	▬	▬	
			50	▬		

Table 5.11.1(c) List of tests

Upstream pressure (bar)	Downstream pressure (bar)	Cavitation number	Stand off (mm)	Erosion test	Indentation counting	Pulse analysis
120	2.4	0.02	18	▬		
			20	▬	▬	
			22	▬		
			25	▬		
			30	▬		
			40	▬		
			50	▬		
			53	▬		
			55	▬		
			57	▬	▬	
			60	▬		
			65	▬		

Table 5.11.1(d) List of tests

Upstream pressure (bar)	Downstream pressure (bar)	Cavitation number	Stand off (mm)	Erosion test	Indentation counting	Pulse analysis
120	3.0	0.025	15	-		
			18	-	-	
			20	-		
			22	-		
			25	-		
			30	-		
			35	-		
			40	-		
			43	-		
			45	-	-	
			47	-		
			50	-		
			55	-		

Table 5.11.1(e) List of tests

Upstream pressure (bar)	Downstream pressure (bar)	Cavitation number	Stand off (mm)	Erosion test	Indentation counting	Pulse analysis
120	3.6	0.03	15	▬		
			18	▬	▬	
			20	▬		
			22	▬		
			25	▬		
			30	▬		
			35	▬		
			38	▬		
			40	▬	▬	▬
			42	▬		
			45	▬		

5.12 Chronological summary of experimental work

The experimental work of this project was started with cavitation erosion tests. The erosion produced by a submerged water jet from a long orifice nozzle with a nominal diameter of 2.0mm was investigated at various stand off distances.

At first, all the erosion tests were carried out until the results clearly showed the optimum stand off distances where cumulative erosion rate CER was higher than adjacent stand off distances. Then, in order to obtain the maximum cumulative erosion rate (defined as peak erosion rate: PER_C) for each pressure condition, the erosion tests were further continued at only the optimum stand off distances.

Initially, approximately seventy target specimens had been machined for erosion tests from two bars of a 6063-aluminium alloy. After using most of them, two more same aluminium bars were ordered and another set of seventy specimens were prepared from them. Then, it was found, however, that the second set of seventy specimens were slightly harder than that of the first set even after the sufficient annealing of 400°C for 2 hours. Vickers hardness was 29.7±1.9 for the first seventy targets and 34.5±0.9 for the targets used from the second set. Soon, it was decided that both sets would not be mixed up in the same pressure condition, otherwise accurate optimum stand off distances would not be obtained. At last, the second set was used for only the tests with pressure condition of P_1=120bar and P_2=2.4bar. Since the tests at all stand off distances under this pressure condition were carried out using same hardness specimens from only the second set, the difference in hardness between the two sets has no significance to find the optimum stand off distances.

In order to correlate the results of erosion capacity of the cavitating jet obtained from the second set of specimens with the ones from the first set, a simple conversion ratio of 1/0.85 was proposed (see Appendix A1).

$$\Delta W_{standard}(t) = \frac{1}{0.85}\Delta W_{hard}(t)$$

$$CER_{standard} = \frac{1}{0.85}CER_{hard}$$

where $\Delta W(t)$ is the weight loss at exposure time t and "standard" and "hard" mean the first set and the second set of specimens, respectively. All the results for P_1=120bar and P_2=2.4bar presented and discussed in the thesis have been converted by the above

equations.

While conducting erosion tests, high speed photographs of free cavitating jets and wall jets using a stainless steel well polished target were taken.

Indentation counting tests were initially planned at only the optimum stand off distances determined by the erosion tests, but later extended to the other stand off distances for P_1=100bar and P_2=3.0bar. Much care was paid for setting the cavitating jet exposure time in the indentation counting, because if indentations are too much densely populated and consequently some are attached to each other, the image analyzer reads such a pair of indentations as one " large " indentation. More time, however, was paid for getting the good finish for specimen surface, since the material was so soft and the surface to be polished was so large.

Shape of some indentations on these soft specimens was observed using both optical and scanning electron microscope.

In order to carry out the cavitation loading pulse measurements, a small piezoelectric pressure transducer had to be developed to meet the particular requirements as described in Section 5.10, simply because dynamic pressure transducer commercially available at the time of testing was too slow in response, too large in sensitive area or too weak against cavitation damage.

To ensure the high speed response of the designed transducer, a calibration device with breaking load method was also developed. This calibration device provides very quick rise time, 7~8μs, for the calibration loading. Its performance was checked before use by comparing the results with those by widely used ball dropping calibration method.

The cavitation loading pulses were successfully measured for three pressure conditions, P_1=80bar and P_2=2.4bar, P_1=100bar and P_2=3.0bar and P_1=120bar and P_2=3.6bar at the second optimum stand off distance S_{off2}=40mm. However, the pressure transducer developed was not sufficiently tough to perform the similar pressure measurements under more intensive cavitation loading. Particularly, at the first optimum stand off distance, the jet power itself was too destructive for the piezofilm arrangement on the transducer. Therefore, tests at this stand off distance had to be abandoned to preserve the transducer.

The photographs of loading pulses were taken from a display of a digital storage oscilloscope.

Finally, in order to confirm that the downstream pressure P_2 in the chamber

can be regarded as the ambient pressure at damaged area (or bubble collapsing zone) on the target specimen, mean pressure distributions on a flat target were measured under various pressure conditions.

CHAPTER SIX - RESULTS:
Cavitating jet and damage produced

6.1 Introduction

6.2 High speed photography

6.3 Mean pressure distribution

6.4 Damage produced on aluminium

6.5 Conclusions

6.1 Introduction

The cavitating jet has been used as a useful cavitation source to test relative material resistance to cavitation erosion by Lichtarowicz, Kleinbreuer and other investigators. Since simply the size of the nozzle and the downstream chamber in the present test rig is much larger than the apparatus used by them, it is possible to obtain some more detailed information about a cavitating jet and the damage produced.

In this chapter, the results of high speed photography of cavitating jets, measurements of mean pressure distribution on a disc target and surface profile measurements of damage patterns on soft aluminium alloy specimen will be presented.

In order to visualize the structure of a cavitating jet, a number of high speed photographs were taken for various pressures in the present test chamber. Some examples of the free cavitating jets are shown in Fig.6.2.2. They were photographed with a 35mm camera with high speed flash from the opposite side of a camera as shown in Fig.6.2.1. Dark shadows are cavitating parts, i.e., bubble clusters, which reflect the flash light so that the light cannot penetrate. In the case with long orifice nozzle, the jet is already intensively cavitating at the inlet edge of the nozzle. When a jet is submerged, a large number of vortices are generated at a shear layer zone around the jet and the cavitation is maintained inside these vortices. They form cavitation bubble clusters and are transported to downstream region with flow. At some distance when the vortices lose the power to maintain sufficiently low pressure inside, they must collapse and disappear. At their end tale, cavitation clouds seems like sets of short strings rather than large portion of pack of bubbles. In Fig.6.2.2 (a) and (b), the jet itself clearly shows the corkscrew type movement which is also observed as a fluctuation of a jet in a two dimensional plane simulated by Shimizu et al. [1990] (see Fig.4.6.6).

As explained in Chapter 4, cavitating jet length is affected by cavitation number σ defined as

$$\sigma = \frac{P_2}{P_1}$$

The cavitating jet lengths from nozzle inlet to end tail as indicated in Fig.6.2.2 were measured from photographs for various pressures ranging P_1=80~120bar and P_2=2.4~3.6bar. The results are normalised with respect to the effective nozzle diameter d_e and plotted with cavitation number in Fig.6.2.3.

The effective nozzle diameter is defined as

$$d_e = d \cdot \sqrt{C_d}$$

where d is nozzle diameter and C_d is the coefficient of discharge. In this case, both values are d=2.08mm and C_d=0.614 and so the effective nozzle diameter is

d_e=1.63mm. Although the number of data points is limited, the cavitating jet length are apparently found to be related with the cavitation number σ. The relation between the average jet length l_j and cavitation number σ seems to be expressed as

$$\frac{l_j}{d_e} \propto \sigma^{-h_1}$$

where the exponential index h_1 is obtained approximately $h_1 \approx 1$.

When a solid object is exposed to the cavitating jet, the object can be damaged. For the purpose of cavitation erosion testing, a flat disc type target placed with a right angle to the jet is used as the specimen. High speed photographs of such impinging jets are shown in Fig.6.2.4. A stainless steel disc was used as the target. At the time these photographs were taken, there was no erosion found on the surface. The pressure condition in this case is P_1=100bar and P_2=3.0bar and stand off distance ranges from S_{off}=15~50mm. Cavity clouds are transported with the jet and impinge the centre of the target. Then the cavities and the wall jet radially spread over the surface of the target. During these process, some cavitating bubbles, mostly located inside the jet collapse in higher pressure zone at the stagnation region, but others are passing outside the stagnation region to collapse further downstream. These bubbles are responsible for erosion on the target. At smaller stand off distance, the cavity cloud is able to cover large area of the target surface, and the amount of cavities found on the surface decreases with increase of stand off distance. The cavity cloud on the target gradually becomes to look more like a single ring cavitation, which probably consists of numerous small cavities, with the increase of the stand off distance. These rings are seen in photographs at relatively larger stand off distance in Fig.6.2.4. Since the images of such ring cavities are reflected in the well polished surface of the target, it is obviously found that generally there is a water gap between the ring cavities and the target surface. It is possible to estimate the distance between the ring cavities and the surface from photographs in Fig.6.2.4 and from some other photographs taken at the same pressures. Figure 6.2.5 shows the distribution of the distance (h) normalised with the effective nozzle diameter (d_e=1.63mm), h/d_e, with dimensionless radial distance from the centre of the jet, r/d_e. The cavity clouds cover the target surface so densely that the height of ring cavities cannot be measured at stand off distance shorter than S_{off}=20mm. The actual heights range approximately h≈0.3~1.5mm for r/d_e=2~12. It is clearly found that the gap between the cavitation

clouds and the surface increases with the distance from the centre of exposure.

The structure of an wall jet was investigated by Bradshaw and Love [1961]. They used an air jet from a cylinder tube whose diameter is d=1in. The corner of the inlet edge of the tube is rounded. The Reynolds number calculated from the nozzle diameter in their measurements, R_e=1.8x10^5, is similar to the one in the present tests (R_e=2.1~2.5x10^5) and their stand off distance normalised by nozzle diameter S_{off}/d=18, is also within the range of S_{off}/d_e=8.0~39.9 (S_{off}=13~65mm) for the present tests. Therefore, although the detailed configuration of the source of the impinging jet (a tube, rather than long orifice nozzle) is slightly different from the present test rig, their results are considered to be comparable to the present cases.

The thickness of the wall jet, $\delta_{0.5}$, was defined as the distance from the wall surface to the point where the mean velocity is half of its peak velocity. The thickness of the wall jet, $\delta_{0.5}$, and the wall jet velocity profile were experimentally obtained by Bradshaw and Love [1961] as shown in Figs.6.2.6 and 6.2.7, respectively. The peak wall jet velocity, U_j, normalised with the velocity of jet just before impingement, U_{j0}, is also plotted in Fig.6.2.6. The wall jet thickness $\delta_{0.5}$ is smallest around the stagnation area up to r/d_e=5 and then increases with the radial distance. The maximum wall jet velocity U_j decreases rapidly. The shapes of the velocity profiles are more or less same at various radial distances in Fig.6.2.7 and so the location of the peak wall jet velocity in the profile seems also almost constant, which is at the 20% of the wall jet thickness $\delta_{0.5}$ above the surface.

In order to compare these results concerning the structure of the wall jet, loci of the thickness $\delta_{0.5}$ and the peak wall jet velocity estimated as 20% of $\delta_{0.5}$, both normalised with nozzle diameter, are also drawn as a solid line and as a broken line in Fig.6.2.5, respectively. In general, ring cavities are distributed just below the wall jet thickness $\delta_{0.5}$ but much higher than the locus of the peak wall jet velocity, 0.2x$\delta_{0.5}$. This indicates that the ring cavities shown in photographs are likely to be transported outside the main stream of the wall jet.

Didden and Ho [1985] clearly observed the secondary vortex on a flat surface produced by an air impinging jet as illustrated in Fig.6.2.8. However, such a secondary vortex was not observed in photographs in Fig.6.2.4. One of the reasons for this can be that Reynolds number of their air jet (R_e=1.9x10^4) is much lower than the one in the present tests (R_e=2.1~2.5x10^5). Moreover, from the locus of the peak velocity of the wall jet in Fig.6.2.5, the size of the secondary vortex can be estimated

to be as small as 0.1mm in diameter. Therefore even if such vortex has sufficient power to form cavitation inside itself, it might be practically difficult to find such a small vortex near the surface of the target in photographs such as Fig.6.2.4.

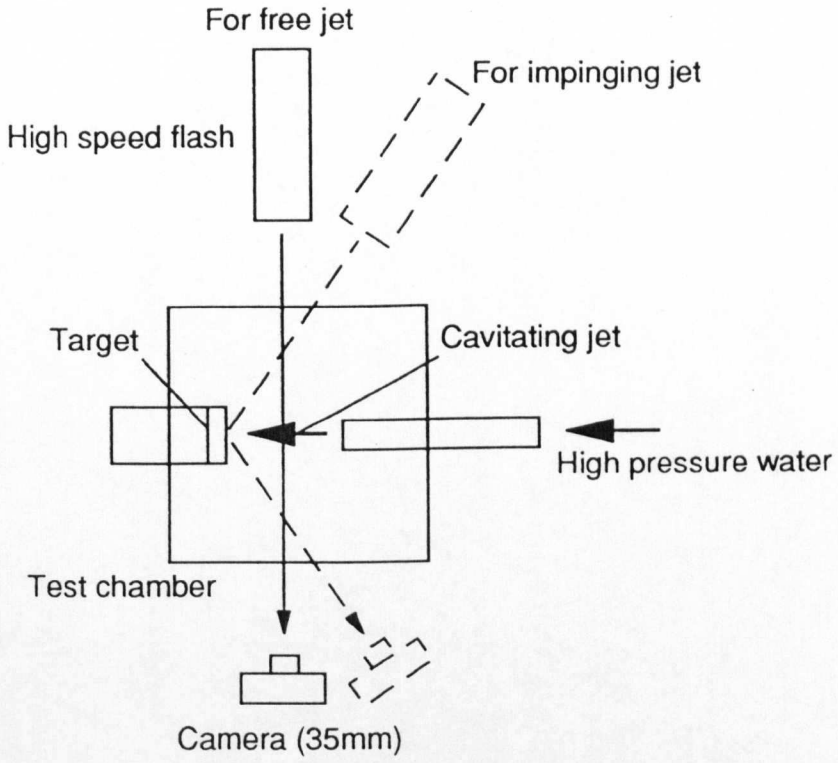

Fig.6.2.1 Camera and high speed flash arrangement.

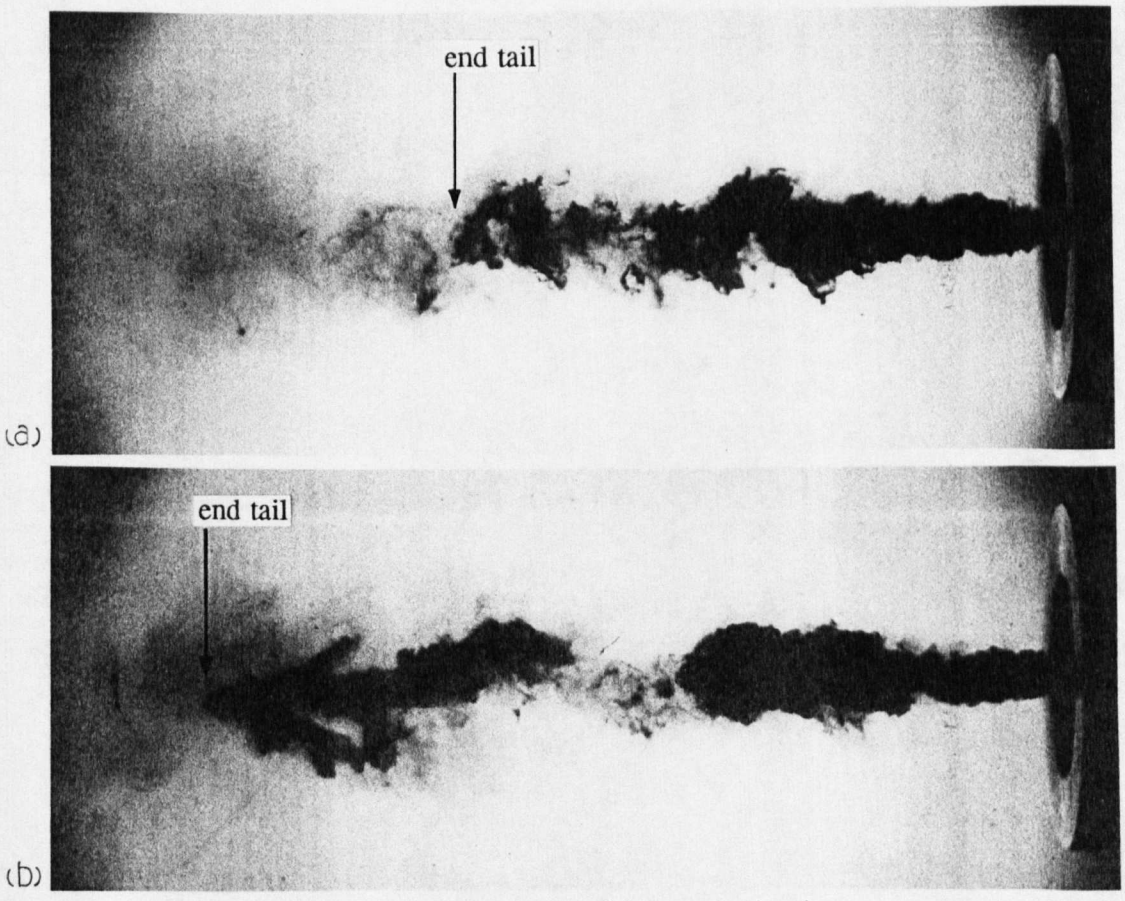

Fig.6.2.2 High speed photographs of free cavitating jets.
(a) P_1=120bar, P_2=3.0bar, σ=0.025; (b)P_1=120bar, P_2=2.4bar, σ=0.02.

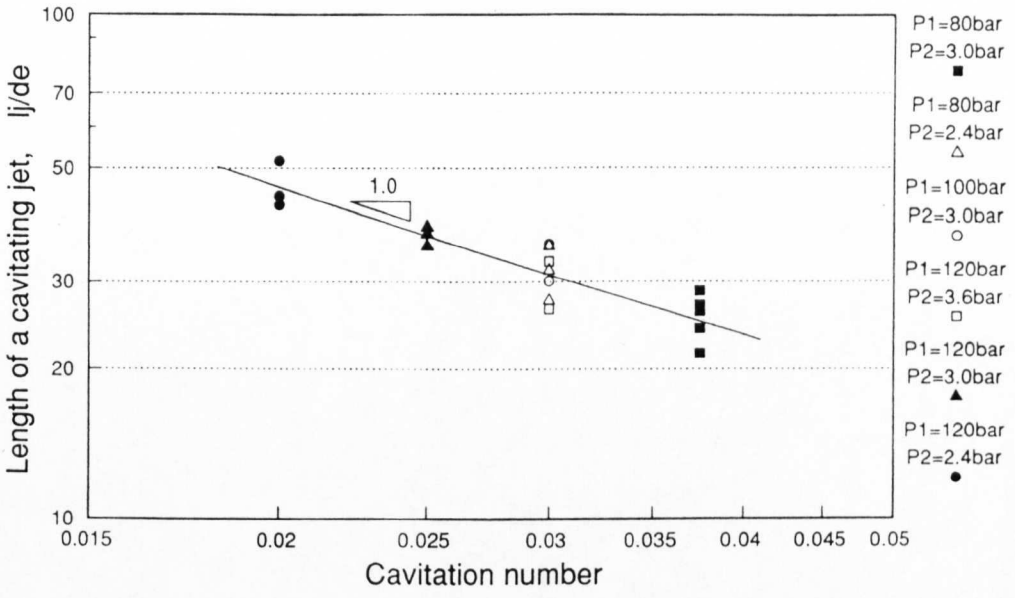

Fig.6.2.3 Variation of cavitating jet length with cavitation number.

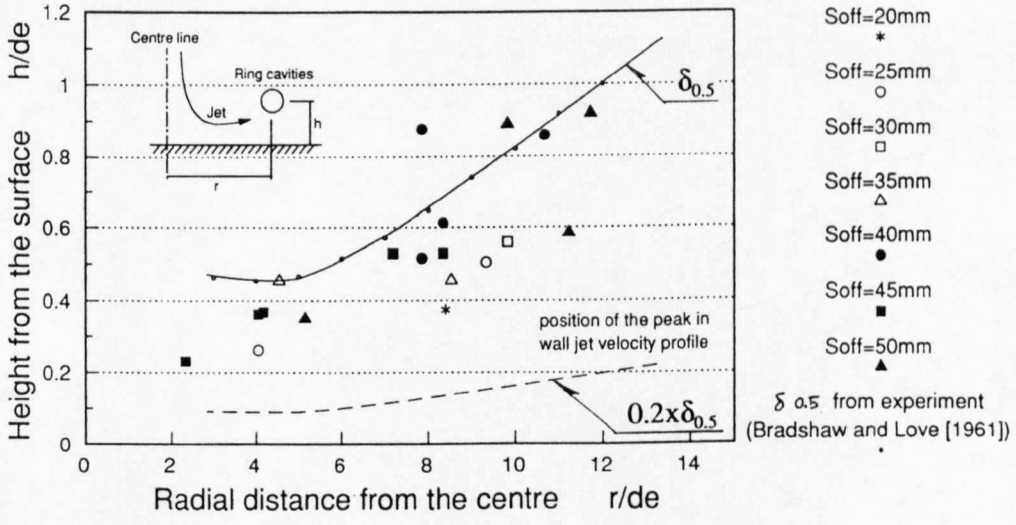

Fig.6.2.5 Distribution of ring cavities found in high speed photographs of cavitating wall jets. P_1=100bar, P_2=3.0bar.

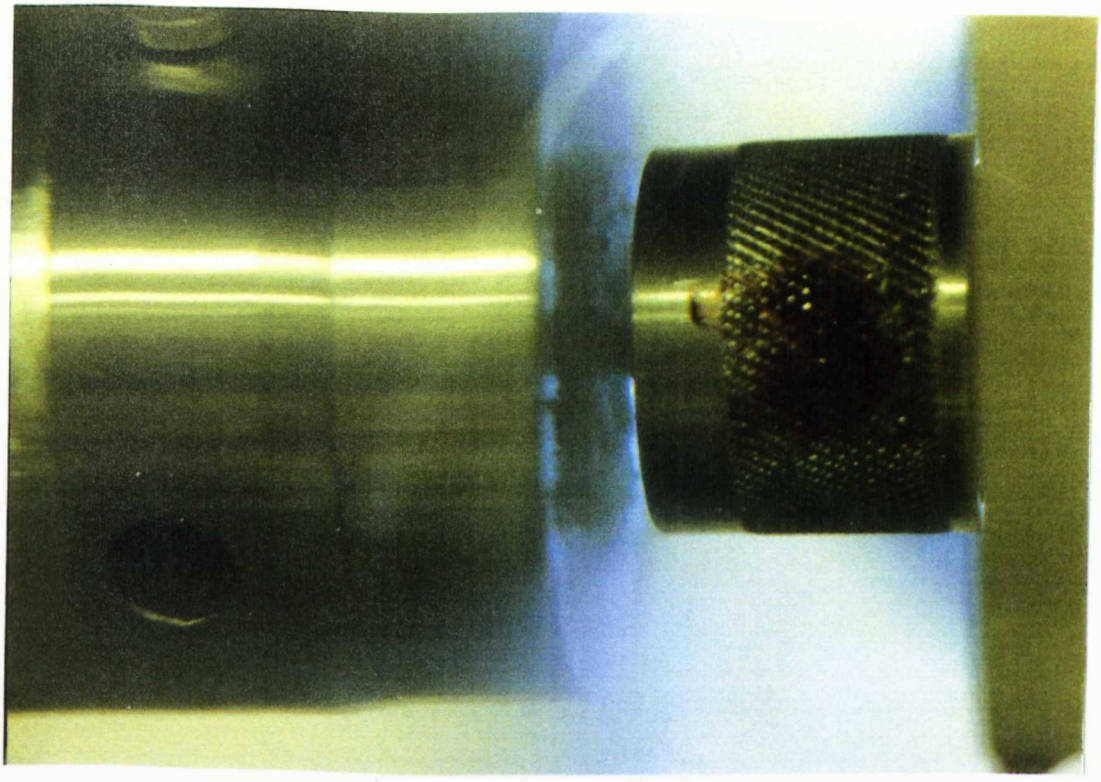

(a)

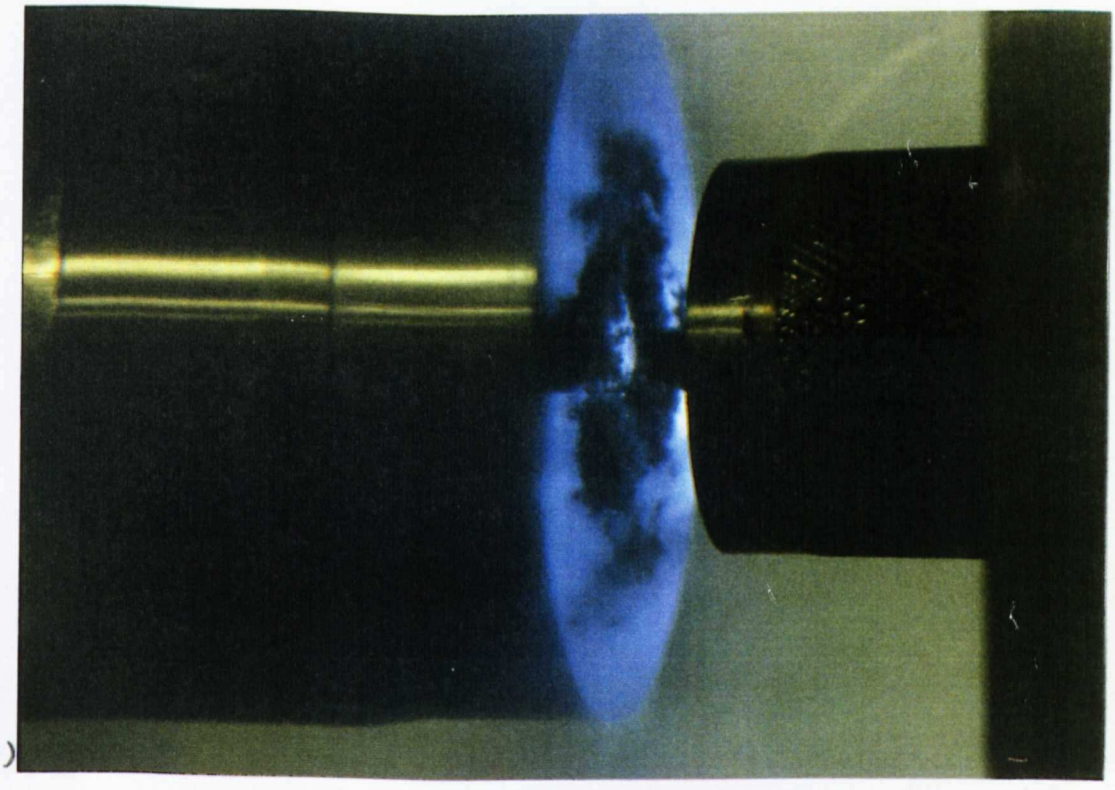

(b)

Fig.6.2.4 High speed photographs of cavitating jets impinging a flat target. P_1=100bar, P_2=3.0bar, σ=0.03. (a) S_{off}=15mm, (b) S_{off}=18mm.

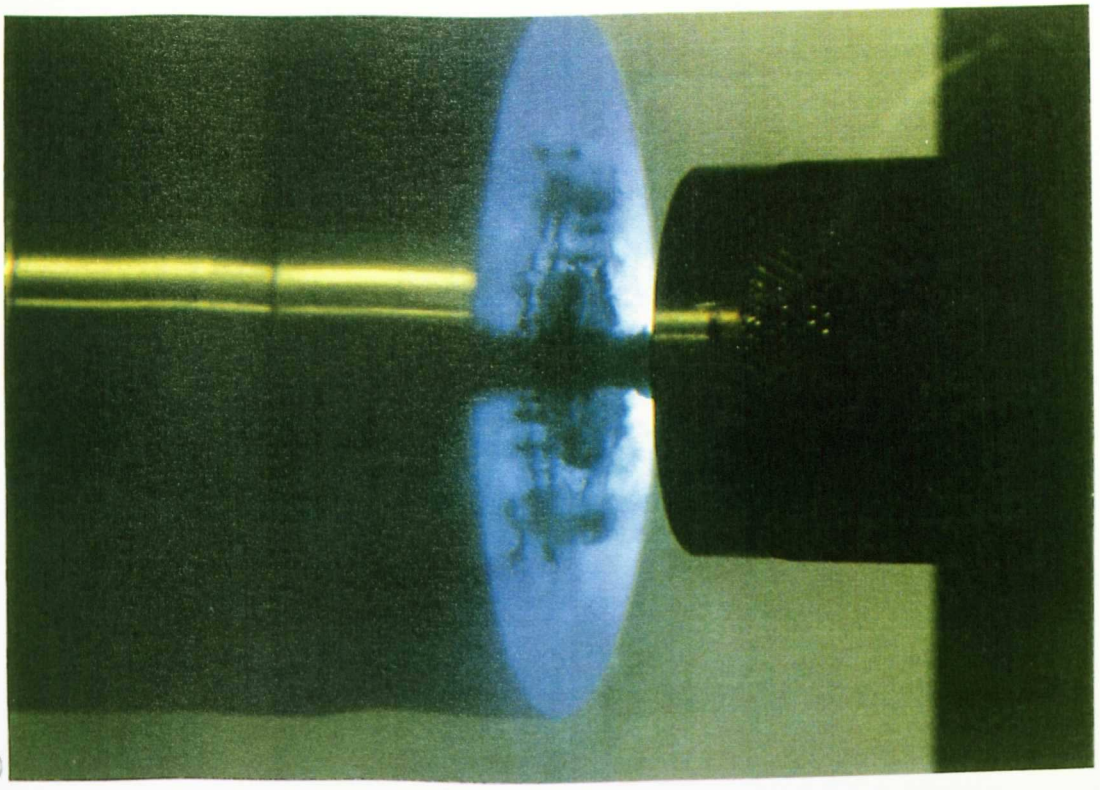

(c)

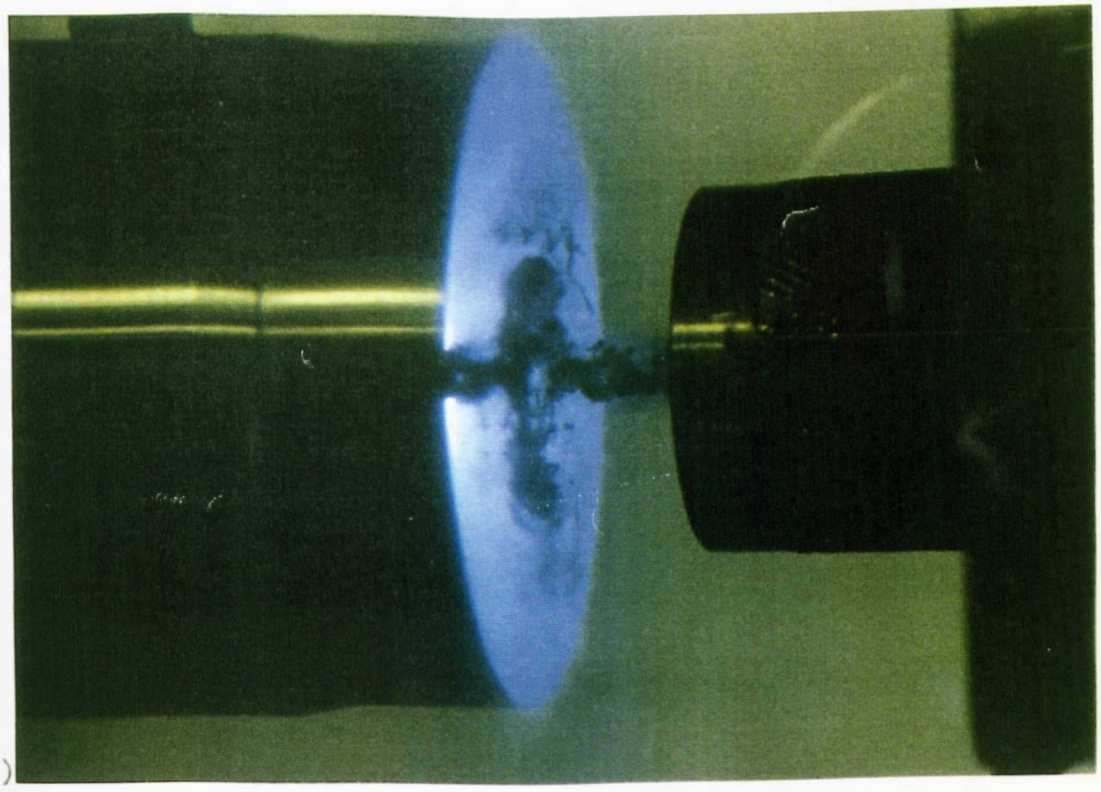

(d)

Fig.6.2.4 High speed photographs of cavitating jets impinging a flat target. P_1=100bar, P_2=3.0bar, σ=0.03. (c) S_{off}=20mm, (d) S_{off}=25mm.

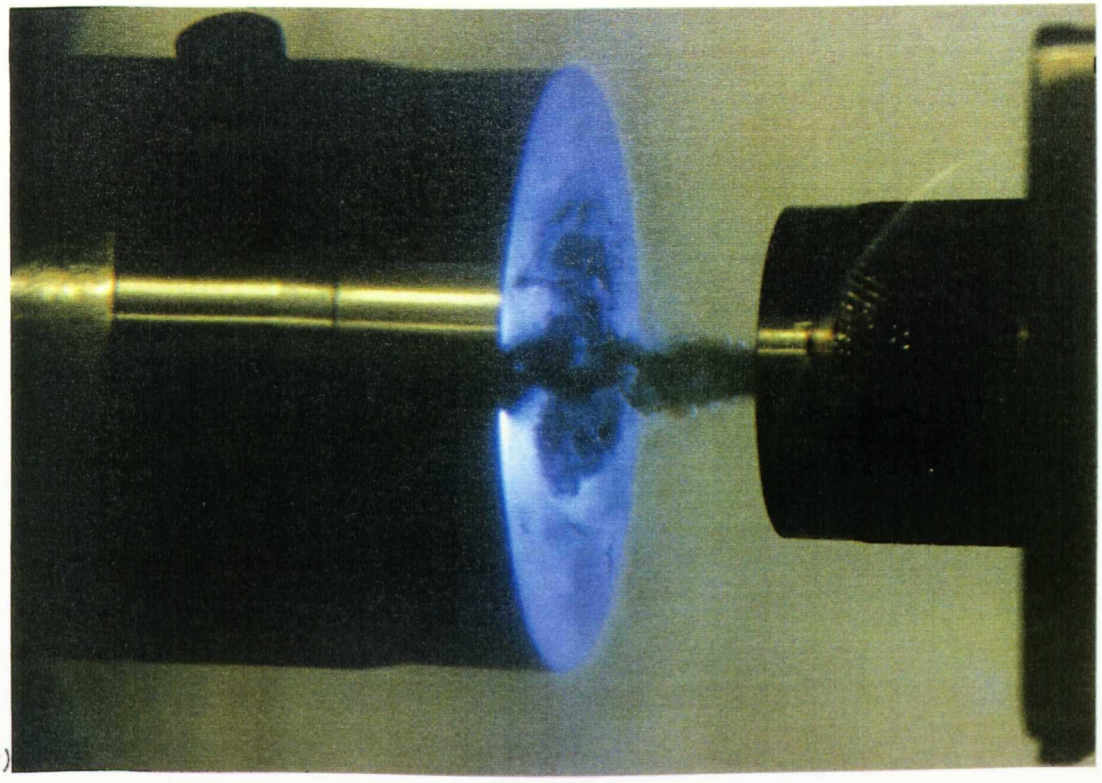

(e)

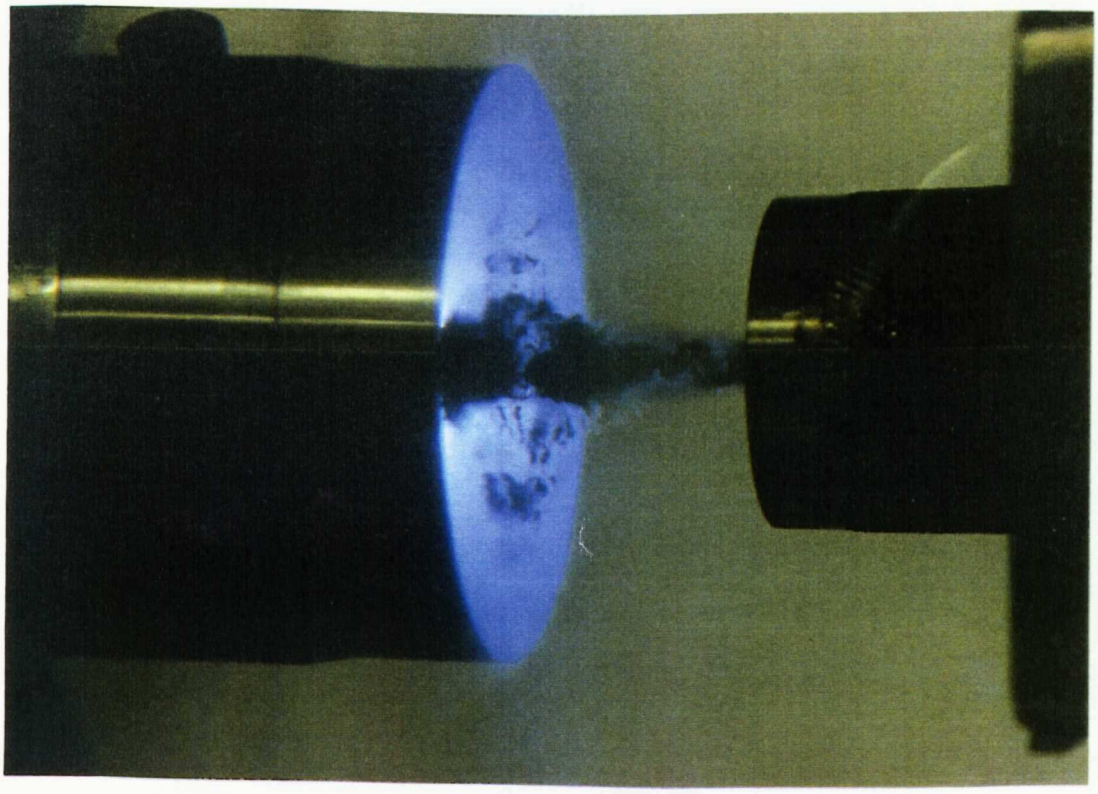

(f)

Fig.6.2.4 High speed photographs of cavitating jets impinging a flat target. P_1=100bar, P_2=3.0bar, σ=0.03. (e) S_{off}=30mm, (f) S_{off}=35mm.

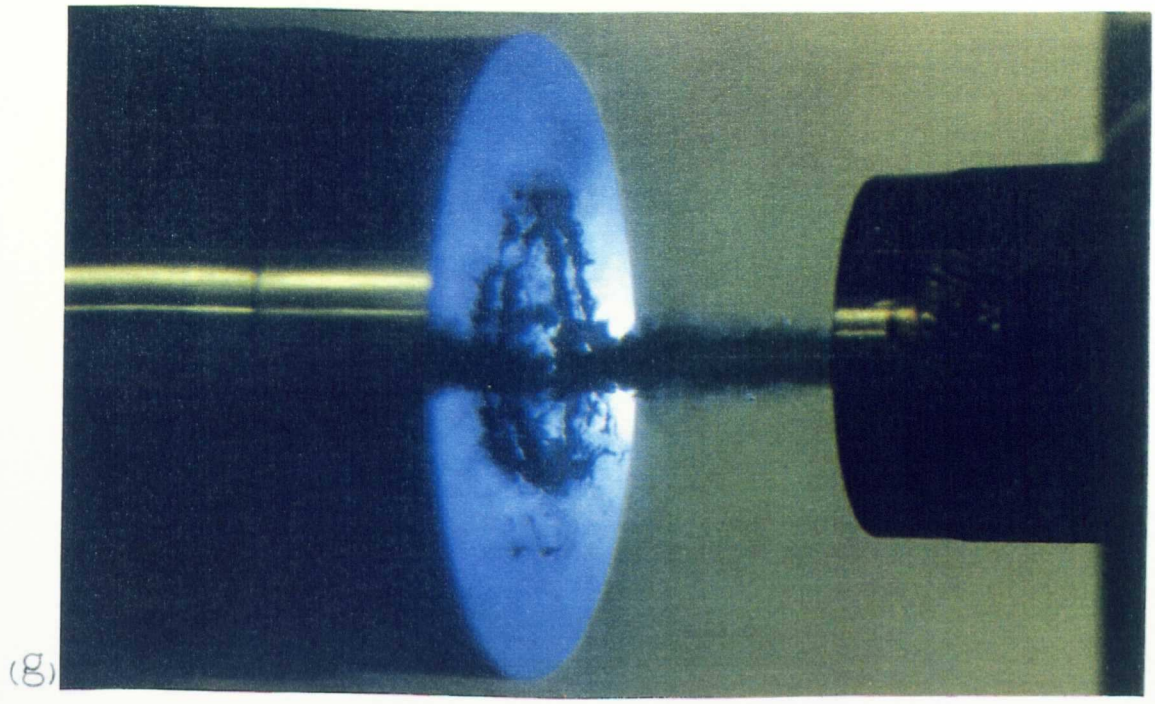

(g)

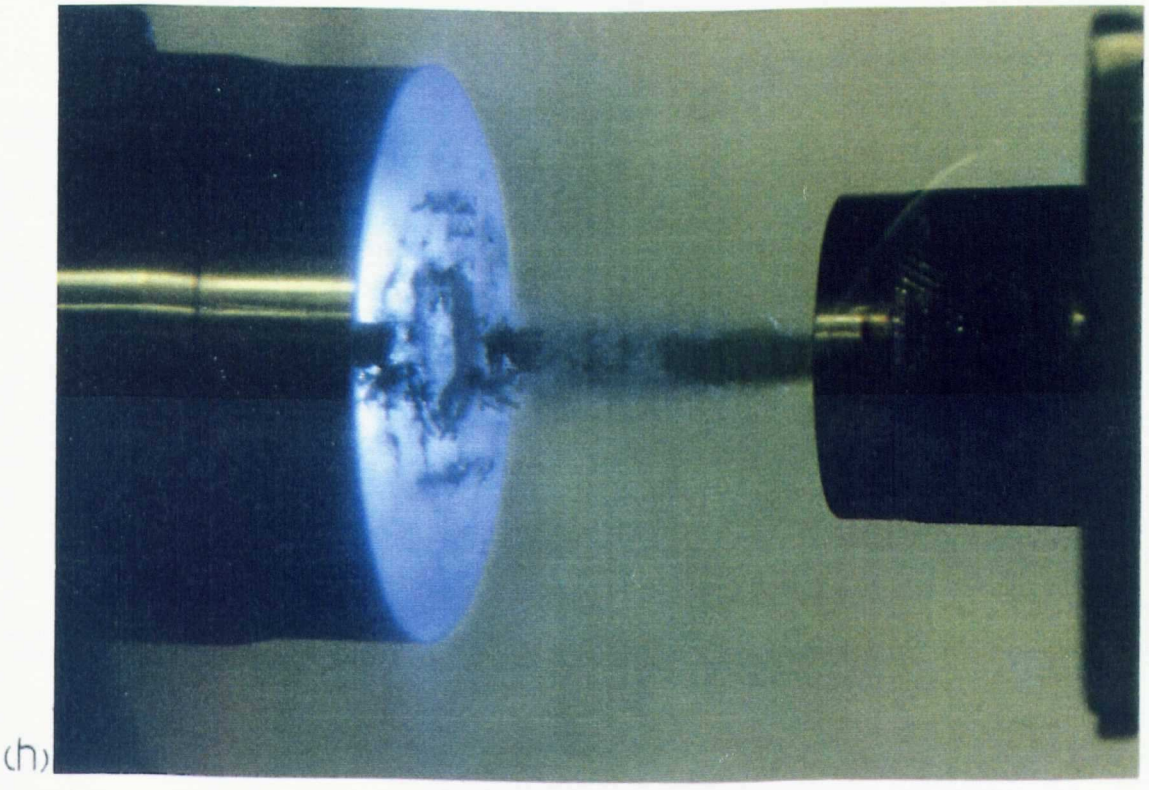

(h)

Fig.6.2.4 High speed photographs of cavitating jets impinging a flat target. P_1=100bar, P_2=3.0bar, σ=0.03. (g) S_{off}=40mm, (h) S_{off}=50mm.

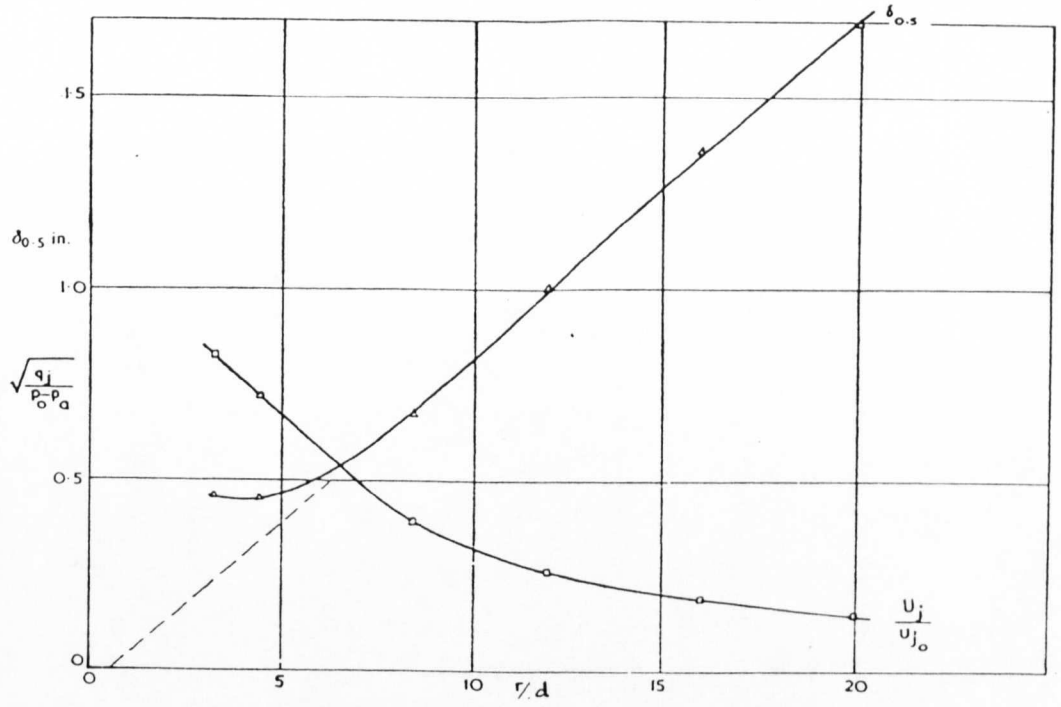

Fig.6.2.6 Radial wall jet velocity and thickness.
(from Bradshaw and Love [1961])

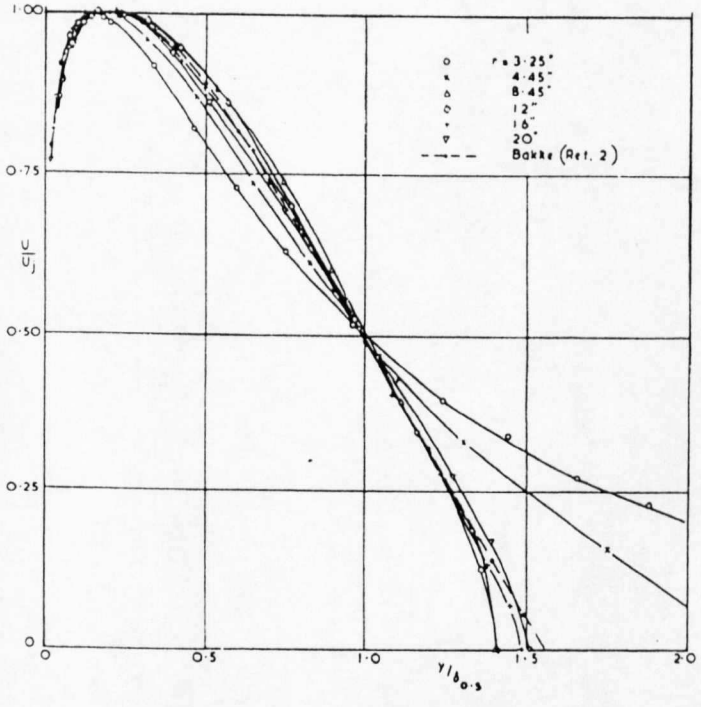

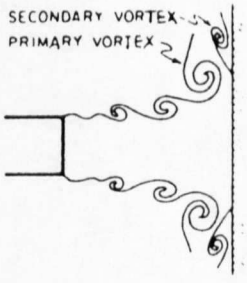

Fig.6.2.7 Wall jet velocity profiles at different radii.
(from Bradshaw and Love [1961])

Fig.6.2.8 Primary and secondary vortex produced by a wall jet.
(from Didden and Ho [1985])

It is important to know the mean pressure distribution on the target surface produced by the cavitating jet to be able to understand cavitation damage on the surface. Although many experimental and theoretical investigations on the structure of a free and impinging air jet have been conducted, there has been no experimental data on cavitating jets available as far as the author's knowledge.

It can be expected that the jet flow and so the distribution of velocity and pressure can be affected by cavitation, but how does the cavitation change them? Figure 6.3.1 shows the mean pressure distribution due to a cavitating jet on a flat target for pressure conditions, P_1=100bar and P_2=3.0bar (σ=0.03), with variation of stand off distances, S_{off}=15~50mm. Small size pressure taps (0.4mm in diameter) drilled on the target were used to measure these data as explained in Chapter 5. Unfortunately the axis of the high pressure supply pipe is inclined at a small angle to the axis of the specimen holder, and so the peaks of the pressure distribution for each stand off distance are not located exactly at the centre of the target. (However, all the tests in this project have been carried out without any correction or adjustment, since the distance of this "off centre", about 0.8~1.0mm at most stand off distance, and the angle, about 0.3 degree, can be regarded to be negligible for the other tests.) The high pressure zone at the stagnation region is limited within the radius of ±3~4mm from the pressure peak. Outside the stagnation area, the pressure distribution is flat and the pressures are just slightly above the downstream pressure P_2. The peak pressure decreases with increase of stand off distance.

In order to estimate the effect of cavitation, the mean pressure distribution for constant upstream pressure P_1=120bar and stand off distance S_{off}=40mm with different cavitation number σ=0.02~0.03 (P_2=2.4~3.6bar) are plotted in Fig.6.3.2. The pressures are normalised with the upstream pressure P_1 after subtracting P_2 to remove the ambient pressure from measured values. The smaller the cavitation number is, the higher the peak pressure is obtained, or in other words, the less the peak pressure is attenuated. It is probably because the friction between the jet and the ambient liquid at the mixing zone can be reduced by cavitating bubbles. Figure 6.3.3 is the mean pressure distribution for three different pressure conditions with constant cavitation number σ=0.03, P_1=80bar and P_2=2.4bar, P_1=100bar and P_2=3.0bar and P_1=120bar and

P_2=3.6bar at the stand off distance S_{off}=18mm and 40mm. For all the pressure combinations, normalised mean pressures show the same distribution on one line. Figure 6.3.4 shows the axial decay of the highest pressure at stagnation region of cavitation impinging jet. The pressure decay of an air jet which was experimentally obtained by Donaldson et al. [1971] is also presented as an example of non-cavitating flow. Since their results are originally expressed as a form of a dimensionless stand off distance normalised by nozzle diameter, S_{off}/d, they are plotted in the present scale in Fig.6.3.4 after being multiplied by the present effective nozzle diameter, d_e=1.63mm. Reynolds number in their measurements is $R_e=1.7\times10^5$. It is apparent in Fig.6.3.4 that the decay of stagnation pressures is clearly dependent of cavitation number. The jet pressure is less attenuated with smaller cavitation number through the stand off distances, while the attenuation is same for all three different upstream pressures P_1=80~120bar but with the same cavitation number σ=0.03.

Then, it is confirmed from above results and results about cavitating jet length in the previous section that the cavitation number is an appropriate parameter to control the effects of cavitation on the mean pressure distribution of a jet. If the cavitation number is maintained constant the structures of cavitating jets, or the intensity of cavitation, are similar for various pressure conditions.

Similar effects have been reported by Yahiro and Yoshida [1974]. They have utilized the effects to improve the excavation capacity of a submerged jet. In their method, the submerged jet is surrounded by a shroud of an air jet instead of cavitating bubbles. A special nozzle (diameter: 2.0mm) was designed as shown in Fig.6.3.5 and the air was discharged from a slit of a concentric circle around the jet. The stagnation pressure decay of the jet with various flow rate of discharged air is shown in Fig.6.3.6. In the same way of cavitating jets, the decay is largely affected by the amount of air discharged; the more the amount of air, the less the pressure is attenuated.

From the ratio of wall jet velocity to the velocity just before the impingement U_j/U_{j0} in Fig.6.2.6 and the decay of stagnation pressures in Fig.6.3.4, it is possible to calculate the peak wall jet velocity for a particular pressure condition at particular stand off distance. For example, the stagnation pressure of cavitating jet for P_1=100bar and σ=0.03 (P_2=3.0bar) at S_{off}=40mm is about 23bar and so U_{j0} becomes 68m/s. The ratio U_j/U_{j0} can be read about 0.74 for r=7.0mm (r/d_e=4.3) on the target in Fig.6.2.6, and finally the peak wall jet velocity is estimated about 50m/s. This is

about 35% of the original jet velocity of P_1=100bar.

Geometric conditions used above, such as S_{off}=40mm and r=7.0mm, are the most damaging condition for σ=0.03 and will be explained later in following chapters.

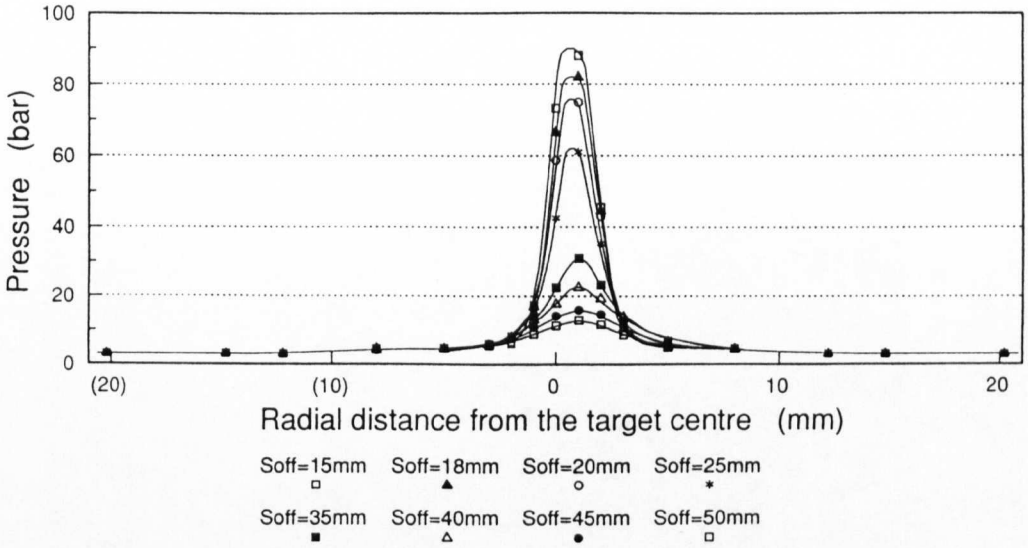

Fig.6.3.1 Mean pressure distributions on a target produced by a cavitating jet. P_1=100bar, P_2=3.0bar, σ=0.03, S_{off}=15~50mm.

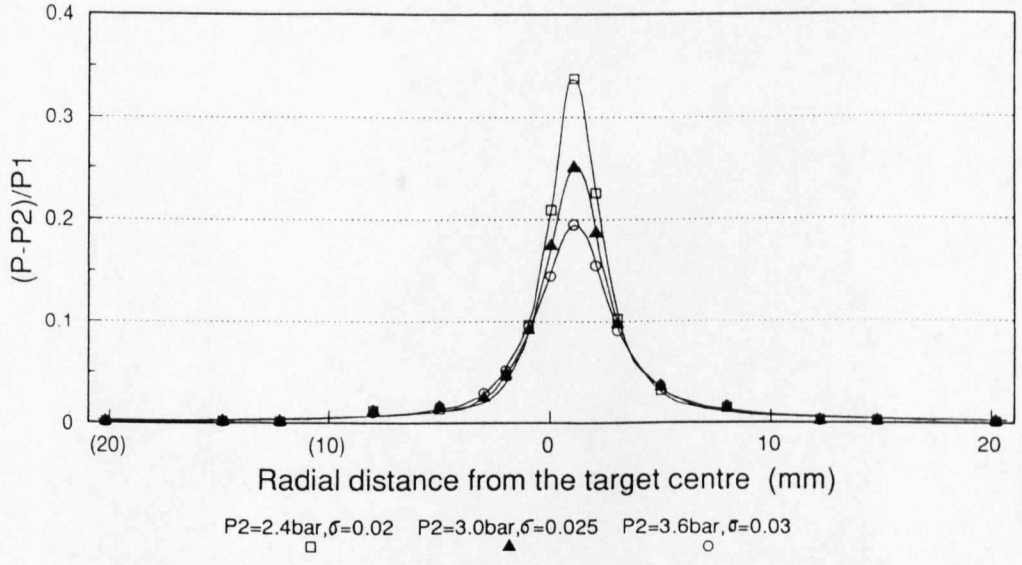

Fig.6.3.2 Effect of cavitation number σ (downstream pressure P_2) on normalized mean pressure distributions on a target produced by a cavitating jet. P_1=120bar, P_2=2.4, 3.0 and 3.6bar, σ=0.02, 0.025 and 0.03, S_{off}=40mm.

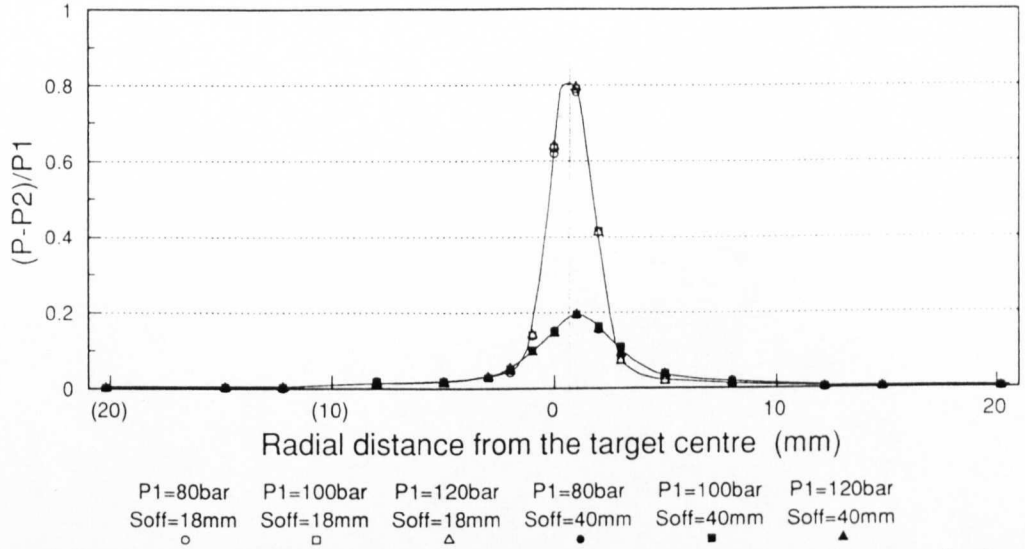

Fig.6.3.3 Normalized mean pressure distributions on a target produced by a cavitating jet with constant cavitation number σ.
P_1=80~120bar, P_2=2.4~3.6bar, σ=0.03, S_{off}=18 and 40mm.

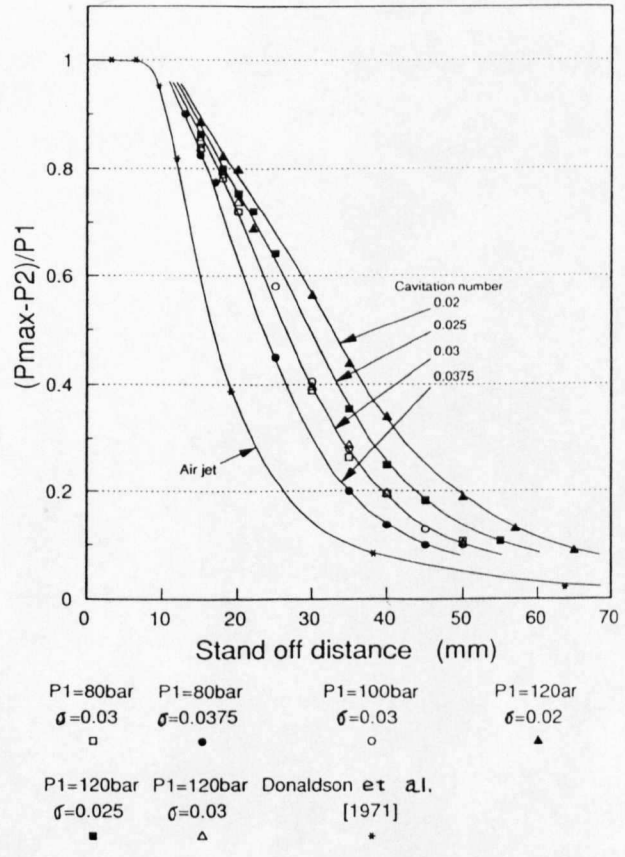

Fig.6.3.4 Effect of cavitation number σ on the decay of the normalized stagnation pressure with stand off distance.
P_1=80~120bar, σ=0.02~0.0375.

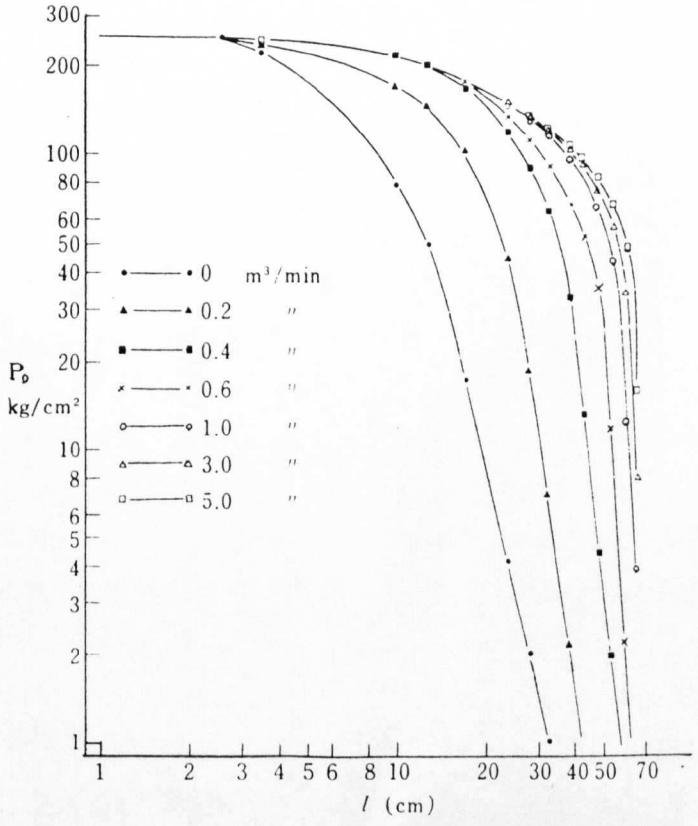

Fig.6.3.6 Effect of air discharge on the decay of stagnation pressure. (from Yahiro and Yoshida [1974])

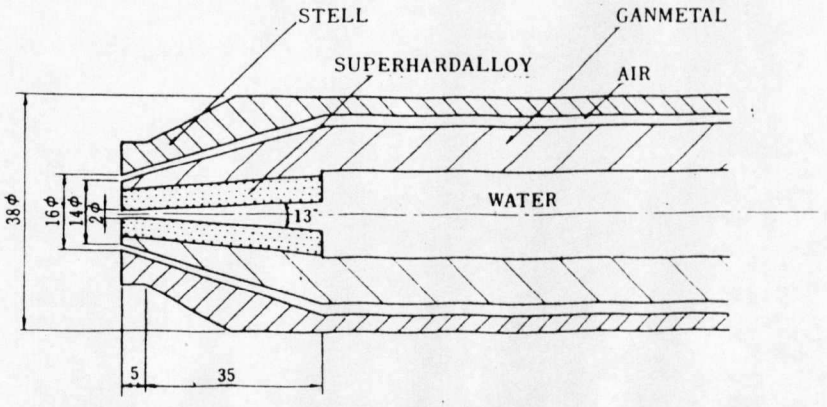

Fig.6.3.5 Section of nozzle (from Yahiro and Yoshida [1974]).

Photographs of initial cavitation erosion damage and its subsequent progress on the surface of 6063-aluminium alloy which was annealed at 400°C for 2hrs and then cooled at room temperature is presented in Fig.6.4.1. Tests were conducted with P_i=120bar and σ=0.03 at two optimum stand off distances, the first optimum stand off distance S_{off1}=18mm and the second optimum stand off distance S_{off2}=40mm. (Discussion about the optimum stand off distances will be in Chapter 7.) In the case of ductile material target like 6063-aluminium alloy used in the present tests, each damage produced by cavitating bubble collapse takes place as a form of plastic deformation; i.e., indentations. As reported by other investigators (Lichtarowicz, Kleinbreuer, Yamaguchi and so on), those damages are characteristically distributed in a ring shape at S_{off2}=40mm and in two rings shape at S_{off1}=18mm. There is almost no damage observed at the centre part of the target. Figure 6.4.2 shows the profile of the surface damage of same specimens at the same exposure time as in Fig.6.4.1, together with the mean pressure distributions (the same one as shown in Fig.6.3.1). It is clearly seen that the damaged area starts just outside the stagnation region.

From the facts obtained above, the behaviour of cavitating bubbles and their damaging process may be explained as follows.

(1) When cavitating bubbles are located inside the impinging jet and are transported into the high pressure zone of the stagnation region, they probably collapse well before the target and cannot damage the surface.

(2) Cavitating bubbles located outside the impinging jet do not need to pass through such a high pressure zone and so they can survive. They are transported outside the wall jet and collapse somewhere outside the stagnation area.

(3) Some of the bubbles which are outside the jet can collapse on the target surface where the wall jet thickness and so the distance from the cavities to the target surface is smallest. Only the cavities which collapse at the sufficiently small distance to the target surface are able to damage the target.

Beyond this point, the wall jet thickness increases with radial distance from the impingement centre, and it becomes more probable for remaining cavities to collapse too far to damage the surface.

There are two erosion rings at S_{off}=18mm and erosion at the outer ring (the second ring) is much less severe than that at the inner ring (the first ring). The mechanism to produce the second ring has not been fully understood yet, though it is considered that the cavitating jet flow on the target surface may be significantly affected by proximity of the nozzle holder surface at the small stand off distance.

The cavitation damage proceeds with increase of surface roughness but it is not accompanied by actual material loss during the incubation period. Then, after the sufficient accumulation of plastic deformation, the weight loss begins and the damage increases with time. Detailed investigation on the cavitation erosion and the initial indentation will be presented in Chapter 7 and 8.

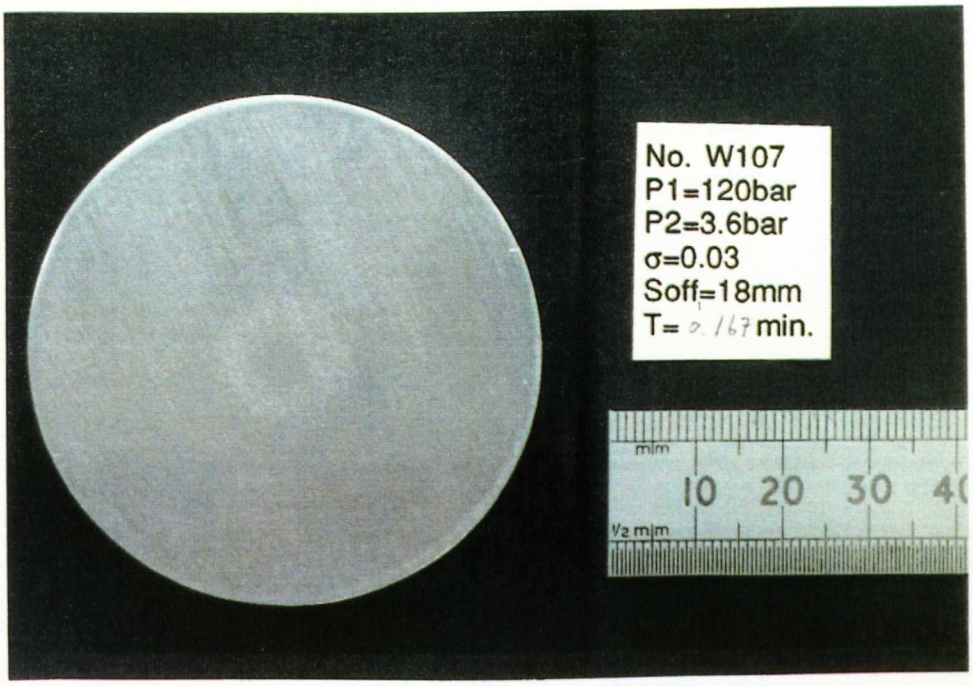

Fig.6.4.1(a) Cavitation damages on annealed 6063-aluminium alloy. P_1=120bar, P_2=3.6bar, σ=0.03, S_{off}=18mm, ΔT=10sec.

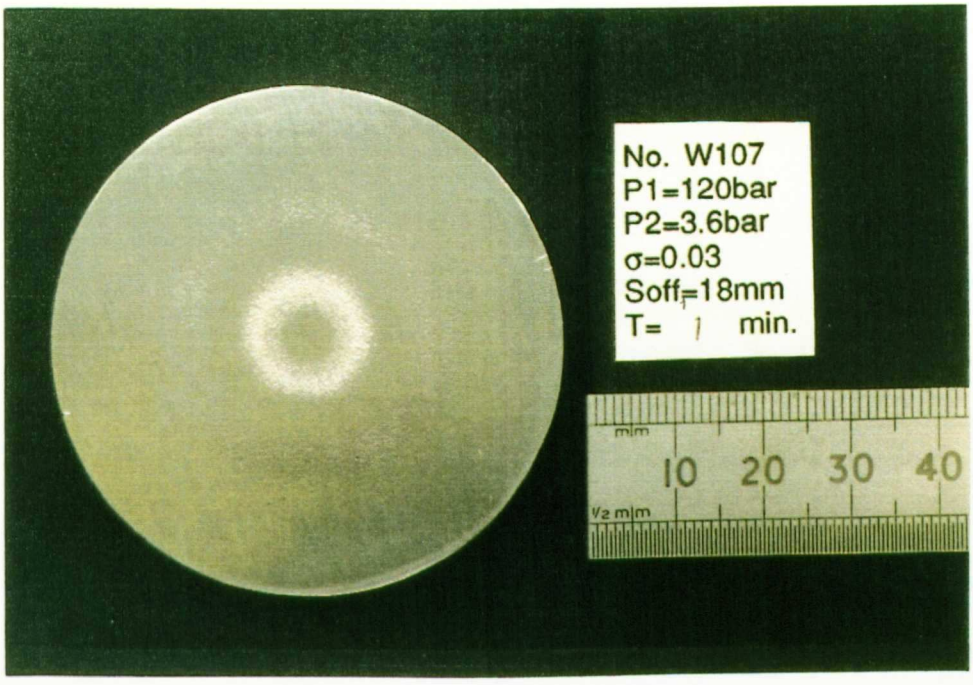

Fig.6.4.1(b) Cavitation damages on annealed 6063-aluminium alloy. P_1=120bar, P_2=3.6bar, σ=0.03, S_{off}=18mm, ΔT=1min.

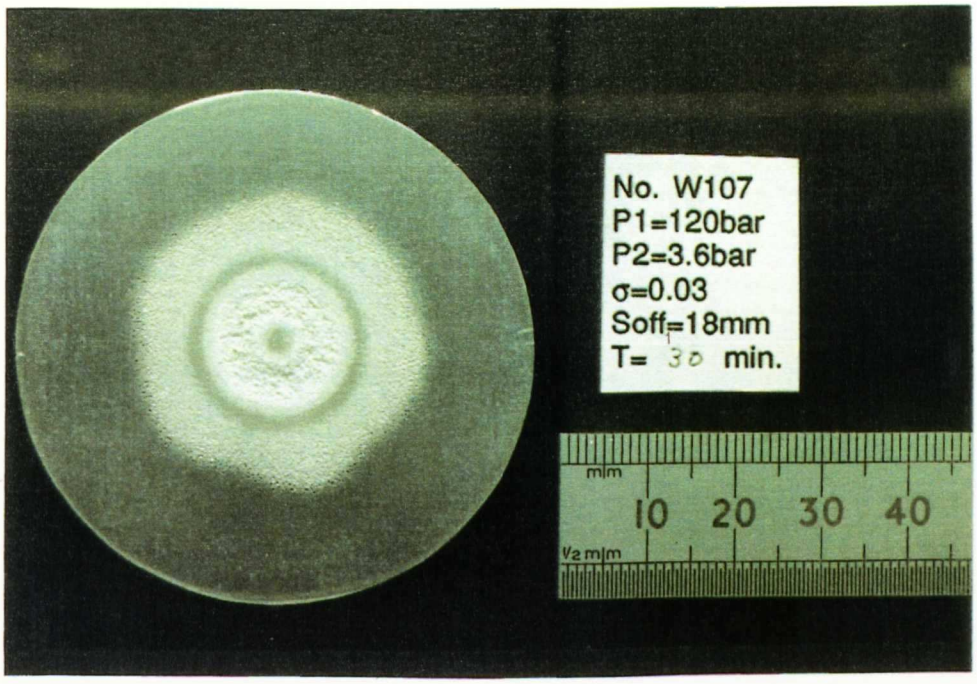

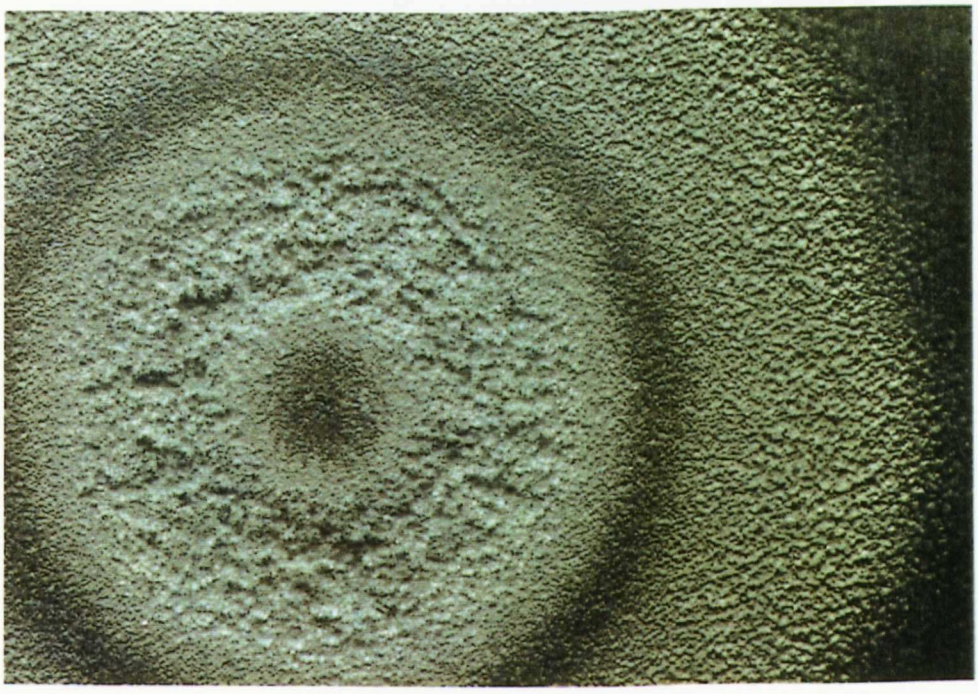

Fig.6.4.1(c) Cavitation damages on annealed 6063-aluminium alloy. P_1=120bar, P_2=3.6bar, σ=0.03, S_{off}=18mm, ΔT=30min.

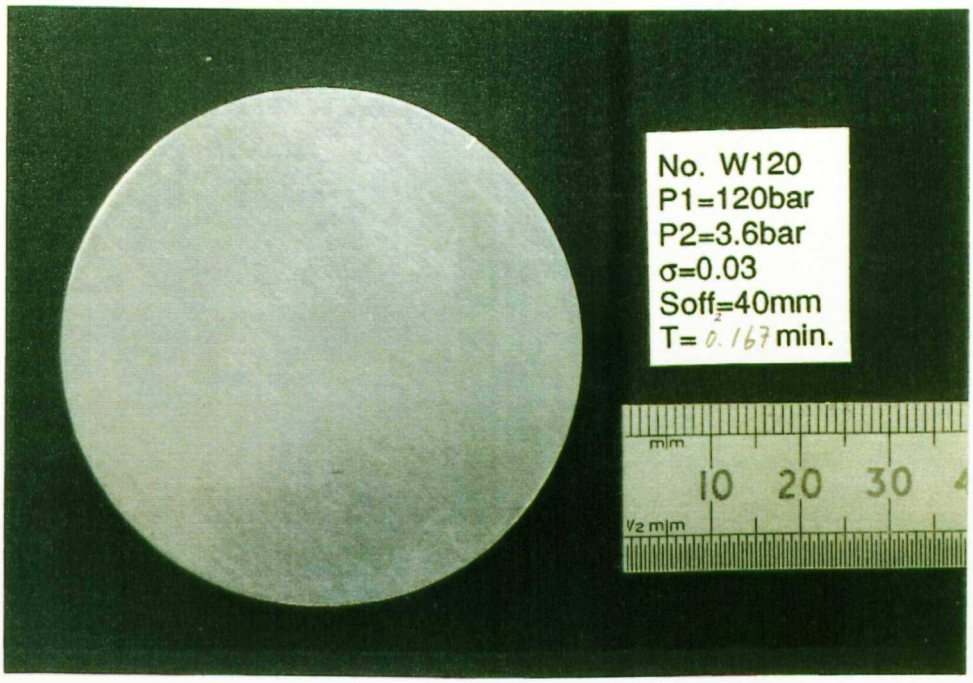

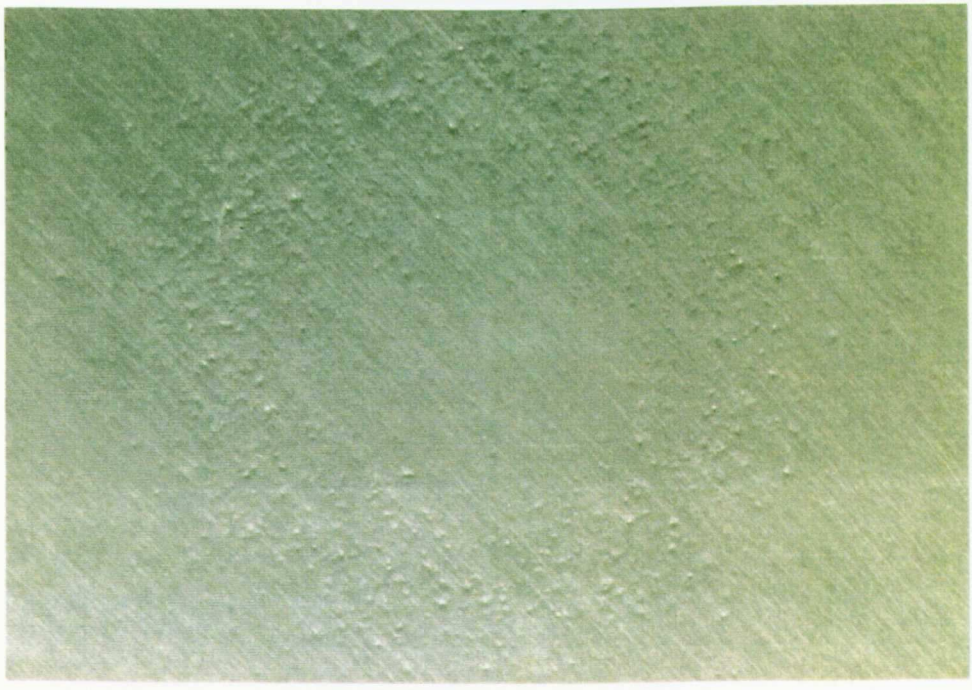

Fig.6.4.1(d) Cavitation damages on annealed 6063-aluminium alloy. P_1=120bar, P_2=3.6bar, σ=0.03, S_{off_2}=40mm, ΔT=10sec.

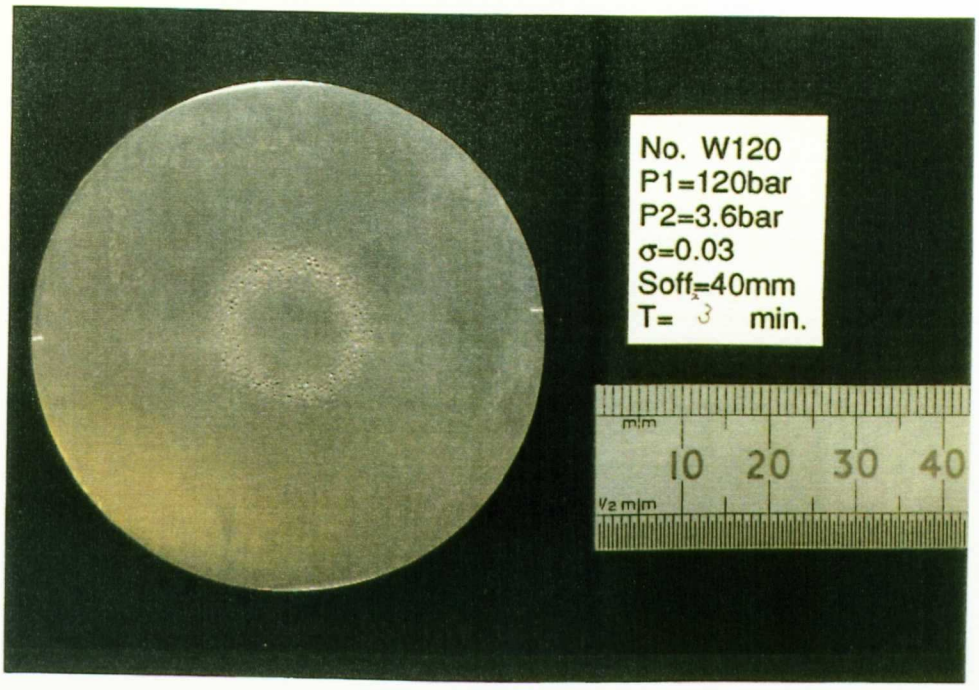

Fig.6.4.1(e) Cavitation damages on annealed 6063-aluminium alloy. P_1=120bar, P_2=3.6bar, σ=0.03, S_{off_2}=40mm, ΔT=3min.

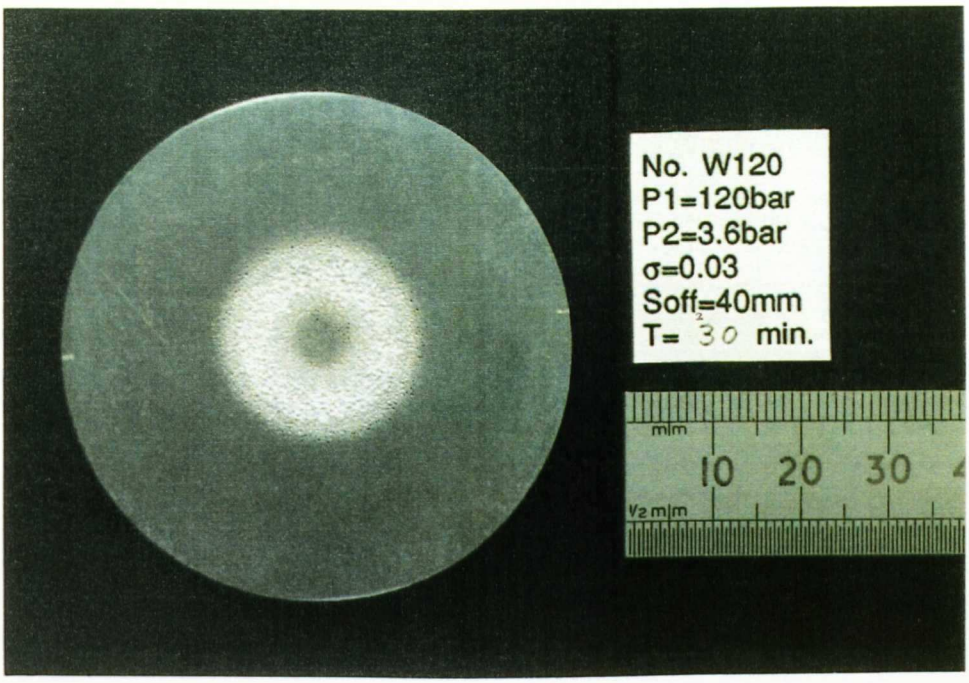

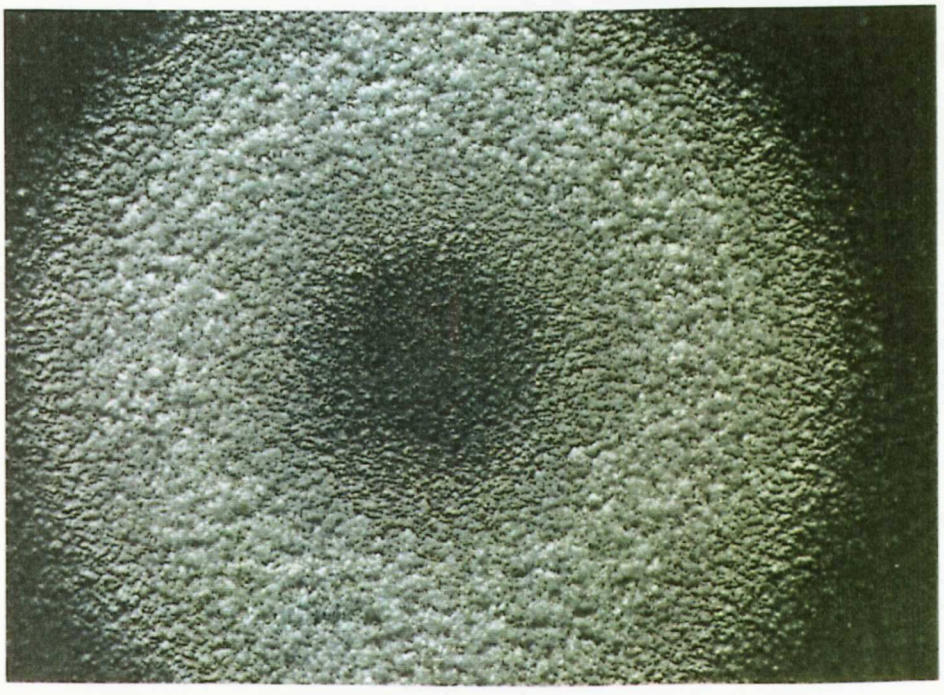

Fig.6.4.1(f) Cavitation damages on annealed 6063-aluminium alloy. P_1=120bar, P_2=3.6bar, σ=0.03, S_{off_2}=40mm, ΔT=30min.

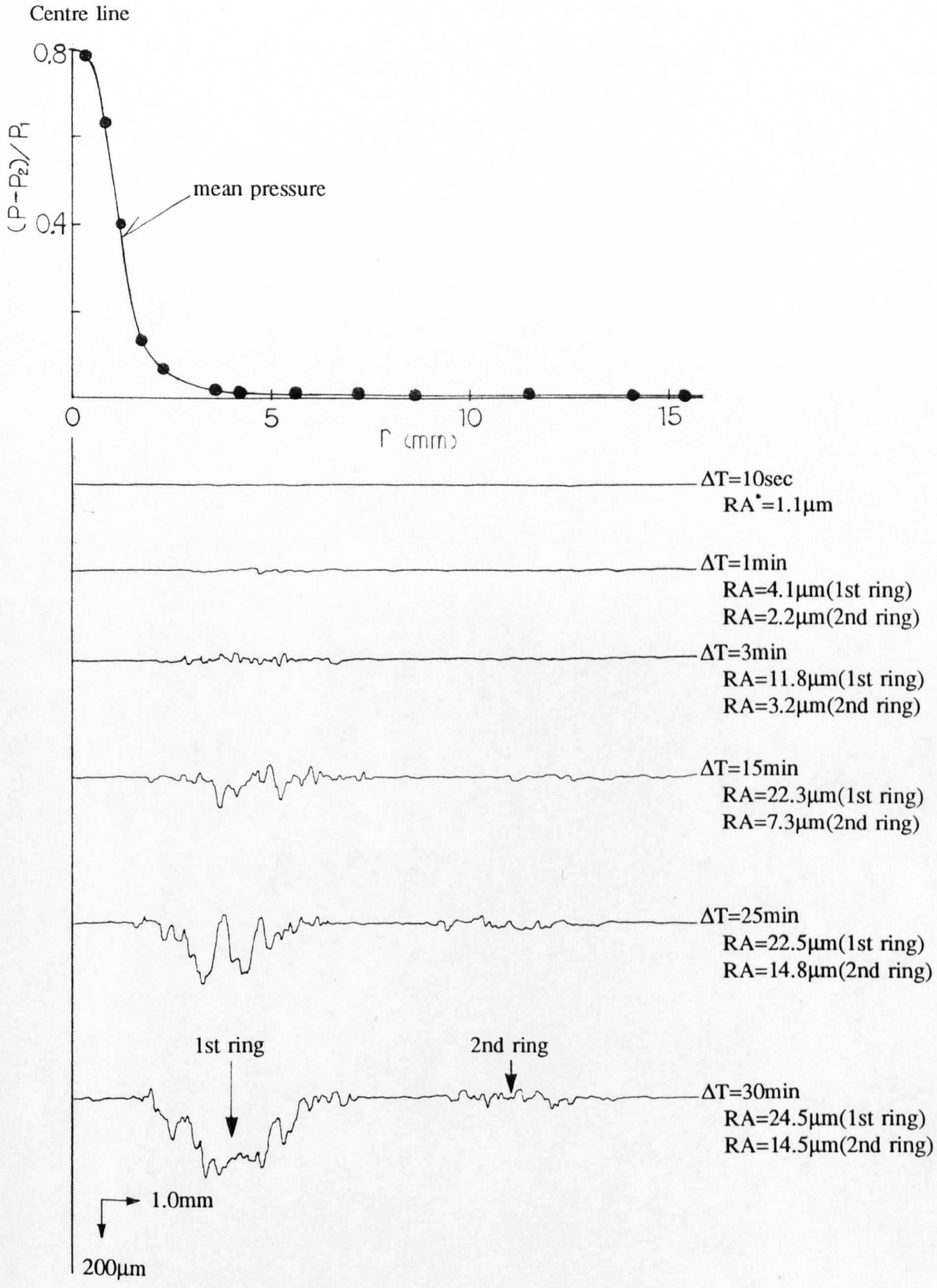

Fig.6.4.2(a) Profiles of damage development on annealed 6063-aluminium alloy (the same specimen shown in Fig.6.4.1(a)~(c)) with a mean pressure distribution.
P_1=120bar, P_2=3.6bar, σ=0.03, S_{off}=18mm.
*Roughness Average, cut off length: 0.8mm.

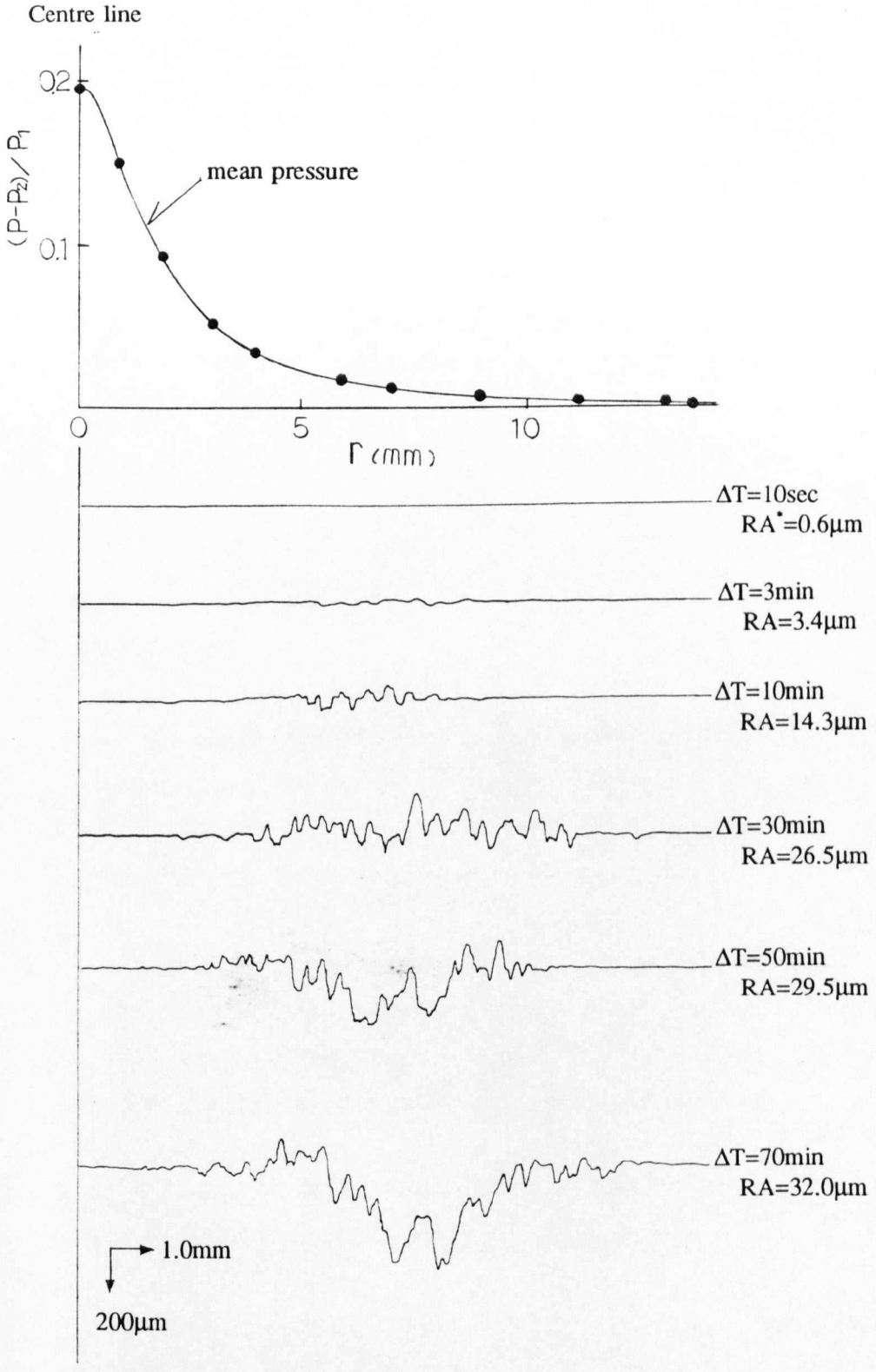

Fig.6.4.2(b) Profiles of damage development on annealed 6063-aluminium alloy (the same specimen shown in Fig.6.4.1(d)~(f)) with a mean pressure distribution.
P_1=120bar, P_2=3.6bar, σ=0.03, S_{off}=40mm.
*Roughness Average, cut off length: 0.8mm.

Main results and discussions in this chapter are summarized as follows.

(1) The cavitating jet lengths from nozzle inlet to the end tail of the cavitation were measured from photographs for various pressure combinations ranging P_1=80~120bar and P_2=2.4~3.6bar. They are apparently found to be related with the cavitation number σ. The relation between the average jet length l_j and cavitation number σ seems to be expressed as

$$\frac{l_j}{d_e} \propto \sigma^{-h_1}$$

where d_e is the effective nozzle diameter and the exponential index is obtained approximately $h_1 \approx 1$.

(2) As shown in Fig.6.3.4, the decay of stagnation pressure is clearly dependent of cavitation number. The pressure is more attenuated with larger cavitation number, while the attenuation is the same for all three cases with different upstream pressures P_1=80~120bar but with same cavitation number σ=0.03.

(3) Ring cavities found in high speed photographs are located just below the locus of $\delta_{0.5}$, the thickness of the wall jet, and well above the locus of the peak wall jet velocity, $0.2x\delta_{0.5}$, as shown in Fig.6.2.5. This indicates that the ring cavities are likely to be being transported only outside the main stream of the wall jet.

(4) The cavitation damage area is located just outside the stagnation region (Fig.6.4.2) where the wall jet thickness is smallest (Fig.6.2.6).

(5) The behaviour of cavitating bubbles and their damaging process may be explained as follows.

a.) Cavities are formed at the inlet edge of the long orifice nozzle.

b.) The potential core of the jet disappears at probably about 5~7 diameter distance downstream after it enters into the downstream chamber. Simultaneously, the cavitating bubbles start spreading with the turbulence of flow toward inside and outside of the jet.

c.) When cavitating bubbles are located inside the impinging jet and are transported into the high pressure zone of the stagnation region, they probably collapse well before the target and cannot damage the surface.

d.) Cavitating bubbles located outside the jet do not need to pass through such a high pressure zone and so they can survive and collapse somewhere outside the stagnation area.

e.) Some of these bubbles which are outside the jet can collapse on the target where the wall jet thickness and so the distance from the cavities to the target surface is smallest. Only the cavities which collapse at the sufficiently small distance to the target surface are able to damage the target. Beyond this point, the wall jet thickness increases with radial distance, and it becomes more probable for remaining cavities to collapse too far above the surface to damage it.

CHAPTER SEVEN - RESULTS:
Erosion produced by a cavitating jet

7.1 Erosion at various stand off distances

--- Effects of cavitation number

7.2 Variation of erosion with exposure time

7.3 Effects of pressures

7.4 Conclusions

7.1 Erosion at various stand off distances --- Effects of cavitation number

Cavitation erosion was produced by a cavitating jet on the surface of specimen disc made from the annealed 6063-aluminium alloy. The chemical composition, Vickers hardness of the material, the heat treatment and surface finish are given in Chapter 5. Variation of weight loss from these specimens due to the cavitation erosion with stand off distances are plotted in Figs.7.1.1(a)~(f) Pressure conditions range from P_1=80~120bar for upstream pressures and from P_2=2.4~3.6bar for downstream pressures. Stand off distance, S_{off}, is measured from the inlet edge of the nozzle to the target surface, and cavitation number σ is defined as a following equation.

$$\sigma = \frac{P_2}{P_1}$$

In all test cases except σ=0.0375 (Fig.7.1.1(a)), two peaks of the weight loss are always observed. The stand off distance where the peak weight loss takes place is called the optimum stand off distance, and in the present thesis, the shorter one and the longer one are defined as the first optimum stand off distance, S_{off1}, and the second optimum stand off distance, S_{off2}, respectively. Though the only one peak is obtained in the case of σ=0.0375, it is also defined as the first optimum stand off distance since this stand off distance is as small as the first optimum stand off distance in the other cases.

It is generally accepted that erosion rate, the weight loss divided by exposure time, depends on the state of damage of the target surface. This means that even if all the testing conditions are kept constant, the erosion rate may vary with exposure time. Thus, there is a possibility that one optimum stand off distance at one exposure time can also be slightly changed to another value due to additional cavitation exposure; for example, from the early stage of damage to more matured stage of erosion. This phenomenon is actually observed in Figs.7.1.1(a) and 7.1.1(b). The first optimum stand off distance, S_{off1}=15mm, at ΔT=200min is replaced with S_{off1}=17mm at ΔT=240min in Fig.7.1.1(a), and similarly S_{off1}=18mm until ΔT=120min is moved

to S_{off1}=20mm at ΔT=160min in Fig.7.1.1(b).

Therefore, before deciding on the optimum stand off distances for each pressure condition for the further investigation, it must be decided at first that which stage of erosion development is going to be studied. In the present project, one of the main objectives is to correlate the cavitation erosion to cavitation loading data and these must be measured on a plain surface. Then it was decided that the optimum stand off distance in an early erosion stage would be taken. Those optimum stand off distances finally decided are listed in Table 7.1.1. In Table 7.1.1 and Figs.7.1.1(a)~(f), there are three cases of pressure combinations with the same cavitation number σ=0.03, P_1=80bar and P_2=2.4bar, P_1=100bar and P_2=3.0bar, P_1=120bar and P_2=3.6bar, and as expected they all have the identical S_{off1} and S_{off2} in spite of the difference in pressure magnitude. Smaller cavitation number shows a larger value for both S_{off1} and S_{off2}.

Table 7.1.1 Optimum stand off distance

P_1 (bar)	P_2 (bar)	σ	S_{off1} (mm)	S_{off2} (mm)	Fig.No.
80	3.0	0.0375	15	-	7.1.1(a)
80	2.4	0.03	18	40	7.1.1(b)
100	3.0	0.03	18	40	7.1.1(c)
120	3.6	0.03	18	40	7.1.1(d)
120	3.0	0.025	18	45	7.1.1(e)
120	2.4	0.02	20	57	7.1.1(f)

As suggested by Lichtarowicz and Kay [1983], the variation of the optimum stand off distances with cavitation number is shown with more results by other investigators at Nottingham, Aachen and Yokohama in Fig.7.1.2 (for reference, see Lichtarowicz and Kay [1983] and Yamaguchi and Shimizu [1987]).

The relation between the optimum stand off distance and cavitation number can be expressed as

$$\frac{S_{off}}{d_e} \propto \sigma^{-h_2} \qquad (7.1.1)$$

Lichtarowicz and Kay [1983] reported that the index h_2 is about 0.8 for their results and the results from Aachen. Yamaguchi and Shimizu [1987] (at Yokohama in Fig.7.1.2) obtained the value of h_2 is 0.9 and 0.3 for two different test configurations; two types of nozzle holder configurations as shown in Fig.7.1.3 and different test chamber size, 40mm and 80mm for apparatus 1 and apparatus 2, respectively. All of these results are considered to be the second optimum stand off distance. The present results for S_{off2} and S_{off1} show that the value of h_2 is about 0.9 and 0.4, respectively. For all cases in Fig.7.1.2, the relations between the optimum stand off distance and cavitation number seem to satisfy Eq.(7.1.1). There are two sets of results using different liquids with the same test rig, one from Nottingham with oil and water and another one from Aachen with oil and emulsion. Both sets of results show the same optimum stand off distances regardless of the difference in the liquid type. Therefore it appears likely that the index h_2 in Fig.7.1.2 depends not on the liquid type but on the individual test rig configuration.

It has been reported by Bin-Ujang [1990] that the nozzle holder which is located at low pressure side of the nozzle disturbs the flow surrounding a jet near the outlet edge of the nozzle and significantly affects the intensity and length of the cavitating jet. A long shroud type nozzle holder has been used in the work by Lichtarowicz and an "open" type nozzle holder was used by Yamaguchi and Shimizu as shown in Fig.7.1.3, whereas there is no nozzle holder in Kleinbreuer's apparatus as shown in Fig.4.1.7. The shape of the nozzle holder used in the present experiments is similar to the "open" type. Yamaguchi and Shimizu [1987] have also reported that there are effects of the nozzle holder configuration and test chamber size on the optimum stand off distance and erosion rate. Although more accumulation of parametric study is necessary to fully understand these effects, all the geometric parameters described above can be considered to be responsible for the difference in the index h_2.

The reason of the dependence of the optimum stand off distance on cavitation number can be understood from the fact that the length of a cavitating jet depends on the cavitation number as shown in Fig.6.2.3 and the value of index h_1, 1.0, for the cavitation jet length in Fig.6.2.3 agrees well with the index h_2, 0.9, for the second optimum stand off distance in Fig.7.1.2. The ratios of the optimum stand off distances to the average jet length in each cavitation number are tabulated in Table 7.1.2. The ratios for S_{off2} show consistent values from 0.75 to 0.78, though ratios for

S_{off1} range rather widely from 0.27~0.36.

Table 7.1.2 Ratio of optimum stand off distance to jet length

σ	S_{off1} (A) (mm)	S_{off2} (B) (mm)	Jet length ave. (C) (mm)	A/C (S_{off1})	B/C (S_{off2})
0.02	20	57	75.2	0.27	0.76
0.025	18	45	60.4	0.30	0.75
0.03	18	40	51.1	0.35	0.78
0.0375	15	-	41.5	0.36	-

The cavitation number determines not only the location of the optimum stand off distance but also the entire shape of the weight loss-stand off distance curve. Figures 7.1.1(b)~7.1.1(d) have the same cavitation number σ=0.03 with P_1=80bar, 100bar and 120bar and show similar weight loss curves with stand off distances. In order to show the effects of cavitation number on the erosion characteristics more clearly, the weight loss for the same P_1=120bar with different σ=0.02, 0.025 and 0.03 (P_2=2.4, 3.0 and 3.6bar) at ΔT=40min are re-plotted from Figs.7.1.1(d)~7.1.1(f) in Fig.7.1.4. As the cavitation number decreases, the weight loss at S_{off2} significantly increases together with the increase of S_{off2} while S_{off1} and the erosion at S_{off1} appears almost not changed despite relatively the large change in cavitation number σ.

Figures 7.1.5(a)~(h) show photographs of the erosion on the specimens with various stand off distances S_{off}=15~50mm at a fixed exposure time of 100min. The upstream pressure is P_1=100bar and cavitation number σ=0.03 (downstream pressure P_2=3.0bar). The erosion shapes are basically rings with much smaller undamaged area at the centre and they can be categorised into two types, one ring erosion and two rings erosion as shown in Chapter 6. Which erosion shape takes place is dependent of the stand off distance with given cavitation number.

The two ring erosion occurs at a small stand off distance where the radial wall jet is more affected by the proximity of the nozzle holder. As shown in Figs.6.4.1 and 6.4.2, both rings are formed from very early stage of erosion. But in more matured stage, the erosion of the first (inner) ring proceeds much more rapidly than the erosion of the second (outer) ring and so the total weight loss is mainly produced by the former one. As stand off distance increases, the wall jet becomes less affected

by the nozzle holder and the outer ring disappears.

As a measure of the extent of the erosion, variation of the radii of inner edge, outer edge (1st ring) and outer edge (2nd ring) are plotted with stand off distances in Fig.7.1.6. Since these radii are not much affected by test duration as will be shown in detail later in this chapter, the exposure time cannot be therefore an important parameter to establish the results. As long as sufficient erosion was obtained to identify those radii at each stand off distance, the tests could be stopped. Except at the very small stand off distance, the size of the first ring erosion (the outer edge) expands with increase of stand off distance and then decreases after showing the maximum radius. As expected from the free cavitating jet length and erosion results previously shown, the smaller the cavitation number is, the larger the erosion size and the longer the stand off distance where the maximum radius takes place. One may have already realised the similarity between the weight loss curve shown in Fig.7.1.4 and the outer edge (1st ring) curve with stand off distances shown in Figs.7.1.6. The erosion ring areas calculated from Fig.7.1.6 are plotted in Fig.7.1.7. It can be observed that both the first and the second optimum stand off distances, S_{off1} and S_{off2}, occur at the point where the peak of erosion area is found. This indicates that the area of the damage may be playing an important role in producing the maximum weight loss at the optimum stand off distance.

Determining the optimum stand off distance from the weight loss data is rather a time consuming process. Normally it takes about a week for one case. Such a procedure must be completed before starting each erosion test with new pressure and temperature conditions, different test rig configuration or even different liquid. Sometimes, it is also carried out after even the slightest change in these and the other test parameters to ensure the same performance. From such a practical aspect, the dependency of the optimum stand off distance on the cavitating jet length and on the size of the erosion ring which has been discussed above is significant. They can be used as techniques which help to find the optimum stand off distance more easily. For example, possible range of the second optimum stand off distance S_{off2} can be predicted by simply obtaining a mean jet length from a number of high speed photographs or perhaps by measuring the jet length from a long exposure photograph. Then, measuring the size of erosion ring on the soft material may also be able to be used to reduce the time to find both S_{off1} and S_{off2}.

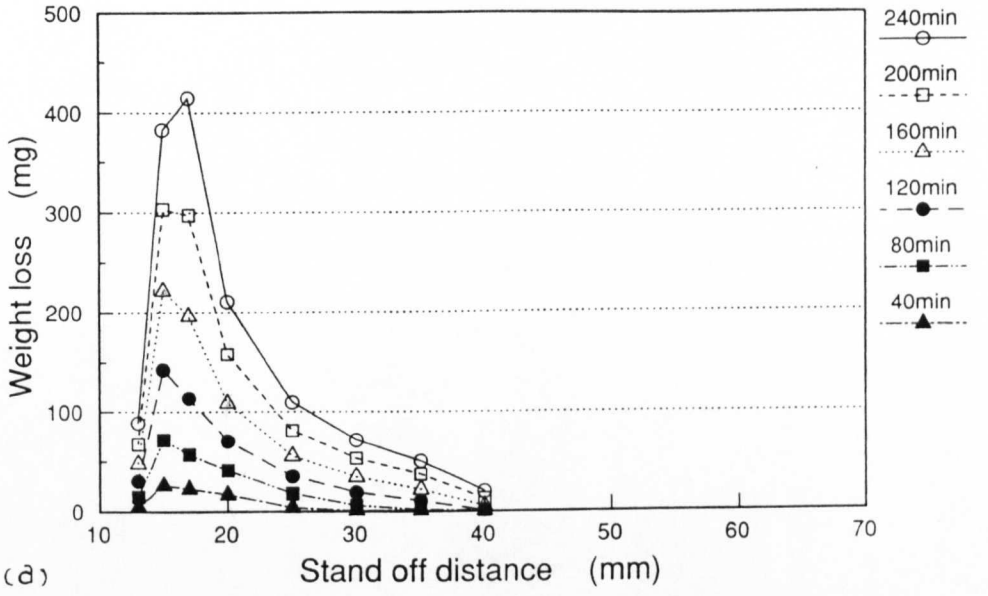

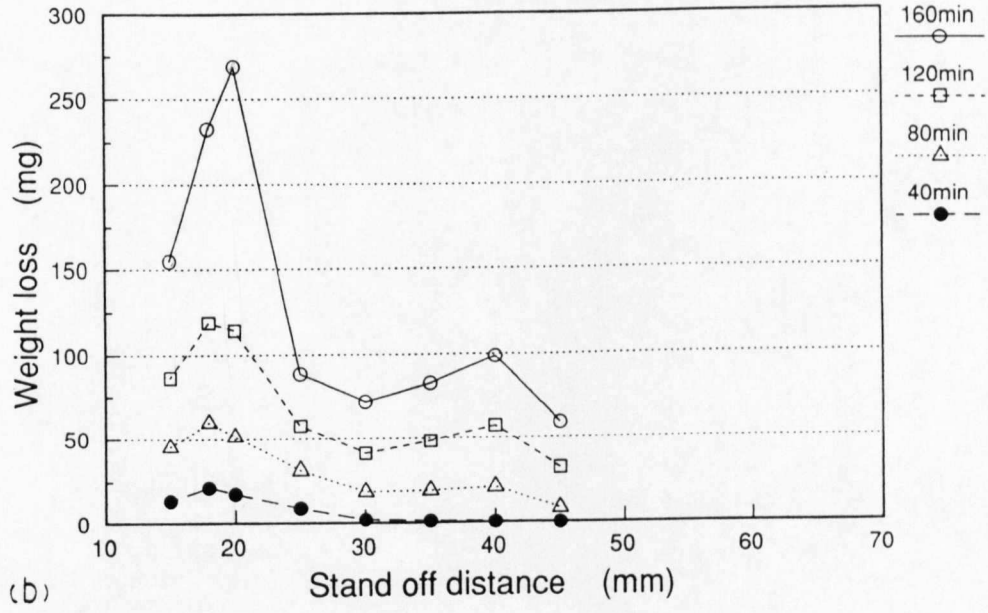

Fig.7.1.1 Variation of weight loss with stand off distance.
(a) P_1=80bar, P_2=3.0bar, σ=0.0375; (b) P_1=80bar, P_2=2.4bar, σ=0.03.

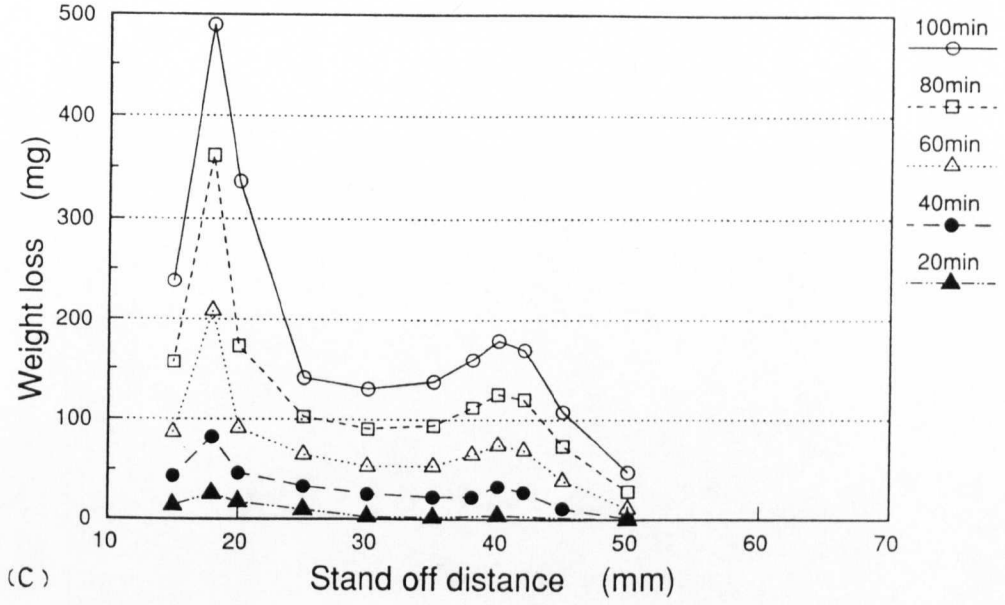

(C)

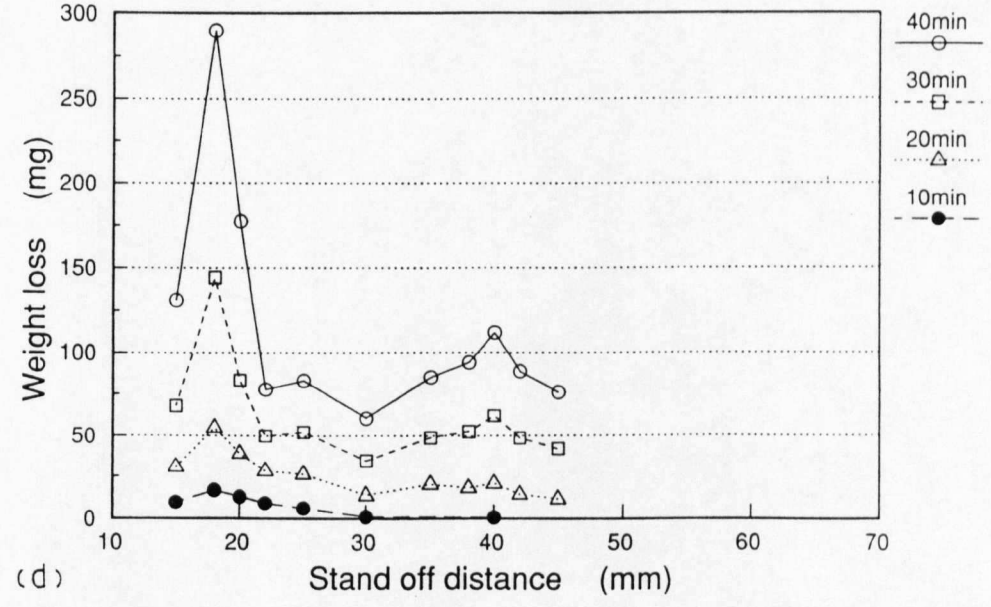

(d)

Fig.7.1.1 Variation of weight loss with stand off distance.
(c) P_1=100bar, P_2=3.0bar, σ=0.03; (d) P_1=120bar, P_2=3.6bar, σ=0.03.

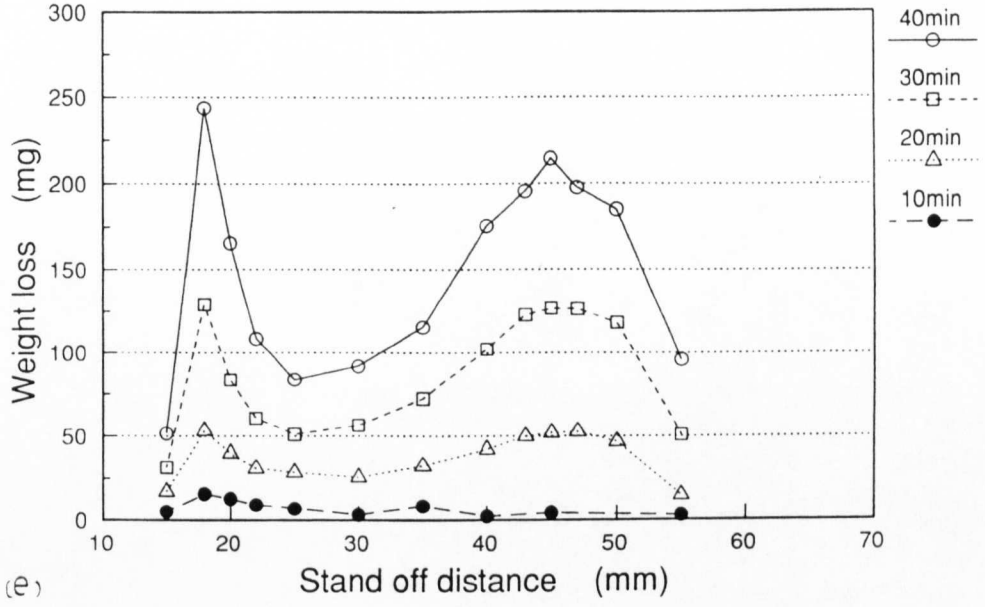

(e)

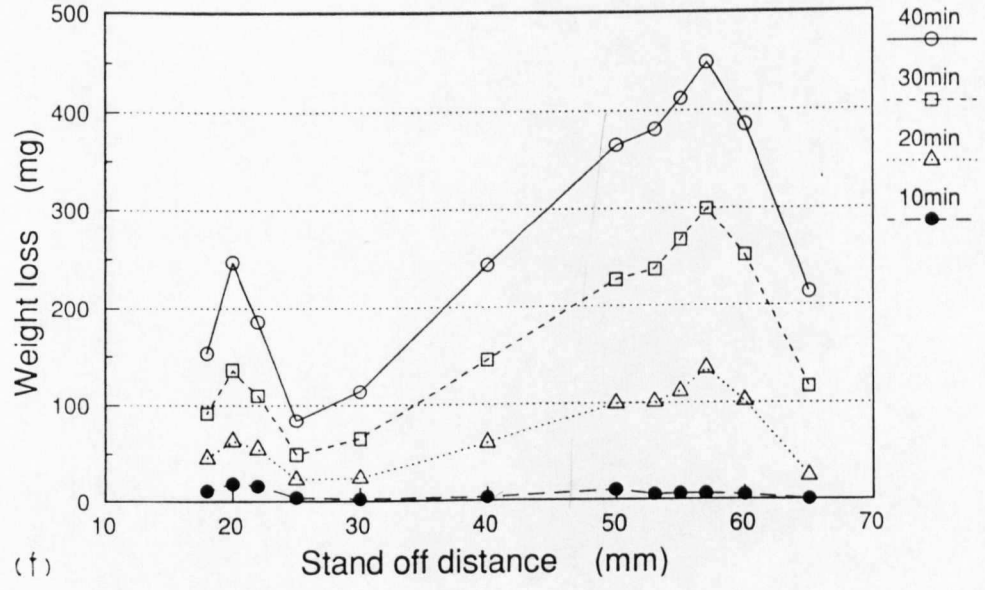

(f)

Fig.7.1.1 Variation of weight loss with stand off distance.
(e) P_1=120bar, P_2=3.0bar, σ=0.025; (f) P_1=120bar, P_2=2.4bar, σ=0.02.

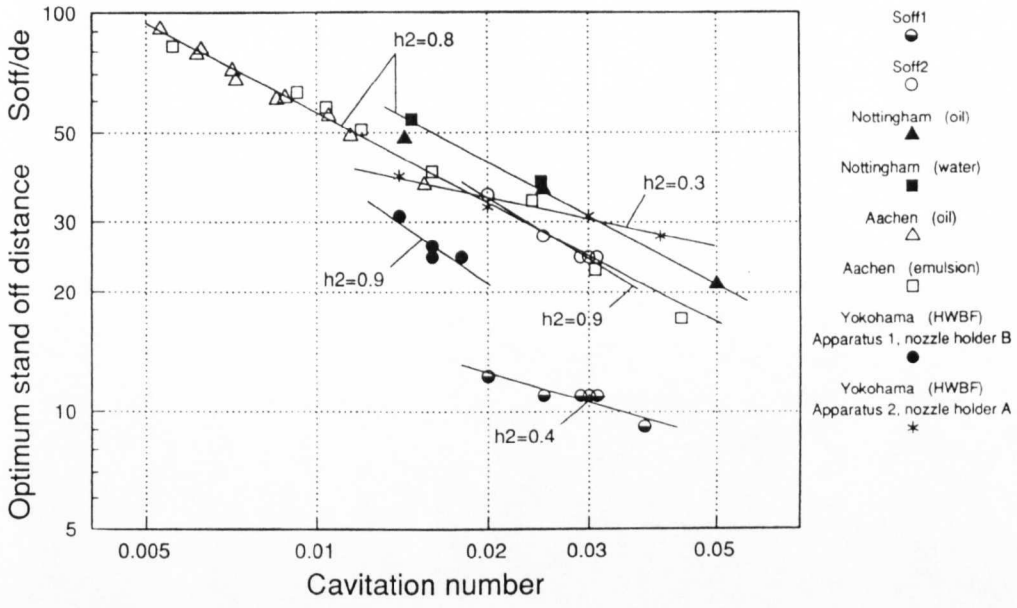

Fig.7.1.2 Variation of normalized optimum stand off distances with cavitation number.

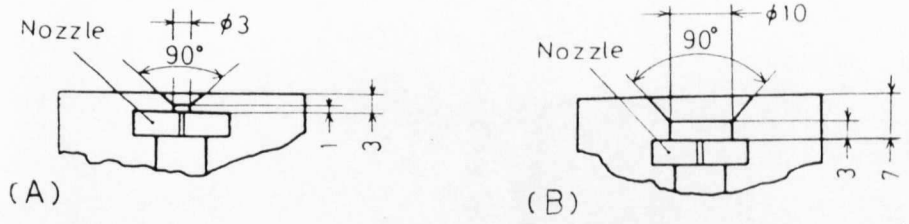

Fig.7.1.3 Configurations of nozzle holders. (from Yamaguchi and Shimizu [1987])

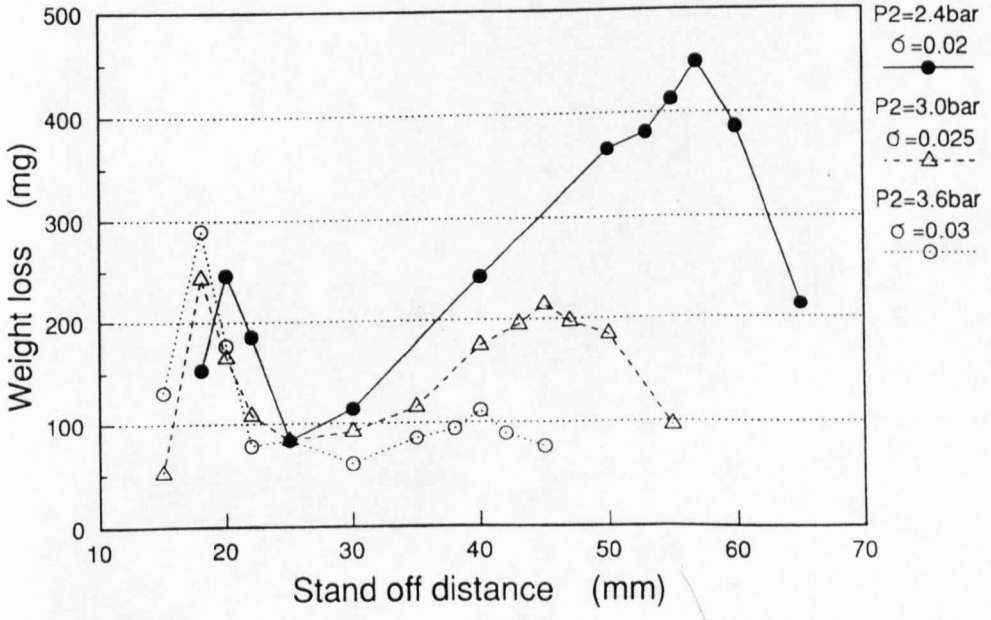

Fig.7.1.4 Effect of cavitation number σ (downstream pressure P_2) on weight loss. P_1=120bar, P_2=2.4, 3.0 and 3.6bar, σ=0.02, 0.025 and 0.03, ΔT=40min.

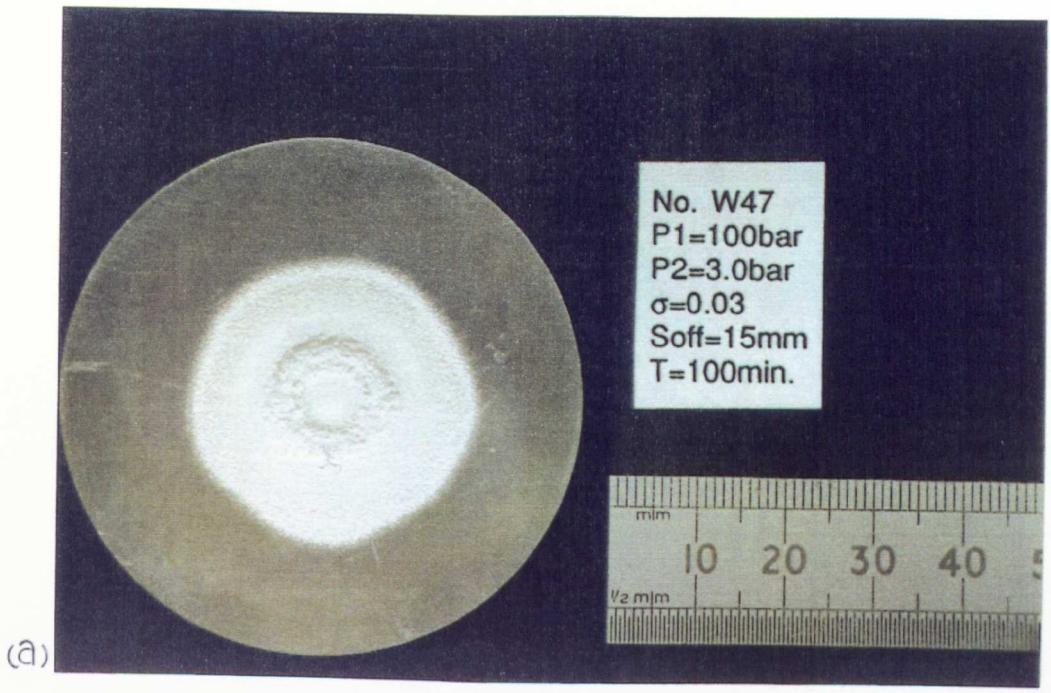

(a)

(b)

Fig.7.1.5 Photographs of erosion on annealed 6063-aluminium alloy. P_1=100bar, P_2=3.0bar, σ=0.03, ΔT=100min, (a) S_{off}=15mm; (b) S_{off}=18mm.

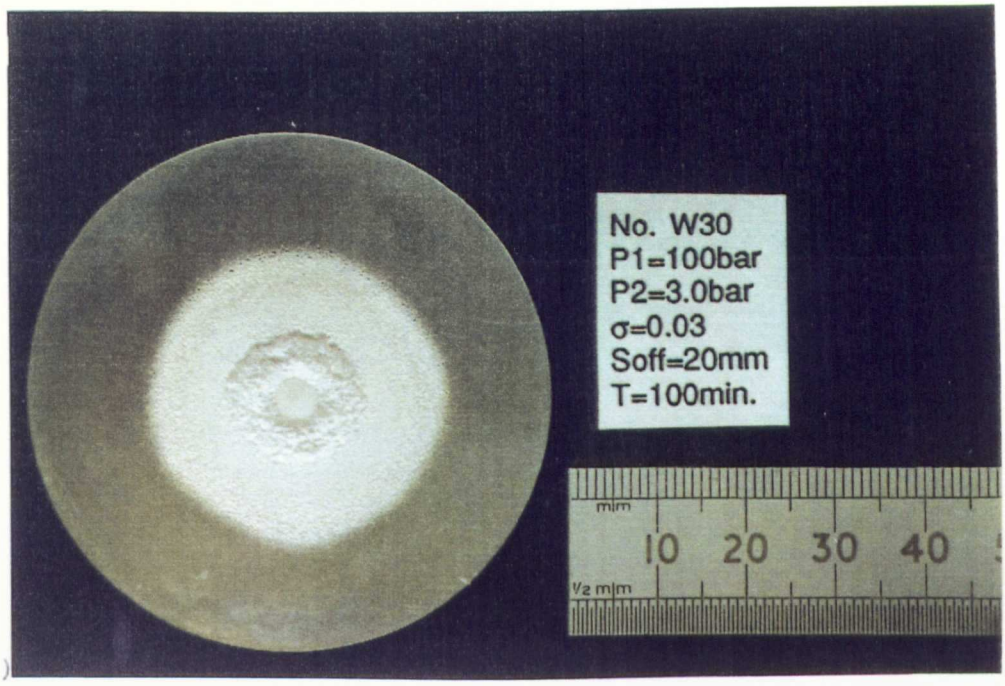

(c)

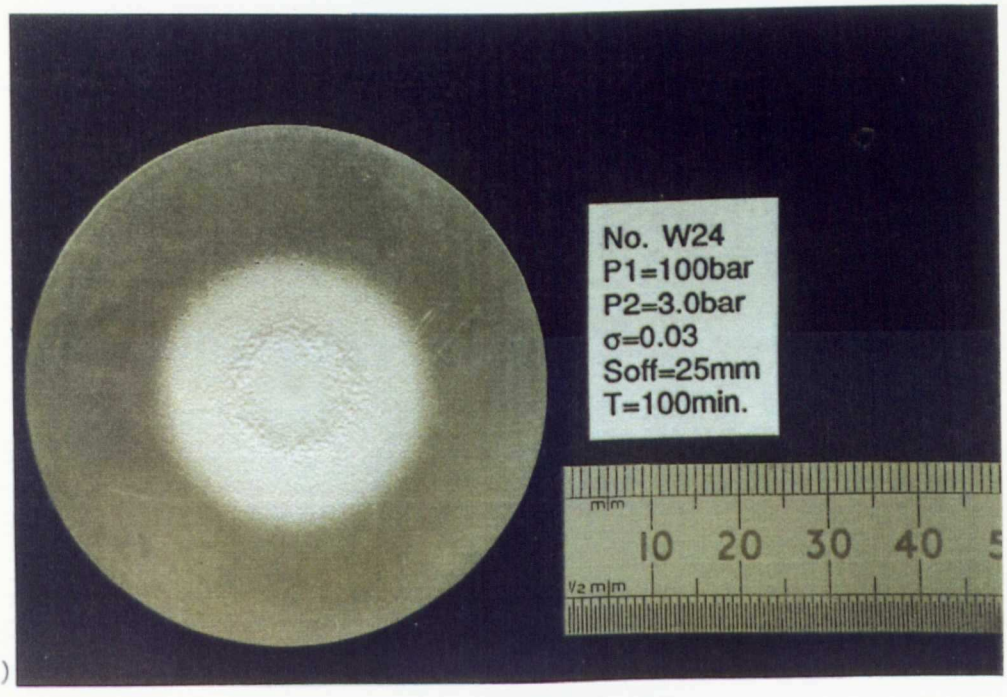

(d)

Fig.7.1.5 Photographs of erosion on annealed 6063-aluminium alloy. P_1=100bar, P_2=3.0bar, σ=0.03, ΔT=100min, (c) S_{off}=20mm; (d) S_{off}=25mm.

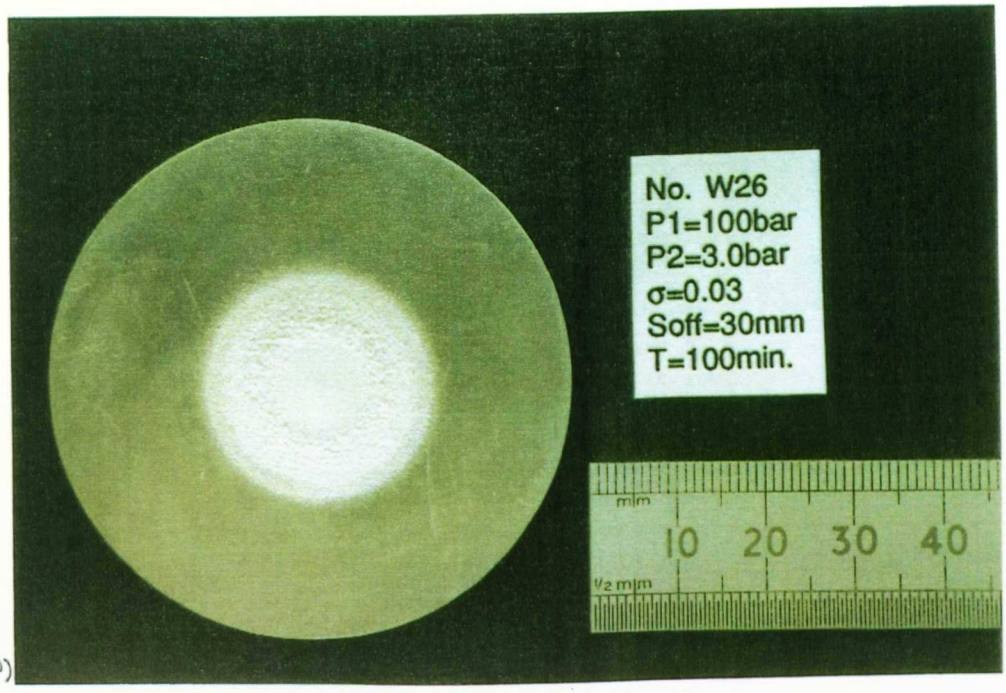

(e)

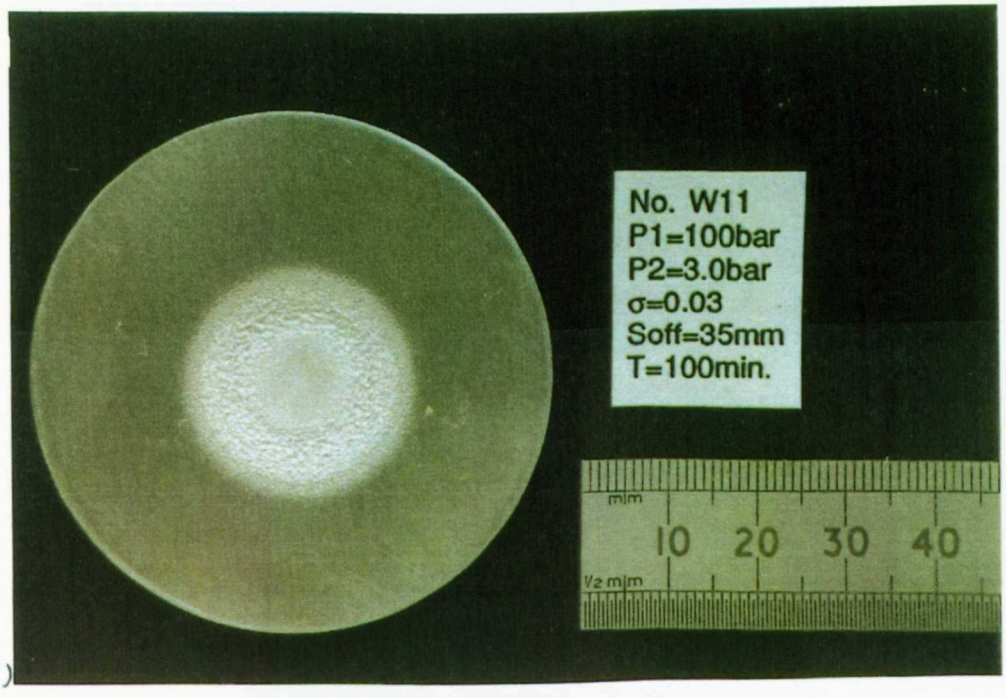

(f)

Fig.7.1.5 Photographs of erosion on annealed 6063-aluminium alloy. P_1=100bar, P_2=3.0bar, σ=0.03, ΔT=100min, (e) S_{off}=30mm; (f) S_{off}=35mm.

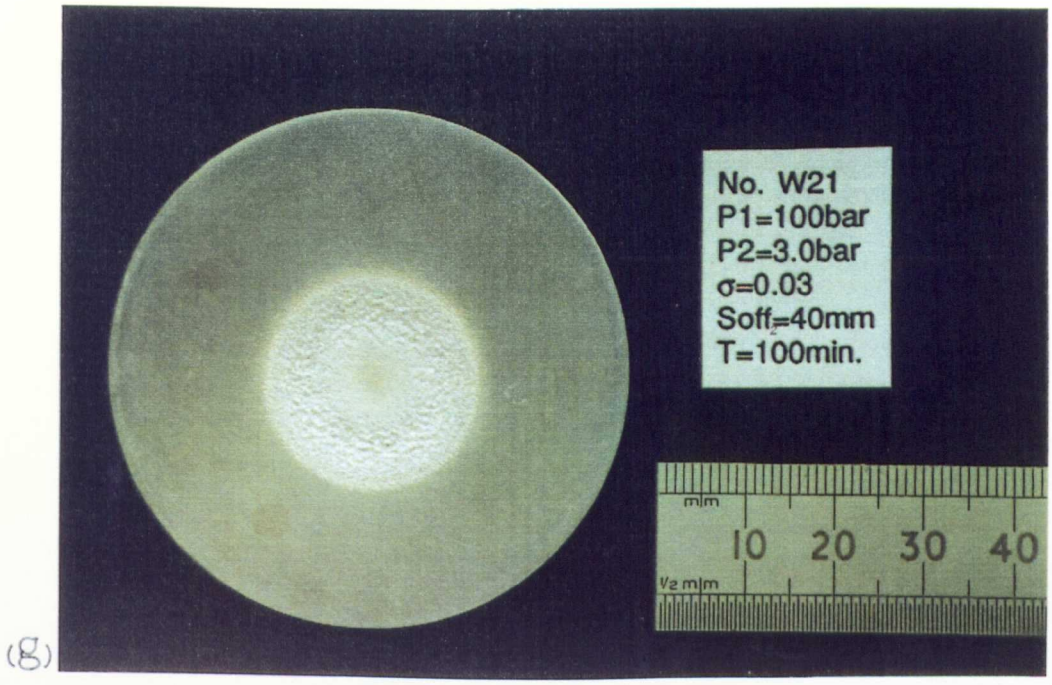

(g)

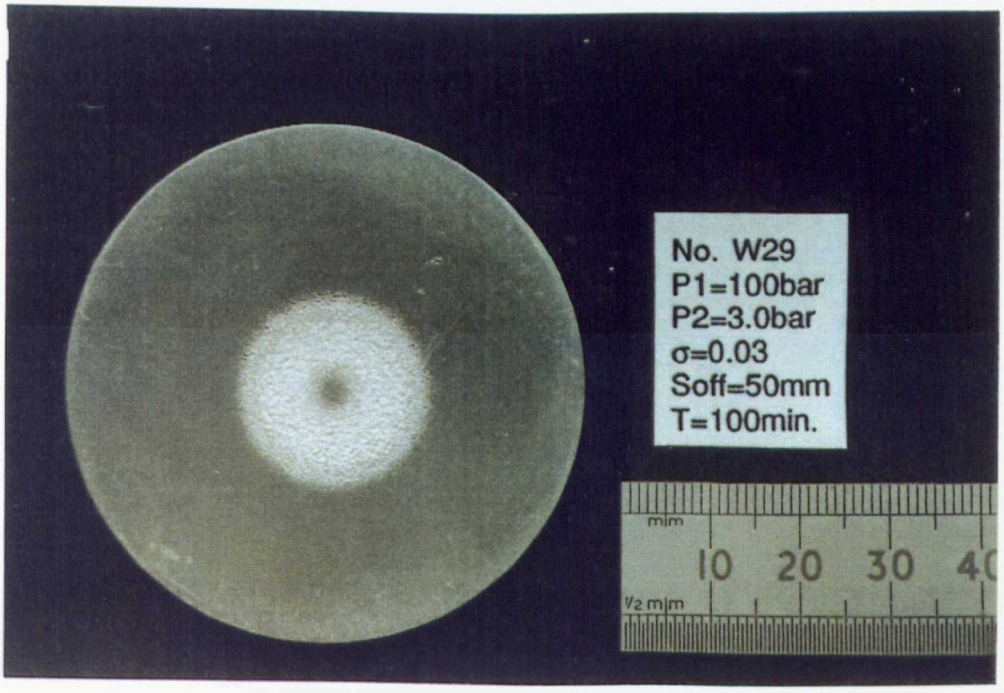

(h)

Fig.7.1.5 Photographs of erosion on annealed 6063-aluminium alloy.
P_1=100bar, P_2=3.0bar, σ=0.03, ΔT=100min, (g) S_{off_2}=40mm; (h) S_{off}=50mm.

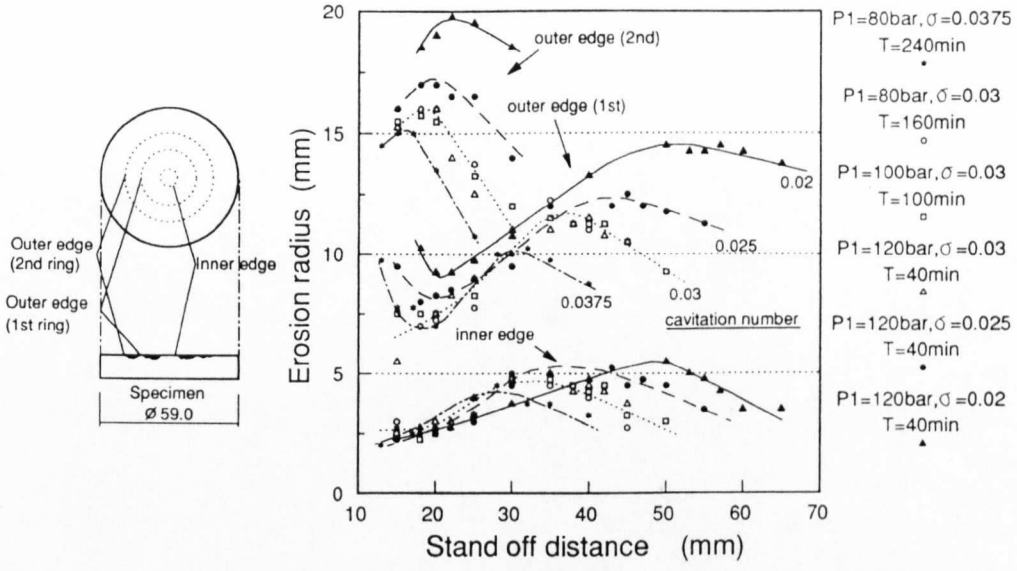

Fig.7.1.6 Variation of erosion ring radius with stand off distance.

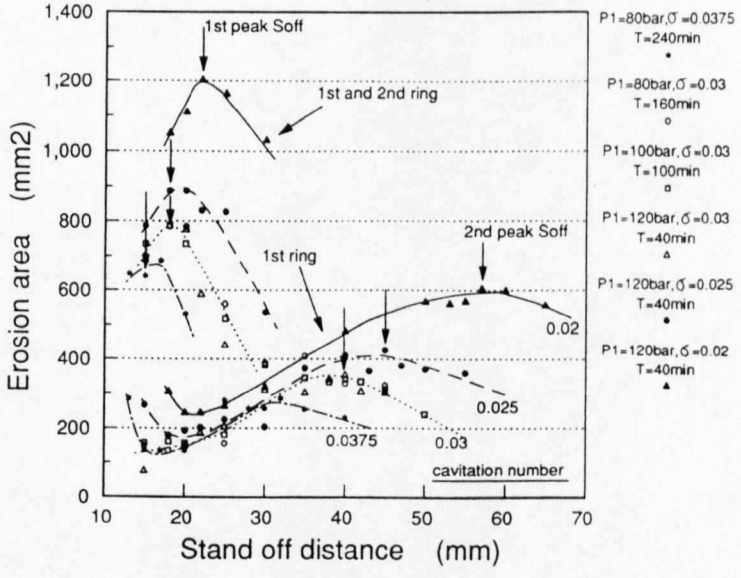

Fig.7.1.7 Variation of erosion ring area with stand off distance.

Typical weight loss development and erosion rate with cavitation exposure time are shown in Figs.7.2.1 and 7.2.2 for P_1=100bar and P_2=3.0bar at the first optimum stand off distance S_{off1}=18mm and at the second optimum stand off distance S_{off2}=40mm, respectively. Cumulative erosion rate (CER) is defined as the weight loss rate using total weight loss divided by total exposure time, and instantaneous erosion rate (IER) is defined as the weight loss rate using weight loss and exposure time between two adjacent measuring points as described in Chapter 5. In the case of the first optimum stand off distance in Fig.7.2.1, the weight loss increases monotonously almost immediately after the exposure begins. Both CER and IER hit the peak at the exposure time around 2hrs and 1.3hrs, respectively and then gradually decrease. The situation is slightly different for the second optimum stand off distance. The weight loss also increases monotonously almost immediately after the exposure but both CER and IER show two peaks in Fig.7.2.2. Figure 7.2.3 shows photographs of erosion specimens with the same conditions of Fig.7.2.2 at various cavitation exposure time ΔT=100min, 5hr, 9hr and 17hr, which are indicated in Fig.7.2.2. Erosion proceeds deeper and deeper and the centre uneroded part becomes smaller and smaller with time. However, the outer edge does not seem to be expanding and even after 17hr exposure (2500mg weight loss) there is no damage found outside the original damage ring. These changes in surface geometry from the flat plate to the deep ring crater must affect the jet flow and so the erosion rate. From the detailed observation of the erosion development on the target surface as will be described below, it was found that the second peak in IER clearly starts to emerge again when the uneroded part at the target centre almost disappears from the surface.

Typical examples of the erosion size development with exposure time is shown with weight loss development at the first and the second optimum stand off distance in Figs.7.2.4 and 7.2.5, respectively. Pressure conditions, P_1=100bar and σ=0.03 (P_2=3.0bar), are same as Figs.7.2.1 and 7.2.2. Each erosion ring radius except the inner edge at the second optimum stand off distance is not changed by the cavitation exposure time in spite of the rapidly increasing weight loss value. Therefore, it can be concluded that the increase in weight loss results mainly from the erosion development in depth. In order to find the effects of geometric change in the

inner edge at the second optimum stand off distance on the erosion rate, the erosion radius and corresponding erosion rate with exposure time are plotted for all six pressure conditions tested in the present project, P_1=80~120bar and σ=0.02~0.0375, in Fig.7.2.6. It is clearly found for all cases that the instantaneous erosion rate suddenly re-increases with the disappearance of the inner edge radius (centre uneroded part) in time. Schematic drawings in Fig.7.2.7 show the impingement of a cavitating flow to the specimen whose surface has been severely damaged. Since there is no flat stagnation area at the centre, the virtual erosion area where the cavities are able to damage the object is much greater on the specimen after the disappearance of the centre part (right, in Fig.7.2.7). This may be the reason of the difference in erosion rate between the specimens before or after losing the "plateau" at the centre.

The reason why there is no decrease in the inner edge radius at the first optimum stand off distance has not been fully understood yet. There is no major difference in degree of cavitation erosion damage between the one at S_{off1} in Fig.7.2.4 and another at S_{off2} in Fig.7.2.5. Both tests were continued until they have a damage just before penetrating through the specimen (7.7mm in thickness, at the centre). Followings can be considered as possible reasons.

(1) The cavities may not be able to damage the centre "plateau" at the first optimum stand off distance, since the stagnation pressure is too high.

(2) Since it can be estimated that the potential core of the jet disappears at only small distance in front of the target at the first optimum stand off distance, there may be fewer bubbles existing in the centre portion of the jet.

The cumulative erosion rate seems more stable and reliable for comparing the intensity of cavitation erosion between a number of different cases, because the instantaneous erosion rate depends on the time interval between two measuring points. As shown by Lichtarowicz [1979], variation of the cumulative erosion rate with exposure time at both optimum stand off distances, S_{off1} and S_{off2}, for all pressures tested is plotted in normalized form in Figs.7.2.8 and 7.2.9. All the normalised CER for the first optimum stand off distance show similar tendency of erosion progress. However, the shape of the erosion rate-time curve for the second optimum stand off distance S_{off2} is different from the one for the first optimum stand off distance S_{off1}. As shown in

Figs.7.2.1 and 7.2.2, the erosion rate-time curve for S_{off2} shows two peaks, whereas the one for S_{off1} shows only one peak. Both CER and exposure time are normalised at the second peak in Fig.7.2.9, since cumulative erosion rate at the second peak shows higher value than the first peak in most cases. There are differences in the degree of relative peak heights between two peaks and they cause relatively large variation of normalised CER around the first peak; i.e., the variation before the normalised point (which is the second peak) in Fig.7.2.9.

Since at least one peak value has been obtained in the cumulative and the instantaneous erosion rate within exposure time, it is possible to define such a maximum erosion rate as the peak erosion rate (PER_C for the cumulative erosion rate and PER_I for the instantaneous erosion rate) of the corresponding pressure condition and stand off distance. Present cavitation erosion tests were continued until these peak erosion rates were obtained at both the first and the second optimum stand off distance for all test cases. Though there is no second optimum stand off distance clearly observed for P_1=80bar and σ=0.0375 (P_2=3.0bar) in the present tests (Fig.7.1.1(a)), by a supposition from the close relation between cavitation number and the optimum stand off distance in Fig.7.1.2, it was decided that the stand off distance S_{off}=35mm would be treated as the second optimum stand off distance for P_1=80bar and σ=0.0375 in the following sections and chapters.

Variation of these peak erosion rates with flow parameters will be presented and discussed in the next section.

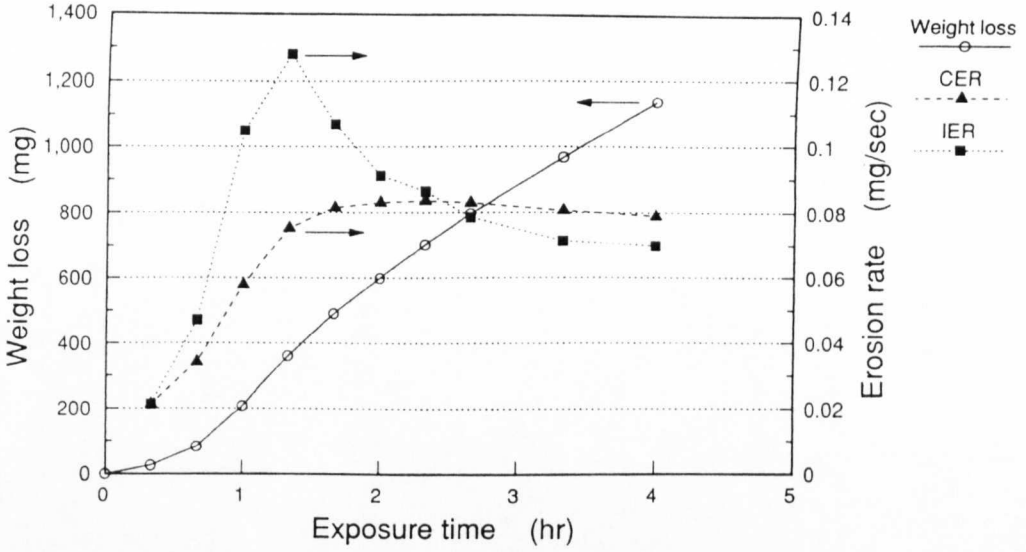

Fig.7.2.1 Weight loss and erosion rate with exposure time.
P_1=100bar, P_2=3.0bar, σ=0.03, S_{off_1}=18mm.

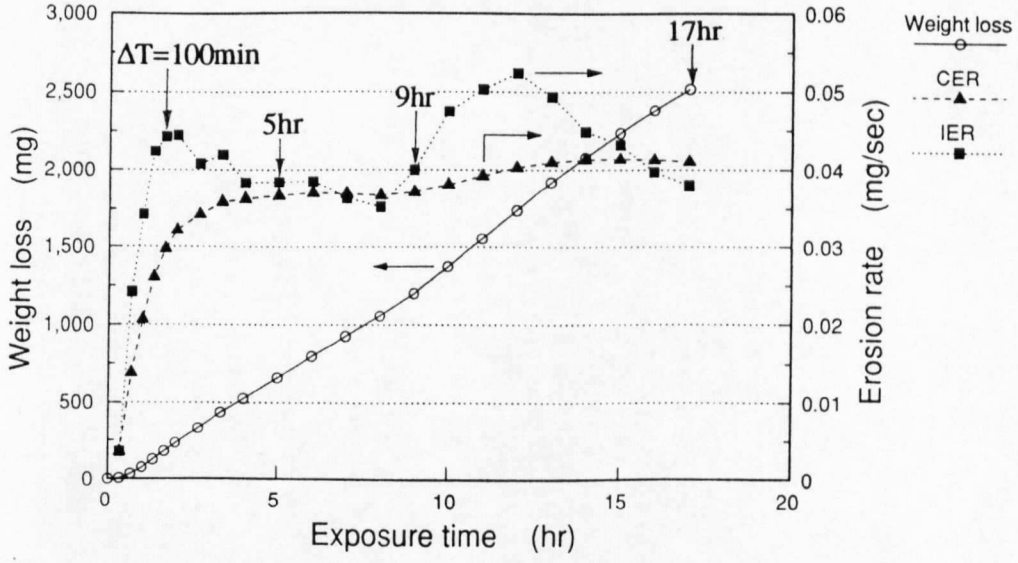

Fig.7.2.2 Weight loss and erosion rate with exposure time.
P_1=100bar, P_2=3.0bar, σ=0.03, S_{off_2}=40mm.

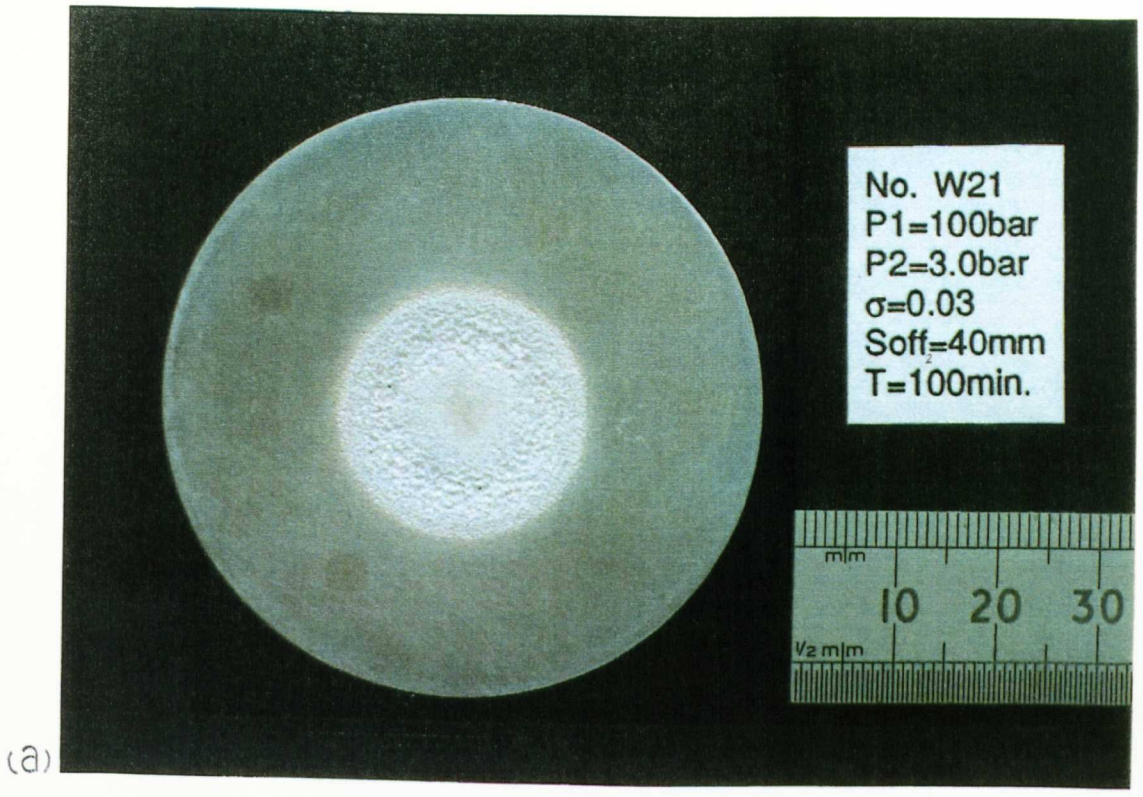

(a)

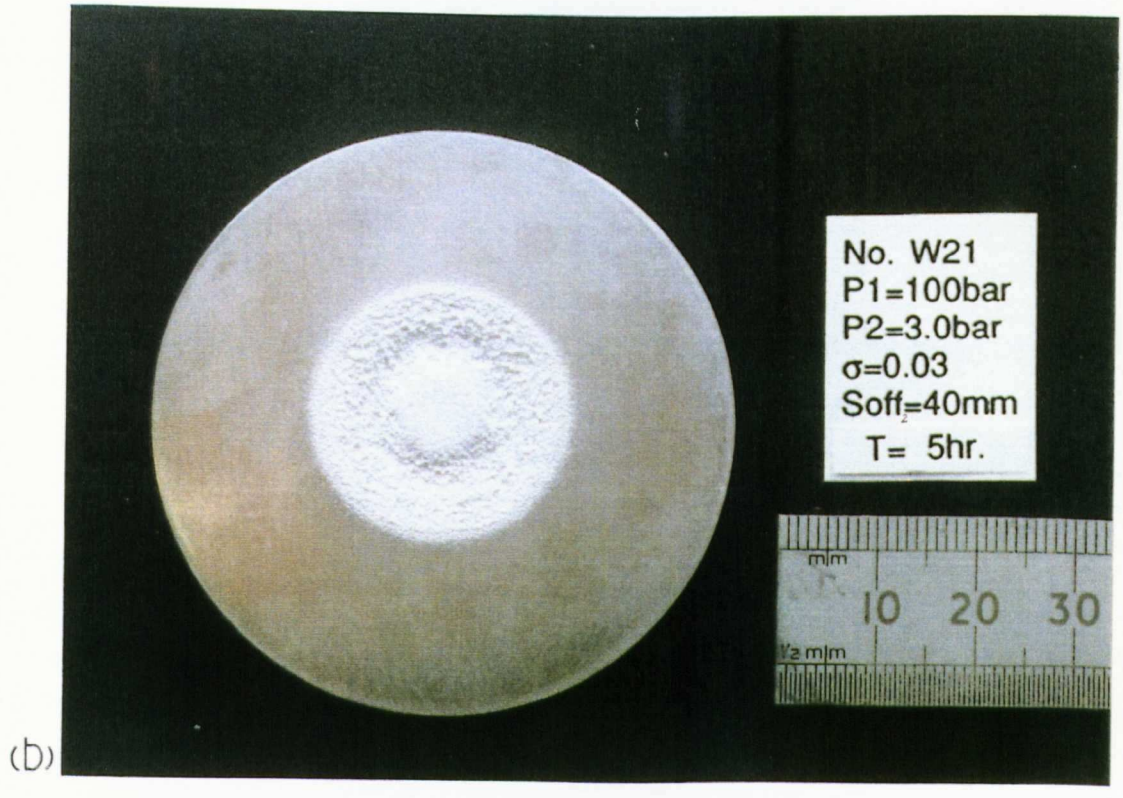

(b)

Fig.7.2.3 Development of erosion on annealed 6063-aluminium alloy with exposure time. P_1=100bar, P_2=3.0bar, σ=0.03, S_{off_2}=40mm, (a) ΔT=100min; (b) ΔT=5hr.

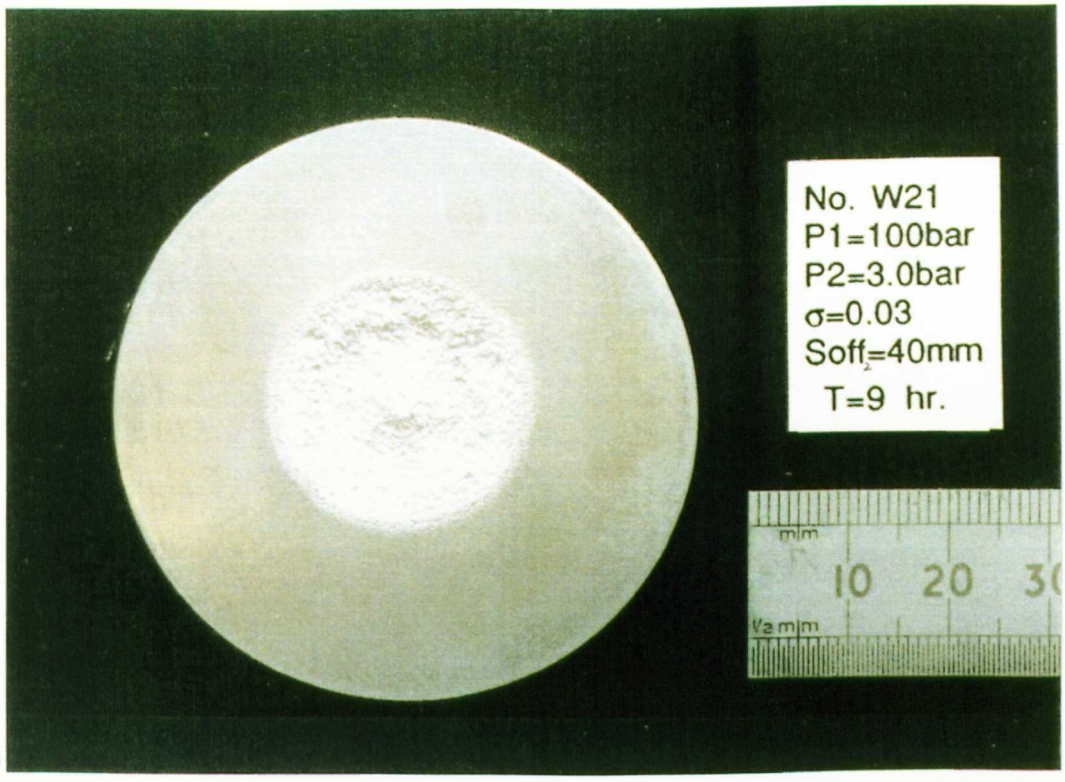

(C)

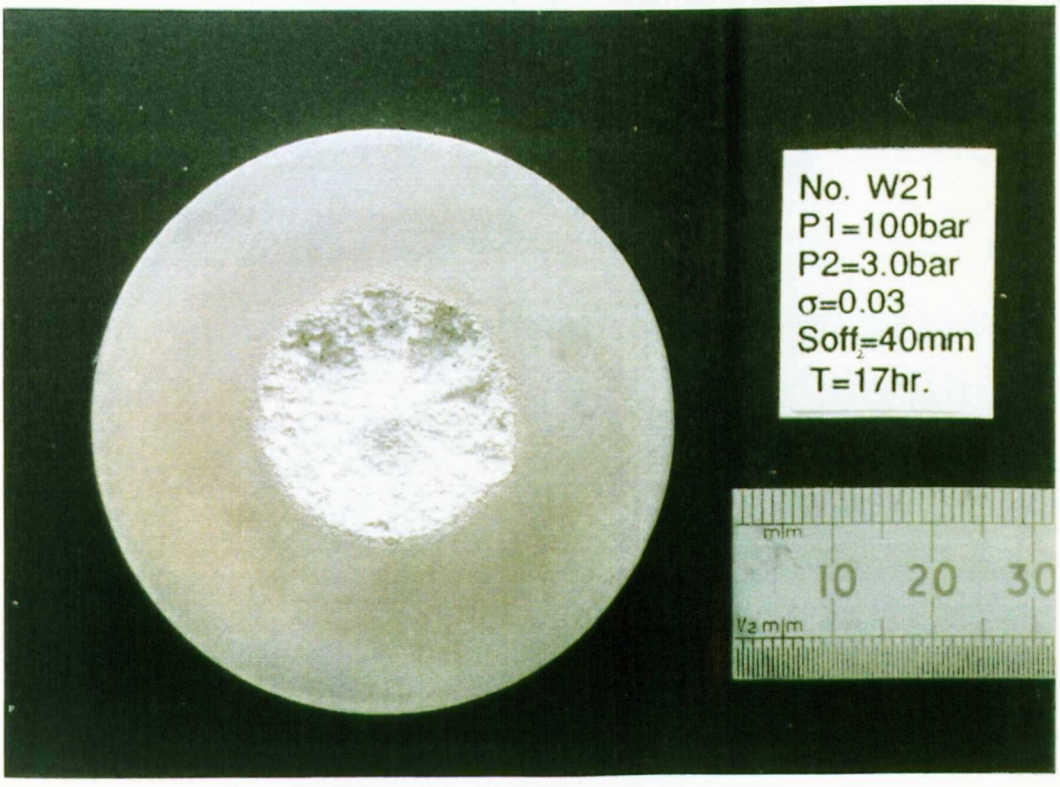

(d)

Fig.7.2.3 Development of erosion on annealed 6063-aluminium alloy with exposure time. P_1=100bar, P_2=3.0bar, σ=0.03, S_{off_2}=40mm, (c) ΔT=9hr; (d) ΔT=17hr.

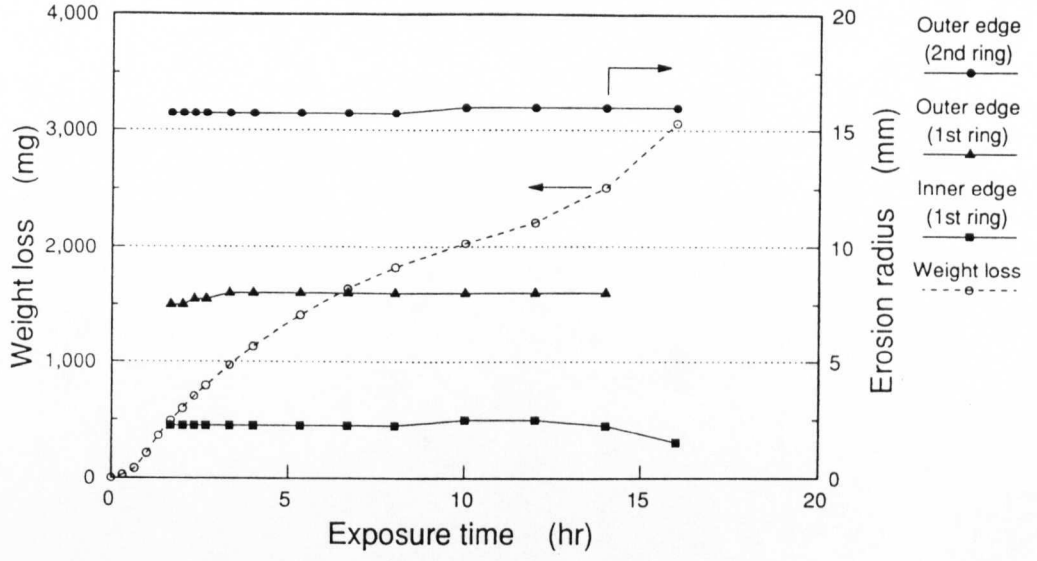

Fig.7.2.4 Erosion ring radius and weight loss with exposure time.
P_1=100bar, P_2=3.0bar, σ=0.03, S_{off_1}=18mm.

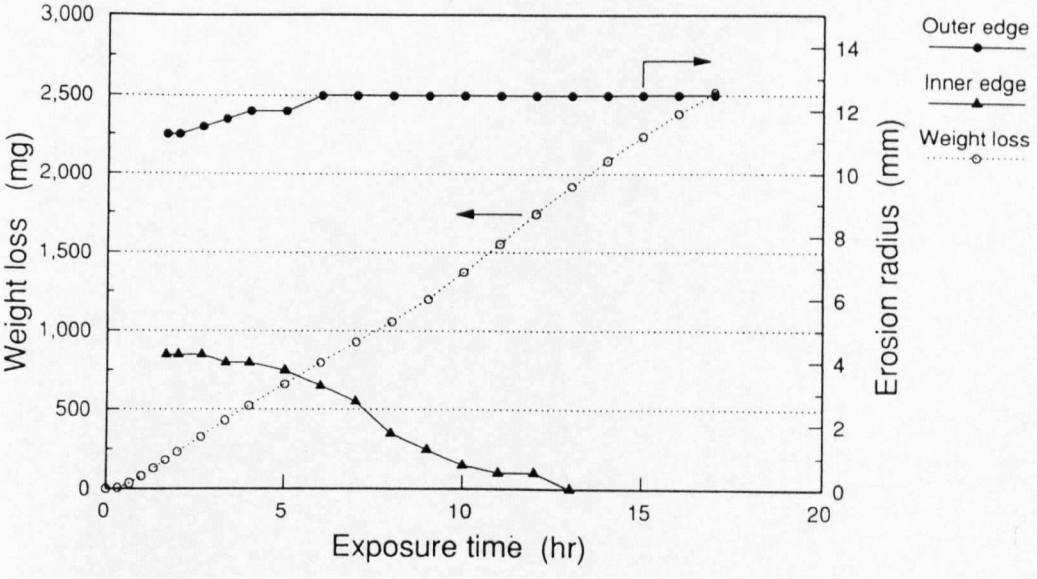

Fig.7.2.5 Erosion ring radius and weight loss with exposure time.
P_1=100bar, P_2=3.0bar, σ=0.03, S_{off_2}=40mm.

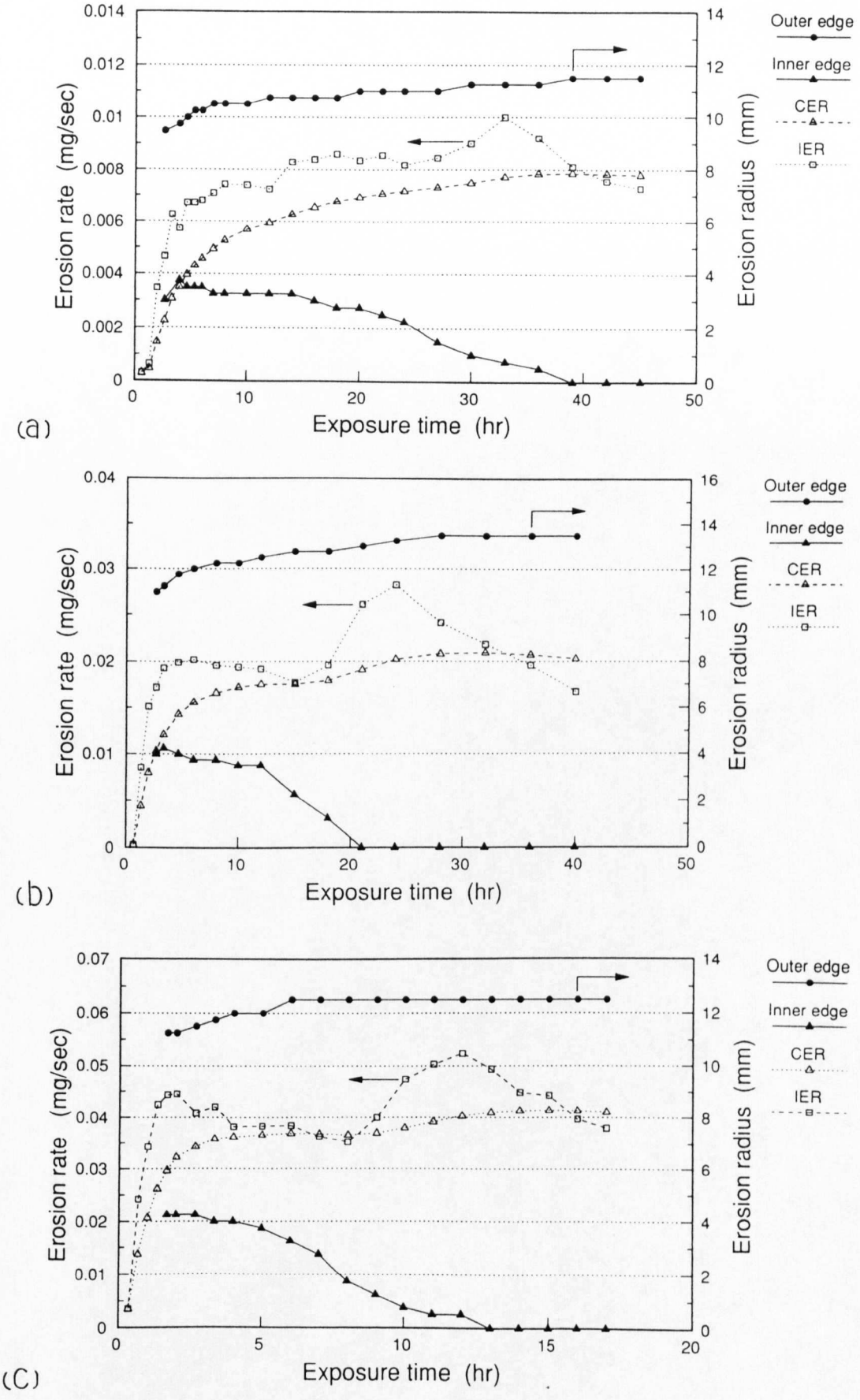

Fig.7.2.6 Erosion ring radius and erosion rate with exposure time.
(a) P_1=80bar, P_2=3.0bar, σ=0.0375, S_{off_2}=35mm; (b) P_1=80bar, P_2=2.4bar, σ=0.03, S_{off_2}=40mm; (c) P_1=100bar, P_2=3.0bar, σ=0.03, S_{off_2}=40mm.

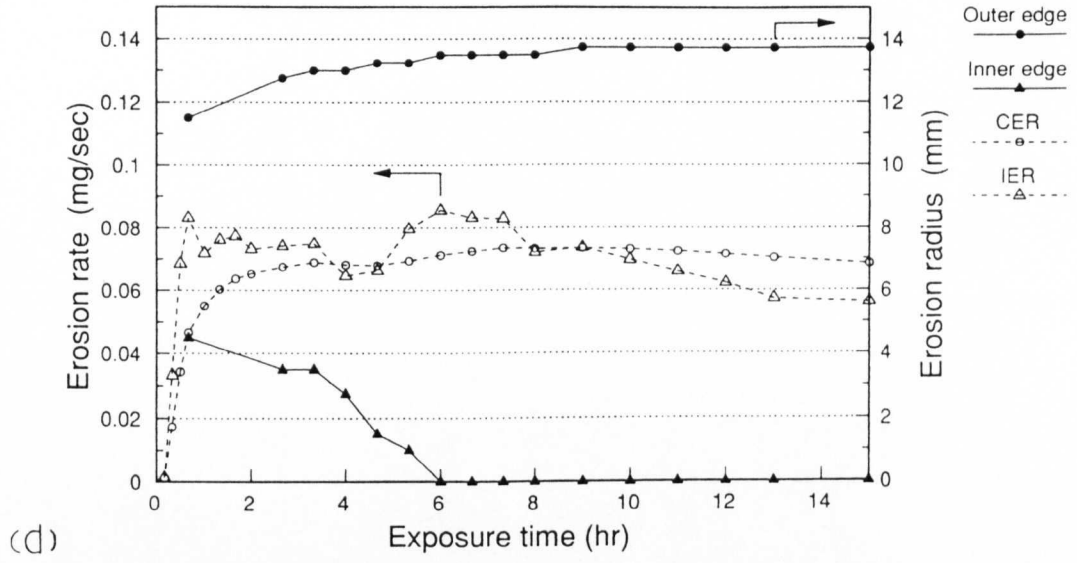

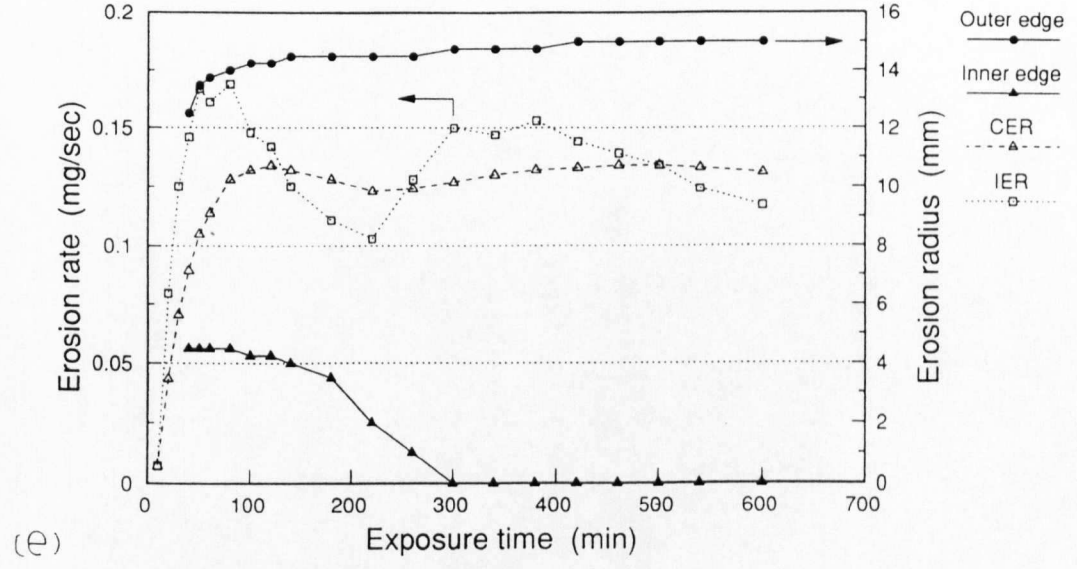

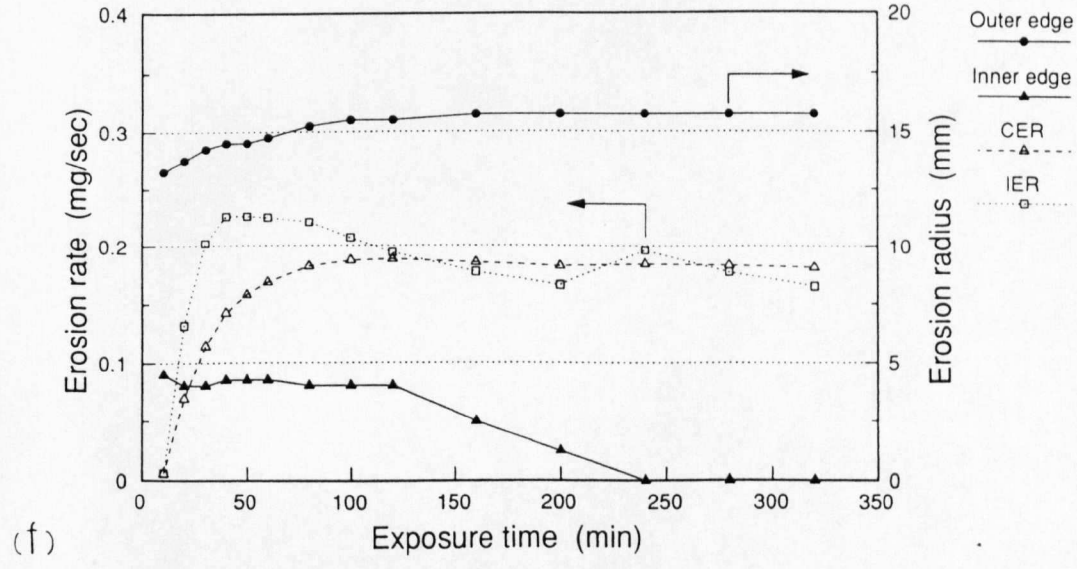

Fig.7.2.6 Erosion ring radius and erosion rate with exposure time.
(d) P_1=120bar, P_2=3.6bar, σ=0.03, S_{off_2}=40mm; (e) P_1=120bar, P_2=3.0bar, σ=0.025, S_{off_2}=45mm; (f) P_1=120bar, P_2=2.4bar, σ=0.02, S_{off_2}=57mm.

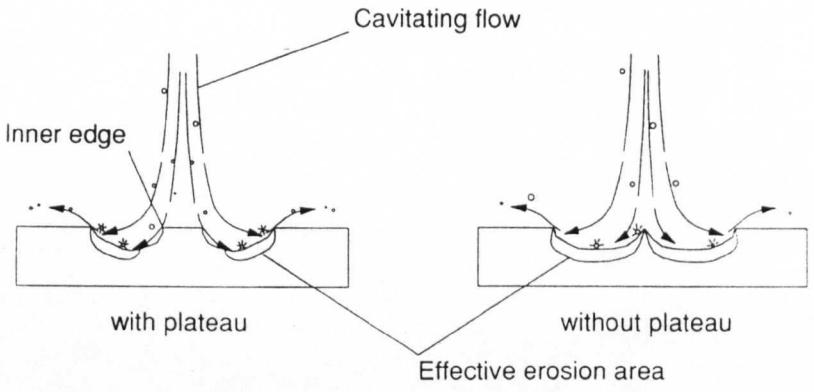

Fig.7.2.7 Schematics of specimen surface condition during erosion development.

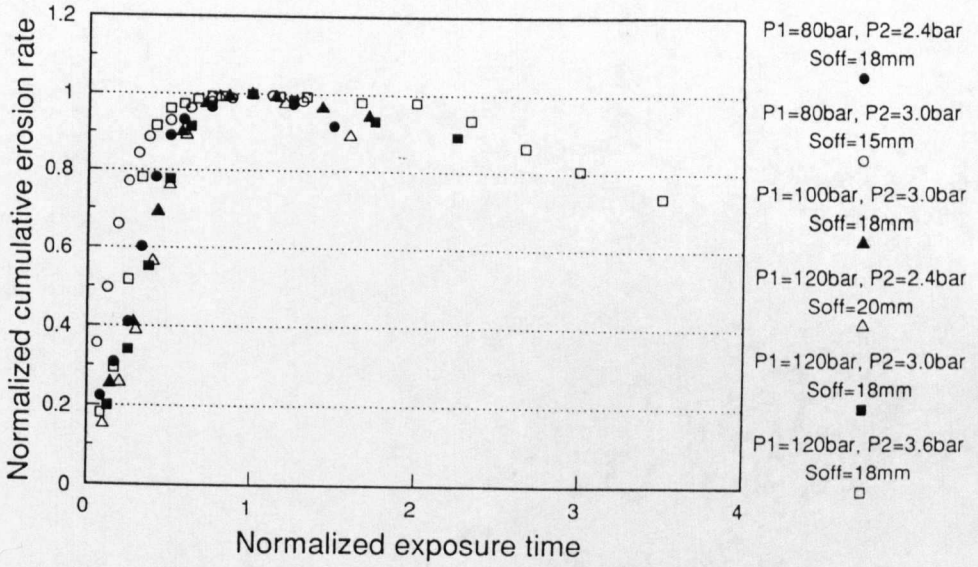

Fig.7.2.8 Normalized cumulative erosion rate with normalized exposure time. At the first optimum stand off distance.

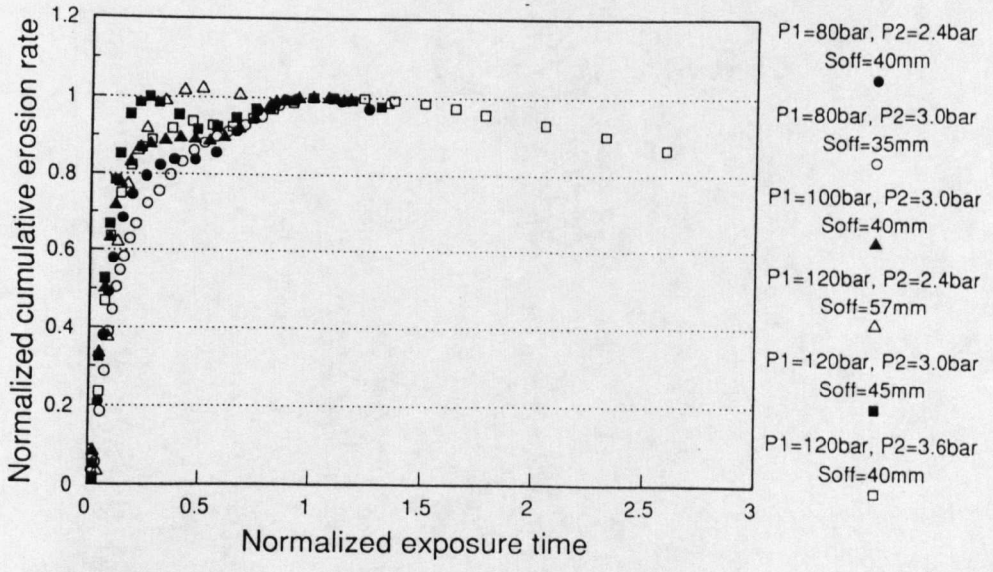

Fig.7.2.9 Normalized cumulative erosion rate with normalized exposure time. At the second optimum stand off distance.

The peak erosion rates PER for several pressures are plotted against upstream pressures P_1 maintaining constant cavitation number σ=0.03 in Fig.7.3.1, and maintaining constant downstream pressure P_2=3.0bar in Fig.7.3.2. All sets of peak erosion rates are showing remarkably good power law relation with P_1 (straight lines on log-log plots) except the ones at S_{off1} with constant P_2.

As described in Chapter 3, Knapp [1955] reported the well known sixth power variation of number of indentations on soft aluminium specimen with flow velocity.

It can be expressed as,

$$N \propto V^n$$

where N is the number of indentations and V is the flow velocity. The index n was calculated to be approximately six in his paper. After this, many other investigators reported rather wide range of index numbers; e.g., mainly six but ranging from -1 to 12 were listed by Ramamurthy and Bhaskaran [1979]. These are normally calculated with some sort of erosion rate instead of counting the number of indentations. The velocity exponent calculated using the peak cumulative erosion rate PER_C from Fig.7.3.1 and Fig.7.3.2 are listed in Table 7.3.1.

Table 7.3.1 Velocity exponent, n

P_1 (bar)	P_2 (bar)	σ	Index n	
			S_{off1}	S_{off2}
80 - 120	2.4 - 3.6	0.03 (const.)	6.6	6.2
80 - 120	3.0 (const.)	0.0375 - 0.025	-	13.8

As long as the cavitation number is kept constant, σ=0.03, the indices n varying only within a small range from 6.6 at the first optimum stand off distance S_{off1} to 6.2 at the second optimum stand off distance S_{off2} were obtained. With the constant downstream pressure P_2=3.0bar, however, the index at S_{off2} is very large, n=13.8, and no linear relation is found on the log-log graph at S_{off1}. It should be realized here that changing the upstream pressure while keeping the downstream pressure constant

means also changing cavitation number. For example, increasing upstream pressure with constant downstream pressure proportionally decreases the cavitation number. Lower cavitation number means longer, wider and usually more damaging cavitating jet. At the same time the decay of the jet velocity (the stagnation pressure) along the jet axis is also reduced (see Fig.6.3.4). Therefore the index n tends to become greater and so the index n=6.2 with constant σ is increased to n=13.8 with constant P_2 at S_{off2}. However, the reason why the good exponential relation at S_{off1} (showing the index n=6.6) with constant σ vanishes, when they are treated with constant P_2, has not been understood. It is thought that probably PER at S_{off1} is not so much affected by the change in cavitation number than PER at S_{off2}.

Kleinbreuer [1977] obtained index n=9 with oil maintaining the downstream pressure constant and Lichtarowicz and Kay [1983] reported n=8.2~9.1 with oil and n=7.5~10.4 with water maintaining cavitation number constant. As Lichtarowicz and Kay presented, those indices are plotted with the present data in Fig.7.3.3. The present data with water, n=6.6 (at S_{off1}) and 6.2 (at S_{off2}) with constant σ, agree well with the results by Lichtarowicz and Kay. The test rig configuration, such as a type of a nozzle holder and a test chamber, is different from the rig used by Lichtarowicz and Kay and the number of data in Fig.7.3.3 is still limited, but they show the possibility of the dependence of index n on cavitation number σ.

Figures 7.3.4 and 7.3.5 show cumulative erosion rates with exposure time at both optimum stand off distance, S_{off1}=18mm and S_{off2}=40mm, for P_1=80, 100 and 120bar maintaining the constant cavitation number σ=0.03. The developments of CER for three different P_1 are in similar shapes. Apparently, as the upstream pressure level increases, degree of CER is raised and the time to reach PER is reduced. Variation of exposure time to reach PER_I and PER_C with P_1 is shown in Fig.7.3.6. Cavitation number σ=0.03 is kept constant. As Lichtarowicz and Kay [1983] described, the results indicate that the relation of the time to reach PER, T_{max}, with jet velocity, V, can be expressed as

$$T_{max} \propto V^{-m}$$

The index is approximately m=7.0 at S_{off1} and S_{off2} for PER_C.

Figure 7.3.7 shows variation of peak erosion rate with cavitation number σ (so downstream pressure P_2) with the constant upstream pressure P_1=120bar. Both peak erosion rate, PER_I and PER_C, at S_{off2} are rapidly decreasing with increase of

cavitation number as expected, but the ones at S_{off} show different tendency. They seem to be not so much affected by cavitation number (or downstream pressure) and in fact, even the highest PER_I and PER_C are found at the largest cavitation number σ=0.03 with which the cavitation erosion capacity is supposed to be the weakest. One of the reasons for this can be understood as follows.

(1) The jet is already cavitating from the inlet edge of the nozzle and so there is no effect of the downstream pressure on the cavitation inside the nozzle.

(2) The actual distance between the nozzle plate and the target is very small (5mm shorter than the stand off distance; 5mm is the thickness of the nozzle.) and the jet is intensively cavitating. In addition, the upstream pressure is much higher than the downstream pressure. Therefore the effect of P_2 on the jet velocity, in other words, on the attenuation of the jet velocity is negligibly small.

(3) Because of such a very small distance between the nozzle plate and the target, there may be no sufficient time for the downstream pressure to actually affect the state of the cavitation of the jet; i.e., the number and the size of cavities.

Then, if the difference in the cavitating jet velocity and the number and the size of cavities are negligibly small, it can be said that there is no substantial effect of changing downstream pressure P_2 on the state of the cavitating jet. On the other hand, the change in the downstream pressure is almost equal to the change in the pressure difference between the ambient pressure and the vapour pressure of the cavity. This clearly has an effect on the collapse and the erosion capacity of each cavity; i.e., the larger the pressure difference is, the more the intensive erosion can be obtained. This may explain the results which show the highest PER_I and PER_C at the least intensive cavitation number σ=0.03 (at the highest P_2) in Fig.7.3.7.

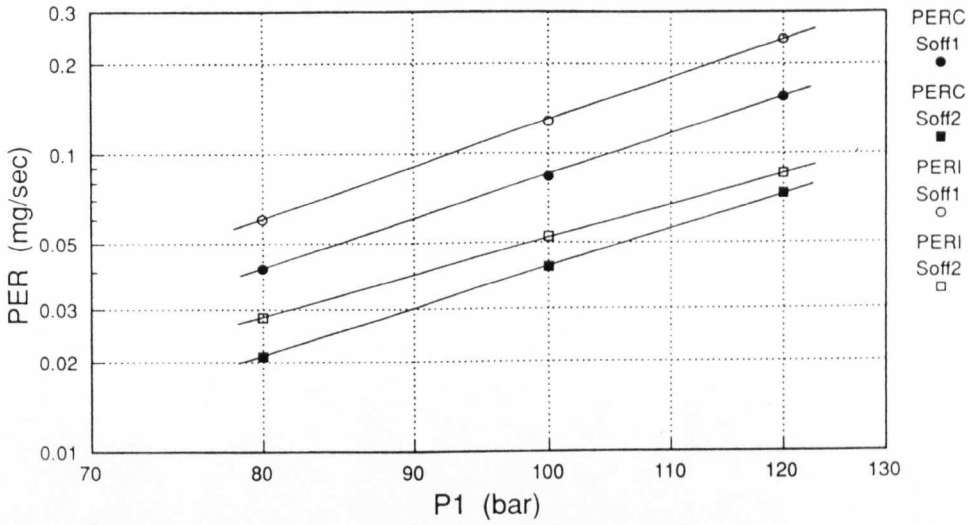

Fig.7.3.1 Variation of peak erosion rate with upstream pressure.
Constant cavitation number σ=0.03, at the first (S_{off1}) and the second optimum stand off distance (S_{off2}).

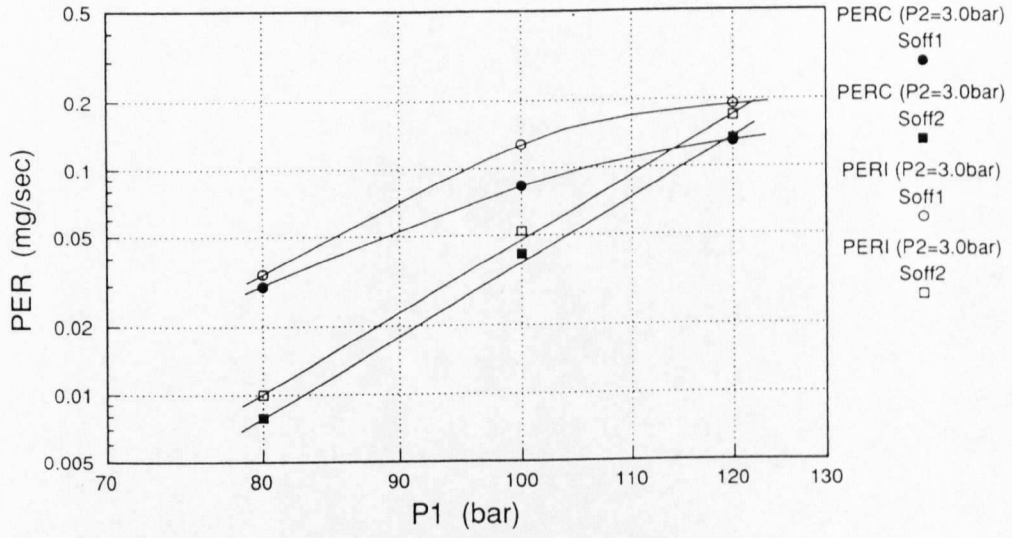

Fig.7.3.2 Variation of peak erosion rate with upstream pressure.
Constant downstream pressure P_2=3.0bar at the first (S_{off1}) and the second optimum stand off distance (S_{off2}).

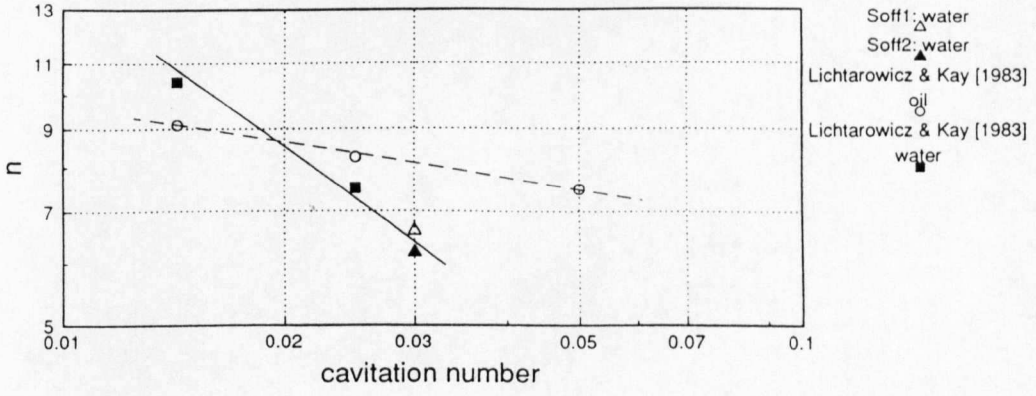

Fig.7.3.3 Variation of index n with cavitation number.

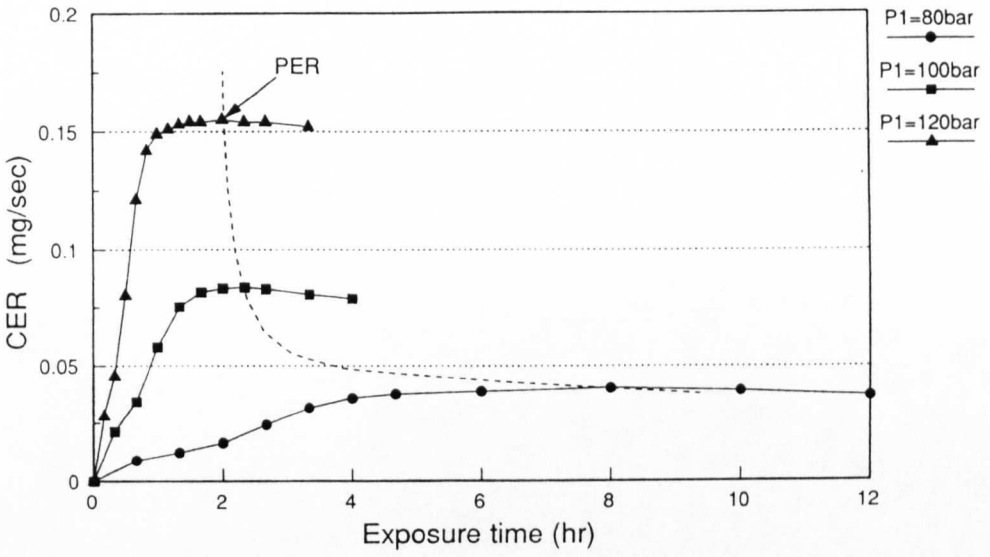

Fig.7.3.4 Cumulative erosion rate with exposure time.
P_1=80, 100 and 120bar, σ=0.03, S_{off_1}=18mm

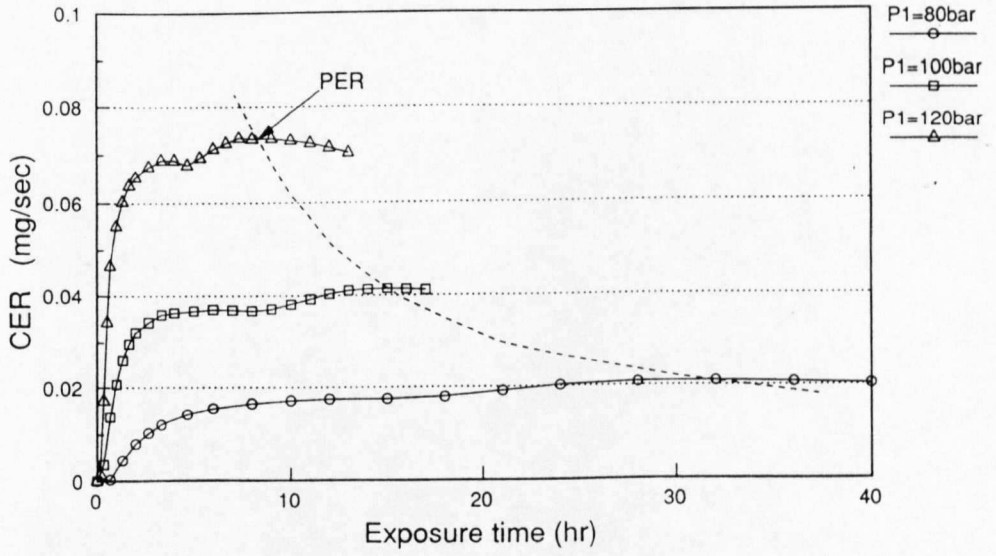

Fig.7.3.5 Cumulative erosion rate with exposure time.
P_1=80, 100 and 120bar, σ=0.03, S_{off_2}=40mm

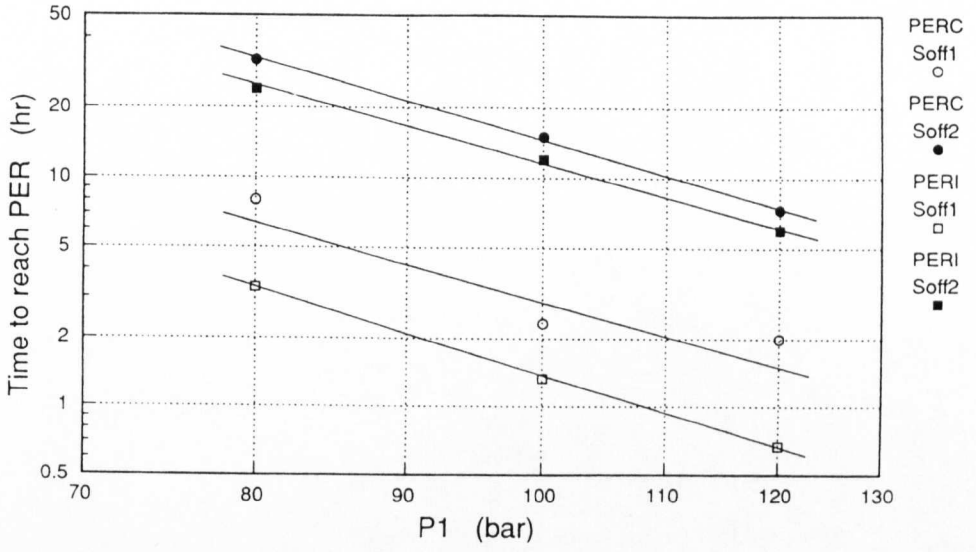

Fig.7.3.6 Variation of time to reach peak erosion rate with upstream pressure. Constant cavitation number σ=0.03, at the first (S_{off1}) and the second optimum stand off distance (S_{off2}).

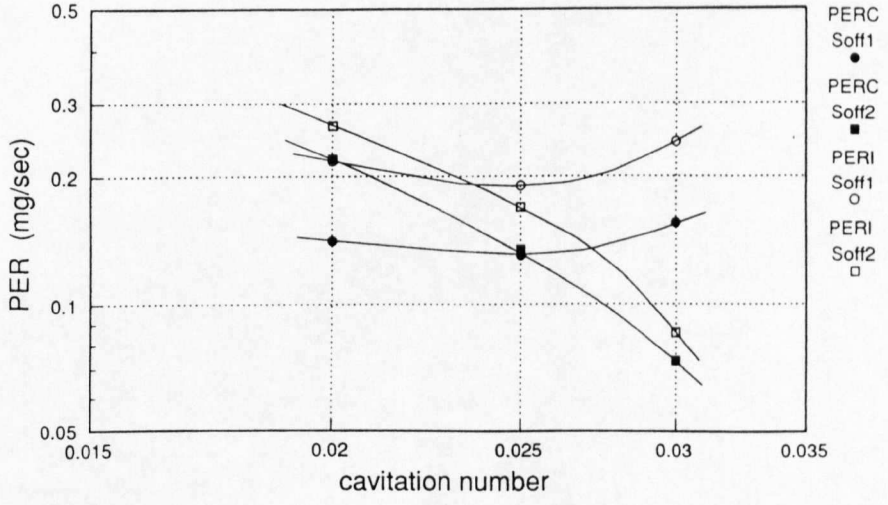

Fig.7.3.7 Variation of peak erosion rate with cavitation number σ (downstream pressure P_2). Constant upstream pressure P_1=120bar, at the first (S_{off1}) and the second optimum stand off distance (S_{off2}).

Main results and discussions in this chapter are summarized as follows.

(1) The shape of the weight loss curve with stand off distances and the position of the optimum stand off distance depend on cavitation number.

(2) The relation between the optimum stand off distance and cavitation number can be expressed as

$$\frac{S_{off}}{d_e} \propto \sigma^{-h_2}$$

where index h_2 is about $h_2 \approx 0.9$ for the second optimum stand off distance S_{off2} and $h_2 \approx 0.4$ for the first optimum stand off distance S_{off1}. The index h_2 for S_{off2} agrees very well with the index $h_1 \approx 1.0$ for the cavitating jet length obtained in Chapter 6, whereas the index h_2 for S_{off1} is much smaller than 1.0. It appears likely that the index h_2 depends on the individual test rig configuration.

(3) As expected from above, the ratios of the optimum stand off distance to the average jet length in each cavitation number show consistent values from 0.75~0.78 for S_{off2}, but range widely from 0.27~0.36 for S_{off1}.

(4) Each erosion ring radius except the inner edge of the first ring at the second optimum stand off distance is not changed by the cavitation exposure in spite of the rapidly increasing weight loss value. Therefore, it can be concluded that the increase in weight loss results mainly from the erosion development in depth.

(5) The optimum stand off distance occurs at the stand off distance where the ring erosion area also shows its peak. This indicates that the area of the damage may be playing an important role in producing the maximum weight loss at the optimum stand off distance.

(6) The dependency of the optimum stand off distance on the cavitating jet length and

on the area of the erosion ring, which has been described in above (3) and (5), can be used as techniques which help to find the optimum stand off distance more easily. For example, possible range of S_{off2} can be predicted by simply obtaining a mean jet length from a number of high speed photographs or perhaps by measuring the jet length from one long exposure photograph. Measuring the size of erosion ring on the soft material may also be able to be used to reduce the time to find both S_{off1} and S_{off2}.

(7) The phenomena that erosion rate depends on the state of the target surface are observed. For example,

a.) One optimum stand off distance at one exposure time was slightly changed to another value after additional cavitation exposure; i.e., from the one at the early stage of damage to another at much more matured stage of erosion.

b.) The erosion rate suddenly re-increases with the disappearance of the inner edge radius (centre uneroded part) in time, at the second optimum stand off distance.

(8) When cavitation number is maintained constant σ=0.03, the velocity exponent to the peak cumulative erosion rate PER_C is n=6.6 at S_{off1} and n=6.2 at S_{off2}. With the constant downstream pressure P_2=3.0bar, however, the velocity exponent at S_{off2} is very large, n=13.8, and no linear relation is found on the log-log graph at S_{off1}.

(9) As the upstream pressure level increases, degree of erosion rate is raised and the time to reach peak erosion rate is reduced. The relation of the time to reach the peak erosion rate, T_{max}, with jet velocity, V, for constant σ=0.03 can be expressed as

$$T_{max} \propto V^{-m}$$

The index is approximately m=7.0 at S_{off1} and S_{off2} for PER_C.

(10) Peak erosion rate at S_{off1} seems to be not so much affected by cavitation number (downstream pressure P_2) as the one at S_{off2}. One reason for this can be understood that there may be no sufficient time for the downstream pressure to actually affect the state of the cavitation of the jet, i.e., the jet velocity and the number and the size of

cavities, since the actual distance between the nozzle plate and the target is very small (5mm smaller than the stand off distance). On the other hand, the increase in downstream pressure means the increase in the pressure difference between the ambient pressure and the vapour pressure of the cavity. This also increases the erosion capacity of each cavity when the other conditions are constant. This may explain the results which show the highest PER at the least intensive cavitation number σ=0.03 (at the highest P_2) in Fig.7.3.7.

CHAPTER EIGHT - RESULTS:
Cavitation loading (I) --- Indentation counting

---

8. RESULTS: Cavitation loading (I) --- Indentation counting

8.1 Indentations on soft material

When a cavitation bubble collapses close to the solid boundary, a microjet is formed during the collapsing process and subsequently shock wave is generated at the moment of rebounding just after the collapse of the bubble. Both microjet and shock wave impingements are regarded as the possible mechanism of cavitation damage. Small plastic deformations (indentations) in relatively soft materials and/or micro cracks in hard materials are direct results of these damage mechanisms and their accumulation causes severe erosion through a fatigue erosion process. The erosion process from the initial indentation to the matured erosion stage was presented by series of photographs of a specimen surface at both the first and the second optimum stand off distance in Fig.6.4.1, and their surface profiles in Fig.6.4.2. There is an incubation time through which the surface roughness is continuously being developed without any change in total weight of the specimen.

Only a limited investigations on the initial indentations have been reported. However, it is regarded as a very useful method for understanding the characteristics of a cavitation damage under various pressure conditions. For example, the number of impingements and the size of each impingement can be regarded as important elements of quantifying cavitation erosion intensity.

In this chapter, the results of indentation counting test using the computer image analyzer are presented. The purpose of the experiments is to obtain the detailed quantitative data concerning cavitation loading under various conditions using the soft aluminium alloy as a "pressure recorder".

Indentations were produced on the soft annealed 1200-aluminium (99.00% purity) target by a short time exposure to a cavitating jet, usually for only a few seconds. They are distributed in a ring like damage area as described in previous chapters. Examples of the 1200-aluminium specimen before and after the testing are shown in a photograph in Fig.8.2.1. The surface of the specimen was polished with 1 micron diamond paste before the cavitation exposure as described in Chapter 5 (the right specimen in Fig.8.2.1). The left specimen in Fig.8.2.1 was exposed to the cavitating jet with P_1=100bar and σ=0.03 (P_2=3.0bar) at S_{off}=18mm for 2.19sec. A lot of small indentations can be seen on the surface.

Typical micrographs of indentations on the target are shown in Fig.8.2.2. The test condition is P_1=100bar, P_2=3.0bar and S_{off}=25mm. These were taken directly from the computer display screen of the image analyzer. The size of each frame is 0.84mmx0.84mm. Because of the enhancement effect due to the use of optical liquid, the surface which is inclined at a small angle and which cannot reflect the light back to an object lens is clearly shown as a black shadow. Fine lines observed on the surface are scratch marks made through the polishing process using one micron diamond paste and hence they are not removable. It seems that the indentations are randomly distributed and each indentation shows generally a circle shape except some of larger ones which have more varieties in their shapes. Some, probably relatively shallow, indentations show their flat bottoms as a brightly shining part at the centre of each indentation. Size of indentations counted ranges widely from few micron to approximately 350 micron, but generally, such very large ones are found only on the severely damaged areas. In order to make sure that the density of indentations is sufficiently low to avoid possible counting of overlapped indentations, the ratio of the total indentation area to the frame was checked. It ranges within 5~10% at the most densely damaged frame in each case. Although there is no information about depth because of its measuring difficulty, their boundary edge seems very distinguishable. According to the many observation of single bubble collapse in still water (Ellis, Lauterborn, etc.), it is likely that the microjet diameter is about one tenth of the initial bubble diameter or smaller, and consequently in the present case the initial bubble diameter for the largest indentation is expected to be around 3mm or larger. No such

large bubbles can be found in photographs of cavitating jets shown in Fig.6.2.4, though the number of photographs is limited.

Figure 8.2.3 shows SEM (scanning electron microscope) photograph of indentations on the same specimen as shown in Fig.8.2.2. The scanning electron microscope was able to show three dimensional view of indentations. Indentations are generally of a conical shape with or without some flat portion at the bottom, and so it is thought that the mechanism to create those indentations is more likely to be of a microjet type impingement than of a shockwave. The size of the particular indentation at the centre of Fig.8.2.3 is approximately 80~100μm in diameter. It may be possible to roughly estimate the depth of the indentation from the photograph, because the angle of SEM is known, 30 degree from the surface. The depth was measured and is approximately 10μm. Robinson and Hammitt [1967], Stinebring et al. [1980] and Rao and Buckley [1983] investigated the ratio of the depth, h, to the radius at the surface, a, of indentations on pure aluminium and aluminium alloy and reported h/a to be 0.068~0.333 in water. Therefore, the ratio, h/a=0.2~0.25, obtained for the particular indentation is within the range of their results.

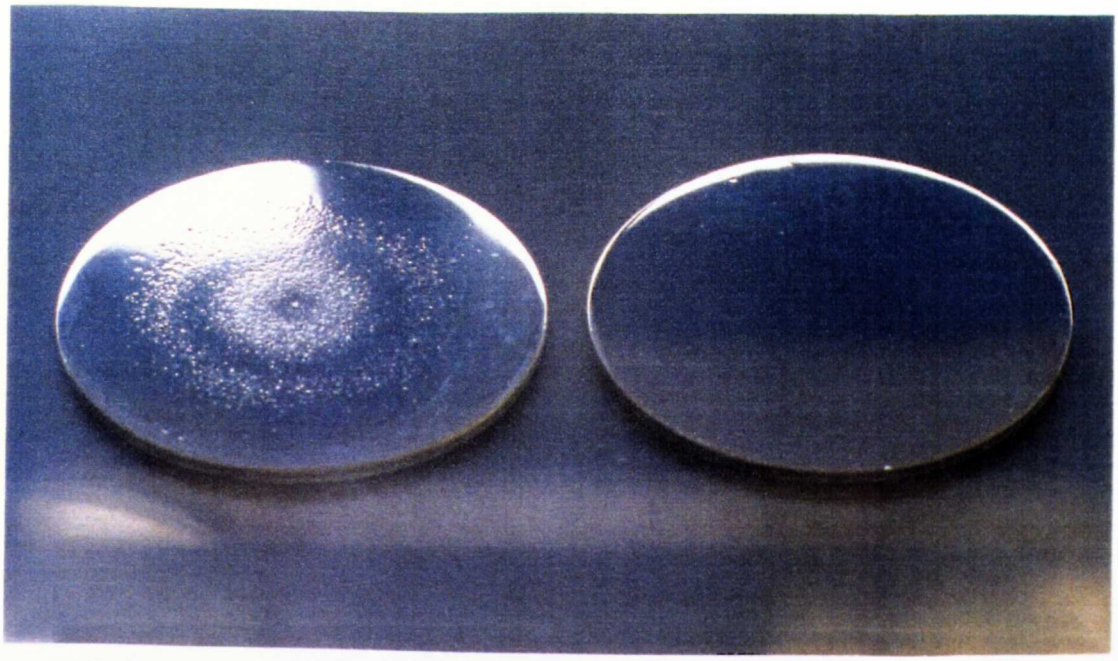

Fig.8.2.1 Indentations produced by cavitation loadings on annealed 1200-aluminium alloy disc.

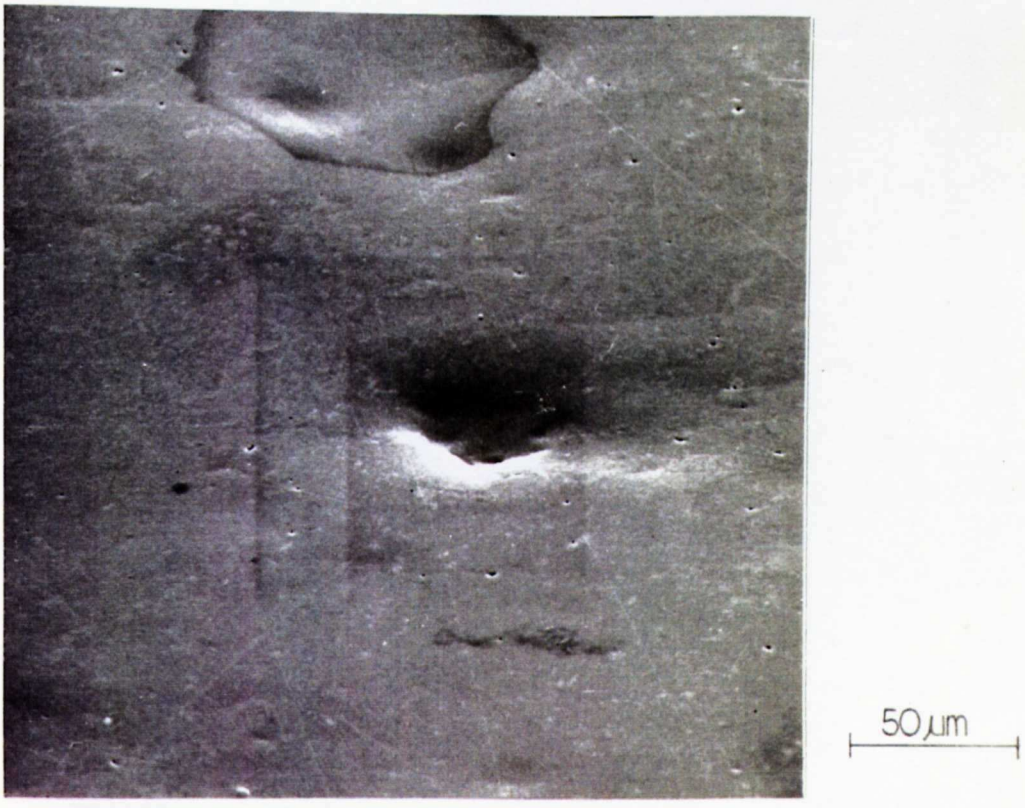

Fig.8.2.3 SEM photographs of indentations.
P_1=100bar, P_2=3.0bar, σ=0.03, S_{off}=25mm.

(a)

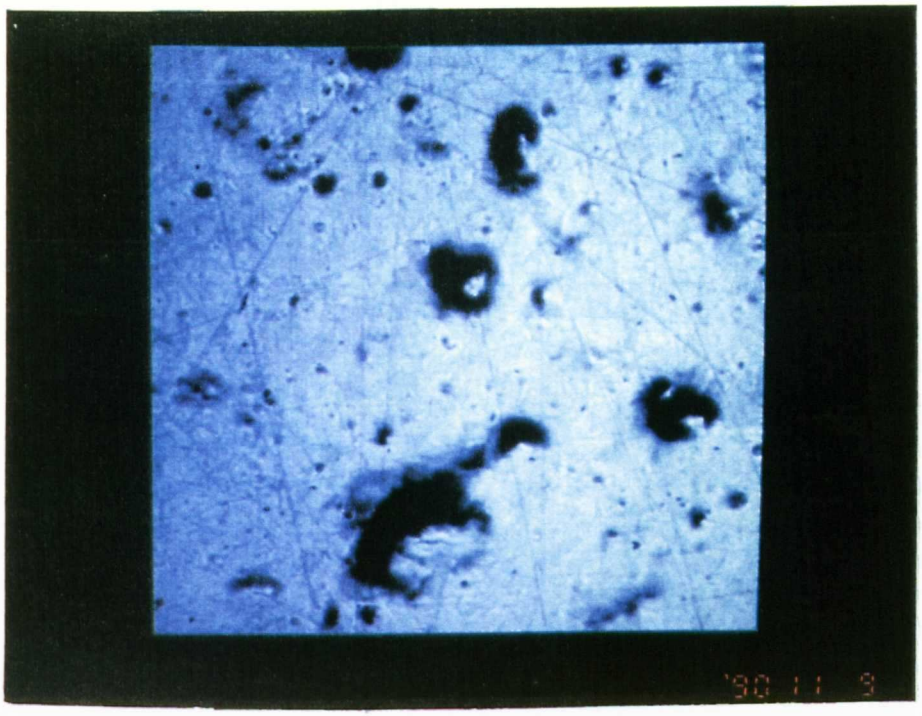

(b)

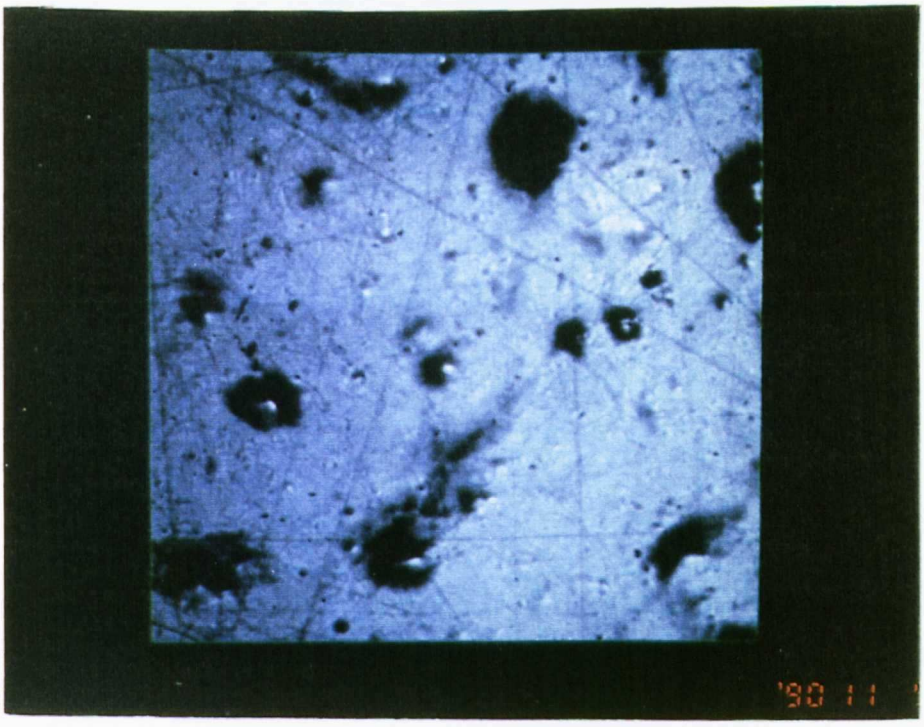

Fig.8.2.2 Micrographs of damaged surface.
P_1=100bar, P_2=3.0bar, σ=0.03, S_{off}=25mm.

As described in Chapter 5, images of the surface condition on the specimen were captured by the image analyzer in a square shaped frame of 0.84mmx0.84mm. Then, the indented specimen surface was scanned, frame by frame, from the centre to the outside edge of the damaged area. Four scanning paths for each disc were used. (See Appendix A2 for the detailed process of image analysis for indentation counting.) The counting results of eight frames (total area is 5.64mm^2; 8x0.84mmx0.84mm), two adjacent frames from each of four scanning paths at the same radial distance from the centre of the damage, were averaged and used as the data at the corresponding radial distance.

Distributions of number density of indentations (number of indentations per unit time and unit area) at the first optimum stand off distance, S_{off1}=18mm, and the second optimum stand off distance, S_{off2}=40mm, for upstream pressure P_1=100bar and cavitation number σ=0.03 (downstream pressure P_2=3.0bar) are plotted in Fig.8.3.1. The size of damage, such as inner edge, outer edge (1st ring) and outer edge (2nd ring), measured in the erosion test for the same condition (Chapter 7) is shown by vertical lines in the figure. There are two peaks for S_{off1} and almost no indentation were counted at the centre of the specimen for both S_{off1} and S_{off2} as observed in the erosion tests. The peak locations of the number of indentations agree very well with the damage area indicated by the vertical lines for both stand off distances. The actual counts at the peak are about 30 counts/(mm^2·sec) and 5 counts/(mm^2·sec) for S_{off1} and S_{off2}, respectively. In the present tests, however, indentations smaller than 10micron in diameter were not counted.

For the same test conditions as Fig.8.3.1, distributions of area density of indentations (the sum of each indentation area per unit time and unit area) are plotted in Fig.8.3.2. Relatively, the peak height of S_{off2} increases, while both curves are in a similar shape of those in Fig.8.3.1. The area density of indentations at the peak is approximately 0.035mm^2/(mm^2·sec) and 0.01mm^2/(mm^2·sec) for S_{off1} and S_{off2}, respectively. This means that in each second 3.5% and 1% of the surface is covered by the damage and on an average it takes about 30sec and 100sec, respectively, to cover the entire surface with indentations at the peak damage area.

Since the material used here is soft and ductile, the volume of plastic

deformation is reasonably regarded to be proportional to the damaging energy of the cavitating jet absorbed to the material. And it is possible to assume that the cube of reference length, e.g. diameter, is proportional to the volume of plastic deformation and is able to be used as a measure of erosion intensity. Figure 8.3.3 shows the sum of $(\text{diameter})^3$ of each indentation ($\Sigma(\text{diameter})^3$ in the figure) for the same test conditions as in Fig.8.3.1. In order to estimate the contribution of $(\text{diameter})^3$ distribution on an entire target to the amount of total damage (weight loss), the sum of $(\text{diameter})^3$ was calculated for the area of 1.68mm width (two frames size) ring at the radial distance as shown in Fig.8.3.4. Therefore, if the $(\text{diameter})^3$ in Fig.8.3.3 is integrated over the area from the centre to the outer edge of the target, the measure of the total cavitation intensity on a whole target disc can be obtained. These values for various cases will be compared with the peak erosion rate later in this chapter and also with cavitation loading pulse height results in the next chapter. In Fig.8.3.3, the relative peak height at S_{off2} to the one at S_{off1} further increases from Fig.8.3.2. This simply means that there is a greater portion of larger size indentations at the peak damage area at S_{off2}. Another increase of the relative peak height at the second ring at S_{off1} to the one at the first ring is due to the difference in area of the 1.68mm width ring used in the calculation (Fig.8.3.4).

The relative distribution curves of the sum of $(\text{diameter})^3$ for P_1=100bar and σ=0.03 (P_2=3.0bar) at S_{off}=15~45mm are shown together with the nozzle and the nozzle holder configuration around the jet in Fig.8.3.5. The peaks of the second ring distribution at relatively small stand off distances, S_{off}=15~25mm, are located just inside the outside edge of the nozzle holder's lip, though no sufficient information is available to find a decisive reason for this hydrodynamic problem. The size of the damage area is not so clearly found this time so that it may be not a straightforward process to predict the location of the optimum stand off distances from the indentation counting. In order to quantify the intensity of cavitation damage, the sum of $(\text{diameter})^3$ is integrated on the entire surface of the target. Variation of those results of integration with S_{off}=15~45mm is plotted and compared with variation of the total number of indentations on a whole target surface and the cumulative erosion rate CER at ΔT=100min in normalised form in Fig.8.3.6. All three show the similar tendencies, but the cumulative erosion rate agrees better with the sum of $(\text{diameter})^3$ than with the total number at S_{off2}=40mm.

Variation of the sum of (diameter)^3 at the first optimum stand off distance, S_{off1}=18mm, for P_1=80bar, 100bar and 120bar with constant cavitation number σ=0.03 are plotted in Fig.8.3.7. All three show similar distribution shapes with identical two peak locations. As expected, the higher the upstream pressure P_1, the higher the peak height of (diameter)^3 at both peaks. Here, however, if the damage mechanism producing these indentations is of the microjet type, there may be a possible effect of downstream pressure on the velocity of a microjet and so on the depth of indentations. Lush [1983] reported that the depth-diameter ratio of indentation produced by microjet impingement on ductile material would be proportional to the microjet velocity, and it is possible to assume the microjet velocity to be proportional to the square root of down stream pressure. In that case, the depth can be greater with higher ambient pressure. This effect is not included in Fig.8.3.7 and if it is likely, the gap of the peak height among three pressures is going to become wider. Figure 8.3.8 is the same sort of distribution as Fig.8.3.7 for the second optimum stand off distance S_{off2}=40mm. Each result also shows a peak in the same region of the erosion ring, but this time the peak for P_1=120bar is lower than the one for P_1=100bar. There is no understandable explanation for this except the one due to the experimental error.

Figure 8.3.9 shows the sum of (diameter)^3 distribution for various cavitation number σ=0.02~0.03 (P_2=2.4~3.6bar) with constant P_1=120bar at S_{off1}. Although the erosion intensity for σ=0.03 is usually supposed to be the smallest among three cases in Fig.8.3.9 because of the largest cavitation number, the results for σ=0.03 (P_2=3.6bar) show larger values than the one for σ=0.025 (P_2=3.0bar). Similar results have also been obtained from the erosion tests in Fig.7.3.7 and have been discussed in Chapter 7 and so this tendency is supported by both techniques, an weight loss measurement and indentation counting. The peak for the smallest cavitation number σ=0.02 is at about the same height as the one for σ=0.03 but much wider than the others. The peak of the second erosion ring for σ=0.02 is much larger and located at greater radial distance from the damage centre. The sum of (diameter)^3 distributions for the same pressure conditions as Fig.8.3.9 at S_{off2} are shown in Fig.8.3.10. The peak for the smallest cavitation number σ=0.02 (P_2=2.4bar) is much higher than the one for σ=0.03 and is about the same level of σ=0.025, but is much wider than the other two.

Generally, the results obtained from indentation counting agree well with the erosion test results concerning the erosion shape, its size and magnitude of erosion

intensity, though there are some which contradict the tendency of cavitation erosion obtained from the weight loss tests. Possible cause of these experimental errors are follows.

(1) The frame size of the image analyzer, 0.84mmx0.84mm, may be too small compared with the size of the indentations ranging up to about 350μm in equivalent diameter. When such a large indentation is located on one edge of the frame, which is quite likely to happen, the analysis must either entirely include it or entirely neglect it (see Appendix A2). Since particularly the greater size indentation plays a predominant role in the distribution of the sum of (diameter)^3, sometime the results may be fluctuating.

(2) Four 0.84mm width paths of scanning the target from the centre may not be able to collect sufficient amount of information to obtain reasonably averaged results.

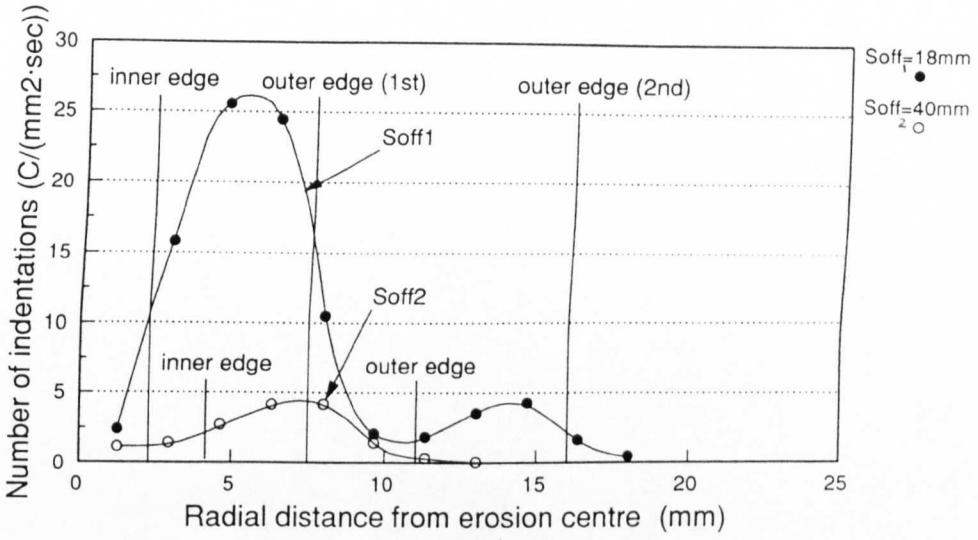

Fig.8.3.1 Distributions of number density of indentations on a specimen disc. P_1=100bar, P_2=3.0bar, σ=0.03, S_{off}=18 and 40mm.

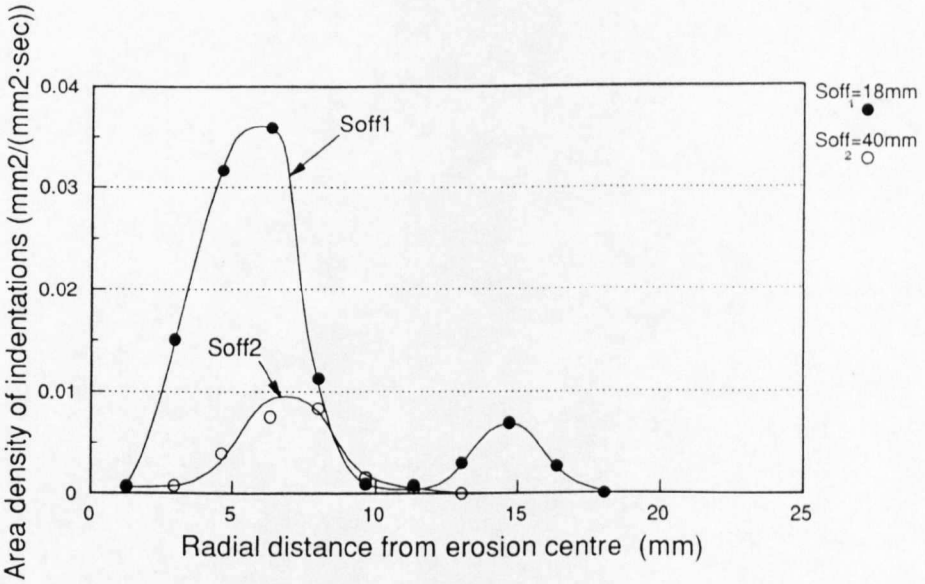

Fig.8.3.2 Distributions of area density of indentations on a specimen disc. P_1=100bar, P_2=3.0bar, σ=0.03, S_{off}=18 and 40mm.

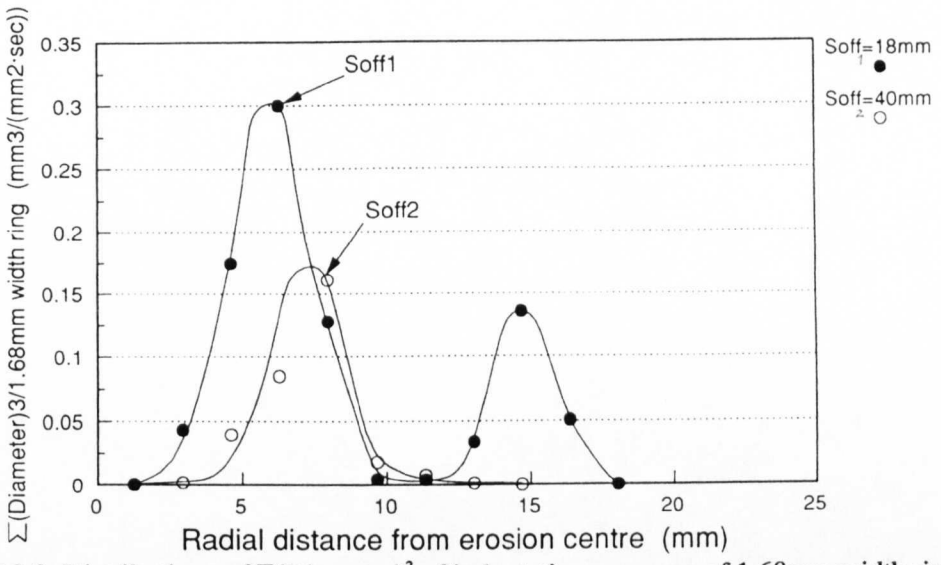

Fig.8.3.3 Distributions of $\Sigma(\text{Diameter})^3$ of indentations per area of 1.68mm width ring at a corresponding radius per unit time.
P_1=100bar, P_2=3.0bar, σ=0.03, S_{off}=18 and 40mm.

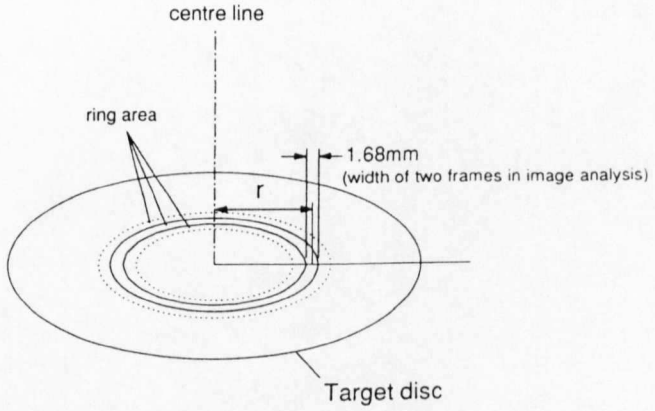

Fig.8.3.4 1.68mm width ring.

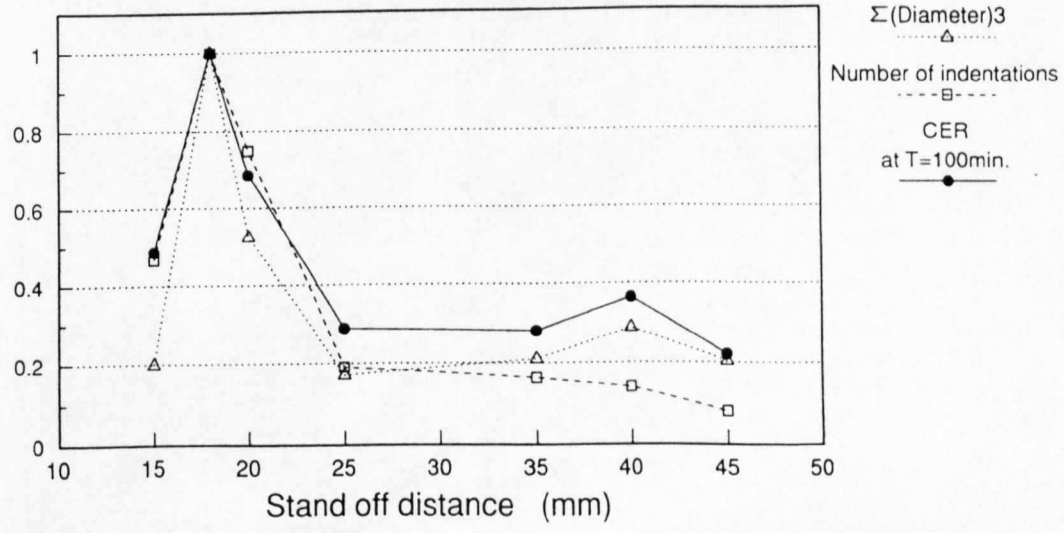

Fig.8.3.6 Variation of number and $\Sigma(\text{Diameter})^3$ of indentations estimated for the entire disc per unit time with stand off distance.
Values are normalized at S_{off_1}=18mm. P_1=100bar, P_2=3.0bar, σ=0.03.

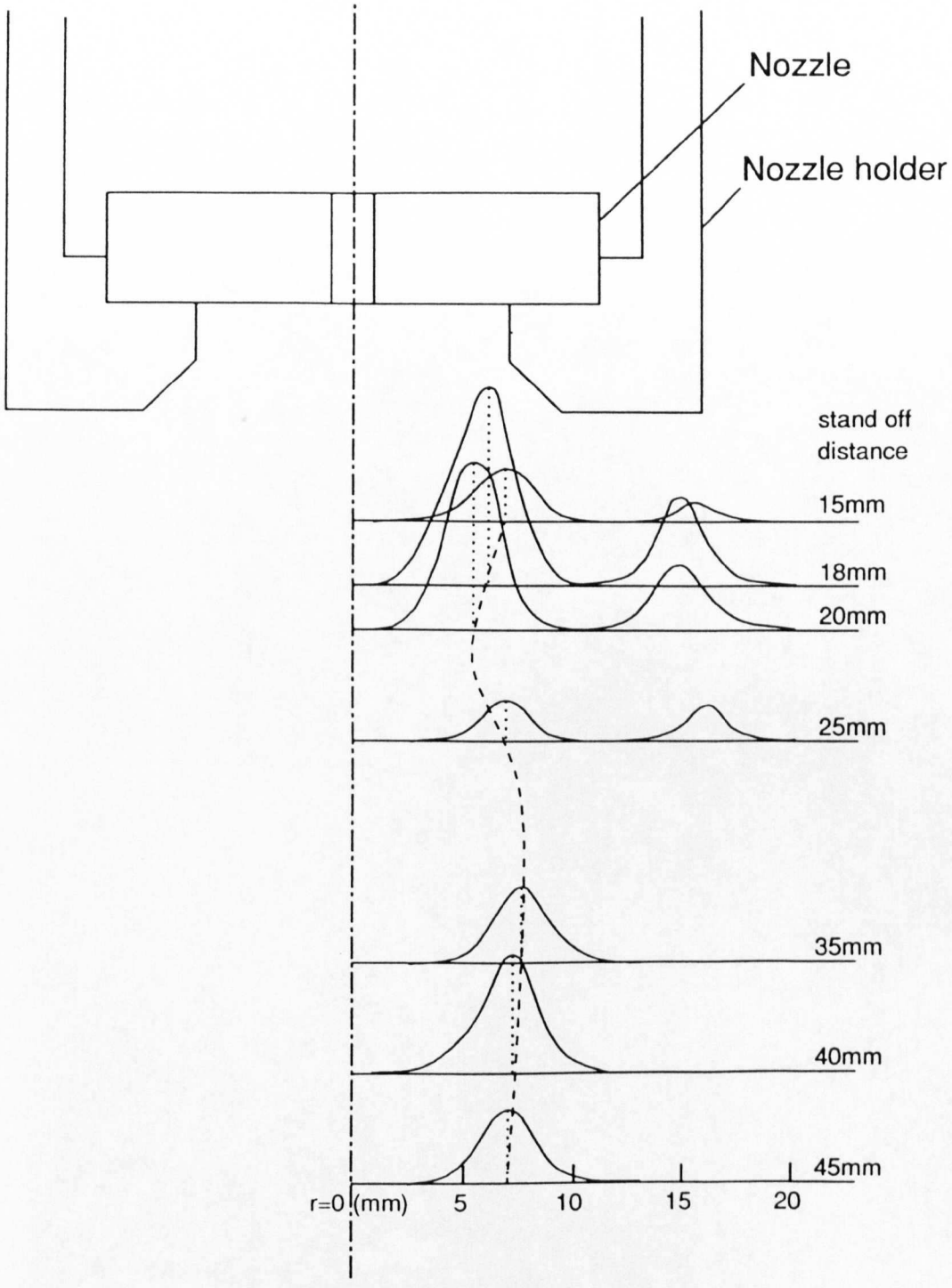

Fig.8.3.5 Relative distributions of $\Sigma(\text{Diameter})^3$ of indentations per area of 1.68mm width ring at a corresponding radius per unit time, with stand off distance. P_1=100bar, P_2=3.0bar, σ=0.03.

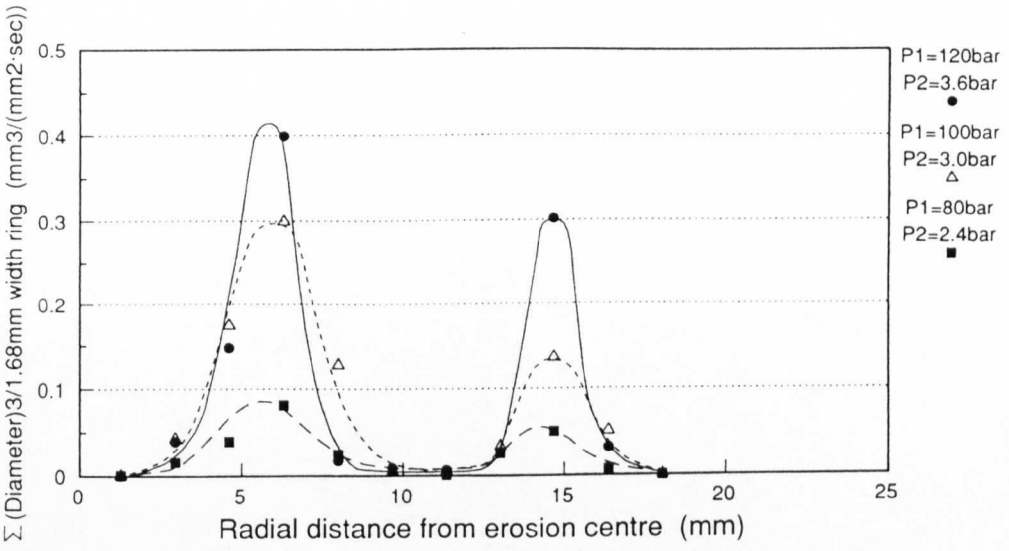

Fig.8.3.7 Distribution of $\Sigma(\text{Diameter})^3$ of indentations per unit time.
Constant cavitation number σ=0.03, P_1=80, 100 and 120bar, S_{off_1}=18mm.

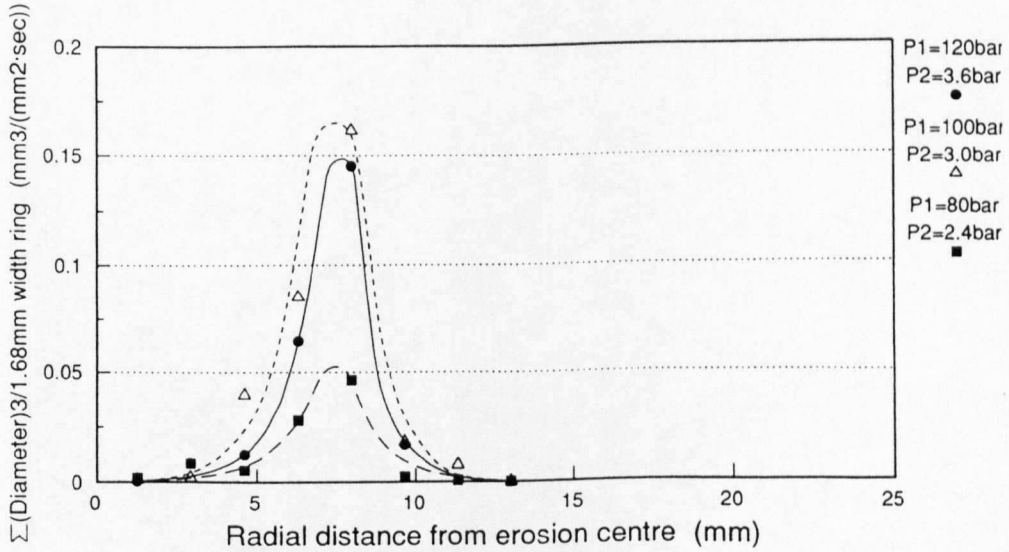

Fig.8.3.8 Distribution of $\Sigma(\text{Diameter})^3$ of indentations per unit time.
Constant cavitation number σ=0.03, P_1=80, 100 and 120bar, S_{off_2}=40mm.

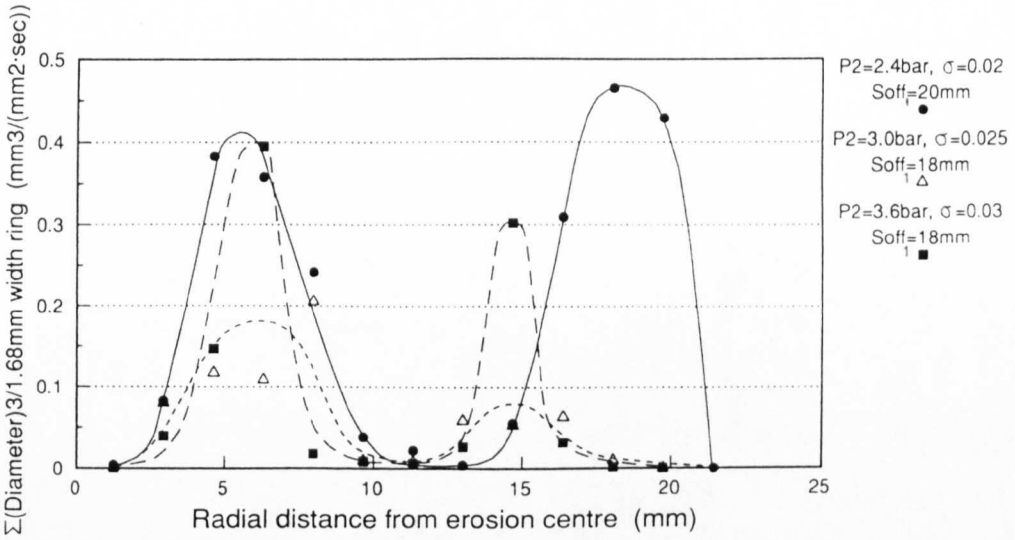

Fig.8.3.9 Distribution of $\Sigma(\text{Diameter})^3$ of indentations per unit time.
Constant upstream pressure P_1=120bar, P_2=2.4, 3.0 and 3.6bar, σ=0.02, 0.025 and 0.03, at the first optimum stand off distance S_{off1}.

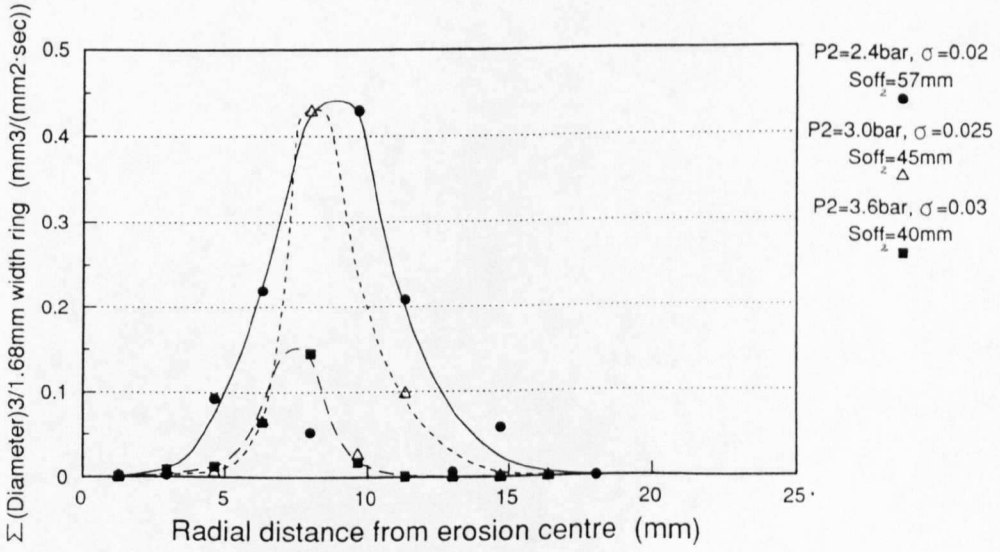

Fig.8.3.10 Distribution of $\Sigma(\text{Diameter})^3$ of indentations per unit time.
Constant upstream pressure P_1=120bar, P_2=2.4, 3.0 and 3.6bar, σ=0.02, 0.025 and 0.03, at the second optimum stand off distance S_{off2}.

Since each indentation on a soft target is regarded as a result of each event of cavitation loading, it is inferred that some form of the measure of cavitation intensity derived from indentation measurement may have close correlation with the erosion rate. One notable difference between these two is that one is obtained from a flat target and another is obtained from a damaged specimen in later stage at which the geometry of the target surface and so the flow pattern of a cavitating wall jet has been changed.

As previously discussed in this chapter, the sum of (diameter)^3 of each indentation on the entire disc is taken to be proportional to the total volume of plastic deformation and is taken as representing the value of cavitation loading intensity. Those values at both the first and the second optimum stand off distance for all the pressure conditions tested are plotted with the peak cumulative erosion rate (PER_C) in Fig.8.4.1. The correlation between the sum of (diameter)^3 and PER_C is very good for the second optimum stand off distance S_{off2}, whereas it is relatively poor for the first optimum stand off distance S_{off1}. One of the reasons for this is that although the erosion at S_{off1} mainly proceeds only in the first ring area at matured stage due to the change in the surface geometry, the indentations are equally counted in both the first ring and the second ring area. Therefore the sum of (diameter)^3 values tend to become greater for S_{off1} than the ones for S_{off2} at the same level of erosion rate. The relative effects of indentation data in the second ring are increased by the integration of the values in entire target area and so even the small experimental error can be multiplied to large one.

For some example, the number of indentation on the entire surface was similarly calculated for each case and its correlation with PER_C is also plotted in Fig.8.4.2. In general, the agreement is rather good, though the gap between S_{off1} and S_{off2} is wider than that with the sum of (diameter)^3. The correlation for S_{off1} seems even better. These results indicate the possibility that only counting the number of indentations on a soft material may provide sufficiently good correlation with the erosion rate from the weight loss tests.

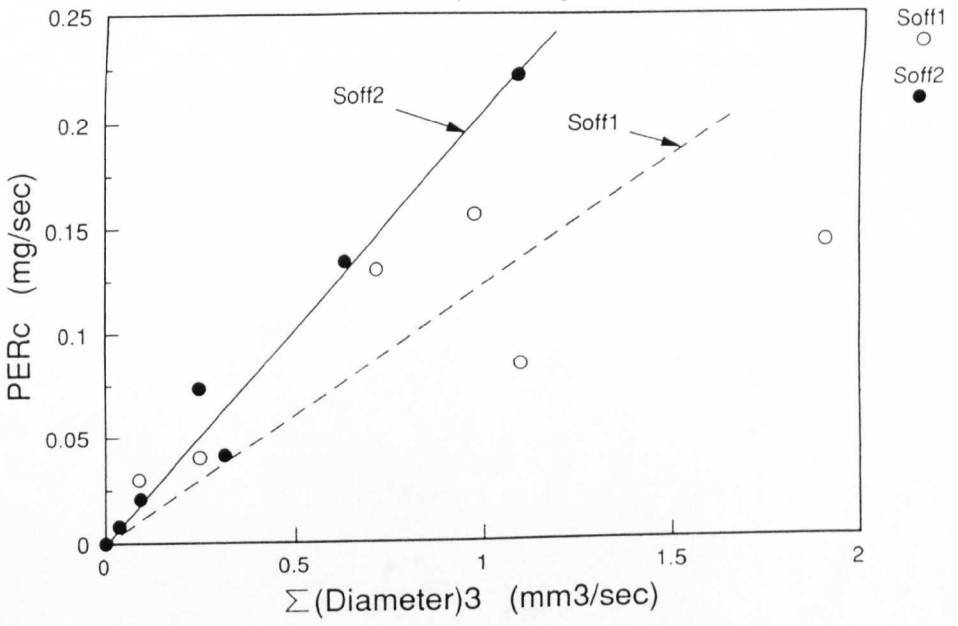

Fig.8.4.1 Correlation between $\Sigma(\text{Diameter})^3$ estimated on the entire disc per unit time and peak cumulative erosion rate (PER_C).

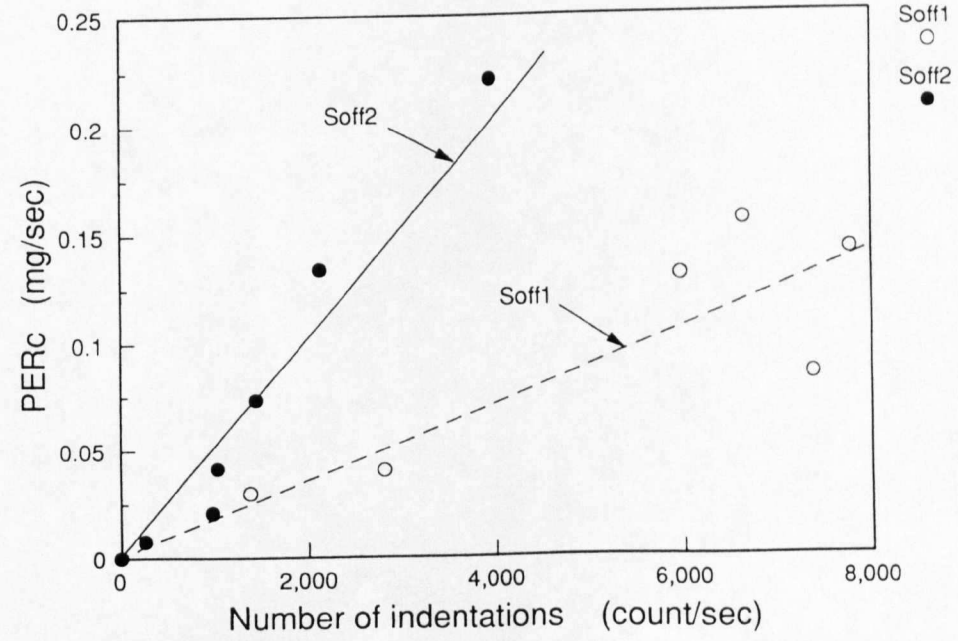

Fig.8.4.2 Correlation between number of indentations estimated on the entire disc per unit time and peak cumulative erosion rate (PER_C).

Raw and accumulated size distributions of indentations for an entire specimen are calculated from indentations measured in each frame of the image analysis. They are plotted in Figs.8.5.1(a)~(l) for all pressure conditions at both the first and the second optimum stand off distances, S_{off1} and S_{off2}. The raw distribution values are counted and plotted at each 5μm step and the threshold size below which the image was not counted was set at 10μm (see Chapter 5). For pressures P_1=100bar and σ=0.03 (P_2=3.0bar), the calculated total number of indentations on an entire target is more than six thousand per second at the first optimum stand off distance and one thousand per second at the second one. Small size indentations ranging from 10μm to 20μm share the majority, approximately 60%, of all the indentations on the specimen in number at both S_{off1} and S_{off2} in all pressure conditions.

Raw distributions seem to be on a straight line for all cases showing same tendency with an index, m, in a log-log graph. It may be expressed as the following equation.

$$N(d) = b \cdot d_s \cdot d^{-m}$$

where N(d) is the number of indentations at the size, d, in diameter, b is a constant determined for each test condition (pressures and stand off distance) and d_s is the distance between two points in diameter in the distribution graph, which is d_s=5μm in Fig.8.5.1. Indices m have been obtained for all the pressure conditions at various stand off distances including S_{off}=15~45mm for P_1=100bar and σ=0.03 (P_2=3.0bar). These indices are listed in Fig.8.5.2, where both the upstream and downstream pressures, cavitation number and the stand off distance are shown at a left side of a bar chart. They show very similar values around m≈2.0. This means that the slope of the raw indentation distribution is very similar in all the test cases in the present measurements regardless of the difference in the pressures, cavitation number and the stand off distance.

To determine the size distribution of indentations after its constant slope index m is given, there are two more factors, the total number and the largest indentation size. Variations of both of them with the average indentation size are plotted in Fig.8.5.3 with stand off distance S_{off}=15~45mm for P_1=100bar and σ=0.03

Raw and accumulated size distributions of indentations for an entire specimen are calculated from indentations measured in each frame of the image analysis. They are plotted in Figs.8.5.1(a)~(l) for all pressure conditions at both the first and the second optimum stand off distances, S_{off1} and S_{off2}. The raw distribution values are counted and plotted at each 5μm step and the threshold size below which the image was not counted was set at 10μm (see Chapter 5). For pressures P_1=100bar and σ=0.03 (P_2=3.0bar), the calculated total number of indentations on an entire target is more than six thousand per second at the first optimum stand off distance and one thousand per second at the second one. Small size indentations ranging from 10μm to 20μm share the majority, approximately 60%, of all the indentations on the specimen in number at both S_{off1} and S_{off2} in all pressure conditions.

Raw distributions seem to be on a straight line for all cases showing same tendency with an index, m, in a log-log graph. It may be expressed as the following equation.

$$N(d) = b \cdot d_s \cdot d^{-m}$$

where N(d) is the number of indentations at the size, d, in diameter, b is a constant determined for each test condition (pressures and stand off distance) and d_s is the distance between two points in diameter in the distribution graph, which is d_s=5μm in Fig.8.5.1. Indices m have been obtained for all the pressure conditions at various stand off distances including S_{off}=15~45mm for P_1=100bar and σ=0.03 (P_2=3.0bar). These indices are listed in Fig.8.5.2, where both the upstream and downstream pressures, cavitation number and the stand off distance are shown at a left side of a bar chart. They show very similar values around m≈2.0. This means that the slope of the raw indentation distribution is very similar in all the test cases in the present measurements regardless of the difference in the pressures, cavitation number and the stand off distance.

To determine the size distribution of indentations after its constant slope index m is given, there are two more factors, the total number and the largest indentation size. Variations of both of them with the average indentation size are plotted in Fig.8.5.3 with stand off distance S_{off}=15~45mm for P_1=100bar and σ=0.03

(P_2=3.0bar). The distribution of the total number of indentations shows a similar shape as weight loss results including a sharp peak at S_{off}=18mm. On the other hand, the largest and average diameters show very small peak at S_{off}=18mm at first, and then they increase with the stand off distance and show the maximum values at S_{off}=40mm and S_{off}=45mm for the largest and the average diameters, respectively. If we assume that the size of indentations is proportional to the maximum bubble size, physical meaning of the increase of the largest diameter can be understood as follows. While most cavities are collapsing in a relatively short distance, some of the others are very large and powerful enough to be still growing with distance along the jet. Then, they collapse at some relatively larger stand off distance and produce larger size indentations. Similar tendency, increasing the number of larger size indentations on a soft material with distance in venturi, has also been reported by Robinson and Hammitt [1967] (see Fig.3.2.6).

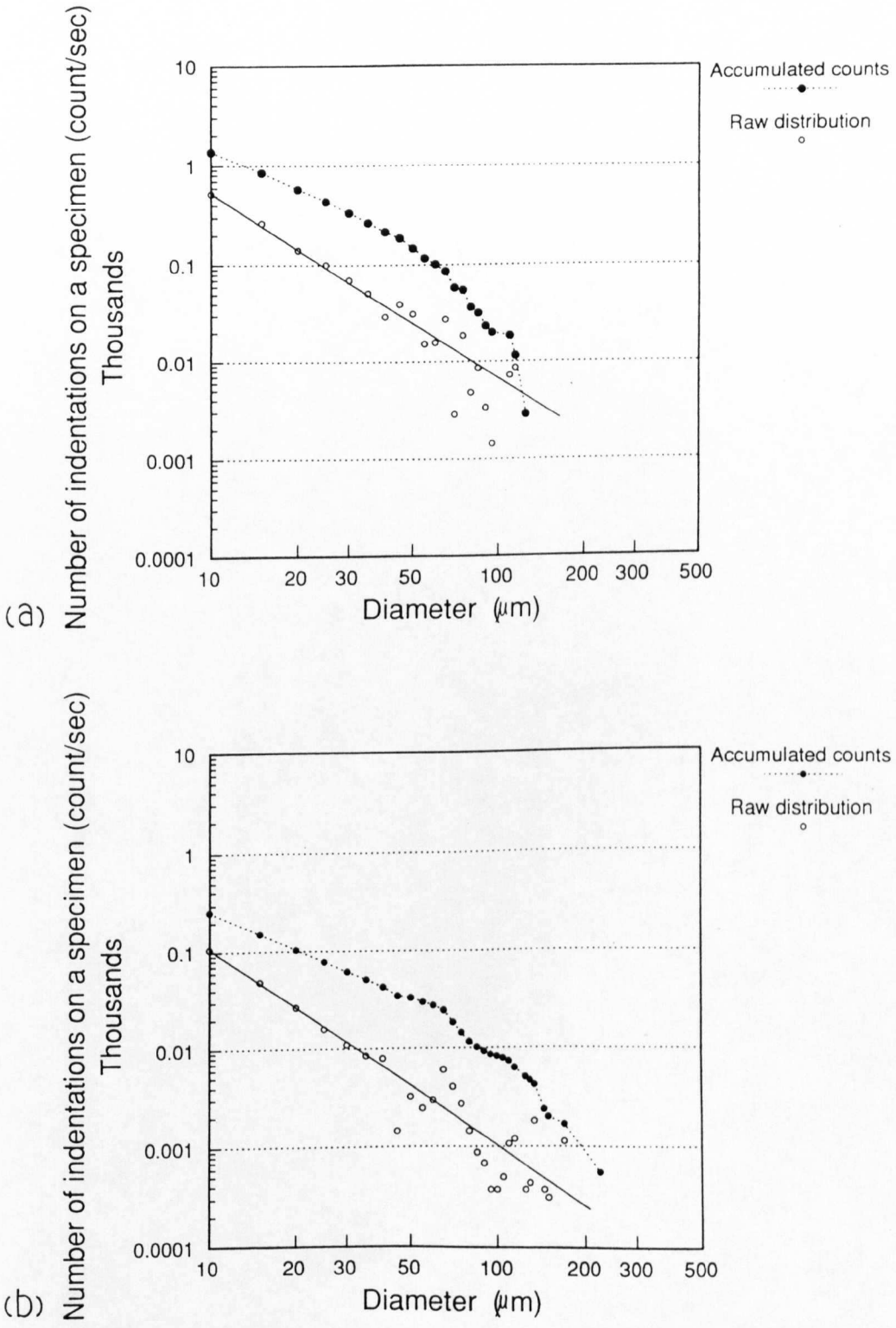

Fig.8.5.1 Size distribution of indentations.
P_1=80bar, P_2=3.0bar, σ=0.0375, (a) S_{off_1}=15mm; (b) S_{off_2}=35mm.

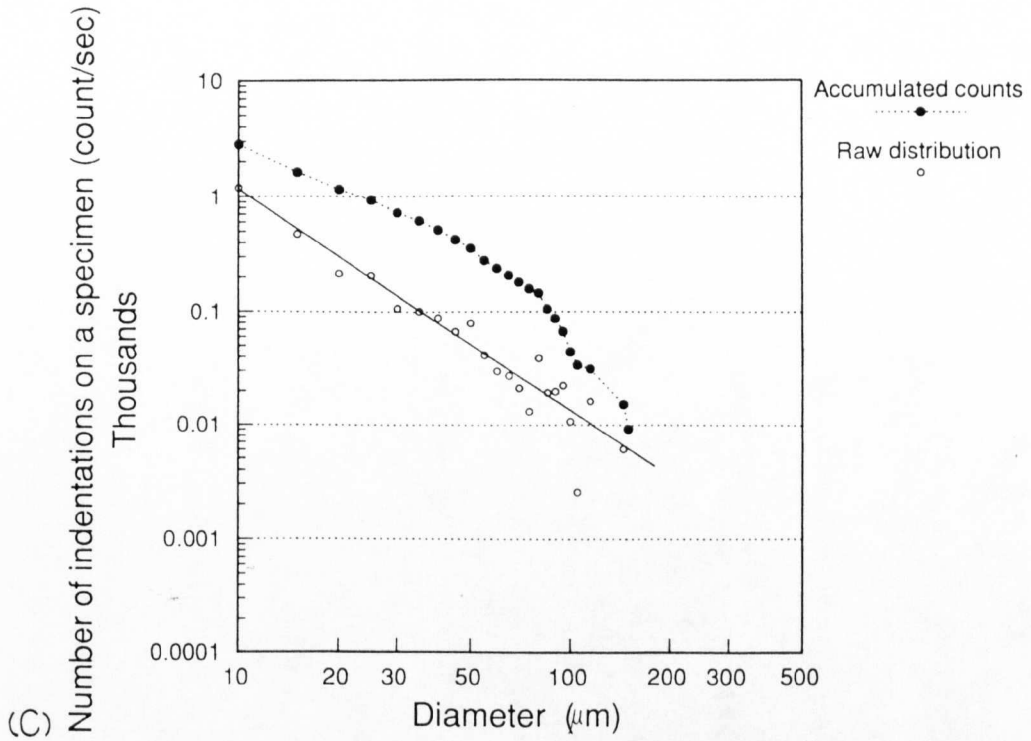

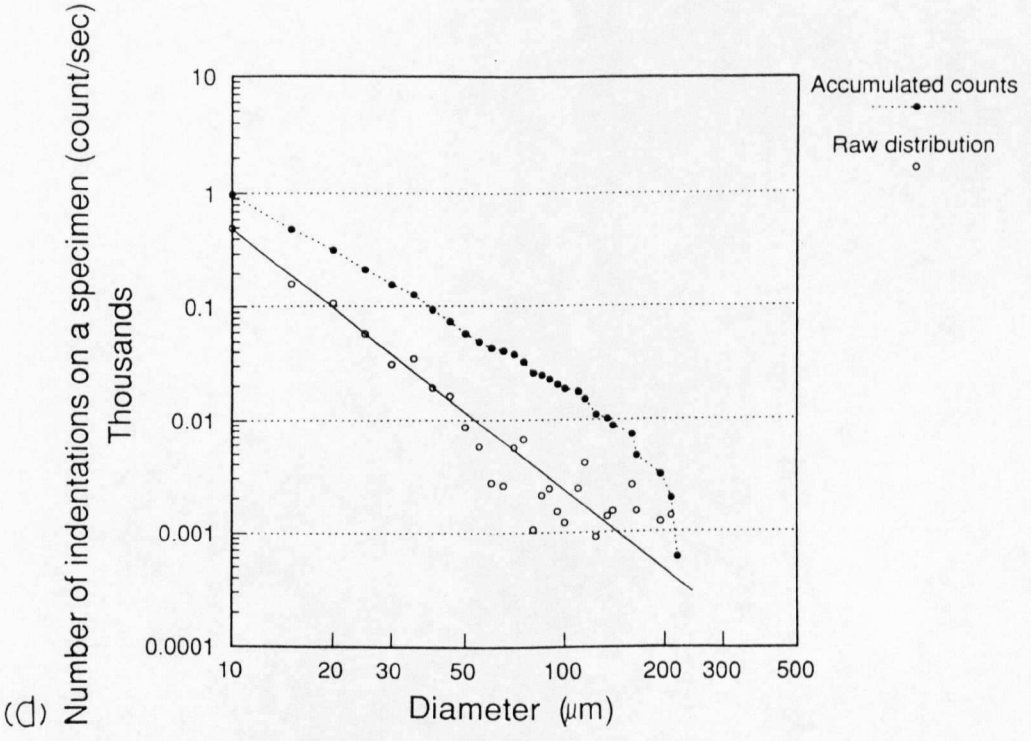

Fig.8.5.1 Size distribution of indentations.
P_1=80bar, P_2=2.4bar, σ=0.03, (c) S_{off_1}=18mm; (d) S_{off_2}=40mm.

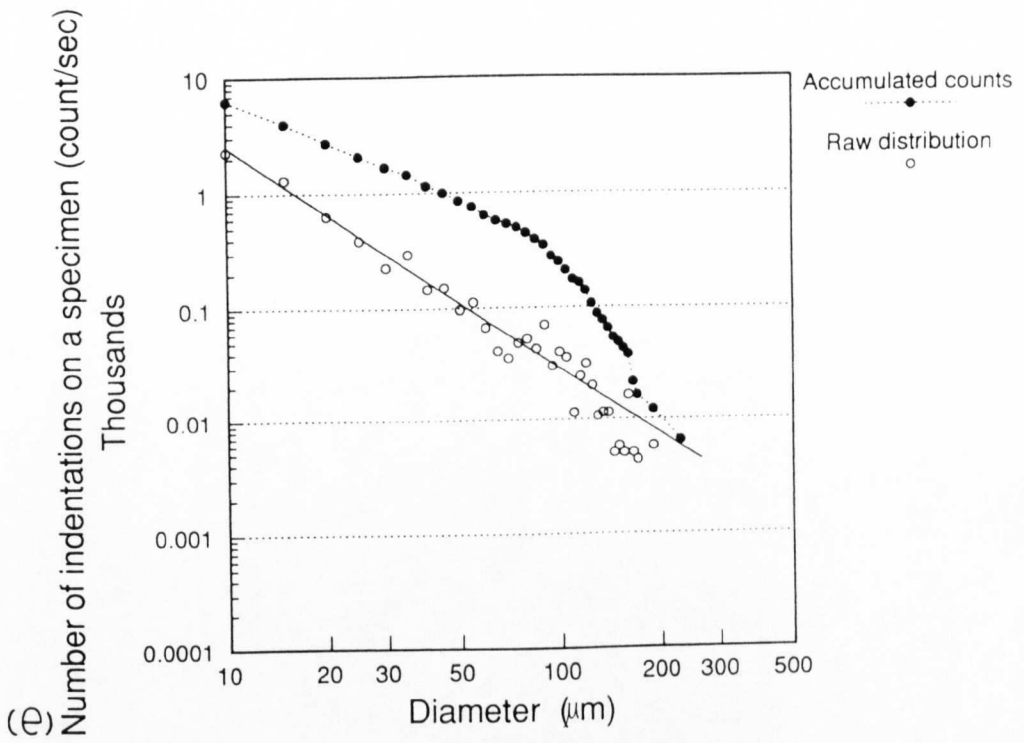

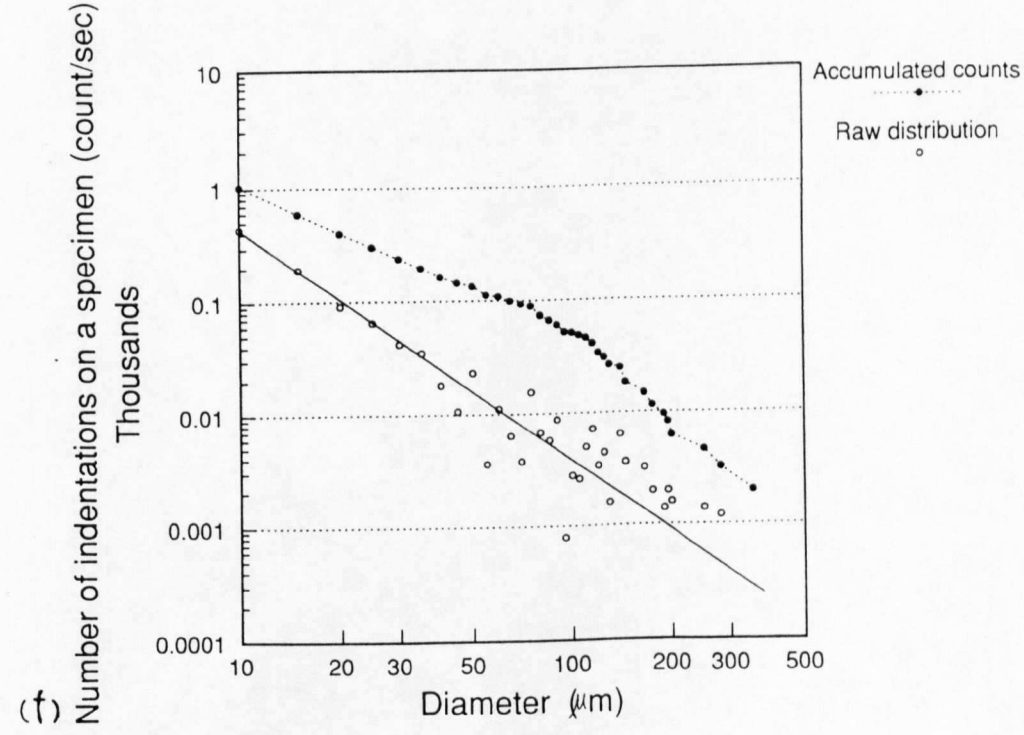

Fig.8.5.1 Size distribution of indentations.
P_1=100bar, P_2=3.0bar, σ=0.03, (e) S_{off_1}=18mm; (f) S_{off_2}=40mm.

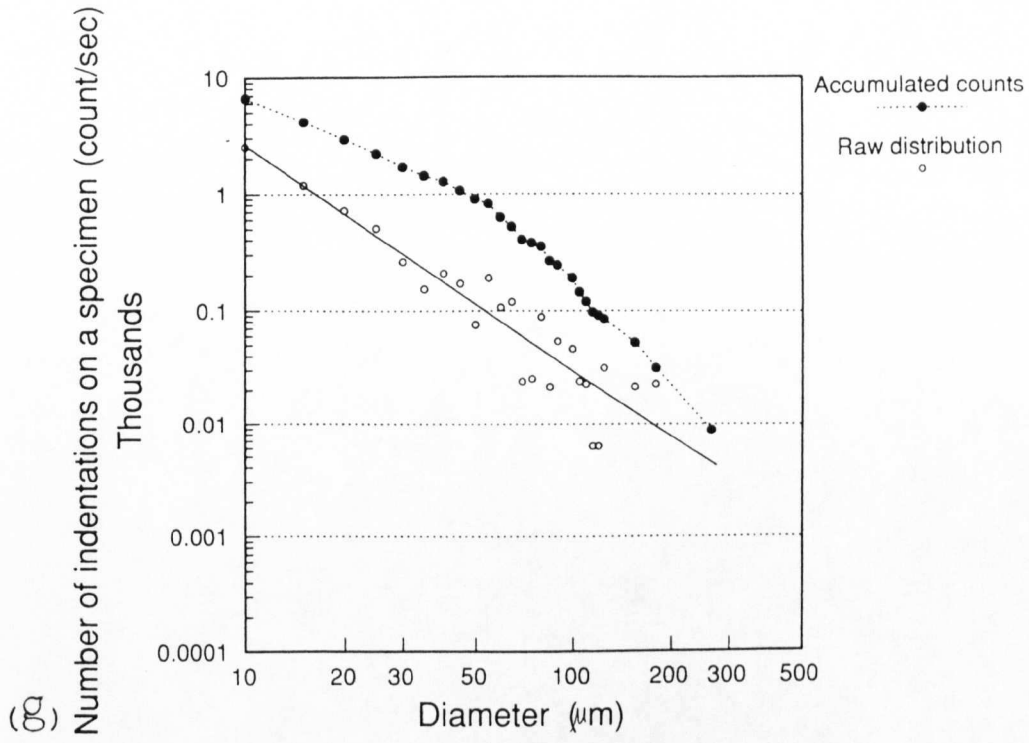

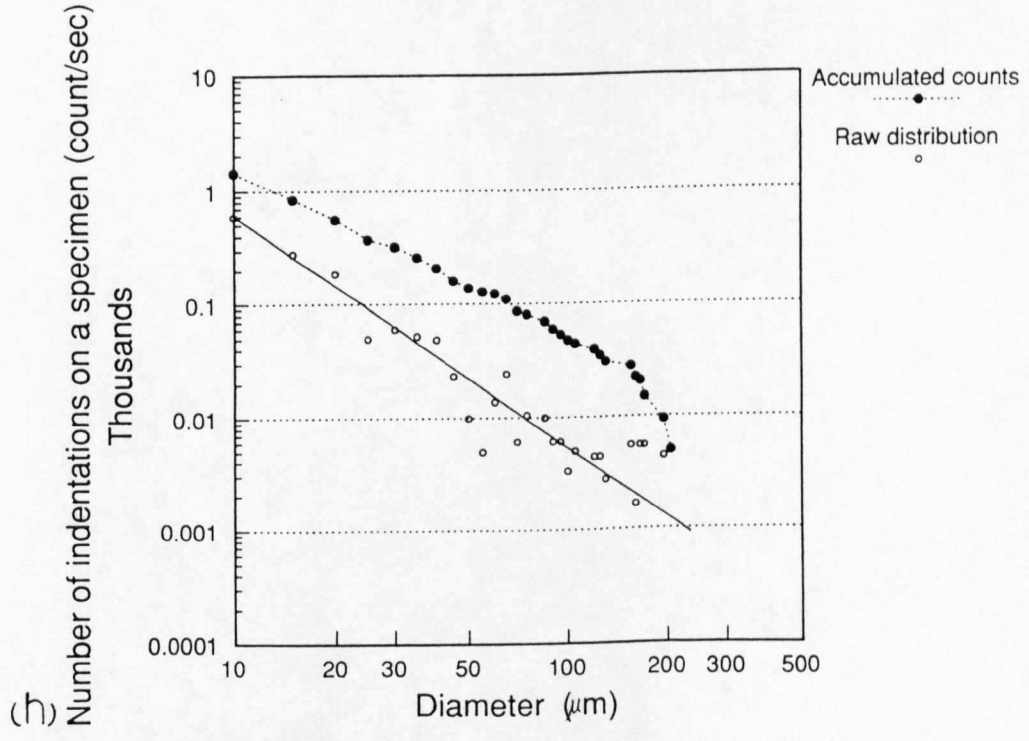

Fig.8.5.1 Size distribution of indentations.
P_1=120bar, P_2=3.6bar, σ=0.03, (g) S_{off_1}=18mm; (h) S_{off_2}=40mm.

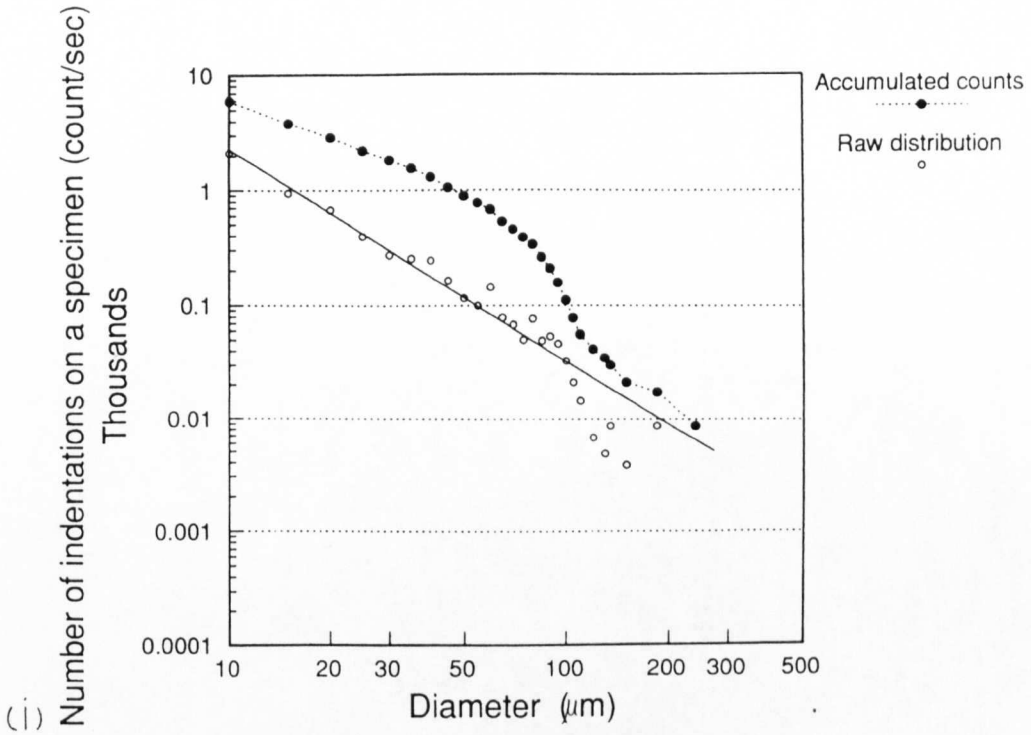

(i)

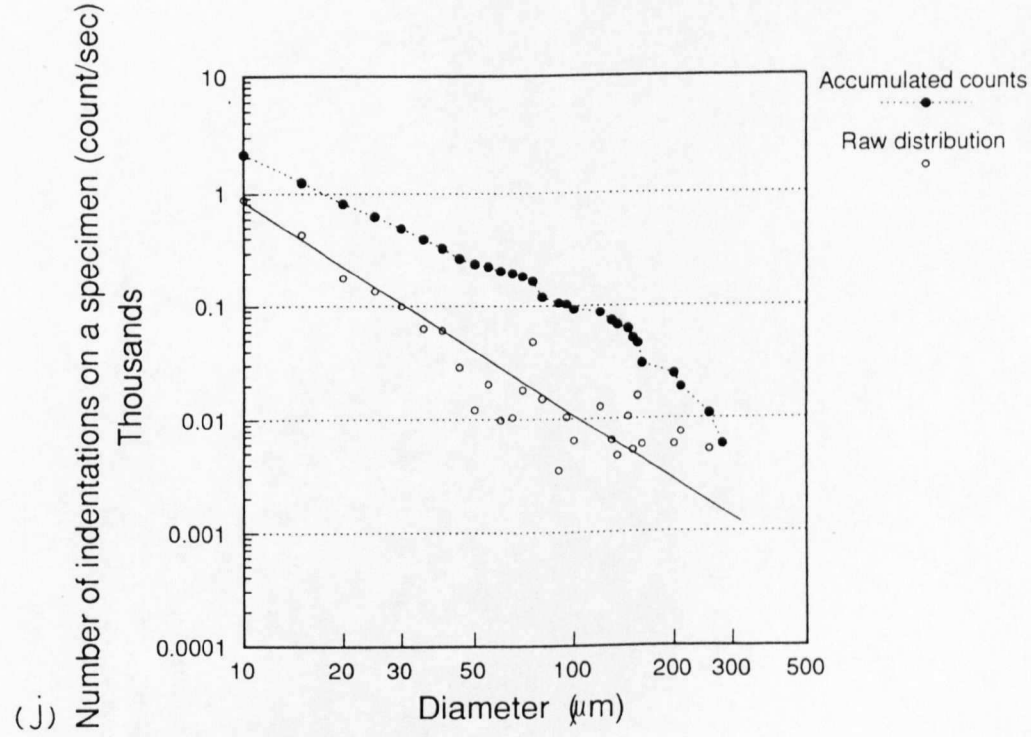

(j)

Fig.8.5.1 Size distribution of indentations.
P_1=120bar, P_2=3.0bar, σ=0.025, (i) S_{off_1}=18mm; (j) S_{off_2}=45mm.

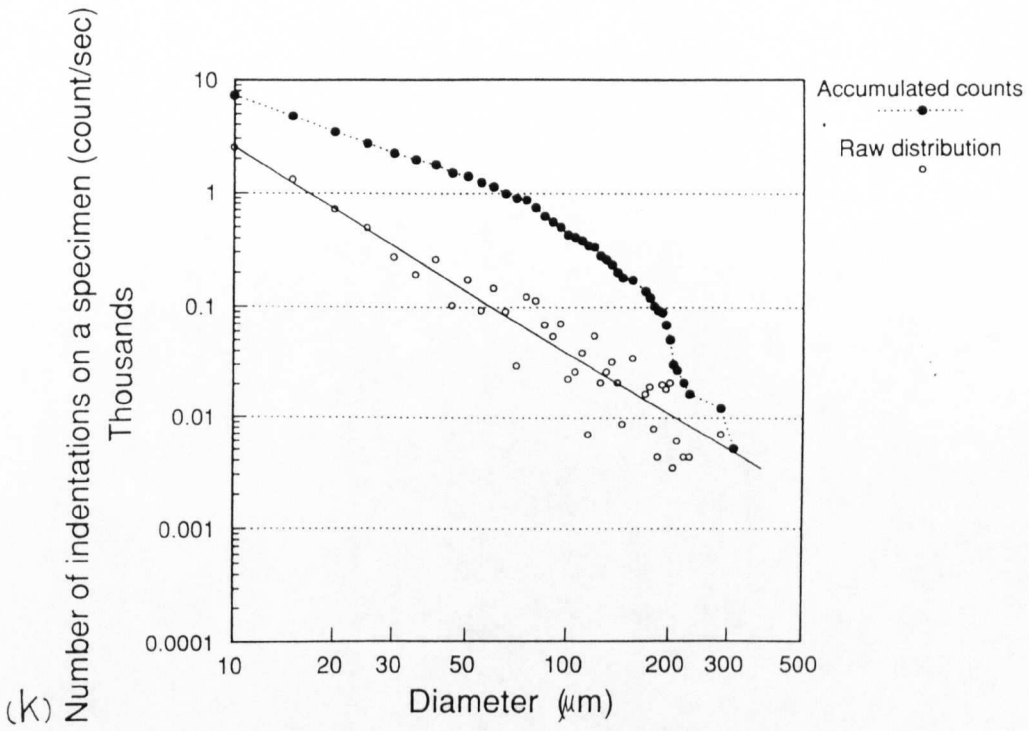

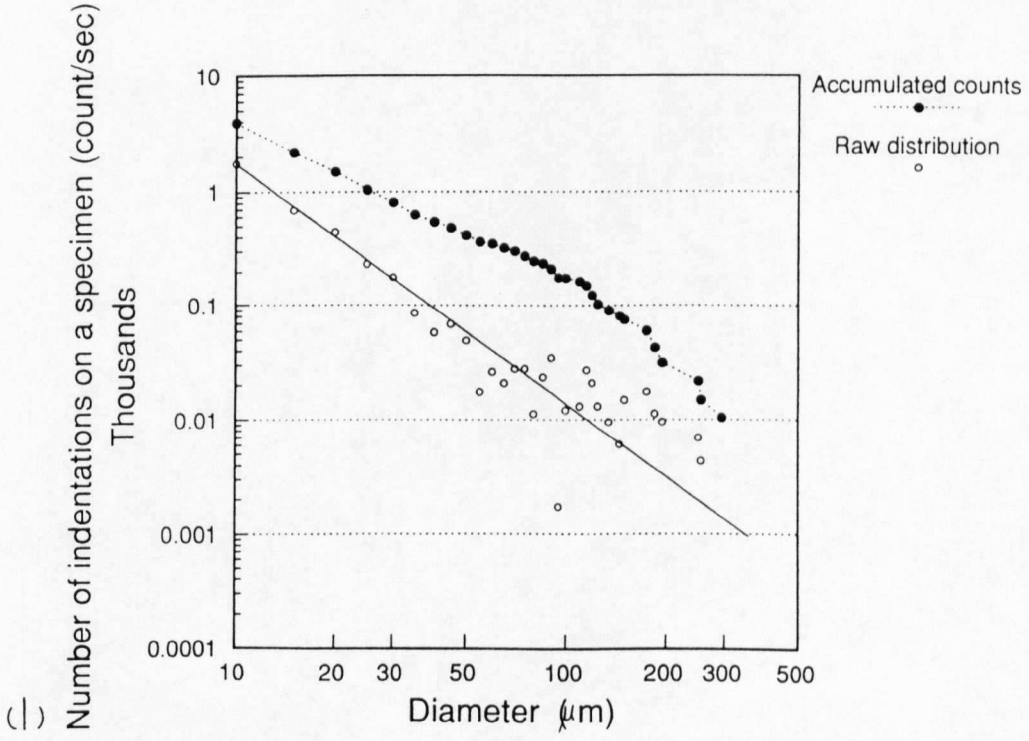

Fig.8.5.1 Size distribution of indentations.
P_1=120bar, P_2=2.4bar, σ=0.02, (k) S_{off_1}=20mm; (l) S_{off_2}=57mm.

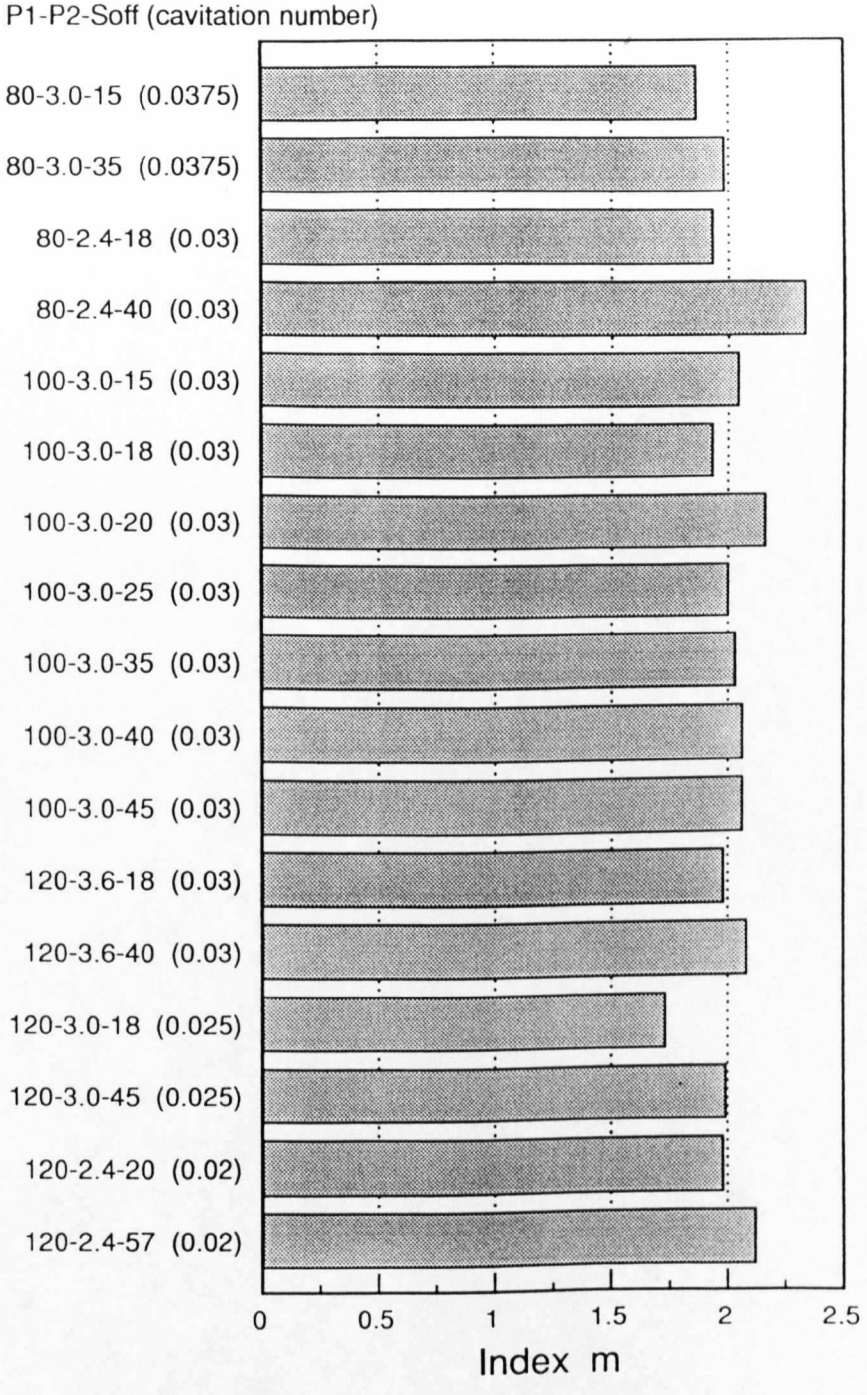

Fig.8.5.2 Index m for indentation size distributions.
P_1-P_2-S_{off} means test conditions: i.e., upstream pressure-downstream pressure-stand off distance, respectively.

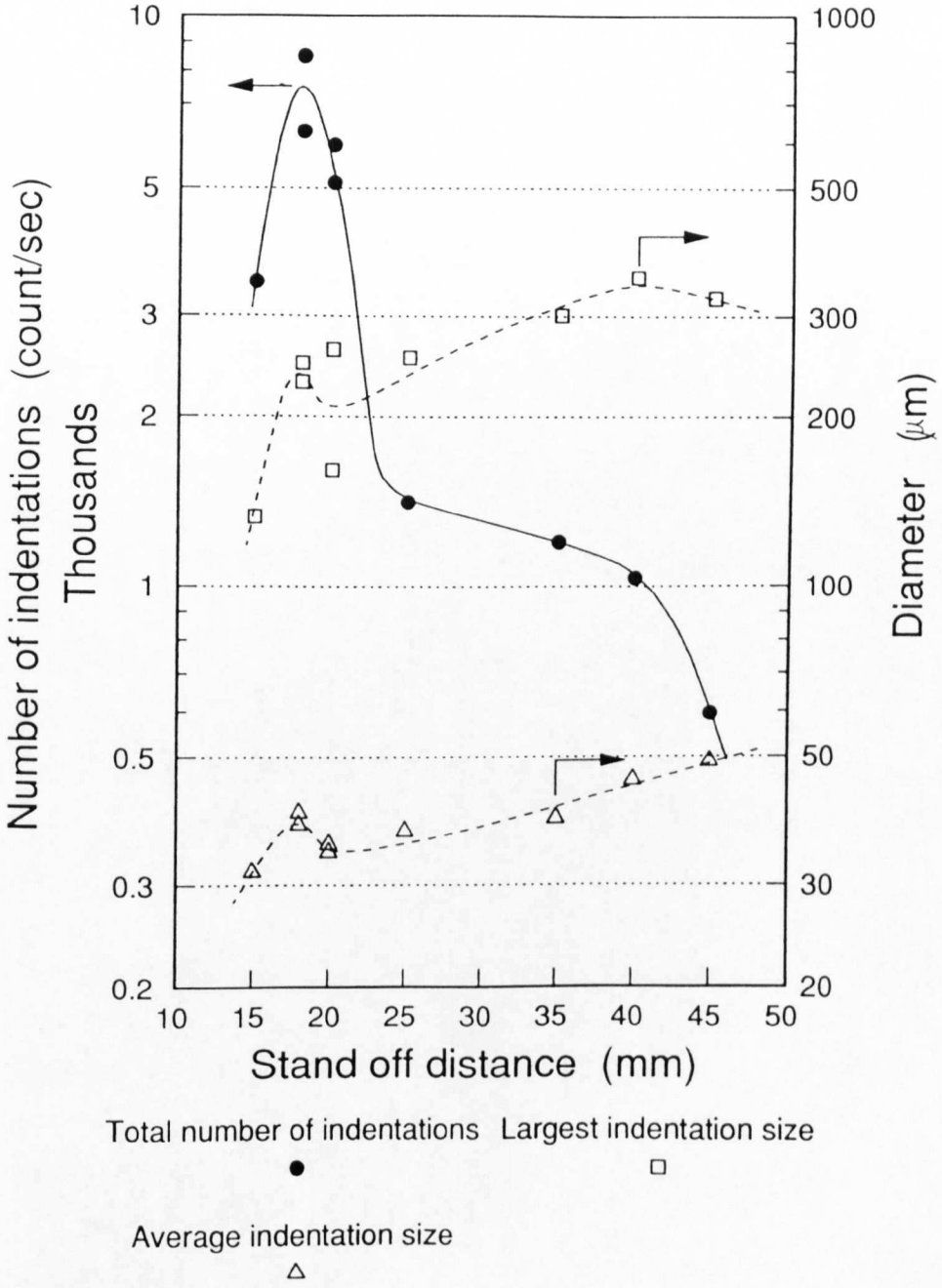

Fig.8.5.3 Variation of number of indentations on the entire disc per unit time and the largest and the average size of indentations with stand off distance.
P_1=100bar, P_2=3.0bar, σ=0.03.

8.6 Conclusions

Main results and discussions in this chapter are summarized as follows.

(1) Indentations are randomly distributed within a ring (or two rings) as the shape of the cavitation erosion introduced in previous chapters. Each indentation is more or less circular in shape except some of the larger ones which are more irregular. Size of indentations ranges widely from few micron to approximately 350 micron, but generally, the very large ones are found only in the severely damaged areas. From three dimensional view of SEM, indentations seem to have a conical shape with or without some flat part at the bottom, and so it is thought that the mechanism to produce those indentations is more likely to be a microjet type impingement.

(2) The number density (number of indentations per unit time and unit area) of indentations larger than 10 μm in diameter at the maximum damage area for P_1=100bar and σ=0.03 is about 30 counts/(mm^2·sec) and 5 counts/(mm^2·sec) at the first optimum stand off distance S_{off1} and the second optimum stand off distance S_{off2}, respectively.

(3) The area density (the sum of each indentation area per unit time and unit area) of indentations at the maximum damage area for the same case above is approximately 0.035mm^2/(mm^2·sec) and 0.01mm^2/(mm^2·sec) for S_{off1} and S_{off2}, respectively.

(4) Generally, the results obtained from the indentation counting agree well with the erosion test results concerning the erosion shape, its size and the magnitude of erosion intensity, though there are some which contradict the tendency of cavitation erosion obtained from the weight loss tests. Possible cause of these experimental errors are follows.

a.) The frame size of the image analyzer, 0.84mmx0.84mm, may not be sufficiently large compared with the size of the indentations up to about 350μm in equivalent diameter.

b.) Four paths of scanning the target from the centre may not be able to collect sufficient amount of information which represents the case.

(5) The correlation between the sum of (diameter)^3 of each indentation and PER_C is very good at S_{off2}, whereas it is relatively poor at S_{off1}. This is because the erosion at S_{off1} proceeds mainly only in the first ring area at the matured stage of erosion when PER_C is measured, but the indentations (the sum of (diameter)^3) are equally counted in both the first and the second ring area at the initial stage of damage. The relative effect of indentations in the second ring is increased by the integration of values in entire target area and so even the small experimental error can become a large one.

(6) The correlation between the number of indentation for the entire surface and PER_C is rather good, though the gap between S_{off1} and S_{off2} is wider than the correlation using the sum of (diameter)^3. This results indicate the possibility that only counting the number of indentations on a soft material may provide sufficiently good prediction on the erosion rate.

(7) The raw distributions of indentation size seem to be expressed as,

$$N(d) = b \cdot d_s \cdot d^{-m}$$

where N(d) is the number of indentations at the size, d, in diameter, b is a constant determined for each test condition (pressures and stand off distance) and d_s is the interval between two measuring points in diameter in the distribution graph, which is 5μm in the present measurements. Indices m have been obtained for all the pressure conditions at various stand off distances and very similar values around m=2.0 are shown regardless of the difference in the pressures, cavitation number and the stand off distance.

(8) Variation of the total number of indentations with stand off distance shows a similar distribution to the weight loss results including a sharp peak at the first optimum stand off distance S_{off1}. On the other hand, the largest and average diameters show very small peak at the first optimum stand off distance S_{off1} at first, and then they increase with the stand off distance and show the maximum values at around the second optimum stand off distance S_{off2}. This indicates that some cavities are

sufficiently large and powerful to be still growing with distance along the jet. Then, they collapse at some relatively larger stand off distance and produce larger size indentations. Similar tendency has also been reported with venturi by Robinson and Hammitt [1967].

CHAPTER NINE - RESULTS:
Cavitation loading (II) --- Pulse height analysis

9.1 Introduction

In order to investigate the magnitude and frequency of cavitation loading in a flow cavitation field, impulsive load produced by cavitating jet was directly measured and its pulse height distribution was analyzed.

As a sensor for this particular measurement where each impingement area is very small, impact duration time is extremely short and impact itself is very damaging, a piezoelectric pressure transducer using PVDF piezofilm has been developed as described in Chapter 5 and Appendix A3. The advantage in using this piezofilm material is its easiness of application. The thickness from 9μm upwards is commercially available and it can be cut simply by a knife or scissors into any size and any shape. The pressure transducer has been calibrated by a pencil lead breaking method calibration which has also been developed for the present investigation and is actually faster than the widely used ball dropping calibration method. At the same time, the analog pulse height measurement system which consists of the pressure transducer, an input pulse height gate circuit and an event counter was also set up, and then the actual cavitation loading signals were successfully measured. Those voltage signals were converted to the unit of impacting force by the calibration constant.

The objectives of the cavitation loading pulse measurements are follows.

(1) To obtain the magnitude of impulsive force of the cavitation loading. Then the magnitude of the loading pressure can be estimated by dividing the impulsive force by an area of the indentation.

(2) To understand the shape of the loading pulse distribution and the threshold level above which the pulse actually damage the material (annealed 1200-aluminium alloy, 99.0% purity, in this project).

(3) To investigate the possibility of the correlation between the loading pulse data and the erosion results.

These results will be presented and discussed in this chapter.

Before treating the cavitation loading data for a pulse height analysis where only the peak height and its count per second are of importance, photographs of each impact output were taken from a display of the digital oscilloscope which was connected to the pulse height measurement system. Figure 9.2.1 shows typical examples of cavitation loading pulses in different time scale of the oscilloscope, 1μs~0.5ms per division. Vertical scale is constant, 1.0volt per division. The test condition for Fig.9.2.1 is P_1=80bar and σ=0.03 (P_2=2.4bar) at the second optimum stand off distance S_{off2}=40mm. The area of the transducer, A_T, is 8.88mm^2 (approximately 3mmx3mm) and it was located at r=7.0mm from the centre of the target. The radial distance 7.0mm was the mid point of the erosion ring (the maximum damage area) for the test condition (see Section 9.3.2 and Fig.9.3.5). The signals in (a) and (b) in Fig.9.2.1 show a single incident. Since a noise level during the measurement is small, the pulse clearly stands out from it. The width of the pulse at the half height of the peak is approximately 1.5μs in both cases, and ranges from 1.0μs to 2.5μs in general. The natural frequencies of PVDF piezofilm (thickness 110μm) and of polyimide tapes (thickness 140μm) are 10MHz and 9.3MHz, respectively, as estimated in Chapter 5 and so they are sufficiently high to accurately detect these pulses. These pulse widths are also longer than 0.8μs which is the minimum countable pulse width at 10V for the comparator circuit (see Chapter 5 and Appendix A3). The output voltage level of PVDF is very high (calibration constant is 6.97~7.50N/V.) and signals up to almost 10V were obtained at the present tests. Therefore, a pre-amplifier was not required for the present system.

Figure 9.2.1(c) shows series of cavitation loadings on the PVDF pressure transducer. Although there is some low frequency pressure fluctuations, the amplitude level is very small compared with the peak values. It was therefore decided not to use a high-pass filter.

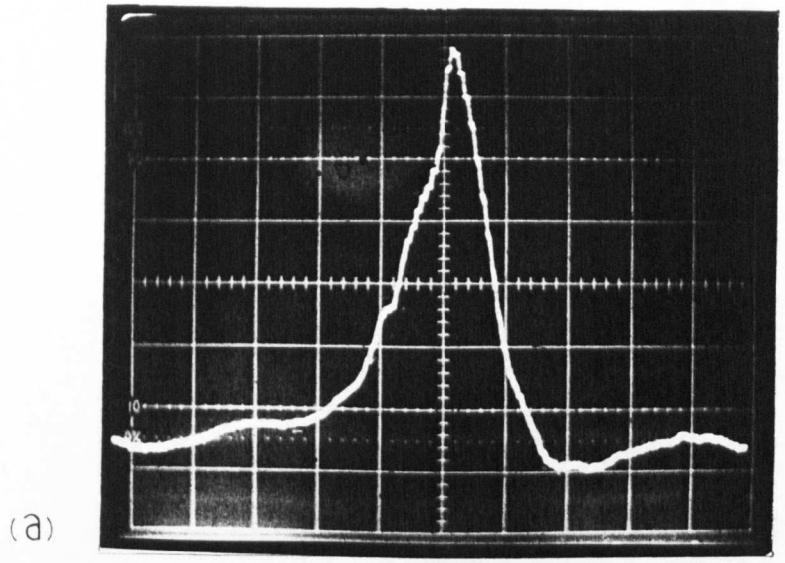

(a)

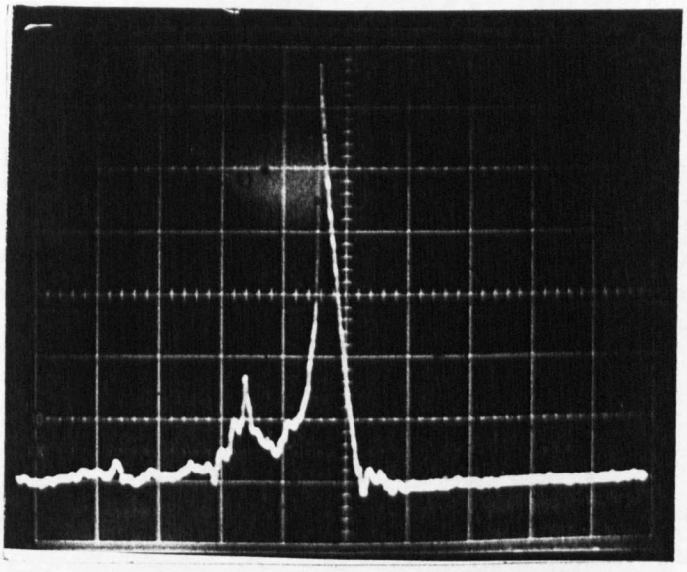

(b)

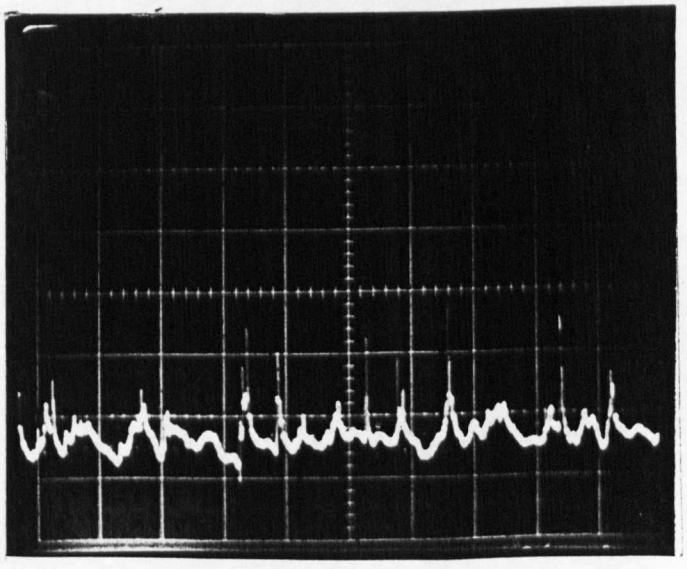

(c)

Fig.9.2.1 Cavitation loading pulses.
P_1=80bar, P_2=2.4bar, σ=0.03, S_{off}=40mm, r=7.0mm, A_T=8.88mm^2.

9.3.1 Effects of protection tapes

As mentioned in Chapter 5, the polyimide protection tape (thickness, 70μm) is one of the strongest tape available. But even for this tough material it was difficult to protect the transducer at the first optimum stand off distance where the flow velocity is much higher than that at the second optimum stand off distance. Then, it was decided that the pressure measurement would be carried out only at the second optimum stand off distance.

The polyimide tape protection was necessary for the present transducer design. However, it was thought that the existence of such medium between the actual loading surface (on top of the protection tape) and the sensitive material (PVDF) might harm the reliability of the data obtained; i.e. the loading pressure might be attenuated by material damping through the protection tapes, or/and a part of the loading pulse might dissipate through the tapes as a form of propagating shockwave.

In order to check whether these attenuation and dissipation effects through the protection tapes are negligible or not, the transducers with different numbers of layers of the protection tapes were tested under the same cavitating jet. One transducer with a sensitive area of 8.88mm^2 (approximately 3mmx3mm) was manufactured and two (thickness, 140μm), four (280μm) and six layers (420μm) of polyimide protection tapes were applied on it. Figures 9.3.1~9.3.3 show the accumulated pulse height distributions for P_1=80~120bar and σ=0.03 at the second optimum stand off distance S_{off2}=40mm and r=7.0mm measured by the transducer covered with the three different thickness of protection tapes. For each pressure condition, all the pulse height distributions with three different tape thickness agree very well each other. The results show that both the attenuation and the dissipation effects through the protection tapes are negligible within the range of the tape thickness from 140μm (for two layers) to 420μm (for six layers) where the ratio of the tape thickness to the transducer dimension is about 5~14%. Therefore, it was decided that the two layers of the polyimide protection tapes would be used throughout the present measurements.

In addition, remarkable agreement among these data with several tape

thickness under various pressure conditions also indicates the repeatability and reliability of the present testing apparatus and method, such as the submerged jet cavitation testing method, the PVDF piezoelectric pressure transducer embedded in the target, the pulse height measurement system and the calibration device using the pencil lead breaking load.

The maximum accumulated counts at the smallest threshold pulse height which is set about 2.3N for most cases is about 1000 counts/(mm^2·sec). The area of the transducer is A_T=8.88mm^2 and so the number of total pulses detected by the transducer is going to be about 10000 counts/sec. If it is assumed that the average pulse duration width of those counts is 2μs, the actual time spent by total pulses would be 20000 μs/sec. This indicates that the pulses occupy only 2% of the total measurement time. Thus, the possibility of counting overlapping pulses is negligibly low.

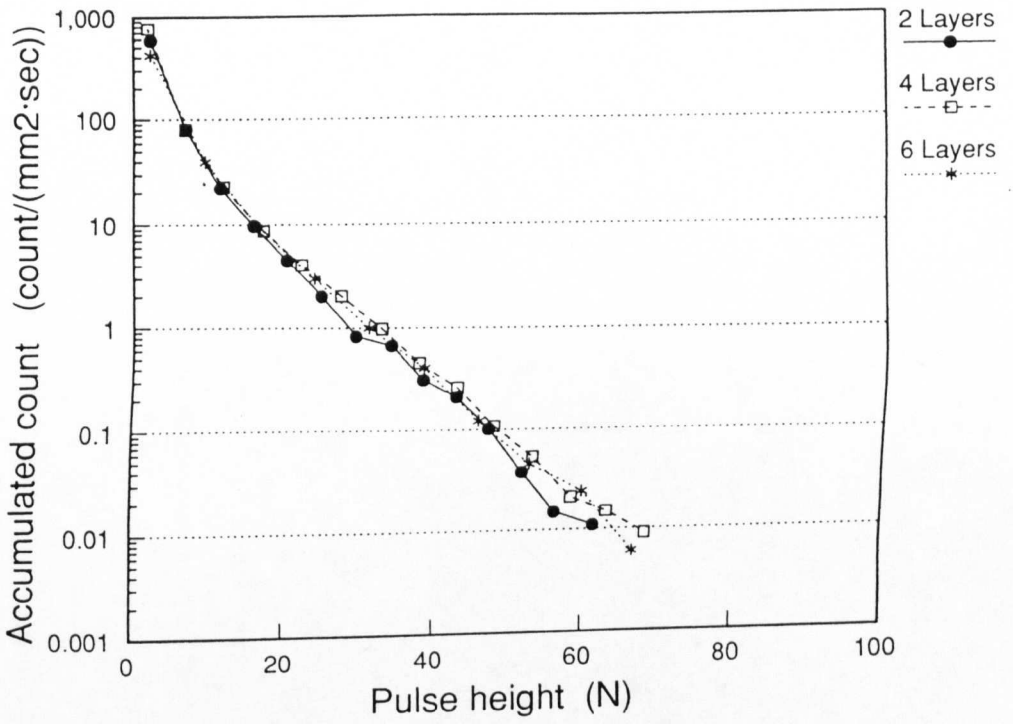

Fig.9.3.1 Effect of protection tapes on pulse height distribution.
P_1=80bar, P_2=2.4bar, σ=0.03, S_{off_z}=40mm, r=7.0mm, A_T=8.88mm^2.

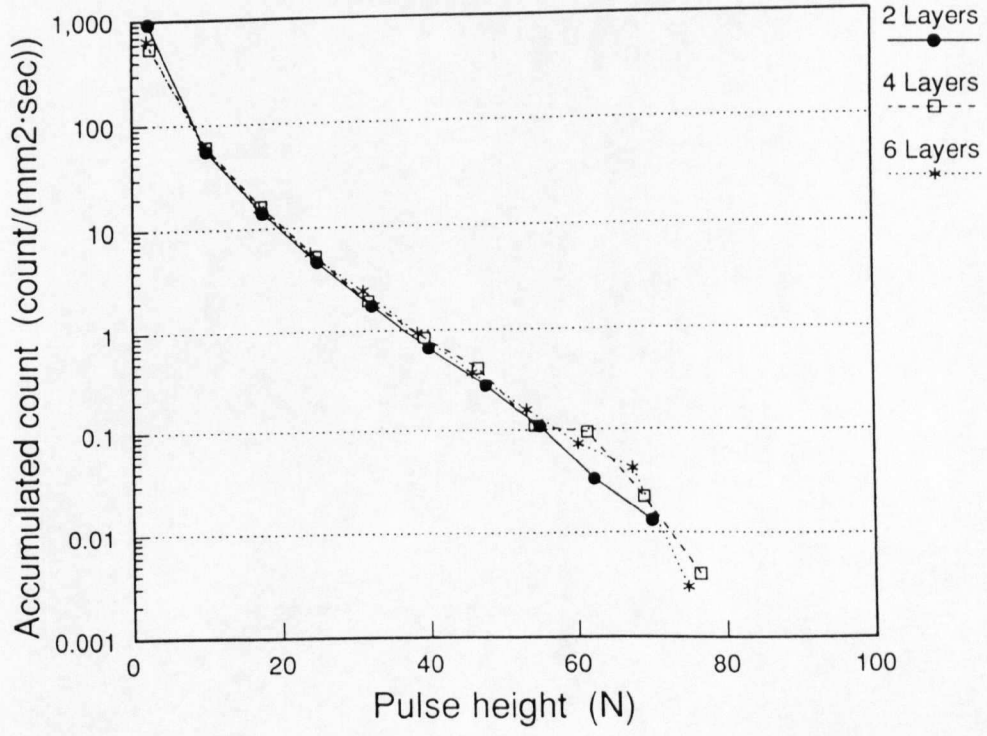

Fig.9.3.2 Effect of protection tapes on pulse height distribution.
P_1=100bar, P_2=3.0bar, σ=0.03, S_{off_z}=40mm, r=7.0mm, A_T=8.88mm^2.

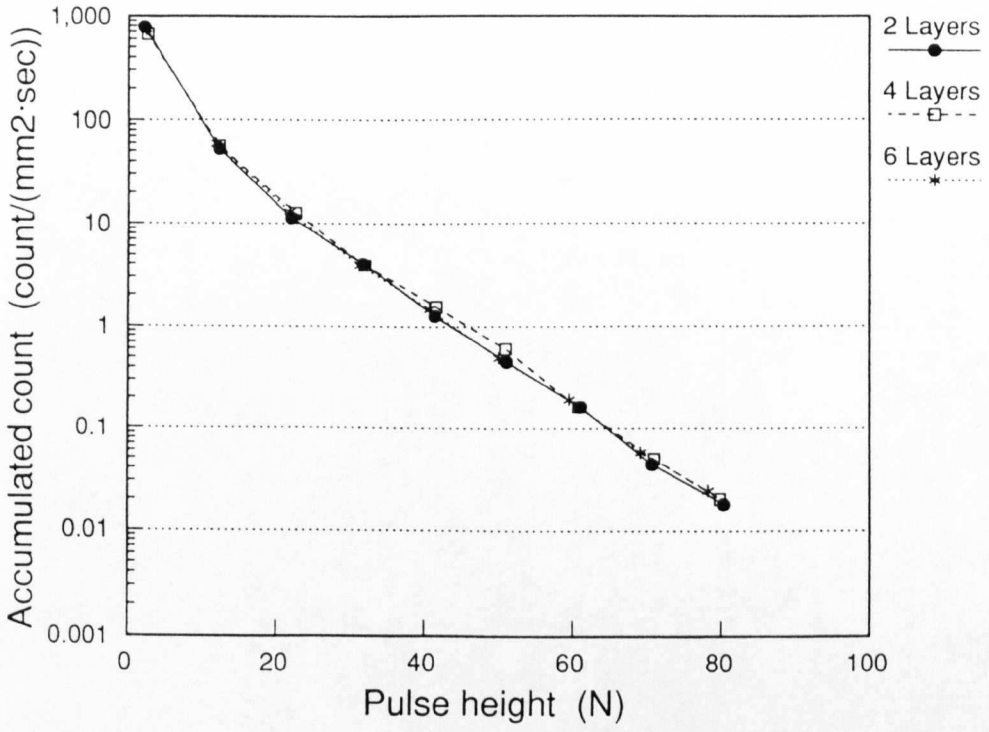

Fig.9.3.3 Effect of protection tapes on pulse height distribution.
P_1=120bar, P_2=3.6bar, σ=0.03, S_{off_2}=40mm, r=7.0mm, A_T=8.88mm^2.

Since normally the cavitation loading area is not known, it is very difficult to convert the electric signal measured from a pressure transducer to the unit of pressure. In that case, the only way to calculate the pressure is to take a fictitious mean pressure by assuming that the impact loading is uniformly distributed on the sensitive part of the transducer. This is why usually investigators have been seeking the smallest possible transducer area. In fact, very small transducers as small as 0.9mm in diameter have been manufactured and used to measure the cavitation loading pressures (The, Franc and Michel [1987] and see Chapter 3 for others). However, the size of the sensitive part is still much larger than the size of the cavitation loading.

On the other hand, the size of cavitation loading is certainly not zero, though it is often described as "very small". The indentation size on the annealed 1200-aluminium alloy (99.00% purity) ranges up to 350μm in the present tests and as it will be discussed later in this chapter, the actual cavitation loading size may become even greater. The loading does not necessarily impinge the centre of the sensitive part of the transducer and some part of the entire loading would be sometime cut off as shown in Fig.9.3.4. If, however, the transducer is not sufficiently large compared to the loading size, there must be some measurement error at the edge of the sensitive part of the transducer. The magnitude of these loading pulses must be reduced by such a cut-off, though the total number of counting can increase because even the impact loading whose centre is located outside the sensitive area may be able to contribute the counting inside it. Therefore, when the objective of the measurement is to obtain the right pulse height distribution in the unit of force and not to estimate the arbitrary pressure from the transducer sensitive area, the transducer with too small size sensitive area may not be the best choice.

It may be obvious that this sort of "edge effect" described above can actually take place. But the questions, such as how the loading pulse would be affected by variation of the size of the sensitive part of the transducer, or whether it is negligible or not, has not been answered yet. In order to investigate the edge effect, six transducers each with different sensitive area of A_T=0.140mm^2, 0.301mm^2, 0.777mm^2, 1.35mm^2, 4.43mm^2 and 8.88mm^2 were manufactured and tested. The shape of all the sensitive area was square. Such an edge effect is expected to be smaller for a larger

transducer sensitive area. The maximum dimension of the sensitive part of transducer is virtually limited by the size of the erosion area, i.e., the width of the erosion ring, as the whole sensitive part should be located within the evenly damaged area on the target so that the pulse height measured can later be normalised by the unit area. Variation of the sum of (diameter)^3 of indentations per unit time and unit area with radial distance from the erosion centre on a specimen is shown in Fig.9.3.5. Pressures are P_1=80~120bar with a constant cavitation number σ=0.03 and the stand off distance is S_{off2}=40mm, which are the same conditions as those for the pulse height measurements. Most of these damages are located at the same range from r=5~9mm. Then, it was decided that the transducer should be located at r=7.0mm and the largest dimension of it would be approximately up to 3.0mm (r=5.5~8.5mm).

Figures 9.3.6~9.3.8 show the accumulated pulse height distributions for P_1=80~120bar and constant σ=0.03 at S_{off2}=40mm. Pulses were measured by transducers with two layers of polyimide protection tapes on six different sensitive area from A_T=0.140~8.88mm^2 placed at the maximum damage area, at a distance from the centre r=7.0mm. Because cavitation number is maintained constant in all the three pressure conditions, location of the maximum damage area, at around r=7.0mm, remains same in all pressure conditions as shown in Fig.9.3.5. In Figs.9.3.6~9.3.8, the greater the transducer area or the upstream pressure P_1, the higher the pulse height is, while all distribution shapes look similar.

In order to compare the magnitude of the pulse height distributions in Figs.9.3.6~9.3.8 each other, the pulse heights at accumulated count 1.0 counts/(mm^2·sec) for each distribution were taken as representing values for the comparison. Their variations are plotted with the area of the sensitive part of transducers in Fig.9.3.9. The pulse height increases with the increase of both the upstream pressure P_1 and the transducer area A_T. Particularly, the pulse height rapidly increases with the increase of the area of the sensitive part at first and then it seems to tend to some saturation value at larger sensitive areas. This tendency is considered to be caused by the edge effect previously discussed. Therefore, it is thought that the larger size transducer should be less affected by the edge effect and so the pulse height obtained from the larger transducer would be closer to the reality.

Then, the transducer with the largest sensitive area of A_T=8.88mm^2 has been regarded to be able to provide the most realistic data among all the transducers used in the present experiments.

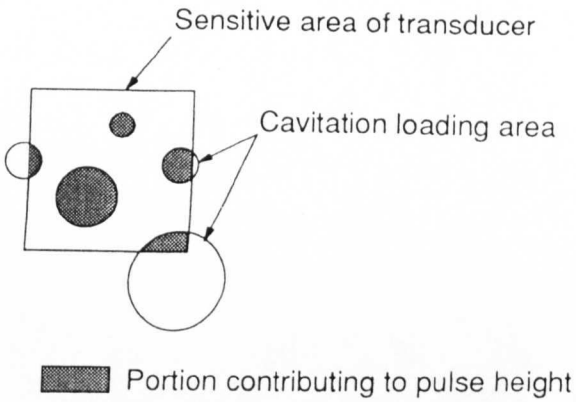

Fig.9.3.4 Relation between a small transducer and large size cavitation loadings, schematic diagram.

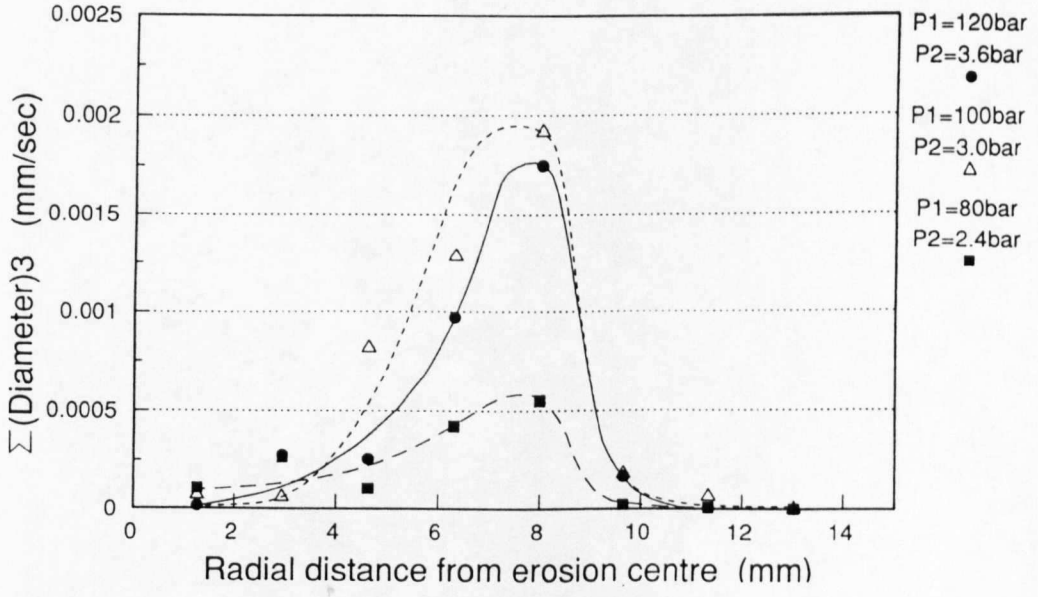

Fig.9.3.5 Radial distribution of Σ(Diameter)^3 of indentations on specimen. σ=0.03, S_{off_Σ}=40mm

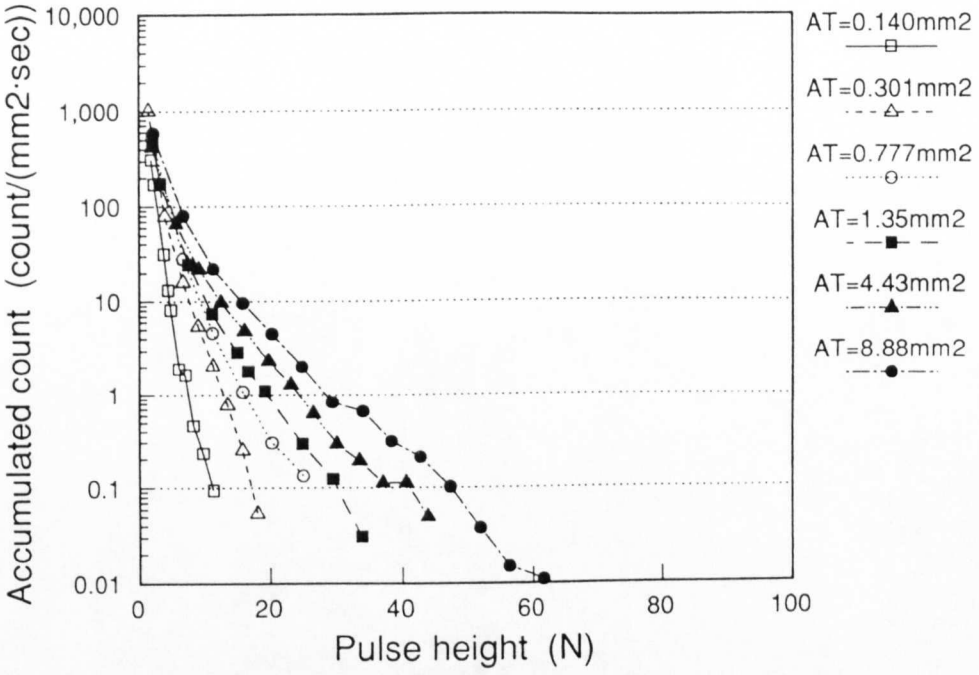

Fig.9.3.6 Pulse height distributions measured by various size of transducers.
P_1=80bar, P_2=2.4bar, σ=0.03, S_{off_2}=40mm, r=7.0mm,
Two layers of protection tapes.

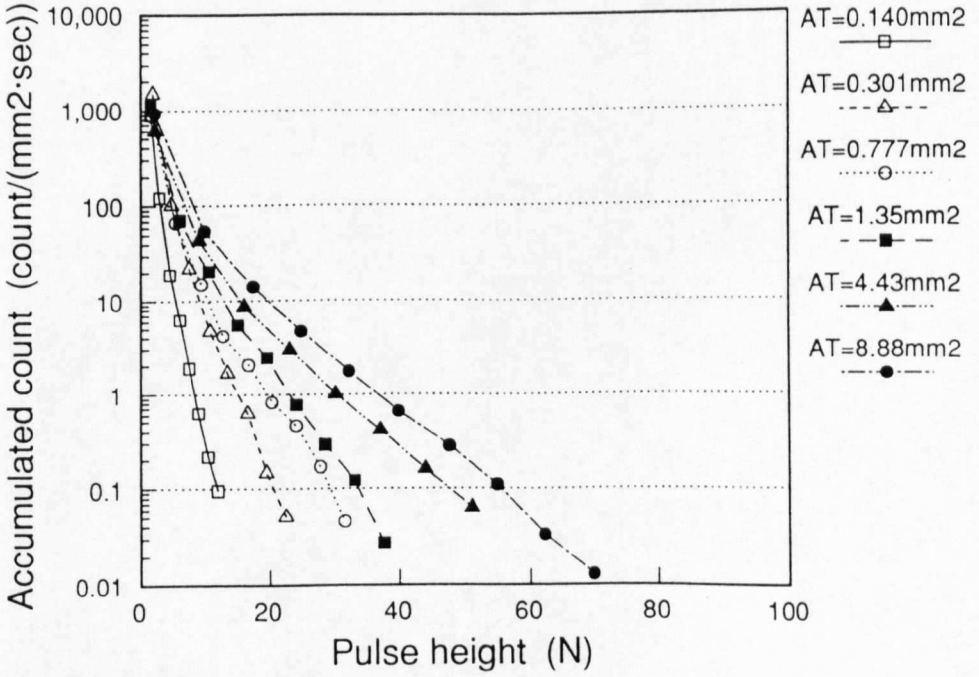

Fig.9.3.7 Pulse height distributions measured by various size of transducers.
P_1=100bar, P_2=3.0bar, σ=0.03, S_{off_2}=40mm, r=7.0mm,
Two layers of protection tapes.

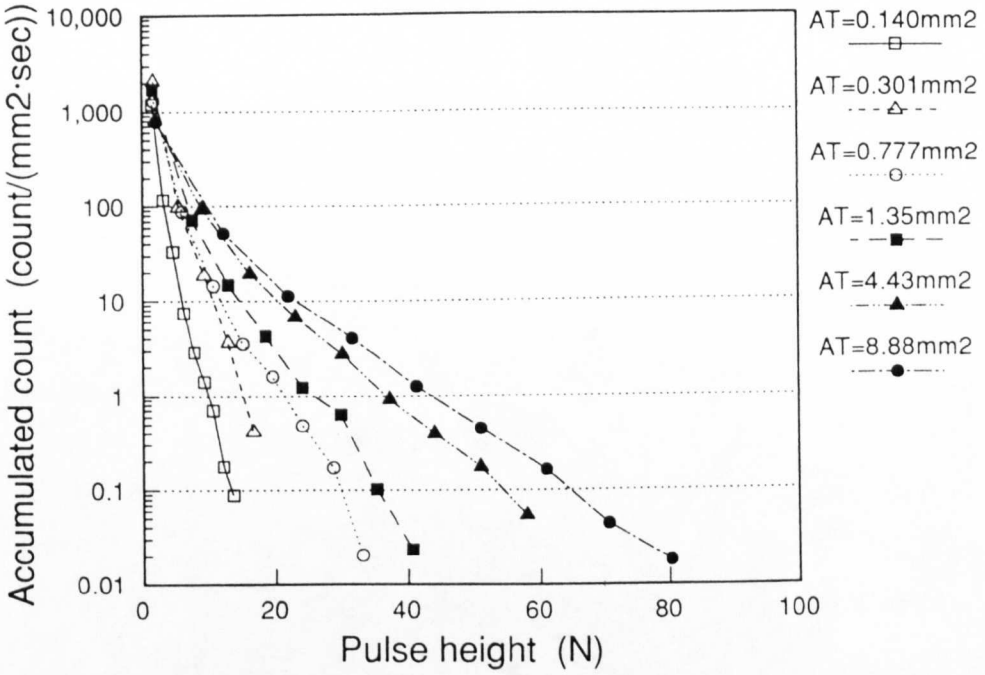

Fig.9.3.8 Pulse height distributions measured by various size of transducers.
P_1=120bar, P_2=3.6bar, σ=0.03, S_{off_2}=40mm, r=7.0mm,
Two layers of protection tapes.

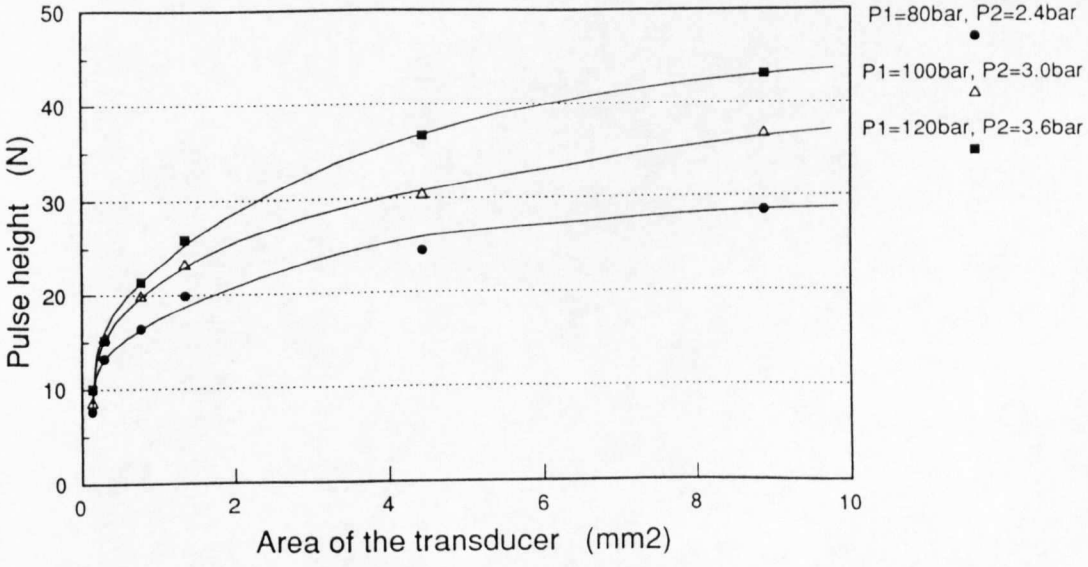

Fig.9.3.9 Variation of pulse heights at accumulated count of 1.0 count/(mm^2·s) with area of sensitive part of transducer. (from Fig.9.3.6~9.3.8.)

The attenuation and the dissipation effect due to the protection tapes and the edge effect due to the relative transducer size to the cavitation loading size were investigated. Variation of pulse height distributions was presented with different layers of protection tapes and various size of transducers in the previous section. It was found that the effects due to the polyimide protection tapes are negligible for up to six layers of tapes. And pulse height distributions measured by the transducer with the sensitive area A_T=8.88mm^2 are thought to be most realistic among the transducers prepared in the present project. Since those pulse height data were obtained in the unit of force (newton, N), if the loading area where the pulse was applied can be estimated, it is possible to calculate the magnitude of the cavitation loading pressure, P_L.

In the present project, the size distribution of indentations on soft aluminium has already been obtained in Chapter 8. If it can be assumed that basically the pulse height distribution and the indentation size distributions correspond each other at any counting frequency, the latter can be used to estimate the loading area with which the loading pressure will be calculated. Both the size distributions of indentations and the pulse height distributions for P_1=80~120bar and σ=0.03 at the second optimum stand off distance S_{off2}=40mm and r=7.0mm are presented in Fig.9.4.1. These pulse height distributions were measured by a transducer with sensitive area of A_T=8.88mm^2 with two layers of protection tapes. The indentation size distributions are plotted for indentations counted only in the maximum damage area, r=5.46~8.82mm which is almost the same position of the sensitive part of the transducer covering r=5.5~8.5mm.

The process of calculating the loading pressure, P_L, is indicated by arrows in Fig.9.4.1 and explained as follows.

(1) The indentation size, A (shown in Fig.9.4.1), with which the cavitation loading pressure will be calculated is decided.

(2) An accumulated count, B, corresponding to the indentation size, A, is read in the indentation size distribution graph ((a) in Fig.9.4.1).

(3) A pulse height, C, corresponding to the accumulated count, B, is read in the pulse height distribution graph ((b) in Fig.9.4.1).

(4) The loading pressure, $P_L(A)$, is calculated by a following equation.

$$P_L(A) = 4C / \pi A^2$$

Then, the cavitation loading pressures P_L were calculated for various size of indentations from 10μm to 200μm as listed together with the pulse height values in Table 9.4.1. Variation of the loading pressure is shown with the size of indentations used in the pressure calculation in Fig.9.4.2. One might expect almost constant loading pressures regardless of the difference in indentation size, or the pressure which increases as the indentation size increases. However, the loading pressure P_L calculated significantly decreases with the increase of the indentation size.

Table 9.4.1 Cavitation loading pressures (σ=0.03)

Indentation size (μm)	P_1=80bar, P_2=2.4bar, S_{off}=40mm		P_1=100bar, P_2=3.0bar, S_{off}=40mm		P_1=120bar, P_2=3.6bar, S_{off}=40mm	
	Pulse height (N)	P_L (MPa)	Pulse height (N)	P_L (MPa)	Pulse height (N)	P_L (MPa)
10	22.4	2.85×10^5	26.5	3.37×10^5	28.8	3.66×10^5
20	27.9	8.88×10^4	33.1	1.05×10^5	35.9	1.14×10^5
30	34.6	4.89×10^4	37.2	5.26×10^4	41.0	5.80×10^4
50	40.0	2.04×10^4	41.8	2.13×10^4	47.5	2.42×10^4
100	46.4	5.91×10^3	50.3	6.40×10^3	56.3	7.17×10^3
150	50.7	2.87×10^3	56.5	3.20×10^3	60.3	3.41×10^3
200	58.0	1.85×10^3	64.1	2.04×10^3	70.3	2.24×10^3

One reason for this tendency can be explained as follows.

Although the annealed 1200-aluminium alloy used is a very soft material with Vickers hardness value 19.6±0.3, it has some elasticity before the plasticity dominates its stress-strain characteristics. When sufficiently high impulsive loading is applied on the elastic-plastic material like aluminium, firstly the surface is deformed and then, after the load is released, elastic part of deformation is recovered leaving the plastic part of deformation as a permanent damage. Therefore, in the present case, there may be some area around the indentation where the cavitation loading actually applied but the surface was not permanently damaged. This means that the actual loading area may be greater than the indentation size.

On the other hand, it is generally accepted that there is a threshold value for plastic deformation above which the deformation remains plastically. Therefore, if it is assumed that the degree of the elastic deformation around the indentation is constant for the given material, the ratio of the indentation area to the total loading area may be much greater for larger indentations (see Fig.9.4.3). Then, the pressure calculated tends to be smaller for larger indentations and it is going to be extremely large for the very tiny indentation size like 10μm.

For example, Hutton and Lobo Guerrero [1975] achieved pit counting with both an aluminium foil on a soft double sided adhesive tape and pure solid aluminium. They reported that the minimum pit sizes were much smaller on the solid aluminium specimen (8μm) than the foil (50μm), while the maximum sizes did not differ so widely (300μm for the solid aluminium and 400μm for the foil). If it can be assumed that the same cavitation impacts produce these differences and, for simplicity, the pit size on the foil is a real cavitation loading size, the area of the indentation on the solid aluminium shows only 2~3% of the loading area for the minimum pit size though it is 50~60% for the maximum size. These results support the discussion above; i.e., (1) even the indentation size on the soft aluminium can be smaller than the real loading size, and (2) the ratio of the indentation size to the real loading size may be greater for cavitation loadings which are larger in size.

Therefore the lowest pressures, P_L=1.85~2.24x10^3MPa for P_1=80~120bar,

calculated with the largest size indentation for each pressure condition in Table 9.4.1 can be regarded as the most realistic values. Considering the situation described above, these pressure values may become even smaller in reality. These pressures are a little lower than 4.8~8.1x10^3MPa reported by Kirejczyk [1979] and much lower than 7.2x10^5MPa reported by Okada et al. [1989] (for detail, see Chapter 3). Both of them applied similar techniques with pulse height distributions and indentations on aluminium alloy (see Chapter 3). The very high pressure obtained by Okada et al., however, was calculated for their smallest observable indentation size, 4μm, and it can be reduced to 4.3x10^3MPa if the largest indentation size is taken for the calculation as suggested above and in Chapter 3 by the present author. At last, in spite of the difference in cavitation source among above results, such as a submerged jet, vibratory cavitation and an water tunnel, the pressures obtained in both papers and in the present study show similar values within the same order of magnitude. One of the reasons for the small difference among these, besides the possible difference in cavitation intensity, may be due to the difference in material hardness of aluminium alloy specimens used in each investigation, though the details about the hardness are not described in both papers.

Vogel, Lauterborn and Timm [1989] pointed out that, from measured and extrapolated jet velocities, the microjet velocity (about 100m/s or less) of a single bubble collapsing in a liquid near a solid boundary is not high enough to lead to erosion of hard material. They supported the idea that the most likely damaging mechanism is the impingement of a microjet produced in the bubble struck by the shockwave. There are two experimental investigations on the formation of such a microjet in particular case by Tomita and Shima [1986] and Dear and Field [1988]. They showed the microjet velocity 200~370m/s produced by 50bar pressure pulse (Tomita and Shima) and 400m/s produced by 2.6kbar shockwave (Dear and Field). From water hammer impact pressure calculation, the impact pressure of the microjet at 200~400m/s becomes P_{wh}=3.0~6.0x10^2MPa. These values can be further increased to P_{wh}=0.9~1.8x10^3MPa, if the tip of the jet has the appropriate wedge shape (Lush [1983]). Latter values seem to show very good agreement with the present results. The pressure magnitude of the order of 1GPa obtained in the present investigation is sufficiently high to damage at least annealed 1200- and 6063-aluminium alloy and probably also high enough to the other harder engineering material through the fatigue erosion process.

In Table 9.4.1, cavitation loading pressures calculated increases with the increase of test pressure conditions from P_1=80bar and P_2=2.4bar to P_1=120bar and P_2=3.6bar. If the shockwave is considered to be the source of the loading and the distance from the surface to the shockwave centre is assumed to be constant for all cases, the increase of the shockwave pressure must be accompanied by the increase of indentation size. However, the indentation size is taken as a constant in the calculation. Therefore, this may be explained as a result of the increase of microjet velocity. There are two mechanisms to increase the microjet velocity. They are,

(1) The mean bubble collapse velocity can be increased by increase of downstream pressure, P_2, and so the microjet velocity is also increased by the ratio of the square root of P_2 (Plesset and Chapman [1971]). Then, if the loading pressure can be assumed to be caused by water hammer pressure, the pressure is proportional to the microjet velocity and to the square root of P_2.

In fact, the loading pressures calculated for P_1=100bar and P_1=120bar are 1.11 and 1.22 times higher than the value obtained for P_1=80bar on an average, and these values agree very well with the ratio of the square root of their downstream pressures, 1.12 for P_2=3.0bar and P_2=2.4bar and 1.22 for P_2=3.6bar and P_2=2.4bar.

(2) In the case of the microjet produced by shockwave impact, the microjet velocity is clearly increased under more intensive shockwave; i.e., when the cavitation number is maintained constant, higher upstream pressure P_1 provides more intensive cavitation field and the higher microjet velocity may result from it.

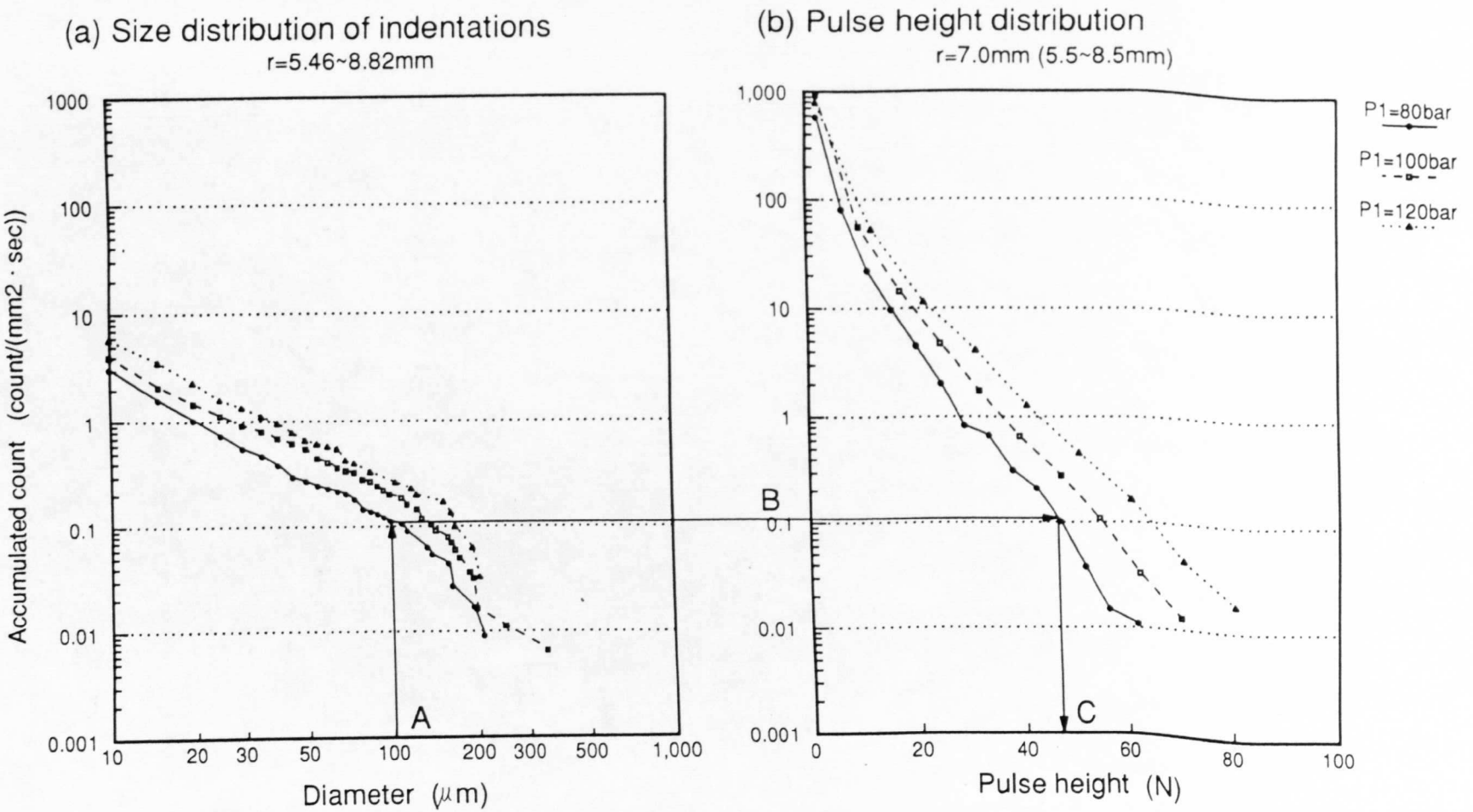

Fig.9.4.1 Indentation size distribution and pulse height distribution.
Indentations are counted from r=5.46~8.82mm (the maximum damage area).
Transducer size is A_T=8.88mm^2 and it covers r=5.5~8.5mm.
P_1=80~120bar, σ=0.03, S_{off_2}=40mm.

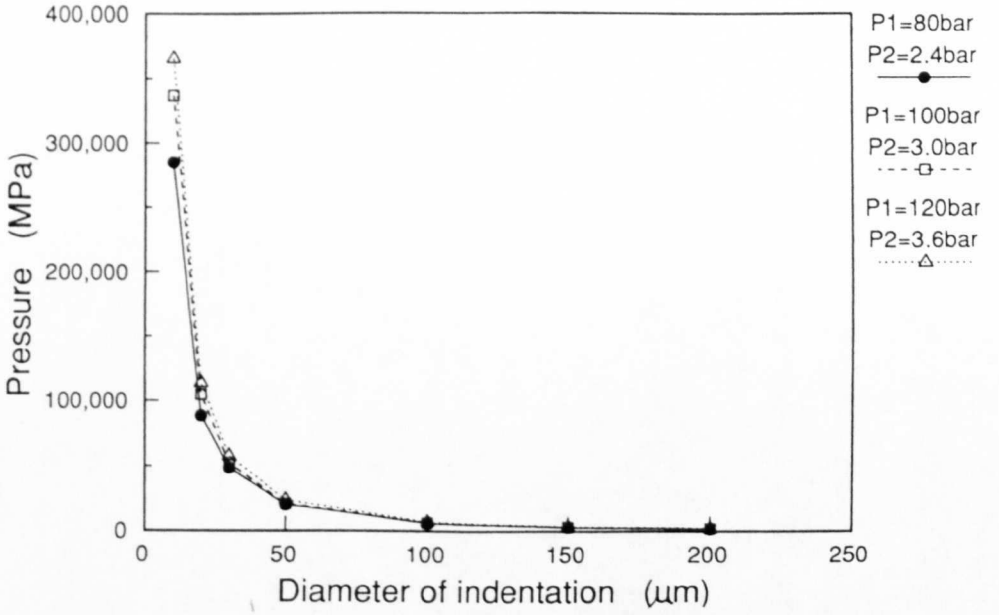

Fig.9.4.2 Variation of cavitation loading pressure with indentation size. P_1=80~120bar, σ=0.03, S_{off_2}=40mm, r=7.0mm, A_T=8.88mm^2.

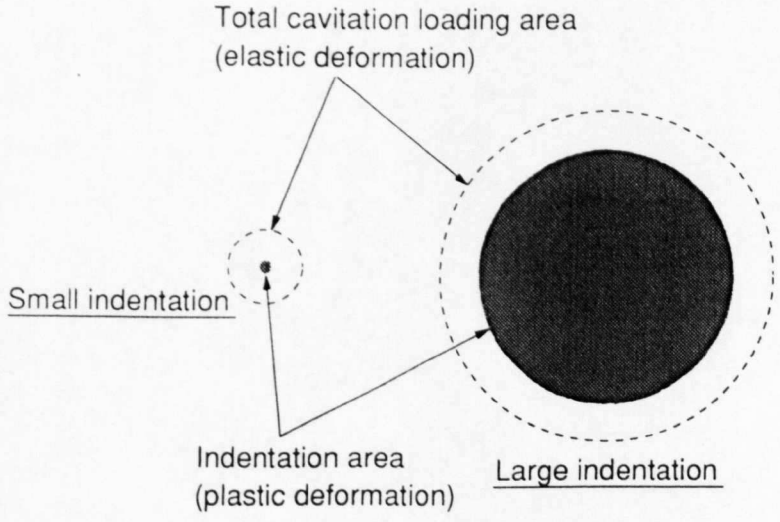

Fig.9.4.3 Relation between indentation size (plastic deformation) and loading size (elastic deformation), schematic diagram.

It is expected that the data of the pulse height analysis of cavitation loading may be correlated with erosion rate and indentation counting results.

The acoustic intensity of pressure wave, I, i.e., the power per unit area, is generally defined as

$$I = \frac{P^2}{2\rho C}$$

Where P is the amplitude of the pressure pulse and C is the velocity of sound.

Then, the energy from individual cavitation loading, E_i, is

$$E_i = I_i \cdot \tau_i \cdot A_i$$

where I_i, τ_i and A_i are the acoustic intensity, duration of the pulse and the area of the individual cavitation loading, respectively.

Above equation is rewritten as

$$E_i = \frac{F_i \cdot P_i \cdot \tau_i}{2\rho C}$$

Where $F_i = P_i \times A_i$ is the pulse height of the individual loading. Here P_i and τ_i are unknown values and if it can be assumed that P_i is proportional to F_i and τ_i is constant, the energy from an individual loading, E_i, becomes proportional to the square of the pulse height, F_i^2.

Then, the total acoustic energy from entire cavitation loading, i.e., the sum of the energy from individual cavitation loading, applied to the transducer can be correlated with the sum of the square of individual pulse height as

$$\sum E_i \propto \sum F_i^2$$

It is generally accepted that there is a threshold value for each material, below which the load produces no permanent damage on the material. Therefore, not all the cavitation loading pulses counted can contribute to the cavitation erosion. In order to correlate the pulse height data to cavitation damage, the summation in the above equation must be carried out for the cavitation loading above the threshold value. In the present pulse height analysis, it can be assumed that the pulse height which

corresponds to the smallest size indentation counted, 10μm, is used as the threshold value defined as the critical pulse height F_c, below which no pulses are responsible for the damage. These values for various pressure conditions are found in Table 9.4.1.

The sums of F^2 of all the pulses higher than or equal to F_c per unit time and unit area (simply described as ΣF^2 in the following part and figures) were calculated for P_1=80~120bar and σ=0.03 at the second optimum stand off distance S_{off2}=40mm. These values are plotted with upstream pressure P_1 in Fig.9.5.1. As expected, they show good power law relation with P_1 (and so with jet velocity). The index is n=2.8 with P_1, which is n=5.6 with the jet velocity. This value agrees well with the index n=6.2 for peak cumulative erosion rate with the jet velocity obtained from erosion tests for the same pressures and stand off distance in Chapter 7.

Figure 9.5.2 shows the correlation between ΣF^2 per unit time and unit area and the sum of (diameter)^3 of each indentation per unit time on an entire target disc from indentation counting tests. The latter is considered to be proportional to the total volume of indentations; i.e., the cavitation loading energy per unit time which was absorbed as a form of a plastic deformation. Figure 9.5.3 shows the same ΣF^2 per unit time and unit area with the peak cumulative erosion rate (PER_C) obtained from erosion tests as a measure of cavitation erosion intensity at a matured stage of erosion. Therefore, these are regarded as the correlation between the acoustic energy flux of a cavitating jet applied to the maximum damage area and the cavitation energy absorbed on the entire target per unit time. Both correlations in Figs.9.5.2 and 9.5.3 are acceptable, though the number of points are only three. Particularly, Fig.9.5.3 shows striking agreements. This indicates the possibility that the cavitation loading intensity can be accurately quantified by measuring a number of loading pulses at each height above the critical pulse height, and then it is possible even to predict the cavitation erosion results for a given material under a given cavitation condition where the cavitation loading intensity is quantified.

From this good correlation, it is also confirmed that the pulse height distribution data measured by the PVDF piezofilm transducer in the present project is quite reliable from the energy standpoint.

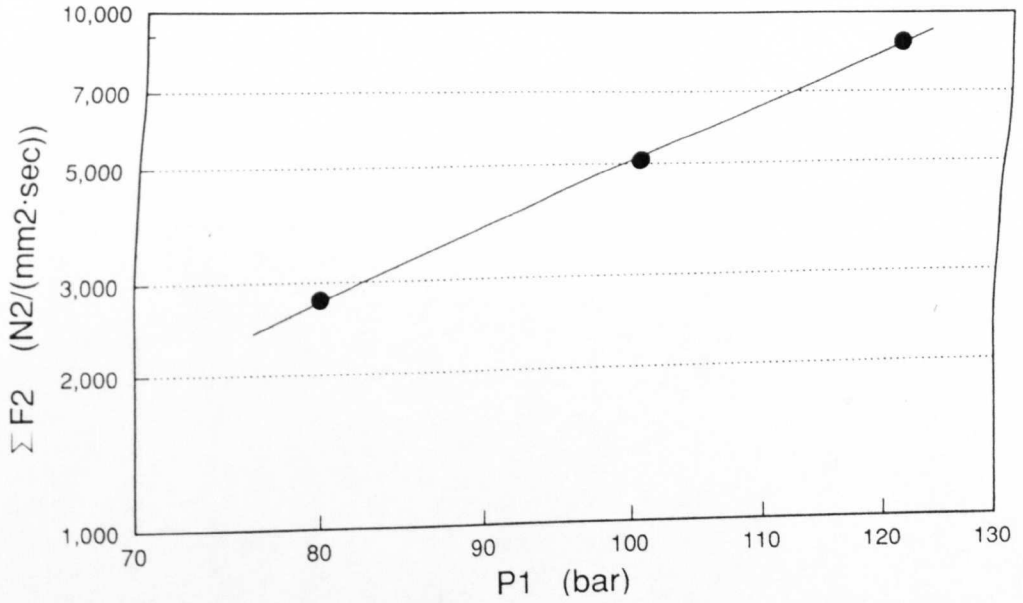

Fig.9.5.1 Variation of sum of pulse height squared, ΣF^2, per unit time and area with upstream pressure.
Constant cavitation number σ=0.03. S_{off_2}=40mm, r=7.0mm, A_T=8.88mm^2.

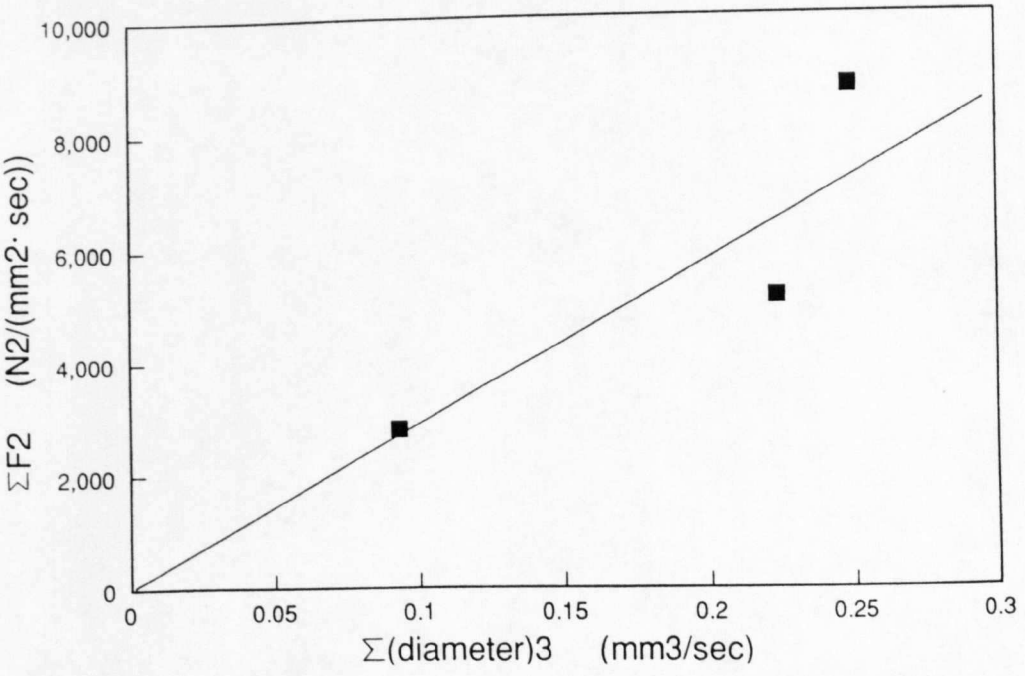

Fig.9.5.2 Correlation of pulse height data (ΣF^2 at the maximum damage area) with indentation data (Σ(diameter)^3 on entire specimen).

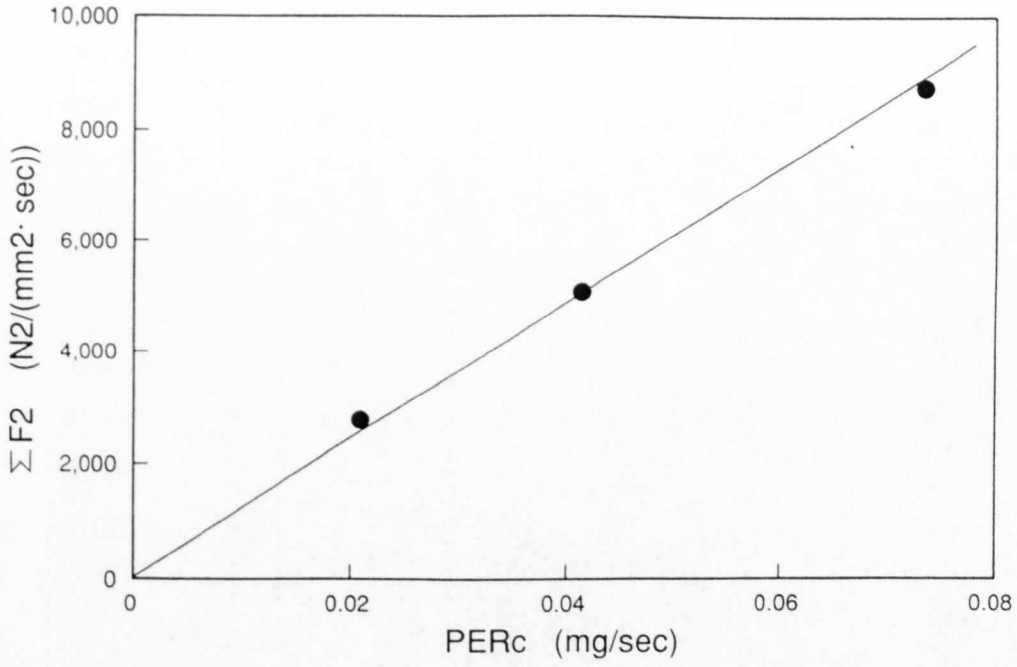

Fig.9.5.3 Correlation of pulse height data (ΣF^2 at the maximum damage area) with erosion data (peak erosion rate, PER_C).

9.6 Conclusions

Main results and discussions in this chapter are summarized as follows.

(1) The width of the cavitation loading pulse at the half height of the peak ranges from 1.0μs to 2.5μs in general, though the number of samples checked is limited. The natural frequency of PVDF piezofilm (thickness 110μm), 10MHz, and of polyimide tapes, 9.3MHz, (estimated in Chapter 5) are sufficiently high to acquire these pulses.

(2) Both the attenuation and the dissipation effects through the polyimide protection tapes are negligible within the range of the tape thickness from 140μm (for two layers) to 420μm (for six layers) where the ratio of the tape thickness to the transducer dimension is about 5~14%. Then, two layers of those protection tapes were used for the rest of the measurements.

(3) Pulse height distributions were obtained by transducers with six different sensitive area from A_T=0.140~8.88mm^2. The pulse distribution height increases with increase of the transducer area A_T, while distribution shapes in all cases look similar. This tendency is considered as a result of the "edge effect" due to the relative size of the transducer sensitive area to the cavitation loading size. It is thought that the larger size transducer should be less affected by the edge effect. Therefore, the largest one with the sensitive part of A_T=8.88mm^2 has been regarded to be able to provide the most realistic data among all the transducers prepared in the present experiments and was used for the rest of the measurements.

(4) The cavitation loading pressures P_L were calculated from the indentations and pulse height distributions. They significantly decrease with the increase of the reference indentation size. The reason for this may be due to some elastic deformation area around the indentation and the actual loading area may be greater than the indentation size. The ratio of the indentation size to the real loading size may be much greater for larger indentations. Then, the pressure calculated tends to be smaller for larger indentations and it is going to be extremely large for the very

tiny indentation size like 10μm.

(5) The smallest loading pressure calculated, P_L=1.85~2.24x10^3MPa for P_1=80~120bar, with the largest size indentation for each pressure condition can be regarded as the most realistic value. Considering the situation described in (4), even those pressure values may become smaller in reality. These pressures are a little lower than, but in the same order of magnitude with 4.8~8.1x10^3MPa reported by Kirejczyk [1979] and 4.3x10^3MPa estimated by the author taking the largest indentation size and its pulse height from Okada et al. [1989]. It is interesting that such loading pressures estimated from experiments using different types of cavitation source, such as a submerged jet, vibratory cavitation and an water tunnel, show similar values.

(6) The loading pressure P_L estimated agrees well with the water hammer impact pressure, P_{wh}=0.9~1.8x10^3MPa, calculated from the microjet velocity 200~400m/s which were obtained by Tomita and Shima [1986] and Dear and Field [1988] for the microjet struck by shockwave.

(7) Cavitation loading pressures P_L increases with the increase of test pressure conditions from P_1=80bar and P_2=2.4bar to P_1=120bar and P_2=3.6bar. Since the indentation size is taken as a constant in the pressure calculation, this may be explained by the increase of microjet velocity.

(8) The sum of F^2 of all pulses counted per unit time and unit area is considered to be proportional to the acoustic energy applied from cavitation loading to the specimen per unit time and unit area.

(9) The sum of F^2 above a critical pulse height F_c (ΣF^2) shows good power law relation with upstream pressure P_1. The index is n=2.8 with P_1, and so it becomes n=5.6 with jet velocity. This agrees well with the index n=6.2 obtained for the peak cumulative erosion rate with the jet velocity in Chapter 7.

(10) The correlation between ΣF^2 at the maximum damage area and the peak accumulated erosion rate PER_C from erosion tests is extremely good. This indicates that it is possible to accurately quantify the cavitation loading intensity by measuring

a number of loading pulses at each height above the critical pulse height. It is also confirmed from this good agreement that the pulse height distribution data measured by the PVDF piezofilm transducer in the present project is quite reliable from the energy standpoint.

CHAPTER TEN - CONCLUSIONS

10.1 Introduction

10.2 Conclusions

10.3 Application of the technique and suggestions for further work

10. CONCLUSIONS

10.1 Introduction

At the end of each chapter of results, conclusions concerning the work described in it have been drawn. This chapter summarizes these conclusions and relates them together.

Also suggestions for further work are made.

(1) Erosion produced by a cavitating jet

Cavities are formed at the inlet edge of the long orifice nozzle. The potential core of the jet disappears at a distance of probably 5~7 diameter downstream from the nozzle outlet and simultaneously, the mixing zone of the jet and the cavitating bubbles begin to spread inside and outside of the jet. If cavitating bubbles are located inside the impinging jet when they approach the target, they must be transported through the high pressure zone at stagnation region. Then, they have to collapse well before the target surface and neither their shockwave nor microjets are able to damage the surface. Therefore, there is almost no damage found at the stagnation area. If they are located outside the jet, they do not need to pass through such a high pressure zone and so they are able to survive and collapse near the surface of the target somewhere outside the stagnation area.

It has been confirmed from the present measurement of mean pressure distribution on a specimen that the cavitation damage is located just outside the stagnation area. High speed photographs have shown that the bubbles seem to exist outside the locus of the peak velocity in the wall jet velocity profile and the distance from the surface to the bubbles increases with the radial distance from the impingement centre. Although bubbles are transported with a wall jet and may collapse anywhere above the surface, the damage area is limited to a ring shape around the stagnation area. Outside this ring damage area, the distance between the bubbles and the surface may be too large for cavities to be damaging.

As soon as a soft aluminium target is exposed to the jet, erosion begins and weight loss increases with time. It was found that in spite of the increasing weight loss value the size of the erosion ring is being maintained almost unchanged throughout the erosion tests except the inner edge at the second optimum stand off distance. Thus, the increase in weight loss mainly results from the erosion development in depth.

(2) Cavitation loading

The cavitation loading pulse heights were successfully measured using a novel piezoelectric pressure transducer with pulse height measurement system, both of which were developed during this project. The transducer uses a PVDF piezofilm as a pressure sensing material. In order to calibrate the transducer, a simple calibration device which employs pencil lead breakage as a source of high speed loading was also developed. The cavitation loading pressure was calculated from the distribution of the pulse heights and the size of indentations produced on a soft material (annealed 1200-aluminium alloy).

The magnitude of the pressure estimated is around 2GPa. It is lower but in the same order of magnitude as the one, 4.8~8.1GPa, which Kirejczyk [1979] reported and another, 4.3GPa, which the author estimated from the results of Okada et al. [1989]. It is very interesting that such loading pressures from different types of cavitation source, such as a submerged jet, vibratory cavitation and an water tunnel, show similar magnitudes. The pressures also agree well with the water hammer pressure P_{wh}=0.9~1.8GPa calculated by assuming the appropriate wedge shape of the jet tip (Lush [1983]) from the microjet velocity of 200~400m/s which were obtained by Tomita and Shima [1986] and Dear and Field [1988] for the bubble struck by shockwave.

The width of the cavitation loading pulses at the half of the peak height ranges from 1.0~2.5μs, though the number of samples checked is limited.

Various size of transducers whose sensitive area ranges A_T=0.140~8.88mm^2 were made. It was found that the magnitude of the pulse height depends on the area of the transducer. One reason for this can be understood as an edge effect; i.e., a part of the loading pulse is cut off at the edge of the sensitive part of the transducer. Therefore, although it has not been often emphasized, the size of the transducer can be a very important parameter.

It was observed that indentations on a soft material produced by cavitation loadings are randomly distributed within the same ring damage area as the one of the erosion. Their size ranges widely from a few micron to 350μm. From the observation using a scanning electron microscope, the profile of them generally seems like a conical shape with or without a flat part at the bottom. This indicates that the microjet type impingement may be a more probable mechanism to produce these

indentations.

In all cases tested in the present work, the raw distributions of indentation size show similar shapes regardless of the difference in pressures and stand off distances.

The raw distribution can be presented as

$$N(d) = b \cdot d_s \cdot d^{-m}$$

where N(d) is the number of indentations at size in diameter, d, and d_s is the range of the measurements within which the number is counted. Almost same index, m≈2.0, was obtained for the all cases.

The frequency of the cavitation loading can be found from the indentation counting results. The number density (number of indentations per unit time and unit area) of indentations larger than 10μm in diameter for P_1=100bar and σ=0.03 at the maximum damage radius on the specimen is 30 counts/(mm^2·sec) and 5 counts/(mm^2·sec) at the first (S_{off1}) and the second optimum stand off distances (S_{off2}), respectively. The area density (the sum of each indentation area per unit time and unit area) for the same case is 0.035mm^2/(mm^2·sec) at S_{off1} and 0.01mm^2/(mm^2·sec) at S_{off2}. This means that the same element of the surface is impinged once in about 30sec at S_{off1} and once in about 100sec at S_{off2} on average.

(3) Effects of stand off distance

The size of the erosion and erosion rate are dependent of stand off distance. As reported by some investigators, two optimum stand off distances are found in the present nozzle and nozzle holder configuration. Two erosion rings are found at the first optimum stand off distance S_{off1}, though there is only one at the second optimum stand off distance S_{off2}. The area of the erosion ring shows its peak value at both S_{off1} and S_{off2}. This means that the maximum erosion rate occurs with the largest area of the damage.

It was found that variation of the number of indentations on the entire target with stand off distance is similar to the one of the weight loss results, including a sharp peak at S_{off1}, whereas the largest and average diameters of indentations increase with stand off distance and seem to show their maximum values at around S_{off2}. This indicates that some cavities are sufficiently large and powerful to be still growing with

distance along the jet and then produce larger size indentations. Similar tendency has also been reported with venturi by Robinson and Hammitt [1967].

(4) Effects of cavitation number

It is generally accepted that the length of the cavity and the optimum stand off distance can be controlled by cavitation number. In the present work the cavitating jet lengths were measured from high speed photographs. They can be related with the cavitation number σ as

$$\frac{l_j}{d_e} \propto \sigma^{-h_1}$$

where l_j and d_e are the average cavitating jet length and the effective nozzle diameter. The index is obtained approximately $h_1 \approx 1$.

Similarly, as suggested by Lichtarowicz and Kay [1983] the relation between the optimum stand off distance and cavitation number σ is expressed as

$$\frac{S_{off}}{d_e} \propto \sigma^{-h_2}$$

where the index is $h_2 \approx 0.9$ for the second optimum stand off distance S_{off2} and $h_2 \approx 0.4$ for the first optimum stand off distance S_{off1}. The value of $h_2 \approx 0.9$ at S_{off2} agrees well with $h_2 \approx 0.8$ obtained by Lichtarowicz and Kay [1983] for their results at Nottingham and the others at Aachen. The index $h_2 \approx 0.9$ at S_{off2} shows good agreement with the index $h_1 \approx 1.0$ for the cavitating jet length.

Since the ratios of the second optimum stand off distance S_{off2} to the jet length l_j for various cavitation number show consistent values about 75%, this can be used as a technique to predict the possible range of the second optimum stand off distance S_{off2} before we start testing in different conditions. The parameter, the jet length, may be useful to express the cavitation intensity, since it can include various effect of nozzle, nozzle holder and test chamber configurations and the effects of cavitation number. The same ratios for S_{off1}, however, range rather widely from 27~36%.

As shown in Fig.6.3.4, the cavitation number also affects the decay of stagnation pressure along the jet axis.

(5) Effects of upstream pressure

The relation of the peak cumulative erosion rate, PER_C, with the jet velocity, V, is expressed as

$$PER_C \propto V^n$$

The indices obtained are n=6.6 at the first optimum stand off distance S_{off1} and n=6.2 at the second optimum stand off distance S_{off2} for upstream pressure P_1=80~120bar with constant cavitation number σ=0.03. However, with the constant downstream pressure P_2=3.0bar, the index at S_{off2} becomes much greater, n=13.8 and no linear relation exists on a log-log graph at S_{off1}.

The sum of the square of each pulse height above the threshold value (critical pulse height F_c) was calculated as a measure of cavitation erosion energy flux applied to the target. This value also shows similar relation with the jet velocity as above; i.e., index n=5.6 is obtained at S_{off2} and agrees very well with n=6.2 for PER_C.

(6) Effects of downstream pressure

Downstream pressure cannot be independently controlled while maintaining the other two parameters, upstream pressure and cavitation number, constant. In erosion tests based on weight loss measurements, the effects of upstream pressure and/or the effect of cavitation number normally predominate over the effects of downstream pressure. However, when the individual loading is concerned, it is the downstream pressure which affects the process of each cavity collapse.

It was observed that cavitation loading pressure estimated, P_L, increases as the upstream pressure increases from P_1=80bar to P_1=120bar with constant σ=0.03 (the downstream pressure also increases from P_2=2.4bar to P_2=3.6bar). Since the indentation size for the loading pressure calculation is same for all cases, one of the reasons for this can be explained as a result of the increase of the downstream pressure which can increase the microjet velocity.

(7) Correlation of the indentation counting and pulse height data with the erosion results

In the present research, a good correlation between the sum of (diameter)^3 of each indentation on the entire target and the peak cumulative erosion rate PER_C was found at the second optimum stand off distance S_{off2}, while it is poor at the first optimum stand off distance S_{off1}. The correlation using only the number of indentation is also good at S_{off2} and relatively poor at S_{off1} (though it is better than the one based on the sum of (diameter)^3 at S_{off1}). Therefore, it appears that only counting the number of indentations on a soft material may provide sufficiently good prediction on the erosion rate.

The correlation of the sum of the square of cavitation loading pulses which are summed from the critical pulse height to the highest pulse height at the maximum damage area with PER_C has also been obtained. These are regarded as the correlation between the energy flux of a cavitating jet applied to the maximum damage area per unit time and the cavitation energy absorbed as a form of damage on the entire target per unit time. The agreement is extremely good. This indicates that it is possible to accurately quantify the cavitation loading intensity by measuring only a number of loading pulses at each height above the critical pulse height.

It is also confirmed from this good correlation that the pulse height distribution data measured by the PVDF pressure transducer with the pulse height measurement system are quite reliable from the energy standpoint.

10.3 Application of the technique and suggestions for further work

The apparatus and techniques for a cavitation loading impact analysis have been developed and reliable results were obtained. The pressure measurements and indentation counting can basically be applied to any situation of cavitation. Particularly, the pulse height analysis is considered to be more reliable to evaluate the cavitation erosion capacity than the erosion tests, since the former is purely hydrodynamic problems while the latter must include various effects of material used.

Since some important parameters in the present study were maintained unchanged, following further works may be recommended to refine the observation and results obtained.

(1) Several materials with different hardness can be used for indentation counting tests. This enable us to investigate the effects of material hardness on the magnitude of the loading pressure calculated, P_L. They should include one or two materials softer than the annealed 1200-aluminium alloy so that the estimation of the loading area can be more realistic and the pressure P_L lower than the one estimated (2GPa) in the present study may be obtained.

(2) The correlation between the pulse height data and the erosion rate should be further investigated for various target materials with different crystal structures. Variation of the threshold pulse height (critical pulse height, F_c) for each material could yield interesting results in both respects of the relative material resistance to cavitation erosion and the magnitude of cavitation loading pressure.

(3) Since the chamber size of the cavitating jet test rig used in the present study is large, more detailed study on the structure of the cavitating jet, on the cavitation with an wall jet and on bubble collapse may be possible with more sophisticated high speed photographs; e.g., high speed motion pictures.

The PVDF pressure transducer has worked very well, but there was a problem with durability at the first optimum stand off distance where the jet velocity is extremely

high. However, since the cavitation intensity and the flow velocity used in the present project are very high, it is expected that the transducer would have less problem for wide range of pressures and flow conditions under more common cavitation situation, such as an water tunnel or the scale model of an actual hydraulic machinery.

It is considered that some further work using the transducer of similar design could yield useful results under various conditions where the characteristics of cavitation erosion have not been well explained by the erosion tests; e.g., the difference in the relative resistance of various materials to cavitation damage produced by the different types of the cavitation source. Another interesting field to investigate would be the detailed study on the cavitation loading with scale and temperature effects.

APPENDICES

A1: Evaluation of erosion results from specimens with slightly harder Vickers hardness value

A2: Image analysis for indentation counting

A3: Pressure transducer using Polyvinylidene Fluoride (PVDF) piezofilm

A4: Calibration of PVDF pressure transducers using pencil lead breaking method

APPENDIX A1: Evaluation of erosion results from specimens with slightly harder Vickers hardness value

Unfortunately, sufficient number of 6063-aluminium alloy specimens from the same lot were not available in erosion tests. Therefore, all tests with pressure condition of P_1=120bar and P_2=2.4bar had to be carried out with the same industrial standard material but from a different lot, which had a slightly higher Vickers hardness value. The Vickers hardness value of this "hard" material (from the first lot) ranges 34.5±0.9 while that of "standard" material (from the second lot) is 29.7±1.9. Since the effects of such a difference in hardness on erosion rate was not fully understood at that time, the erosion tests with both standard and hard materials were performed for selected conditions and the results were compared. Erosion results of standard material for upstream pressure P_1=120bar and downstream pressure P_2=3.0bar and 3.6bar at the first (S_{off1}) and the second optimum stand off distance (S_{off2}) were used for comparison. These stand off distances are S_{off1}=18mm and S_{off2}=45mm for P_1=120bar and P_2=3.0bar and S_{off1}=18mm and S_{off2}=40mm for P_1=120bar and P_2=3.6bar. The comparison was continued until the harder ones lost the weight as much as the standard ones did at the cumulative erosion ratio under same testing conditions. The results are plotted in Fig.A1.1 as a form of variation of conversion ratio, i.e., the weight loss of a hard specimen divided by the weight loss of a standard one at the same exposure time. As the erosion is developed, the conversion ratio seems to show a constant value, 0.85. The number of examples to withdraw the conclusion is only four cases and such a single conversion ratio actually does not cover the relatively early stage of erosion as observed in Fig.A1.1, but for the convenience sake, every weight loss result obtained for hard material, only under the pressure condition P_1=120bar and P_2=2.4bar, was simply multiplied by a conversion ratio of 1/0.85 in this project. That is,

$$\Delta W_{standard}(t) = \frac{1}{0.85}\Delta W_{hard}(t)$$

$$CER_{standard} = \frac{1}{0.85}CER_{hard}$$

where $\Delta W(t)$ is the weight loss at exposure time t and CER is cumulative erosion rate. All the results with pressure P_1=120bar and P_2=2.4bar presented and discussed in the

thesis have been already converted by the above equation.

The difference 15% in weight loss is relatively not a significant value and basically, the optimum stand off distance, the erosion curve with various stand off distances and the erosion radius are not affected by this slight change of material hardness.

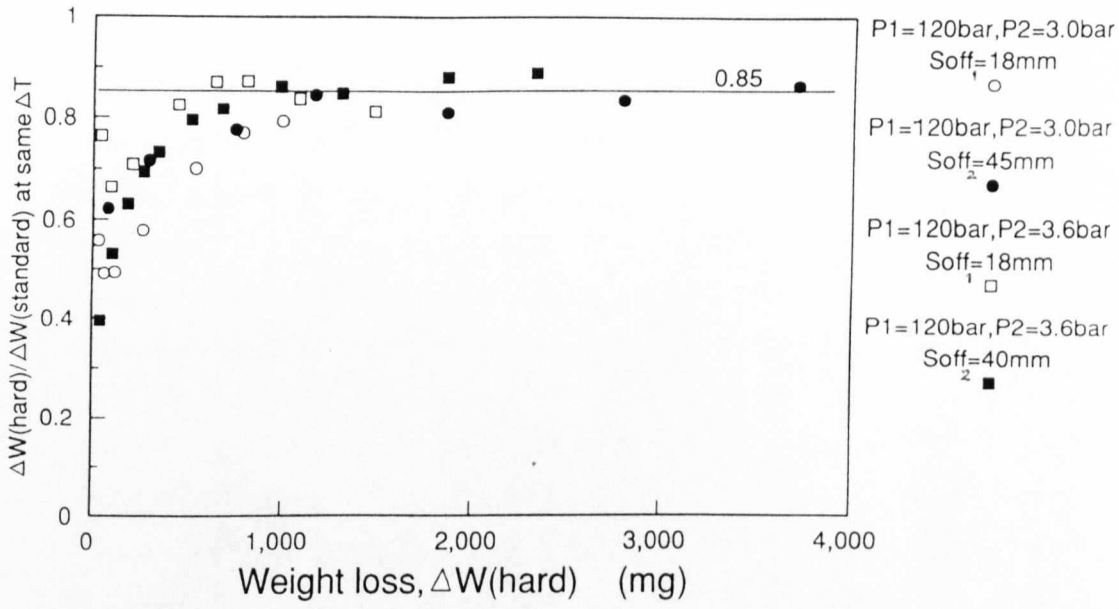

Fig.A1.1 Variation of ratio of weight loss between two annealed 6063-aluminium alloy from different lots with slightly different hardness, $\Delta W_{hard}/\Delta W_{standard}$, with ΔW_{hard}. Vickers hardness; 30.6~31.4 (standard specimens) and 33.5~34.9 (hard specimens).

Quantifying the information on the image of a damaged specimen, such as counting the number and/or measuring size and location of indentation, is not always an easy task. Especially this case, the size of indentations ranges from a micron to a few hundred micron, and the data varies with distance from the erosion centre to the outside edge of the erosion which is almost twenty millimetre.

An image analyzer with a top range of optic microscope was used to perform this work. Schematics for setting up the machine and the machine scanning direction on a specimen with image capturing frames are presented in Fig.A2.1 and A2.2, respectively. In the present case, the "image" captured through the microscope consisted of a lot of indentations with polishing scratches and original surface flaws in a square shaped frame. They were captured by a video camera, and then digitized and analyzed by a computer system. The horizontal scanning move of the specimen is also automatically controlled by the computer. The image analyzing process can be briefly explained as follows,

(1) Image capture

The indentations on the specimen surface are captured by a video camera through the microscope with magnification x100.

(2) Image digitization

The captured image is divided into 262144pixels (512x512) as shown in Fig.A2.3 and "grey value" which corresponds to the darkness of the colour varying from 0 for black to 255 for white is allocated to each pixel for handling the image in later process.

(3) Image manipulation

Various unfavourable reflection throughout the frame due to particular illumination is corrected by subtracting a filter which is made from the blank image with the same illumination. Without this process, grey value at corners of the frame is usually much lower, darker, than the average (Fig.A2.4).

(4) Image segmentation

Before this process, each pixel has each own grey value spreading from 0 to 255. Then, they are classified into only two levels (binary image), black (0) or white (255), by setting an appropriate threshold grey value between 0 and 255 as shown in Fig.A2.5. (Filtering process in Fig.A2.5 was not used for the indentation counting in the present work.)

(5) Image identification

Objects (indentations etc.) are identified in a simple black and white image. Because of no information outside the frame, there is difficulty to properly quantify the object lying over the edge of the frame. To avoid this problem, rather time consuming process was taken for the present measurements. Such objects were neglected at the first identification which was for objects only inside the frame (Step 1 in Fig.A2.6). Then at Step 2, the frame moved half width to the scanning direction and objects only on the centre line, which had been neglected in the previous step, were identified this time. Same procedure was taken as Step 3 moving half width to the direction of 90 degree from the scanning direction for the "top" edge of the frame of Step 1 as well, although there is no drawing for Step 3 in Fig.A2.6.

Even by these procedure, inappropriate measurements can happen at the corner where the object is counted twice. But most of them were spotted by the operator and corrected afterwards, and in fact, number of such particular events were even negligible compared with the total indentation counts. After all, three continuous whole image analyzing processes had to be taken to obtain reliable data for one frame.

In the indentation counting here, the objects smaller than 30pixels (approximately equivalent to 10micron in diameter) were discarded at the end of the identification process, because vast number of micron scratches and very small pits were found before the cavitation exposure, which had been generated through the process of polishing the surface of this very soft 1200-aluminium alloy and could be very much affected by even the slightest change in illumination.

(6) Image quantification

Necessary data about the identified objects can be calculated in many ways and stored in a computer file. For example, equivalent circle diameter and the maximum diameter can be calculated for a non-circle object as shown in Fig.A2.7.

Finally, photographs of computer display images actually showing some processes described above are presented in Fig.A2.8.

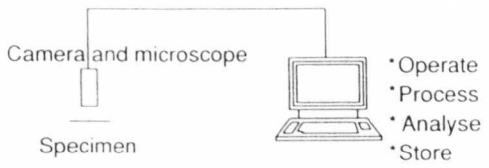

Fig.A2.1 Image analyzer.

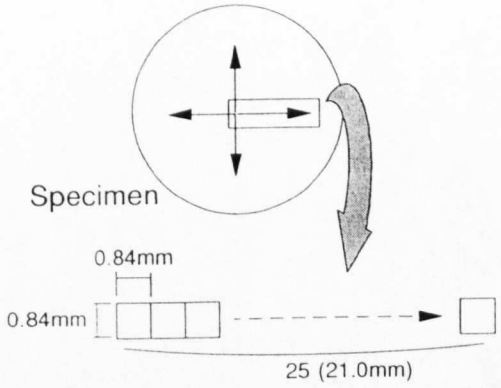

Fig.A2.2 Scanning path for image analysis.

512 x 512 = 262144 pixels

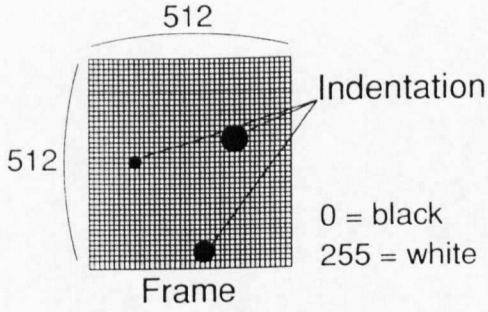

Fig.A2.3 Digitization.

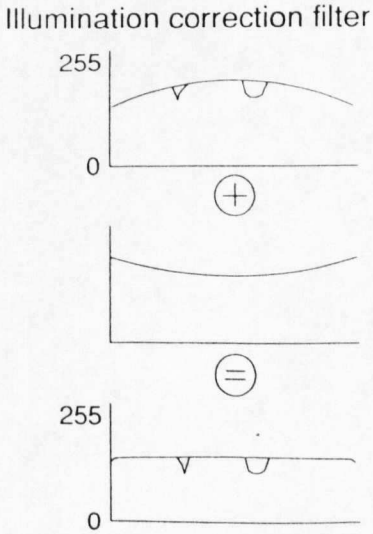

Fig.A2.4 Manipulation.

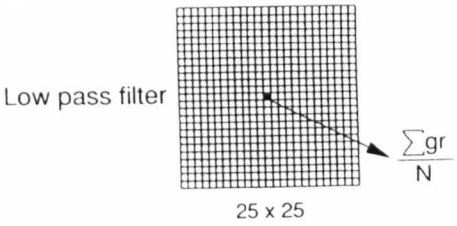

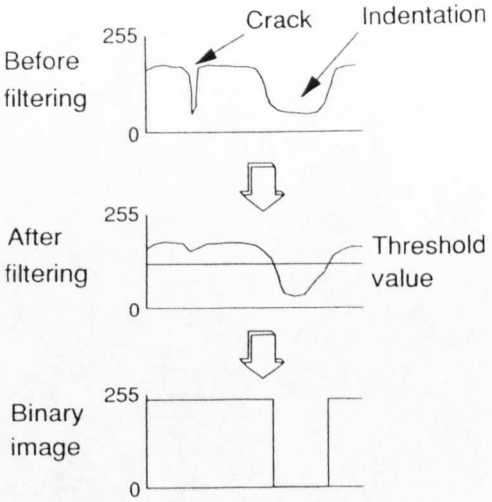

Fig.A2.5 Segmentation.

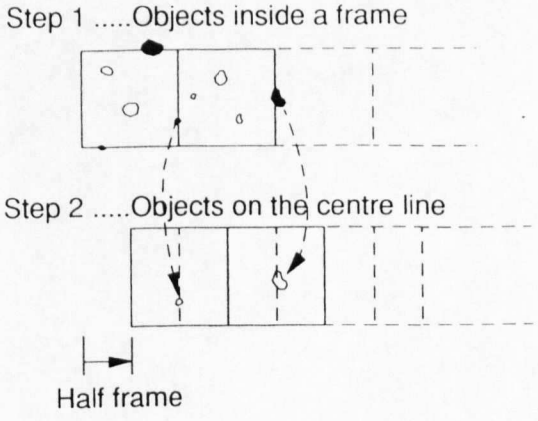

Fig.A2.6 Identification

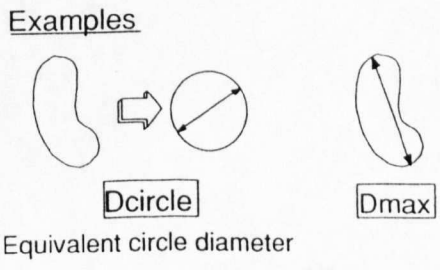

Fig.A2.7 Quantification.

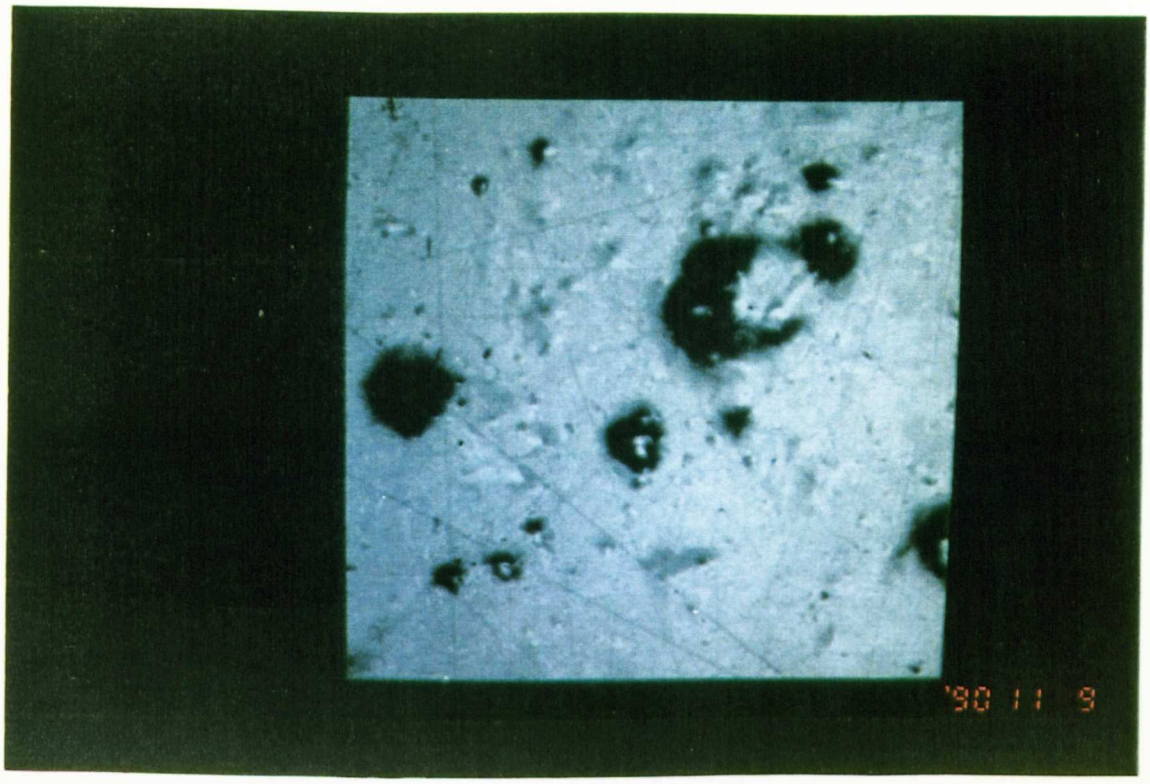

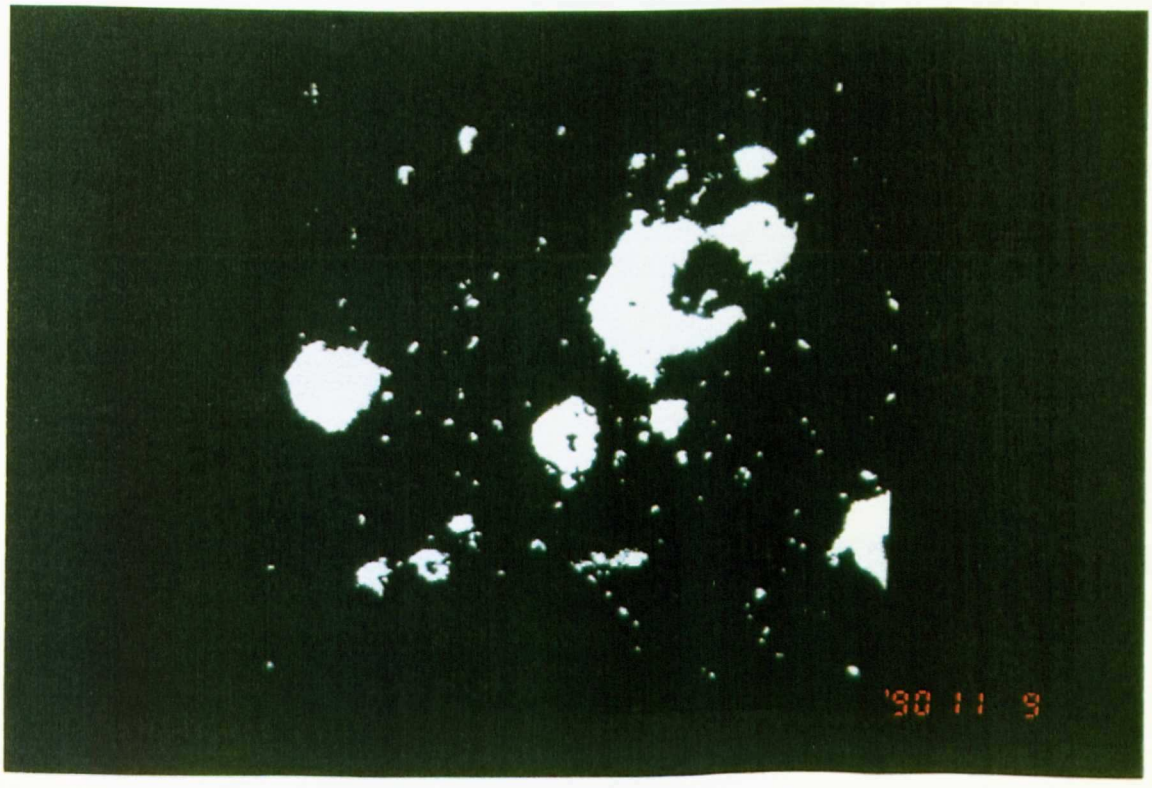

Fig.A2.8 Image analyzing process.
(a) Image capture, digitization and manipulation.
(b) Image segmentation. (A binary image is produced.)

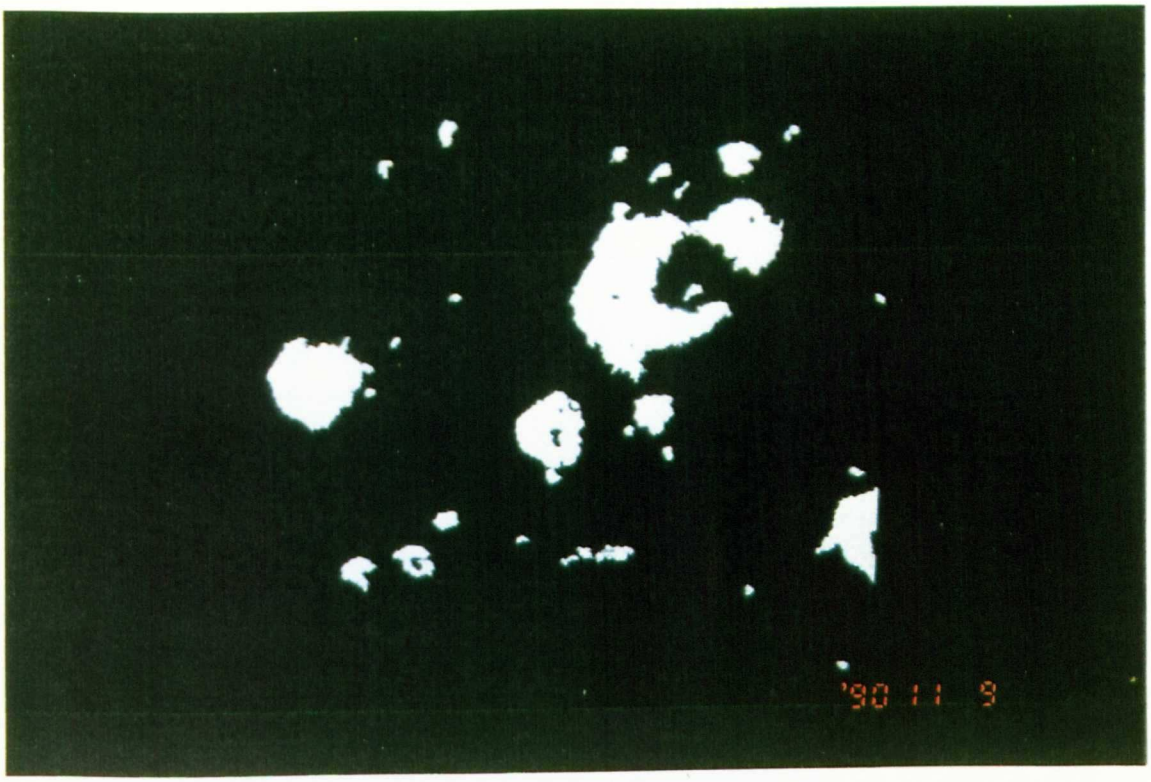

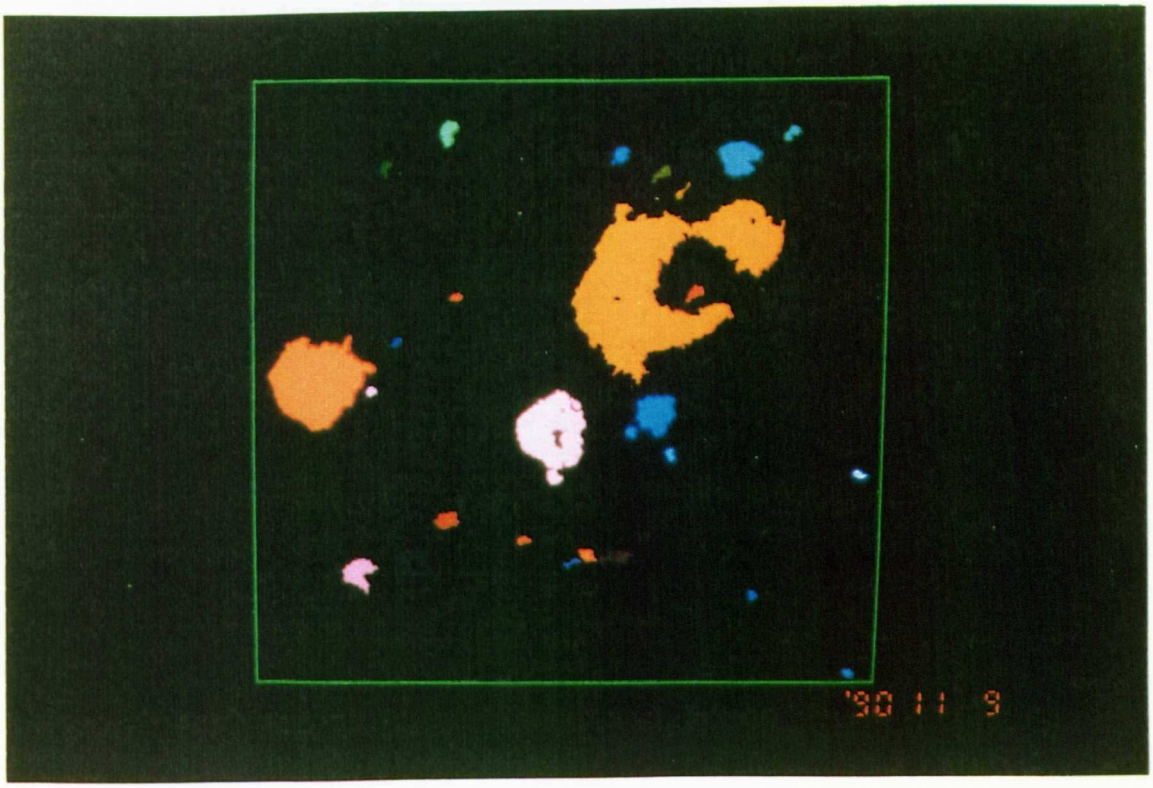

Fig.A2.8 Image analyzing process.
(c) Image identification. (Indentations smaller than 10μm are removed.)
(d) Image quantification. (Number is counted and size is calculated.)

Regardless of its detailed mechanism, it is generally accepted that cavitation loading is a sort of repetitive high pressure impact. It is very damaging and the loads are applied within a very short time as short as 1~5μs. From the results of indentation measurements on a very soft and ductile material, it is probable that the each loading is limited to a very small area as it can be seen from the size of the indentations which range from a few microns to a few hundred microns in diameter. Therefore, the measurement device for it must be durably resistant to erosion and its sensor part must have very fast dynamic response and have a very small area. However, there are almost no suitable dynamic transducers available in the market, which can meet all the requirements at sufficiently high level, and so it was decided that the desirable dynamic transducer would be developed for this particular purpose.

Figure A3.1 shows the transducer setting on a stainless steel target (see also Fig.5.10.1 for photographs). It consists of a PVDF piezofilm, two leads, two layers of polyimide adhesive tape for protection and a Kapton insulation film. They are mounted into the shallow groove on the target and are bonded with cyanoacrylate type adhesives. A cross painted part by silver conductive painting is the sensitive area. Working principles, material specifications, manufacturing procedures and points in designing are described below.

(1) Piezoelectricity

If a force is applied to a solid crystalline dielectric as shown in Fig.A3.2, it will produce stress within the crystal and a deformation of the crystal lattice. In certain crystals with asymmetrical charge distributions, the lattice deformation is, in effect, a relative displacement of the positive and negative charges within the lattice. And the displacement of the internal charges will produce equal external charges of opposite polarity on opposite sides of the crystal. Then, the crystalline structure produces a charge proportional to the force. Conversely, when an electric field is applied to these crystalline structures, they change shape and produce dimensional changes in the crystal. This is called piezoelectric effect (The word "piezo" means "pressure" in Greek.). The charge can be measured by applying electrodes to the surfaces

and measuring the potential difference between them.

Since the magnitude and polarity of the induced surface charges are proportional to the magnitude and direction of the applied force F,

$$Q = d \cdot F$$

where Q is the electric charge induced and d is a constant of the piezoelectric material. The force F causes a thickness displacement Δt. The induced charge, written in terms of the displacement Δt, is

$$Q = d \frac{aY}{t} \Delta t$$

where a is the area of the material, t is its thickness and Y is Young's modulus.

$$Y = \frac{stress}{strain} = \frac{Ft}{a\Delta t}$$

The charge at the electrodes gives rise to an output voltage E_0,

$$E_0 = \frac{Q}{C} = \frac{dF}{C}$$

where C is the capacitance between the electrodes.

The equivalent circuit of a piezoelectric input transducer is shown in Fig.A3.3. C_C and R_C are the capacitance and the leakage resistance of the piezoelectric element, respectively. R_C is usually high, of the order of 10^8 to 10^{10}ohms and so the resistance between the terminals is, in general, determined by the load resistance R_L (order of 10^6 to 10^7ohms). C_L is the capacitance of the subsequent stage (load) plus that of the connecting cables.

At medium and high frequencies, the voltage E_0 across the load is determined primarily by the capacitance C_C and C_L. These capacitors form a voltage divider, the voltage E_0 is $EC_C/(C_C+C_L)$, independent of the frequency. If the output voltage is large, it can be reduced by an increase of C_L, i.e., by the parallel connection of a shunt capacitor C_S. For more information, see Lion [1959].

(2) PVDF piezofilm

The piezoelectric properties of polymers were already investigated in 1920's. However, the break through was the discovery of strong piezoelectric effect in PVDF achieved by Kawai in 1969. Now a commercial PVDF piezofilm is available at a very modest price on the market. The piezofilm differs in many respects from the other more conventional piezoelectric materials such as certain crystals and ceramics. The piezofilm has the characteristics of flexibility, softness, light weight and relatively low acoustic impedance and is available in very thin films (9~500μm from Kynar[1]) and in large sheets. High humidity has no effect on its characteristics. Particularly for the measurements in this project, its pliability is the most attractive property. It can be easily shaped into any configuration without degrading any of its piezoelectric capabilities so that there was no basic difficulty to manufacture various size of transducers. The mechanical and electrical properties of the Kynar piezofilm are listed in Table A3.1 and several important properties among them are compared with those of other well known piezoelectric materials in Table A3.2. Coordinate system of the piezofilm for properties in Tables is shown in Fig.A3.4. (See Dutta and Kalafut [1990] for more information.)

In this project, the piezofilms with two thickness, 52μm and 110μm, were both preliminarily tested. Then, it was found that the thicker film would always show much better durability against the cavitation loading. The thicker film, 110μm, lasted more than a few hours while the thinner one, 52μm, was damaged within an hour under some severe pressure conditions. Since obviously it was expected that it would not be easy to use the thickest products, 500μm, for this small fabrication, the thickness 110μm was finally chosen as the piezofilm thickness for the sensor for the pressure transducer.

[1]Atochem Sensors Inc., Kynar Piezo Film Department
P.O.Box 799, Valley Forge, PA 19482 USA

Table A3.1 Typical properties of piezofilm

Thickness	t	9,28,52,110,500μm
Piezoelectric strain constant	d_{31} d_{33}	$23x10^{-12}$(m/m)/(V/m) or (C/m)/(N/m) $-33x10^{-12}$(m/m)/(V/m) or (C/m)/(N/m)
Piezoelectric stress constant	g_{31} g_{33}	$216x10^{-3}$(V/m)/(N/m^2) or (m/m)/(C/m^2) $-339x10^{-3}$(V/m)/(N/m^2) or (m/m)/(C/m^2)
Capacitance	C	380pF/cm^2 for 28μm film
Young's modulus	Y	$2x10^9N/m^2$
Speed of sound	c_{v11} c_{v33}	1500m/s 2200m/s
Mass density	ρ	1780kg/m^3
Volume resistivity	P_R	10^{13} ohm meters
Compressive strength		$60x10^6N/m^2$
Tensile strength	T_{11} T_{33}	$160\sim300x10^6N/m^2$ $30\sim55x10^6N/m^2$
Operating temperature		-40~100°C*
Max operating voltage		750V/mil = 30V/μm
Breakdown voltage		2000V/mil = 100V/μm

*with temperature annealing

Table A3.2 Comparative properties of piezofilm and other piezoelectric materials

Materials	Density ρ (kg/m^3)	Young's modulus Y (N/m^2)	Piezoelectric constant g_{33} (V/m)/(N/m^2)	Acoustic impedance ρc_{v33} kg/(m^2/s)
Quartz	2650	77.2×10^9	50×10^{-3}	14.3×10^6
PZT-5	7700	106×10^9	24.8×10^{-3}	21.6×10^6
Rochelle salt	1770	17.7×10^9	90×10^{-3}	5.6×10^6
$BaTiO_3$	5700	110×10^9	5.2×10^{-3}	30×10^6
PVDF Piezofilm	1780	2×10^9	339×10^{-3}	3.9×10^6

(3) Pressure transducer manufacture

The transducer consists of a PVDF piezofilm with silver painting on both sides of it, two wire leads, two layers of polyimide adhesive tapes (No.5413, 3M[2]), a Kapton® insulation film (polyimide film, Du Pont[3]) and a stainless steel target as a base material. Preparation of each part and procedures of setting them up on the target are described below.

a. Target preparation

Stainless steel was selected as the target base material because of its relatively high hardness, so the durability against the cavitation erosion, among several standard metals ordinarily used in laboratory.

The transducer on a stainless steel target consists of a PVDF piezofilm, two leads, two layers of polyimide adhesive tape and a Kapton film for insulation between the silver painted area on the film and the stainless steel target. In order to obtain the very flat and smooth surface exposed to flow after setting the piezofilm into a shallow groove on the target, the target surface had to be recessed to the same depth as the thickness of a piezofilm and a Kapton film plus adhesives, as shown in Fig.A3.1. The thickness of these materials are,

PVDF Piezofilm:	110μm (120μm with silver paint)
Kapton insulation film:	25μm
Cyanoacrylate adhesive:	5μm (approx.)

Thus, the total thickness of 150μm was used as the depth of the recessed groove on the target.

Before setting up these parts inside the groove on the target, the surface of the transducer and particularly the bottom of the groove were cleaned with degreaser and then roughened with emery paper grade No.240 and finally cleaned again with neutralizing liquid to have the best bonding condition for adhesives.

---

[2]3M Industrial Tape and Adhesive Specialties Group
3M House, P.O.Box 1, Bracknell, Berkshire, RG12 1JU, U.K.

[3]Du Pont (U.K.) Limited
Wedgwood Way, Stevenage, Hertfordshire, SG1 4QN, U.K.

b. PVDF piezofilm preparation

The piezofilm was in sheet form 150mm x 150mm with thickness of 110μm and the both sides of the film had been already painted by its manufacturer with silver conductive paint as the electrodes. The sheet was, at first, cut using a scalpel into the shape of the groove, and then the required parts of the silver paint were marked out and the rest was removed by scraping. The final shape of the silver painting left on the both side of the piezofilm is shown in Fig.A3.5. Cross (both side) painted areas are the sensitive part of the transducer. It is located at the position where the cavitation loading is to be measured. The painted strips remaining on either side are the leads from the sensor area of the film which conduct the electric charge to wire leads connections. The wire leads were joined to the connections by threading them through the enlarged areas to give mechanical strength. Good electrical contacts were ensured by painting over the connections with silver conductive paint. The lead connection part should be placed outside the area on the target where damage takes place because it is mechanically the weakest part of this transducer. Six transducers were made, each sensitive areas of 0.140mm^2, 0.301mm^2, 0.777mm^2, 1.35mm^2, 4.43mm^2 and 8.88mm^2.

It should be noted here that the active side of the lead must be connected to the bottom side silver painting. If it is connected to the top side silver painting, the whole painted part on the top side including both the cross painted area and the other single side painted part will act as the sensitive part, because the stainless steel target which is normally earthed or has sufficient electric capacity to act as an electrode of the piezofilm capacitance through a Kapton insulation film. Even more care must be paid with design, if the working liquid were also very conductive; e.g., a liquid metal. In that case, every silver painted area may be regarded as the sensitive part and this should be realized from the early stages of planning the measurements so that suitable design of painting pattern can be devised to minimize the problem.

c. Insulation

Electric insulation is very important to isolate the piezofilm from any electric noise source outside and to avoid unnecessary charge dissipation. Moreover, if some part at the bottom of the piezofilm is not properly insulated, the

sensitive area of the transducer, i.e. the cross painted area, can not be precisely defined. Care should be taken not only with the piezofilm but also with the leads. For the transducer in this project, a sheet of thin Kapton film (25μm) whose resistance is very high was used as the insulation material between the piezofilm and the stainless steel target and vinyl coated wires with small diameter (O.D.=0.5mm) were used for the leads.

d. Adhesive

Ordinary cyanoacrylate type adhesives were used to bond the Kapton insulation film to the target and then the piezofilm to the Kapton insulation film. Basically, cyanoacrylate type adhesives are not very good for bonding PVDF but can be very thin and plain. The "gel" type of the cyanoacrylate was found to be very useful with its primer for filling the gaps and to give sufficient mechanical strength to the joint between the piezofilm and the Kapton film near the connections to the leads. Some gaps were unavoidable because of the parts of the leads must pass between the piezofilm and Kapton insulation. Similarly to protect the leads against the external loading, both the piezofilm and the leads at the connecting part were covered with small amount of epoxy resin adhesives.

e. Protection tape

After setting the Kapton insulation film and the piezofilm with leads inside the groove on the target and making sure that the transducer surface was flat, the whole top surface of the piezofilm and some part of the transducer were covered with two layers of polyimide adhesive tapes (thickness; 70μm, each) for protection against the cavitation damage. Although the polyimide tape is, mechanically, one of the strongest tape commercially available, it lasts only about 20minutes under the testing condition in this project, P_1=120bar and σ=0.03 and at the second optimum stand off distance S_{off2}=40mm. Therefore, the uppermost layer of two tapes was replaced after each testing run before the damage could penetrate to the second layer. Then, at last, the transducer itself was able to survive for longer than a few hours.

f. Pulse height measurement system

In order to carry out the pulse height analysis, analog pulse height measurement system with an input pulse height gate circuit was designed as shown in Fig.A3.6. The system consists of the piezofilm transducer, the input pulse gate circuit, a digital voltmeter, a digital oscilloscope and a counter. Firstly, every input signal detected by the transducer is transmitted to the gate circuit (comparator). Then, only the pulse whose peak height is higher than the preset "gate" threshold level generates a trigger signal to activate the counter. After all, by changing the preset level from low to high, an accumulated pulse height distribution can easily be obtained. The circuit diagram of the gate circuit is shown in Fig.A3.7. The circuit consists of two parts, an operational amplifier (magnification x1.0 and x5.83) and a comparator. However, since the input pulse voltage from the PVDF piezofilm was sufficiently high, as high as 10V, higher amplification was not used.

The merit of the analog signal treatment is its speed and accuracy on catching the peak pulse height value. For example, to expect a reasonably accurate peak value from a pulse as wide as one micro second, the sampling frequency of ten million counts per second or even faster is necessary for a digital method and ten million data per second or more must be stored in a computer memory! Variation of the minimum duration time of a detectable pulse for the gate circuit with various pulse input voltage is plotted in Fig.A3.8. The circuit can count the pulses whose duration time at the half peak value is as short as 0.8μs within the input voltage range up to 10V which was the largest input in the present measurements. Since the maximum detectable frequency of the counter or the pulse resolution is much faster than that of the circuit, which ranges up to 50MHz or down to 20ns, respectively, the response of the total system is determined from the Figure A3.8.

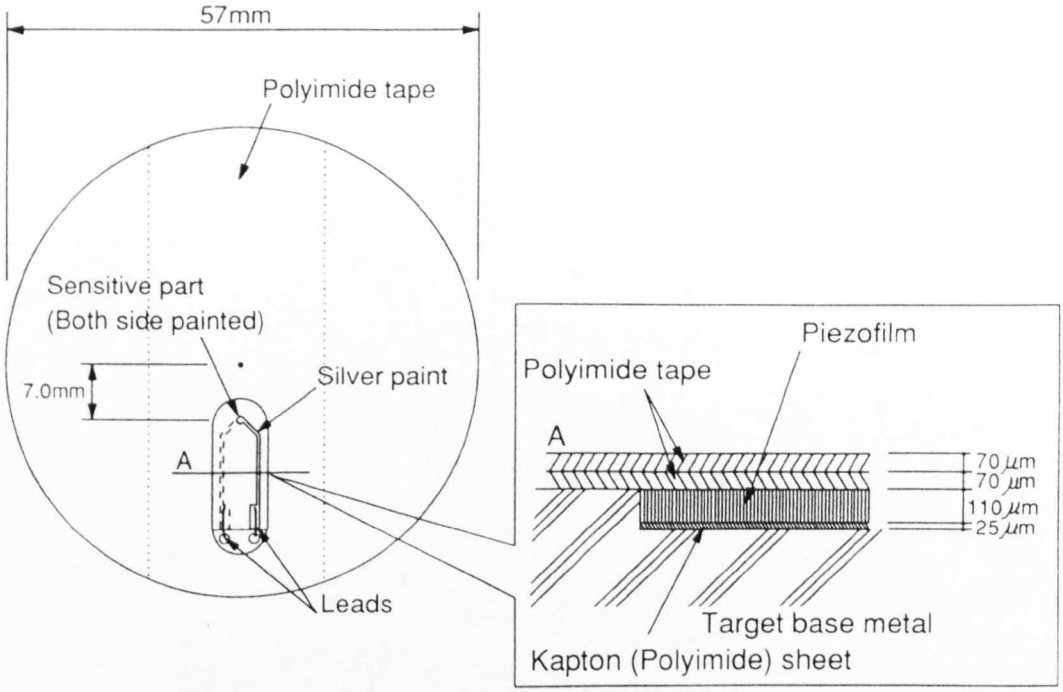

Fig.A3.1 PVDF piezofilm assembly of a pressure transducer.

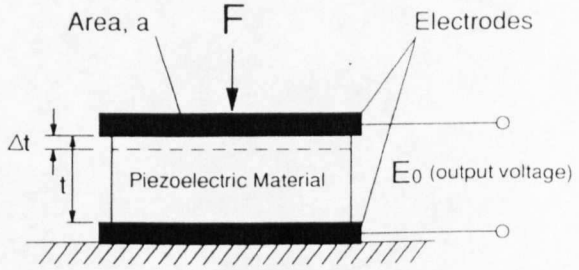

Fig.A3.2 Piezoelectric effect, schematic diagram.

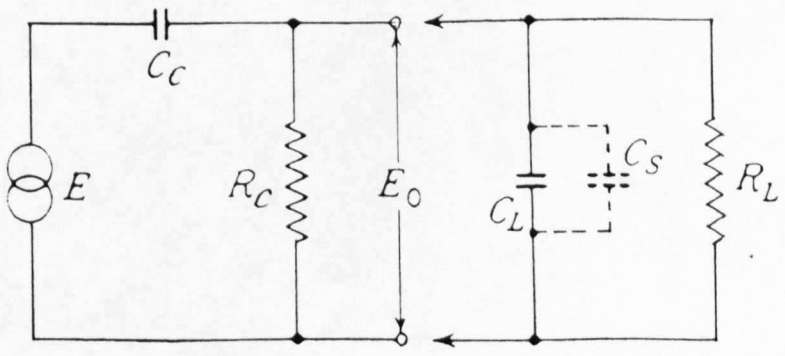

Fig.A3.3 Equivalent circuit of a piezoelectric transducer and electric load.

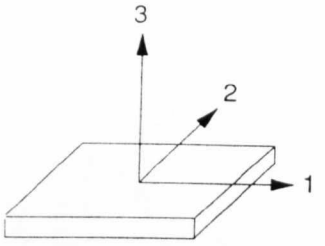

Fig.A3.4 Coordinate system of piezofilm.

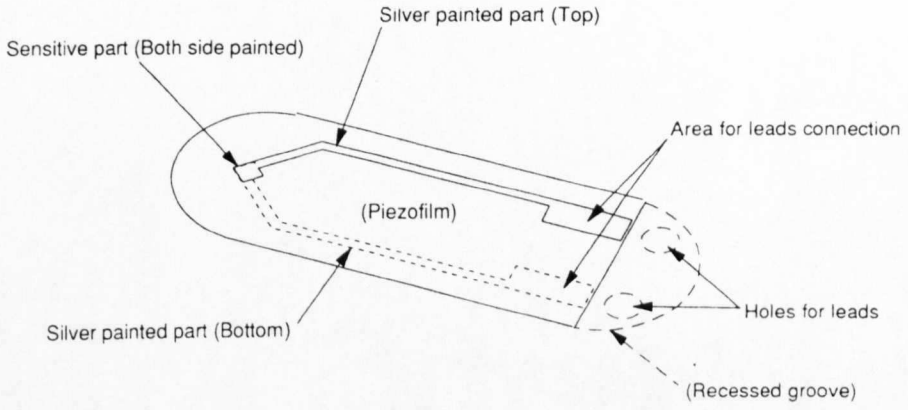

Fig.A3.5 PVDF piezofilm preparation.

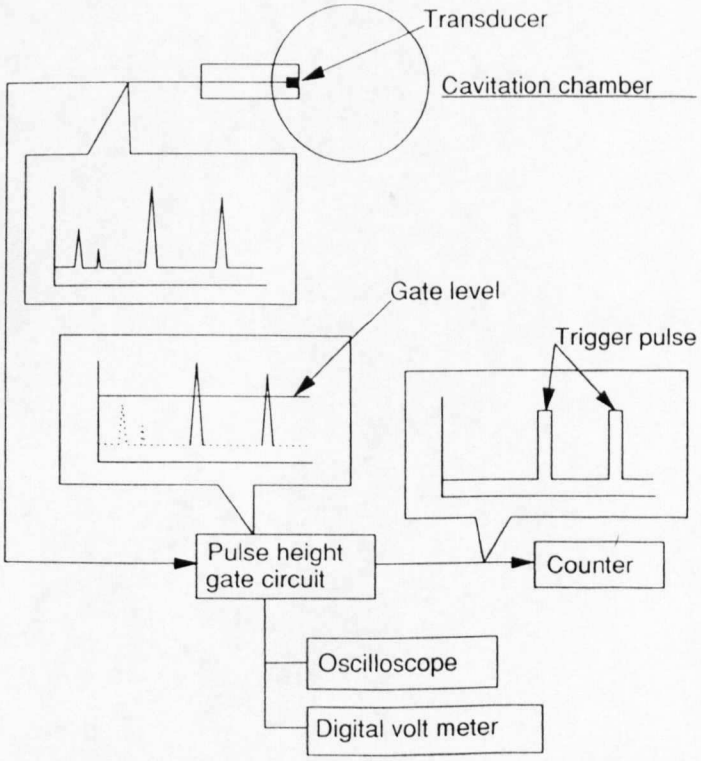

Fig.A3.6 Diagram of pulse height counting system.

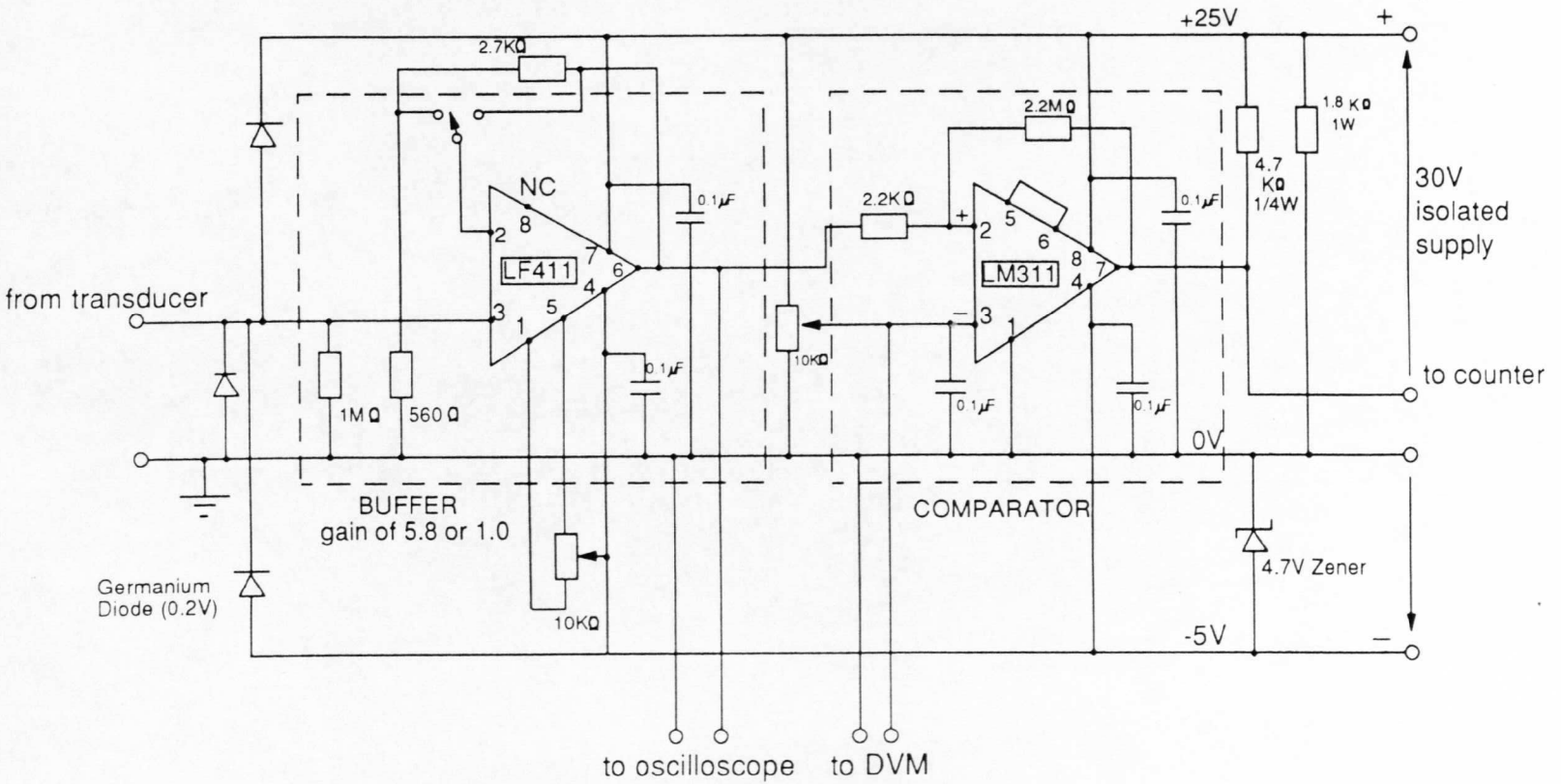

Fig.A3.7 Buffer/comparator circuit (pulse height gate circuit).

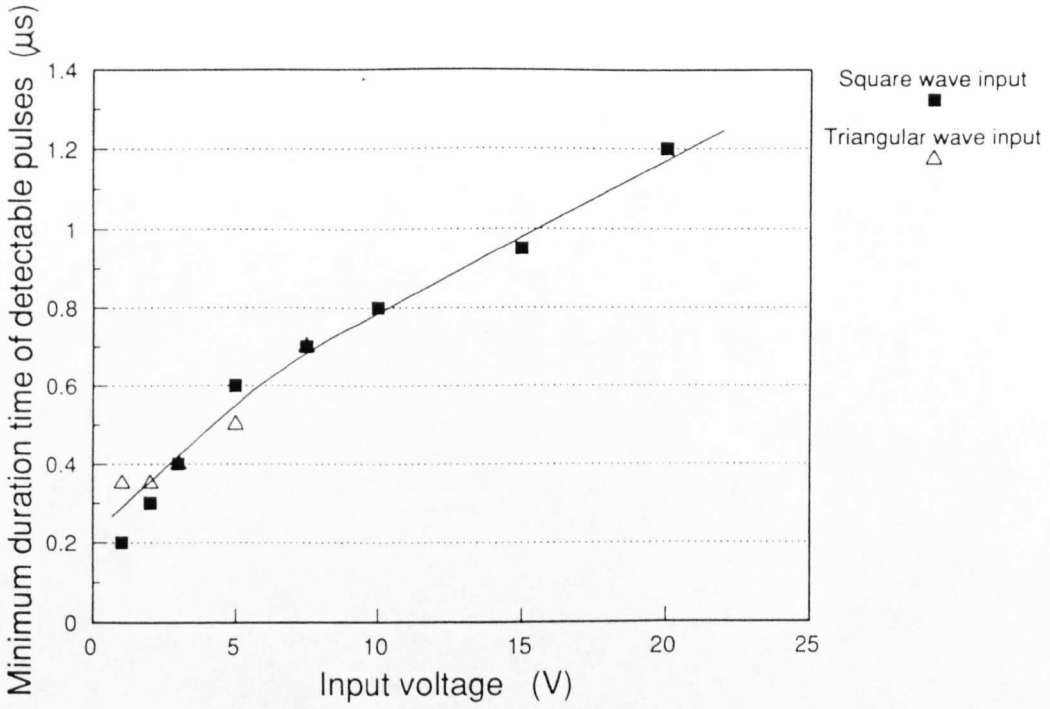

Fig.A3.8 Variation of minimum countable pulse width for comparator circuit with input voltage.

APPENDIX A4: Calibration of PVDF pressure transducers using pencil lead breaking method

Since it was already known from literatures that the duration time of the cavitation loading would be as short as 1~5μs, dynamic loading with extremely fast rise time should be used for calibrating PVDF pressure transducers. As described in the text (Chapter 5), the rise time of steel ball dropping calibration which has been most widely used method so far is around 40~80μs and is very slow compared with the duration time of the cavitation loading pulse.

In order to obtain the calibration value for much faster loading, a calibration device using a pencil lead breaking load was developed. Figure A4.1 shows a drawing of main parts. It consists of a steel plate beam with a pencil lead at one end and a static weight hanging at the centre. The beam is supported on a knife edge at its another end as shown in Fig.A4.1.

Working principle is simple. At first, the active part of the PVDF pressure transducer is placed right under the tip of the pencil lead and then a bottle hanging at the middle of the beam is gradually filled with pre-determined volume of water to provide initial static weight. From the weight of the device, the amount of water poured into the bottle and the ratio between two length of the beam, it is possible to calculate the total static load applied to the pressure transducer at any instant. Finally, when the amount of the filled water reaches the breaking point of the pencil lead, the lead breaks and the applied total static load is suddenly released. Such releasing motion is much quicker than that of the ball in the dropping test, because virtually there is no inertial mass on the transducer. An example of calibration loading signal by the breaking method is shown in Fig.A4.2. After showing the maximum output voltage, the signal is dissipated rather quickly. The rise time of the breaking load is 7~8μs which is up to ten times faster than that of the ball dropping method. Calibration value is obtained by taking the ratio of the applied static force to an output voltage. Some of these values with various loading force magnitudes are compared with those obtained from the steel ball dropping method in Fig.A4.3. Regardless of the rise time difference, they show good agreement with each other and this may suggest that the response of this PVDF piezofilm pressure transducer is very constant and reliable within this loading magnitude and frequency range. Although points

plotted for the ball dropping method in Fig.A4.3 are the values averaged from three drops, variation of the results are even slightly better for the pencil lead breaking method. Because of these advantages, it was decided to use the pencil lead breaking calibration method in the present measurements.

As shown in Fig.A4.1, there is a stopper to prevent the damage of the piezofilm surface due to a direct collision of the bottom edge of the beam with the surface, and are guides to make placing the lead tip on the transducer easier. Since the hardness of the pencil lead can be varied and its length is also adjustable, the breaking point or the magnitude of the calibration force can be easily controlled.

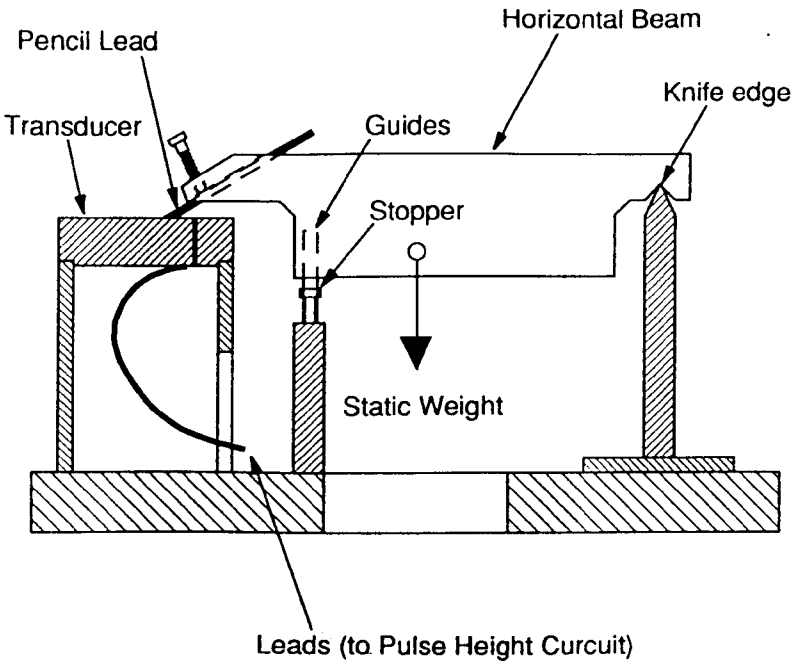

Fig.A4.1 Calibration apparatus using pencil lead breaking load.

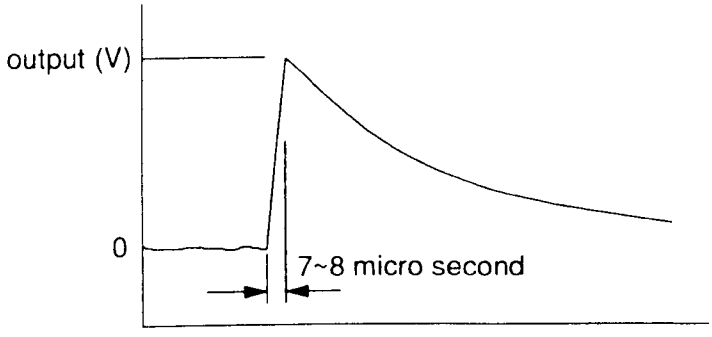

Fig.A4.2 Typical electric output shape of piezofilm produced by pencil lead breaking load.

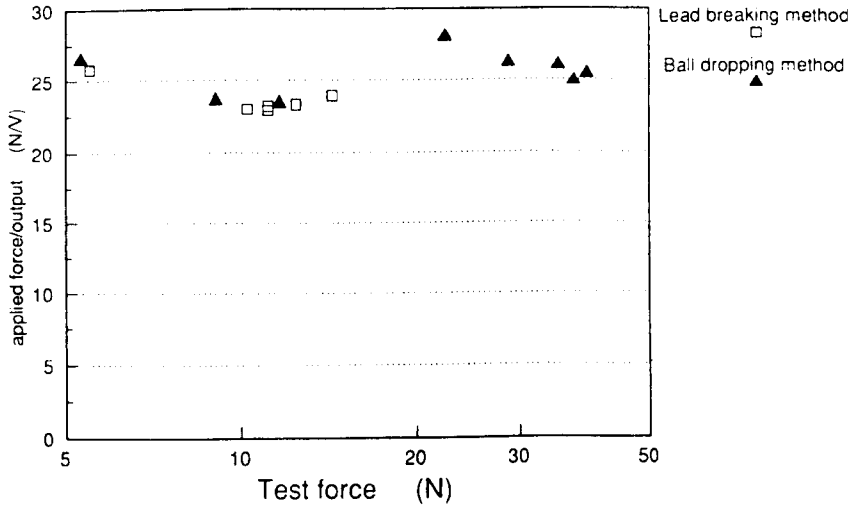

Fig.A4.3 Comparison of calibration values for PVDF pressure transducer between pencil lead breaking method and ball dropping method.

REFERENCE

REFERENCE TABLE

Arakeri,V.H. and Shanmuganathan,V. [1985]
"On the evidence for the effect of bubble interference on cavitation noise"
JFM, 1985, vol.159, pp.131

Backe,W. and Berger,J. [1984]
"Kavitationserosion bei HFA-fluissigkeiten"
Olhydraulik und Pneumatik, 28, Nr.5, 1984, pp.289

Benjamin,T.B. and Ellis,A.T. [1966]
"The collapse of cavitation bubbles and the pressures thereby produced against solid boundaries"
Phil.Trans.Royal Soc. London, s.A, n.1110, v.260, July, pp.221, 1966

Besant [1859]
"Hydrostatics and hydrodynamics"
1859, §158

Bin-Ujang,A.G. [1990]
"The effect of flow pattern on the cavitation and erosion produced by a jet"
Ph.D. Thesis, The University of Nottingham, 1990

Blake,J.R. and Gibson,D.C. [1987]
"Cavitation bubbles near boundaries"
Ann. Rev. Fluid Mech. 19, pp.99, 1987

Bradshaw,B.A.P. and Love,E.M. [1961]
"The normal impingement of a circular air jet on a flat surface"
Reports and Memoranda, Aeronautical Research Council, n.3205, 1961, pp.1

Brunton,J.H. [1970]
"Cavitation damage"
Proc. 3rd Int'l. Conference on Rain Erosion and Associated Phenomena, August, 1970, pp.821

D'Agostino,L. and Brennen,C.E. [1983]
"On the acoustical dynamics of bubble clouds"
ASME Cavitation and Multiphase Flow Forum, pp.72, 1983

D'Agostino,L. and Brennen,C.E. [1989]
"Linearized dynamics of spherical bubble clouds"
JFM, vol.199, pp.155, 1989

Dear,J.P. and Field,J.E. [1988]
"A study of collapse of arrays of cavities"
J.F.M., v.190, pp.409, 1988

De,M.K. and Hammitt,F.G. [1982]
"New method for monitoring and correlating cavitation noise to erosion capability"
Trans.ASME, J.Fluid Eng., 104, 1982, pp.434

Didden,N. and Ho,C.M. [1985]
"Unsteady separation in a boundary layer produced by an impinging jet"
JFM 1985, v.160, pp.235

Donaldson,C.Dup., Snedeker,R.S. and Margolis,D.P. [1971]
"A study of free jet impingement. Part 2. Free jet turbulent structure and impingement heat transfer"
J.Fluid Mech. v.45 part3 1971 pp.477

Duncan,J.H. and Zhang,S. [1991]
"On the interaction of a collapsing cavity and a compliant wall"
JFM v.226, pp.401, 1991

Dutta,P.K. and Kalafut,J. [1990]
"Evaluation of PVDF piezopolymer for use as a shock gauge"
Special Report 90-23, U.S. Army Corps of Engineers, June, 1990

Ellis,A.T. [1956]
"Techniques for pressure pulse measurements and high speed photography in ultra sonic cavitation"
Cavitation in hydrodynamics, Proc.Symp. at N.P.L. 1955 8p.1 publ. H.M.S.O. London 1956

Ellis,A.T. [1965]
"Parameters affecting cavitation and some new methods for their study"
Rep.E115.1, Cal. Tec., Hydrodyn. Lab. 1965

Fry,S.A. [1989]
"The damage capacity of cavitating flow from pulse height analysis"
Trans.ASME, J.Fluid Eng., v.111, 1989, pp.502

Fujikawa,S. and Akamatsu,T. [1978]
"Experimental investigations of cavitation bubble"
Bulletin of J.S.M.E., v.21, n.152, Feb. pp.223, 1978

Fujikawa,S. and Akamatsu,T. [1980]
"Effects of the non-equilibrium condensation of vapour on the pressure wave produced by the collapse of a bubble in a liquid"
J.Fluid Mech., 97, pp.481, 1980

Gibson,D.C. and Blake,J.R. [1982]
"The growth and collapse of bubbles near deformable surfaces"
Applied Scientific Research 38, pp.215, 1982

Gilmore,F.R. [1952]
"The growth and collapse of a spherical bubble in a viscous compressible liquid"
Rep.26-4, Caltec., Hydrodyn. Lab. 1952

Gibson,D.C. [1968]
"Cavitation adjacent to plane boundaries"
Aus. Conf on Hyd. and Fluid Mech. pp.210, 1968

Hansson,I. and Mørch,K.A. [1980]
"The dynamics of cavity clusters in ultrasonic (vibratory) cavitation erosion"
J.Appl.Phys., 51, pp.4651, 1980 and 52, pp.1136, 1981

Hansson,I., Kedrinskii,V. and Morch,K.A. [1982]
"On the dynamics of cavity clusters"
J.Phys.D:Appl.Phys., 15, pp.1725, 1982

Herring,C. [1941]
Colombia Univ. NDRC Rep.C-4-sr10-010, 1941

Hickling,R. and Plesset,M.S. [1964]
"Collapse and rebound of a spherical bubble in water"
Phys.Fluids, 7, pp.7, 1964

Hutton,S.P. and Lobo Guerrero,J. [1975]
"The damage capacity of some cavitating flows"
Proc. 5th Conf. on Fluid Machinery, Budapest, 1975, pp.427-438

Ivany,R.D. and Hammitt,F.G. [1965]
"Cavitation bubble collapse in viscous compressible liquids - numerical analysis"
Trans.ASME, Ser.d, 87, pp.977, 1965

Jones,I.R. and Edwards,D.H. [1960]
"An experimental study of the forces generated by the collapse of transient cavities in water"
J.Fluid Mech., 7, pp.596, 1960

Kawai,H. [1969]
"The piezoelectricity of PVDF"
Japanese Journal of Applied Physics, 8, pp.975, 1969

Kimoto,H., Kamoto,A., Hirose,T. and Yoshinobu,H. [1987]
"A study on impulsive pressure of a collapsing cavitation bubble (Evaluation of the effect of a water microjet)"
JSME, Int.J., v.30, n.261, pp.449, 1987

Kimoto,H. [1987]
"An experimental evaluation of the effects of a water microjet and a shock wave by a local pressure sensor"
ASME Int. Symp. on Cavitation Research Facilities and Techniques, Boston, 1987 pp.217

Kirejczyk,J. [1979]
"The energy flux of cavitating flow"
Proc. 6th Conf. on Fluid Machinery, Budapest, 1979, pp.555

Kirkwood,J.G. and Bethe,H.A. [1942]
OSRD Rep.588 1942

Kleinbreuer,W. and Pohl,M. [1981]
"Vorgane beim materialabtrag durch kavitation in olhydraulischen systemen"
olhydraulik und pneumatik v.25 n.5 1981 pp.409
and English translation,
"Processes in material erosion due to cavitation in (oil) hydraulic systems"

Kleinbreuer,W. [1976]
"Werkstoffzerstorung durch kavitation in olhydraulichen systemen"
Industrie-Anzeiger v.98 n.61 1976 pp.1096
and English translation,
"Damage of metals through cavitation in hydraulic systems"

Kleinbreuer,W. [1977]
"Kavitationserosion in hydraulischen systemen"
Industrie Anzeiger 99, Nr.3, 1977, pp.609
and English summary,
"Cavitation erosion in hydraulic systems"

Kleinbreuer,W. [1980]
"MaBnahmen zur vermeidng bzw. verminderung von kavitationserosion in hydraulischen systemen"
Olhydraulik und Pneumatik, 24, Nr.6, 1980 pp.455

Kling,C.L. and Hammitt,F.G. [1972]
"A photographic study of spark-induced cavitation bubble collapse"
J.Basic Eng., 94, pp.825, 1972

Knapp,R.T. and Hollander,A. [1948]
"Laboratory investigations of the mechanism of cavitation"
Trans.A.S.M.E., v.70, pp.419, 1948

Knapp,R.T., Daily,J.W. and Hammit,F.G. [1970]
"Cavitation"
McGrow-Hill, New York, 1970

Knapp,R.T. [1955]
"Recent investigations on the mechanics of cavitation and cavitation damage"
Trans.A.S.M.E. 1955 v.77 pp.1045

Kornfeld,M. and Suvorov,L. [1944]
"On the destructive action of cavitation"
J.Appl.Phys., v.15, n.6, pp.495, 1944

Lauterborn,W. and Bolle,H. [1975]
"Experimental investigation %w cavitation bubble collapse in neighbourhood of a solid boundary"
J.Fluid Mech., v.72, Nov. pp.391, 1975

Lauterborn,W. [1974]
"General and basic aspects of cavitation"
Proc. Finite-Amplitude Wave Effects in Fluids (Bjorno,L., Ed.), I.P.C. Sci.Tech.Press, Guilford, pp.195, 1974

Lichtarowicz,A. and Kay,P. [1983]
"Erosion testing with cavitating jets"
Proc.6th Int'l Conf. on Erosion by Liquid and Solid Impact 1983 pp.15-1

Lichtarowicz,A. and Scott,P.J. [1979]
"Erosion testing with cavitating jet"
Proc.5th Int'l Conf. on Erosion by Solid and Liquid Impact 1979 pp.69-1

Lichtarowicz,A. [1972]
"Use of a simple cavitating nozzle for cavitation erosion testing and cutting
Nature Physical Science v.239 n.9 Sept. 1972 pp.63

Lichtarowicz,A. [1974]
"Experiments with cavitating jets"
Proc.2nd Int.Symp.on Jet Cutting Technology, Cambridge, 1974, pp.D1-1

Lichtarowicz,A. [1984]
"Hydromechanics of cavitating jets and their applications"
Proc.Symp.Water Jet Technology, Tokyo Dec. 1984 pp.1-17

Lichtarowicz,A. [1979]
"Cavitating jet apparatus for cavitation erosion testing"
A.S.T.M. STP 664 pp.518 1979

Lichtarowicz,A. [1981]
"Erosion testing with cavitating jet"
Proc.ASME The Fluid Eng. Conf. on "Cavitation erosion in fluid systems", Colorado, 1981, pp.153

Lion,K.S. [1959]
"Instrumentation in scientific research"
McGraw-Hill New York 1959

Lush,P.A. [1983]
"Impact of a liquid mass on a perfectly plastic solid"
J.Fluid Mech. 1983 v.135 pp.373

Mader,C.L. [1965]
"Initiation of detonation by the interaction of shocks with density discontinuities"
The Physics of Fluids, vol.8, No.10, October, pp.1811, 1965

Mørch,K.A. [1978]
Proc. Acoust. Cavitation meeting, 1977 (Institute of Acoustics, London) 1978, pp.62

Mørch,K.A. [1979]
"Dynamics of cavitation bubbles and cavitating liquids"

Treatise on materials science and technology, v.16, "Erosion"(Preece,C.M.:Editor), Academic Press, New York pp.309, 1979

Mørch,K.A. [1980]
"On the collapse of cavity clusters in flow cavitation"
Proc.1st Int.Conf.Cavitation and Inhomogeneities in Underwater Acoustics 1979 Springer Ser. in Electrophys, 4, 1980 pp.95

Mørch,K.A. [1980]
"On the collapse of cavity clusters in flow cavitation"
Springer Series in Electrophysics, vol.4, "Cavitation and Inhomogeneities" 1980, pp.95

Mørch,K.A. [1982]
"Energy considerations on the collapse of cavity clusters"
Appl.Sci.Res., 38, pp.313, 1982

Mørch,K.A. [1987]
"The structure of cavity clusters and their damage capability"
Proc.7th Int.Conf.on Erosion by Liquid and Solid Impact, 1987, pp.26-1

Naude,C.F. and Ellis,A.T. [1961]
"On the mechanism of cavitation damage by nonspherical cavities collapsing in contact with solid boundary"
Trans. A.S.M.E. J.Basic Eng. v.83D, n.4, Dec. pp.648, 1961

Okada,T., Iwai,Y. and Awazu,K. [1989]
"A study of cavitation bubble collapse pressures and erosion Part 1 : A method for measurement of collapse pressures"
Wear, 133, 1989 pp.219

Plesset,M.S. and Chapman,R.B. [1971]
"Collapse of initially spherical vapour cavity in the neighbourhood of a solid boundary"
J.Fluid Mech., 47, pp.283, 1971

Plesset,M.S. [1949]
"The dynamics of cavitation bubbles"
Trans.A.S.M.E. J.Appl.Mech. v.71 pp.1277, 1949

Ramamurthy,A.S. and Bhaskaran,P. [1979]
"Velocity exponent for erosion and noise due to cavitation"
A.S.M.E. publ.no.79-FE-9

Rao,B.C.S. and Buckley,D.H. [1983]
"Cavitation pitting and erosion of aluminium 6061-T6 in mineral oil and water"
NASA, Tech.Paper 2146, 1983, pp.1

Rayleigh,L. [1917]
"On the pressure developed in a liquid during the collapse of a spherical cavity"
Phil.Mag. v.34 pp.94, 1917

Robinson,M.J. and Hammitt,F.G. [1967]
"Detailed damage characteristics in cavitation venturi"
Trans.ASME, J.Basic Eng., 89(1), 1967, pp.161

Rouse,H. [1953]
"Cavitation in the mixing zone of a submerged jet"
La Houille Blanche 1953 v.8 n.1 pp.9

Selim,S.M.A. and Hutton,S.P. [1983]
"Classification of cavity mechanics and erosion"
Proc.IMechE Second Int'l Conf. on Cavitation, 1983, pp.41

Selim,S.M.A. [1981]
"Cavitation erosion in fluid flow"
Ph.D. thesis, Dept. Mech. Eng. Southampton University, 1981

Shima,A., Tomita,Y., Gibson,D.C. and Blake,J.R. [1989]
"The growth and collapse of cavitation bubbles near composite surfaces"
JFM v.203, pp.199, 1989

Shimizu,S. and Yamaguchi,A. [1988]
"Erosion due to impingement of cavitating jet" (Japanese)
J.Japan Hydraulics and Pneumatics Soc. v.19 n.1 1988 pp.68

Shimizu,S. and Yamaguchi,A. [1989]
"Erosion due to impingement of cavitating jet" (in Japanese)
Spring Annual Meeting of Japan Hydraulics and Pneumatics Soc., 1989, pp.17

Shimizu,S., Murai,H. and Nishii,S. [1990]
"Effect of nozzle lip on structure of two-dimensional submerged jets"
Proc.10th Int'l Symp. on Jet Cutting Technology, Amsterdam 1990 paper.B3

Stinebring,D.R., Holl,J.W. and Arndt,R.E.A. [1980]
"Two aspects of cavitation damage in the incubation zone: scaling by energy considerations and leading edge damage"
Trans.ASME, J.Fluid Eng., 102, 1980, pp.481

The,M.N'G., Franc,J.P. and Michel,J.M. [1987]
"On correlating pitting rate and pressure peak measurements in cavitating flows"
ASME, Intl. Symp. on Cavitation Research Facilities and Techniques, Boston, 1987

Thiruvengadam,A. [1974]
"Handbook of cavitation erosion"
Hydronautics Incorporated, 1974, pp.135-136

Thomas,G.P. and Brunton,J.H. [1970]
"Drop impingment erosion of metals"
Proc. Roy. Soc. London A.314, pp.549 1970

Tomita,Y. and Shima,A. [1986]
"Mechanisms of impulsive pressure generation and damage pit formation by bubble

collapse"
JFM v.169, pp.535, 1986

Tomita,Y., Shima,A. and Ohno,T. [1984]
"Collapse of multiple gas bubbles by a shock wave and induced impulsive pressure"
J.Appl.Phys., 56, 1984, pp.125

Trevena,D.H. [1987]
"Cavitation and tension in liquids"
Adam Hilger, Bristol and Philadelphia, 1987

Trilling,L. [1952]
J. Appl. Phys. 23, 1952, pp.14

Tulin,M.P. [1969]
"On the creation of ultra-jet"
Problems of hydrodynamics and continuum mechanics, edited by Sedov,L.I., Moscow, pp.725, 1969

van Wijngaarden,L. [1964]
"On the collective collapse of a large number of gas bubbles in water"
Proc.11th Int.Congr.of Applied Mechanics, Munich, (Gortler,H. Ed.), 1964, pp.854

Vogel,A., Lauterborn,W. and Timm,R. [1989]
"Optical and acoustic investigations of the dynamics of laser-produced cavitation bubbles near a solid boundary"
JFM v.206, pp.299, 1989

Vyas,B. and Preece,C.M. [1976]
"Stress produced in a solid by cavitation"
J.Appl.Phys., 47, n.12, 1976, pp.5133

Yahiro,T. and Yoshida,H. [1974]
"On the characteristics of high speed water jet in the liquid and its utilization on induction grouting method"
2nd Intl. Symp. on Jet Cutting Technology, Cambridge, 1974, pp.G4-41

Yamaguchi,A. and Shimizu,S. [1987]
"Erosion due to impingement of cavitating jet"
Trans.A.S.M.E. J.Fluid Eng. v.109 n.4 1987 pp.442

Yamaguchi,A. Shimizu,S. et al. [1986]
"Erosion by impingement of jet accompanied with cavitation" (in Japanese)
Spring Annual Meeting of Japan Hydraulics and Pneumatics Soc., 1986, pp.53

Young,F.R. [1989]
"Cavitation"
McGrow-Hill, London, 1989